Master's thesis

NTNU
Norwegian University of Science and Technology
Faculty of Natural Sciences
Department of Physics

Cathrine Thorsen Becker

Polarised Synchrotron Emission from Electrons in the Galactic Magnetic Field

Master's thesis in Applied Physics and Mathematics
Supervisor: Michael Kachelriess
June 2024

NTNU
Norwegian University of
Science and Technology

Cathrine Thorsen Becker

Polarised Synchrotron Emission from Electrons in the Galactic Magnetic Field

Master's thesis in Applied Physics and Mathematics
Supervisor: Michael Kachelriess
June 2024

Norwegian University of Science and Technology
Faculty of Natural Sciences
Department of Physics

Abstract

The fractional polarisation measured towards the northern Galactic pole is much lower than expected from synchrotron emission. In this thesis we investigate different Galactic magnetic field models to fit polarisation and intensity data. We provide descriptions of both turbulent magnetic fields and the theory of synchrotron radiation, with a focus on polarisation. Formulas for the degree of circular and linear polarisation are derived for a single electron and a power-law electron distribution. Furthermore, magnetic field models are presented for turbulent and regular fields. We argue that the regular field models may not reproduce the low measured polarisation degrees, either alone or in combination with a turbulent field. An extended turbulent field may be added to solve the issue. A simplified total field model consisting of a turbulent disk and corona field with a regular halo field is also investigated. Simulations of synchrotron polarisation and intensity for this model may be in agreement with the measured data in a significant amount of cases, for some given parameters and assumptions.

Sammendrag

Polarisasjonsfraksjonen målt mot den nordlige galaktiske polen er mye lavere enn forventet fra synkrotronstråling. I denne oppgaven undersøker vi ulike galaktiske magnetfeltmodeller for å sammenligne med polarisasjons- og intensitetsdata. Vi beskriver både turbulente magnetfelt og teorien rundt synkrotronstråling, med et fokus på polarisasjon. Formler for den sirkulære og lineære polarisasjonsgraden blir derivert for et enkelt elektron og en distribusjon av elektroner som følger en potenslov. Videre presenterer vi magnetfeltmodeller for turbulente og regulære felt. Vi argumenterer for at de regulære feltmodellene ikke kan reprodusere de lave polarisasjonsverdiene målt, verken alene eller i kombinasjon med et turbulent felt. Et utvidet turbulent felt kan inkluderes for å løse problemet. En forenklet totalfeltmodell bestående av et turbulent disk- og korona-felt med et regulært "halo"-felt blir også utforsket. Simulasjoner av synktrotronpolarisasjon og -intensitet for denne modellen kan stemme overens med de målte dataene i et betydelig antall tilfeller, gitt visse parametre og antagelser.

Preface

This thesis concludes my Master of Science in astrophysics at the Norwegian University of Science and Technology (NTNU). It is a part of the 5-year study program Applied Physics and Mathematics with main profile in Applied Physics, and is written in the spring of 2024 under the supervision of Prof. Michael Kachelriess at the Department of Physics. The work on this thesis is a continuation of a specialisation project done in the fall of 2023. With minor corrections and additions, it therefore includes some chapters taken directly from the project report. This includes parts of the introduction, a few sections of chapter 2, most of chapter 3 and 4, as well as some parts of chapter 5 and 8.

Writing this thesis has been a challenge, albeit a very enjoyable one. I would especially like to thank Prof. Michael Kachelriess for his supervision on this interesting project. His comments and helpful critique throughout the year have been essential in shaping this thesis. I would also like to thank my friends and family who have supported me throughout my studies, and in everything I choose to do.

June 5, 2024
Cathrine Thorsen Becker

Contents

List of figures

List of tables

Chapter 1

Introduction

Arguably the most important emission process in astrophysics is synchrotron radiation. Synchrotron radiation is electromagnetic emission from ultra-relativistic charged particles accelerated by magnetic fields. This interaction of charged particles, in particular electrons, with the magnetic fields of our Universe dominates most of high-energy astrophysics, and its characteristics are therefore of large interest.

The theory of relativistic electrons emitting electromagnetic radiation in a uniform magnetic field was treated by Schott as early as 1912. However, the first direct observation of synchrotron radiation was made much later, in 1947. The observation was made by chance by a technician in a 70 MeV synchrotron[1] at the General Electric Laboratory in Schenectady, New York. Ivanenko and Sokolov in 1948 and Schwinger in 1949 developed the theory of synchrotron radiation, and Sokolov and Ternov in 1956 and Westfold in 1959 the theory of its polarisation effects. These developments are the basis for the modern treatment of synchrotron radiation, although much of the theory can be dated back to the nineteenth century. In particular, Larmor derived an expression for the total power radiated by an accelerated charged particle in 1897, the same year as the discovery of the electron by Thomson. Just one year later, in 1898, Liénard extended the treatment to relativistic particles.

In the field of astrophysics, it became clear in 1950 that the observed radio emission required the presence of magnetic fields, and that the synchrotron radiation should be highly polarised. In 1953 it was suggested by Shklovsky that the radiation from the Crab Nebula was due to synchrotron radiation, which was later confirmed by observations. In particular, observations of optical linear polarisation were made by Vashikadze in 1954 and Dombrovski in 1954. Additionally, in 1957 Mayer et al. detected polarised radio emission from the Crab Nebula at optical wavelengths. Further observations have lead to the conclusion that the Milky Way contains widespread, significant magnetic fields, and that synchrotron radiation processes are responsible for the majority of the radio emission in the Galaxy. The presence of magnetic fields in galaxies are indicated through low-frequency radio observations where non-thermal spectra are found. Specifically, Mathewson et al. in 1972 were the first to detect radio linear polarisation from a nearby galaxy, the Whirlpool Galaxy (M51)[2].

[1] A circular particle accelerator. Today the largest synchrotron-type accelerator is the Large Hadron Collider (LHC) finished in 2008 at CERN in Switzerland.

[2] See Refs. [1, 2, 3, 4] for further historical context.

1.1 Motivation and objectives

The cosmic microwave background (CMB) and Galactic emission spectra are shown in Fig 1.1. At frequencies below 30 GHz, synchrotron radiation from cosmic ray (CR) electrons is the main emission process [5]. We see that in this range, the synchrotron emission dominates over both the free-free and dust emission. Understanding the dominant component of the Galactic radio emission is central for understanding the Galactic structure as a whole. However, this is not an easy task.

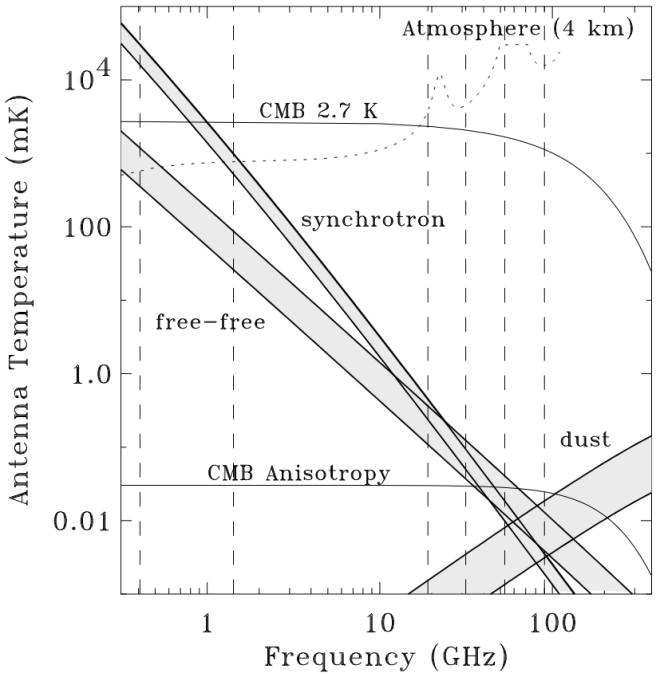

Figure 1.1: CMB and Galactic emission spectra at Galactic latitudes $15° < |b| < 75°$, including the ranges of synchrotron, free-free, dust and atmospheric emission. From Smoot [6].

Observations of the radio emission towards the northern Galactic pole from the C-Band All Sky Survey (C-BASS) project give the fractional polarisation in Fig. 1.2. The polarisation is lower than 10% in almost all pixels, and the resulting mean degree of polarisation is 3.3% [7]. This measured polarisation degree is much lower than expected from synchrotron radiation in the Galactic magnetic field (GMF) by commonly used numerical models. The measured values therefore question our current methods of modelling the magnetic fields of our Galaxy.

To create a realistic description of the GMF is very difficult, as there are several components that need to fit all the measured data. Usually models are optimised to fit a few different parameters, however GMF models often give too high polarisation of synchrotron radiation compared with the result of the C-BASS project. The Milky Way is believed to have a large-scale coherent magnetic field, as well as a small-scale turbulent magnetic field. The measured low polarisation degrees may point to a stronger or more widespread turbulent component than originally expected and accounted for in GMF models.

Simulations of synchrotron radiation in magnetic fields require, however, a theoretical foundation. The motivation for this thesis is therefore to both understand the process of synchrotron radiation and its theory of polarisation, as well as understand and investigate different Galactic magnetic field models. The objectives of the thesis are the following.

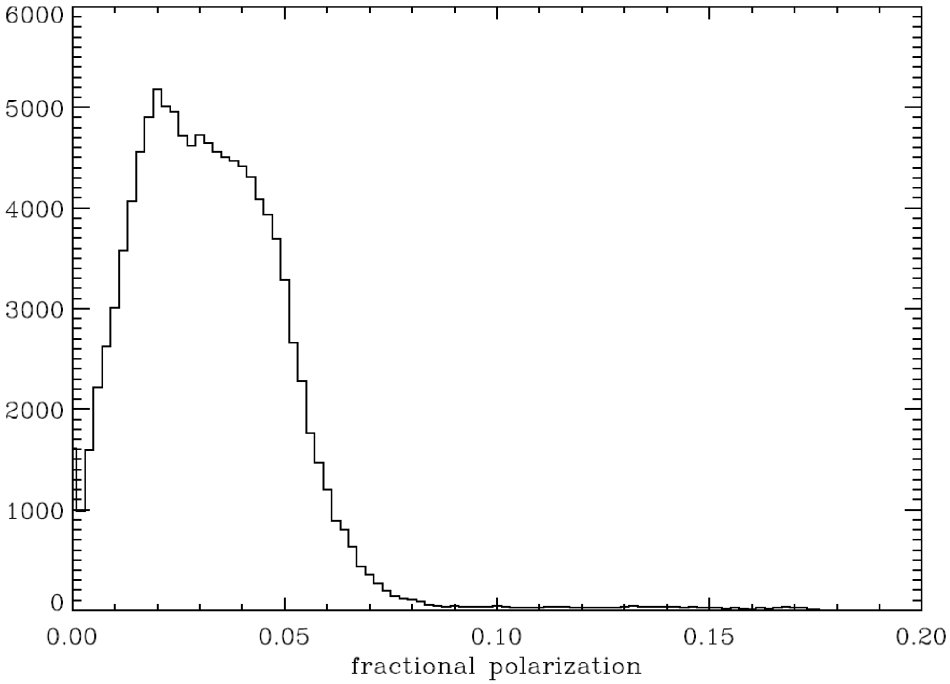

Figure 1.2: Observed fractional polarisation of the radio emission towards the northern Galactic pole from the C-BASS project. From Leahy [8].

- Describe and discuss the magnetic fields in our Galaxy. Considering both the structure of the GMF and the theory of turbulence is essential for investigating numerical models.
- Theoretically describe the process of synchrotron radiation, both for a single electron and a collection of electrons with a power-law distribution. The theory is well known, and the comprehensive treatments found in the books by Rybicki and Lightman [9] and Longair [10] will be used.
- Derive and discuss formulas for the degree of polarisation of synchrotron radiation. The description of polarisation proposed by Westfold [11] in 1959 and Legg and Westfold [12] in 1968 will be used to consider both the linear and circular degree of polarisation.
- Use numerical models to simulate synchrotron radiation in magnetic fields. We wish to investigate which parameters of given GMF models give polarisation degrees in accordance with the low measurements of the C-BASS project.

1.2 Structure of the thesis

The main part of the thesis can essentially be divided into two parts. The first part consists of chapters 2-6 and contains the theory of magnetic fields and synchrotron radiation. The second part consists of chapters 7-8 and contains numerical simulations, results and a final discussion. Lastly, the main results and conclusions of the thesis are summarised in chapter 9. Outside the main part of the thesis, we have appendix A-C, which include some additional derivations and discussions, as well as nomenclature. Below is a more detailed overview of the chapters of the thesis.

Chapter 2 - Magnetic fields in the Universe. In this first chapter we discuss the magnetic fields in our Galaxy and Universe, including the overall structure of the GMF and turbulence. Here, we also present two models used for our numerical simulations.

Chapter 3 - Radiation of relativistic particles. This is the first of several chapters specifically focused on the theory of synchrotron radiation. The most basic theory of synchrotron radiation is introduced, from how a relativistic charged particle moves in a magnetic field to its total emitted power and radiation field.

Chapter 4 - Spectrum of synchrotron radiation. In this chapter we consider the intensity spectrum of synchrotron radiation. The expression for emitted power per frequency of a single particle is derived and used to find the spectrum of a power-law distribution of electrons. In addition, the last section introduces restrictions to the derived theory.

Chapter 5 - Polarisation. Building on the previous chapters, we now consider the polarisation of synchrotron radiation in order to calculate the degree of circular and linear polarisation. The emission-polarisation tensor and the Stokes parameters are derived, both for a single electron and a power-law electron distribution.

Chapter 6 - Radiative transfer. The last chapter of theory includes a brief discussion of radiative transfer, including the line-of-sight integral and diffusion. This chapter provides us with the final methods necessary for our numerical simulations.

Chapter 7 - Numerical simulations and results. With all the theory outlined in the previous chapters, we now present the numerical simulations and their results. Here we consider different Galactic magnetic field structures, and calculate both polarisation degrees and intensity profiles.

Chapter 8 - Discussion. In the discussion, the results from the previous chapter are further analysed and discussed in more detail.

Chapter 9. Conclusion. The final chapter of the main part of the thesis contains a short summary and our conclusions based on the discussions in the previous chapter.

Appendix A - Useful integrals. Throughout the thesis, some special integrals are used. These are presented and derived in this appendix.

Appendix B - Second order pitch angle distribution approximation. Adding on the derivation of the emission-polarisation tensor in chapter 5, we consider a higher order approximation in the particle pitch angle distribution. The derivation of the emission-polarisation tensor is included, as well as a brief discussion on its relevance.

Appendix C - Nomenclature. For a better overview of the abbreviations, symbols and physical constants used throughout the thesis, the most relevant ones are presented here.

Chapter 2

Magnetic fields in the Universe

Magnetic fields in the Universe are still not well understood, although they are important in many astrophysical processes. In particular, the magnetic fields may be turbulent. Turbulence is characterised by disordered, or chaotic, motion of flows and formations of eddies [13]. It is the result once some amount of friction is allowed in the treatment of a fluid. The behaviour of turbulent flows is still an unresolved problem in physics, albeit progressions in the field are consistently being made.

In this chapter we will introduce the Galactic magnetic field (GMF) and discuss its structure, as well as which effects and processes are used to measure the magnetic fields in our Galaxy and Universe. We intend to further motivate the importance of understanding synchrotron radiation given the turbulent GMF. We will also briefly look at magnetohydrodynamic (MHD) turbulence, and describe models used to generate both turbulent and regular magnetic fields.

2.1 The Galactic magnetic field

Magnetic and electric fields are described by the well-known Maxwell's equations, which are (in Gaussian-cgs units)

$$\nabla \cdot \mathbf{E} = 4\pi\rho, \tag{2.1.1a}$$

$$\nabla \cdot \mathbf{B} = 0, \tag{2.1.1b}$$

$$\nabla \times \mathbf{E} = -\frac{1}{c}\frac{\partial \mathbf{B}}{\partial t}, \tag{2.1.1c}$$

$$\nabla \times \mathbf{B} = \frac{4\pi}{c}\mathbf{j} + \frac{1}{c}\frac{\partial \mathbf{E}}{\partial t}. \tag{2.1.1d}$$

Here, $\mathbf{B}$ is the magnetic field, $\mathbf{E}$ is the electric field, $\mathbf{j}$ is the electric current density, ρ is the charge density and c is the speed of light. Together with the Lorentz force law, which we will consider in Sec. 3.1, these equations are the foundation of classical electromagnetism. Any electromagnetic system in vacuum must necessarily obey the laws of Eq. (2.1.1). The first two laws are also commonly known as Gauss' law, while the third and fourth are known as the Maxwell–Faraday law and Ampère's (or Maxwell-Ampère's) law, respectively.

Maxwell's equations provide us with a tool to describe the behaviour of magnetic (and electric) fields along with charges and currents. The existence of magnetic fields has been established to be present not only on Earth, but throughout the Universe; in stars, pulsars, quasars, intergalactic space and galaxies such as ours; the Milky Way. We still do not know the origin of the first magnetic fields, and the generation of the first "seed" fields remains a mystery. However,

the matter in the Universe is mostly ionised, which means that magnetic fields can be generated [3].

The non-thermal parts of the interstellar medium (ISM) consists of significant magnetic fields and cosmic rays (CRs). The magnetic fields contribute to about half of the pressure balancing the ISM against gravity, and thus play an important role in the Galactic structure [14]. In particular they influence the gas density and the star formation rate. The evolution of galaxies and accretion of gas, as well as in- and outflows are also affected by GMFs and CRs [3].

The GMF has been measured to have a mean strength of a few μG [14]. The magnetic field varies throughout the ISM and objects can have magnetic field strengths much higher than this. In particular, compact objects like white dwarfs can have surface magnetic fields up to 10^9 G, while neutron stars can have surface magnetic fields in the range 10^8 to 10^{15} G [15]. The central magnetic field of a white dwarf can reach 10^{13} G, while the most extreme case of neutron stars, magnetars, can have central magnetic fields up to 10^{18} G. In comparison, Earth's magnetic field has an average strength of about 0.5 G [16].

We will in Sec. 2.2 look into different methods of measuring the GMF. However, to characterise the magnetic field in the Milky Way is a difficult task, and no magnetic field model can fit all the measured data [17]. The task is made even more difficult considering the Earth is located within the Milky Way and we are not outside observers. Nevertheless, we may make some distinctions of the structure of the Milky Way and its magnetic field. In Fig. 2.1, a diagram of the structural components of the Galaxy is shown. The figure presents a side view of the Milky Way, where the coordinate system is defined by choosing the x-axis horizontally with the Sun at negative x and the z-axis vertically.

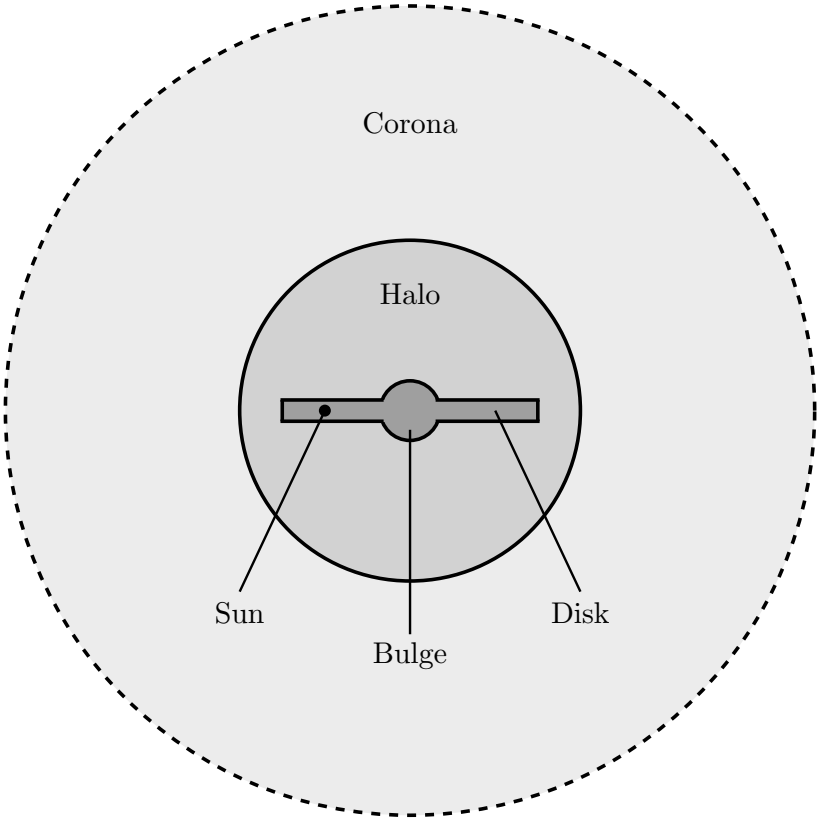

Figure 2.1: Diagram illustrating the structure of the Milky Way, including the disk, halo and corona, as well as the bulge and the approximate location of the Sun (not to scale).

Components of the GMF

The GMF is generally considered to be a combination of a large-scale and a small-scale magnetic field. The large-scale field is the component that is coherent, or regular, on larger scales, typically of the order of the Galaxy [17]. The large-scale structure of the GMF is not yet determined and remains a topic of discussion [3], but it has been established that the Milky Way has a magnetic field aligned with the Galactic plane. Generally, the magnetic field follows the spiral arms of the Galaxy [14], and is strongest in the central regions of the Galactic plane. It may be described by the dynamo theory, based on turbulent magnetic fields being generated by a small-scale dynamo which is driven by interstellar gas motions. Furthermore, large-scale magnetic fields may be generated due to the rotation of the Galaxy, as well as stratification of the turbulent interstellar medium [14]. On the other hand, the small-scale field is the turbulent component of the GMF. The turbulence is usually assumed to follow a power spectrum with a given injection and dissipation scale, which we will study in Sec. 2.4. The small-scale component is believed to be caused by interstellar turbulence, shock waves from e.g. supernovas, etc. [17].

In addition to the large-scale coherent field and the small-scale turbulent field, some models include a third component. This component may be called ordered random or striated, and consists of a field which on small scales has a constant orientation, but varying direction [17].

Although the Galaxy consists of a large-scale and small-scale magnetic field, it is believed that the Solar System is located inside the so-called Local Bubble resulting from supernova explosions [18]. This is a region of space where the local ISM differs from the large-scale GMF, and it is believed to extend more than 250 pc towards the Galactic poles. Our location inside the Local Bubble poses additional difficulties in understanding the large-scale coherent magnetic field.

Galactic disk

The Milky Way has its centre around the supermassive black hole Sagittarius A* (or simply Sgr A*)[1]. The Solar System is located within the Galactic disk at a distance of about 8 kpc from the centre [16], close to one of the minor spiral arms, the Orion arm. The disk is estimated to have a total diameter of around $40 - 50$ kpc and is usually divided into the *thin* and *thick* disk[2]. The thin disk consists of mostly young stars, dust and gas, while the thick disk consists of mostly older stars.

It is common to define the scale height z_t of parameters such as the number density of electrons or the magnetic field strength. Given the quantity Q, one estimates

$$Q(z) = Q_0 \exp\left(-\frac{|z|}{z_{t,Q}}\right). \tag{2.1.2}$$

That is, for e.g. the number density n, it decreases outwards from the disk as a function of distance through the above relation. The scale height may be approximately $z_{t,n} \simeq 0.35$ kpc in the thin disk and $z_{t,n} \simeq 1$ kpc in the thick disk [16]. However, towards the centre of the Galaxy one finds the Galactic bulge, which is considered to be an independent component of the Milky Way. Here, the scale height may increase from that of the thin disk.

The turbulent component of the magnetic field in the thin disk is estimated to have a mean strength of about $3 - 4\,\mu$G [17]. In the thick disk, however, the field is believed to be mostly uniform, where the estimated mean strength ranges from $2 - 12\,\mu$G, and the scale height of the magnetic field $z_{t,B}$ is about $5 - 6$ kpc [17].

[1] In March of 2024 the Event Horizon Telescope (EHT) published results of the observed horizon-scale synchrotron emission region around Sgr A*, indicating a strong and ordered magnetic field through its highly polarised emission ring [19].

[2] Note that in the literature, the thick disk is sometimes called the halo, but this must not be confused with our definition of the halo.

Galactic halo and corona

Outside of the Galactic disk and bulge, we have the Galactic halo and corona extending far out into space. The extent of the these regions are not well defined, and only in recent times it has been suggested that there is a so-called "corona" extending beyond the halo. The corona is therefore rarely standard in the literature, however we will keep its existence in mind as it becomes an important consideration in Sec. 7.4.

A motivation for the additional turbulent corona field is the recent ultra-high-energy cosmic ray (UHECR)[3] event Amaterasu[4]. The event was observed in 2021 by the Telescope Array (TA) Collaboration, and the particle's energy was calculated in 2023 to be approximately 2.44×10^{20} eV [20]. By attempting to localise the particle through backtracking its path in the GMF, Unger and Farrar [21] found its localisation region. This was done using the magnetic field models `UF23` [22] (see Sec. 2.5.2) for the regular field and the Planck-tune of the `JF12` random field [23, 24] for the turbulent field. The localisation resulted in a region where no candidates for powerful radio galaxy sources could be found. This treatment did not include the additional turbulent corona field component, and the inclusion of this field might alter the resulting localisation of the Amaterasu event, although this would have to be investigated further.

The magnetic field in the halo may be expected to have a strong regular component to satisfy the requirements of CR propagation [25]. Given a dominating isotropic turbulent field, the CRs escape too slow from the Galactic disk, which therefore implies the existence of a stronger regular field.

2.2 Measuring magnetic fields

Measuring the magnetic fields in our Galaxy is a difficult task. Since the magnetic fields vary throughout the ISM, it is necessary to obtain a large number of measurements to even determine their large-scale properties. Measurements can be done in-situ by e.g. spacecrafts, which gives us information about the magnetic fields nearby Earth [3]. To obtain information about more distant objects and regions of space, however, we rely on electromagnetic radiation associated with CRs, dust or gas. In addition, the local effects of space along the line-of-sight (LoS) might lead to projection effects [26]. This further complicates the analysis of the observations. As the magnetic fields cannot be measured directly, the observables used can be sensitive to many quantities which we do not fully understand.

Some of the most used so-called observational tracers are Faraday rotation, synchrotron intensity and polarisation, the Zeeman effect and polarised emission from dust [14]. These tracers are dependent on magnetic fields, however each of them may provide different information, which could e.g. be the strength or orientation of the field. One should therefore use the tracers in combination to create a more complete image of the magnetic fields in our Galaxy. Although we are interested in the synchrotron process, we will briefly describe the use of Faraday rotation, polarised dust emission and the Zeeman effect as well.

2.2.1 Faraday rotation

Faraday rotation affects the magnetic field component along the LoS. However, since the Faraday rotation is measured along the LoS, it is influenced by contributions from outside our Galaxy. In addition, the density of thermal electrons is an influence. Therefore, not only the magnetic field strength determines the measured Faraday rotation, but several other factors have to be considered [26].

[3] CRs with energies exceeding 10^{18} eV.
[4] Named after the goddess of the sun in Japanese mythology.

For a linearly polarised source, the rotation of its plane of polarisation when it passes through a medium containing magnetic fields results in the rotation measure (RM). The rotation angle is given by [3]

$$\Phi = \lambda^2 \mathrm{RM}, \tag{2.2.1}$$

where λ is the wavelength of the source and RM is the rotation measure. One can define this measure, in units of $\mathrm{rad\,m^{-2}}$, as [27]

$$\mathrm{RM} = 0.812 \int_{\mathrm{source}}^{\mathrm{observer}} n_e(s) B_{\parallel}(s) \mathrm{d}s, \tag{2.2.2}$$

where $n_e(s)$ is the thermal electron density in units of $\mathrm{cm^{-3}}$ and $B_{\parallel}(s)$ is the magnetic field strength along the LoS with strength in units of μG. The sign of $B_{\parallel}$ is chosen to be positive if $\mathbf{B}_{\parallel}$ points from the source to the observer. The quantity $s \equiv |\mathbf{s}|$ is the distance away from the observer in units of pc. However, Eq. (2.2.1) is only true in some rare cases. The rotation angle is no longer linear in λ^2 when there is significant Faraday depolarisation[5] or when several sources are located in the same region traced by the telescope [3]. In the latter case, the rotating angle is given by

$$\Phi = \lambda^2 \mathrm{FD}. \tag{2.2.3}$$

One uses instead the Faraday depth (FD), which is defined similarly to the RM in Eq. (2.2.2). This is a more general property that can be defined at any point throughout the ISM [27].

A synthetic sky map of the Faraday rotation measure caused by the Milky Way is shown in Fig. 2.2, in which the orientation of the magnetic field is visualised. In particular, red and blue indicate that the magnetic field direction is pointing towards and away from the observer, respectively, and the Galactic disk is seen extended horizontally with its centre in the middle of the image. The sky map provides a visualisation of the large-scale structure of the magnetic field in our Galaxy, as well as small-scale features. On the smaller scales, we see that the magnetic fields in our Galaxy are turbulent.

2.2.2 Synchrotron intensity and polarisation

Synchrotron intensity and synchrotron polarisation are the observational tracers we are most interested in. After this chapter we provide an in-depth treatment on the theory of synchrotron radiation, however we introduce some of the concepts now to see how the synchrotron process is used for observational purposes.

Ultra-relativistic electrons interacting with magnetic fields such as the GMF emit synchrotron radiation. As opposed to Faraday rotation, the synchrotron process depends on the magnetic field component perpendicular to the LoS. Together, these two methods are therefore complementary. The intensity of synchrotron radiation scales with the cosmic ray number density $n_{\mathrm{CR}}(E, s)$, the frequency ν and the magnetic field perpendicular to the LoS $\mathbf{B}_{\perp}(s)$ in the following way [14],

$$I(\nu) \propto \int_{\mathrm{source}}^{\mathrm{observer}} n_{\mathrm{CR}}(E, s) B_{\perp}^{1+\alpha}(s) \nu^{-\alpha} \mathrm{d}s. \tag{2.2.4}$$

α is called the spectral index and s is still the distance away from the observer. The power per unit frequency of a single CR electron therefore scales as $P(\nu) \propto \nu^{-\alpha}$. For the intensity relation one assumes that the CR number density follows a power-law distribution, that is

$$n_{\mathrm{CR}}(E)\mathrm{d}E \propto E^{-p}\mathrm{d}E, \tag{2.2.5}$$

where p is the particle distribution index. The term $n_{\mathrm{CR}}(E)\mathrm{d}E$ is the number density of CR electrons in the interval of energies from E to $E + \mathrm{d}E$. Integrating the product of $P(\nu)$ and the

[5] See Rainer and Wielebinski [3] for a further description of Faraday depolarisation.

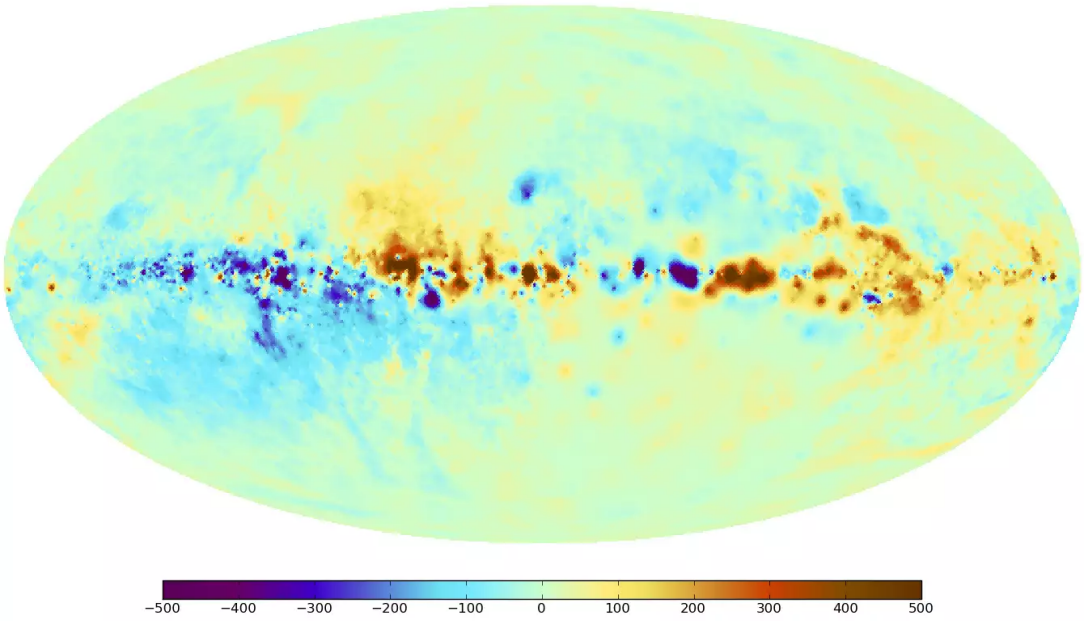

Figure 2.2: Sky map of the Faraday rotation measure caused by the Milky Way's magnetic fields. Red indicates the magnetic field is pointing towards the observer, while blue indicates it is pointing away from the observer. The plane of the Galactic disk extends horizontally, with the centre in the middle of the image. From Opperman et al. [26].

power-law expression in Eq. (2.2.5) over all energies E gives the total power per unit volume and frequency of the distribution, which scales as

$$P_{\text{tot}}(\nu) \propto \nu^{-(p-1)/2}. \tag{2.2.6}$$

Hence, the spectral index is related to the particle distribution index by $\alpha = (p-1)/2$ or equivalently $p = 2\alpha + 1$ [9]. Observations give typical values of the spectral index from the GMF around $\alpha \simeq 0.7$ corresponding to a particle distribution index of $p \simeq 2.4$ [14]. There are however several complications to the process of synchrotron radiation to take into account when interpreting the observations. Effects like free-free absorption and self-absorption may contribute at low frequencies [14]. These factors, along with the uncertainties of the quantities such as the CR electron number density, makes the observations difficult to interpret.

We will see in chapter 5 a derivation of the degree of linear polarisation of synchrotron radiation emitted by a power-law electron distribution, such as the CR electron distribution given by Eq. (2.2.5). The result is only dependent on the particle distribution index p, and is given by

$$\Pi_{\text{lin}} = \frac{p+1}{p+\frac{7}{3}}. \tag{2.2.7}$$

For the typical value of $p \simeq 2.4$, the linear polarisation degree is $\Pi_{\text{lin}} \simeq 0.72$. This is very high and is rarely observed due to depolarisation of the radiation when travelling towards the observer [14].

The *Planck* mission, with the objective of studying the cosmic microwave background (CMB)[6], traced polarised synchrotron emission in the GMF at 30 GHz. The resulting sky map is shown in Fig. 2.3. The colours represent the intensity, where the red areas clearly show the presence of magnetic fields in the Galactic disk lying horizontally in the image.

[6]Microwave radiation from the primordial Universe that fills all of space. The CMB is sometimes considered an "echo" of the Big Bang.

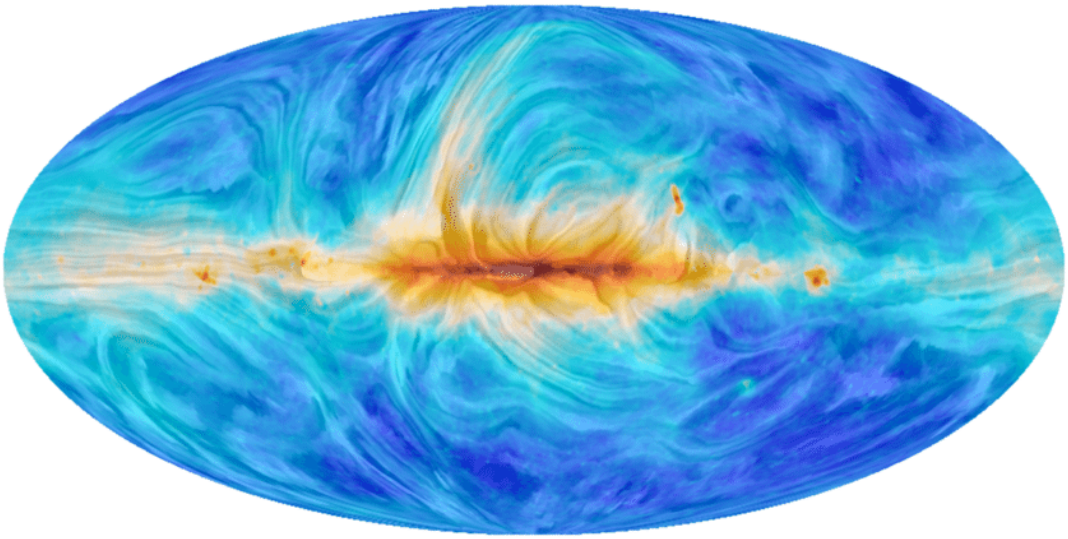

Figure 2.3: Sky map of the angle of polarisation of synchrotron emission at 30 GHz caused by the Milky Way's magnetic fields. The colours represent intensity, and the view is rotated 90° to indicate the direction of the Galactic magnetic field projected onto the plane of the sky. From Adam et al. [28].

2.2.3 Polarised dust emission

In addition to synchrotron emission, polarised (thermal) dust emission also depends on the magnetic field component perpendicular to the line-of-sight [26]. This is because the emission from non-spherical dust grains is polarised along its long axis. As the spin axis of the dust grain is statistically aligned with the orientation of the magnetic field, we get the dependence on the perpendicular component of the local GMF. However, one should also take into account the absorption by dust. The absorption of dust grains can lead to linearly polarised light parallel to the magnetic field lines. Both the emission and absorption by dust grains depend on their intrinsic properties [14].

We will not go into more detail on the polarised thermal dust emission or absorption, but present Fig. 2.3. This is the obtained sky map from the *Planck* mission of dust emission at 353 GHz caused by the GMF. Similarly to Fig. 2.4, the intensity is represented by the colours. It is clear from both figures, as well as Fig. 2.2 for the Faraday rotation, that the Milky Way contains significant magnetic fields. The Galactic disk is clearly visible horizontally in all three figures, showing a greater magnetic field density. The figures also indicate that there are stronger magnetic fields towards the centre of our Galaxy.

2.2.4 The Zeeman effect

Finally we wish to mention the Zeeman effect, which is the most direct method of measuring the GMF. The Zeeman effect can be used for measuring in the optical wavelength range and has lead to the detection of magnetic fields in stars. In fact, this effect was in 1908 the first direct measurement indicating magnetic fields outside Earth, in sunspots in the Sun [3].

The Zeeman effect relates to the atomic structure of the charged particle. In the presence of a magnetic field B, the frequency of the radiation emitted by a harmonic oscillator is classically split into three distinct frequencies, or lines. These are

$$\nu_0, \quad \nu_\pm = \nu_0 \pm \frac{eB}{4\pi mc}, \tag{2.2.8}$$

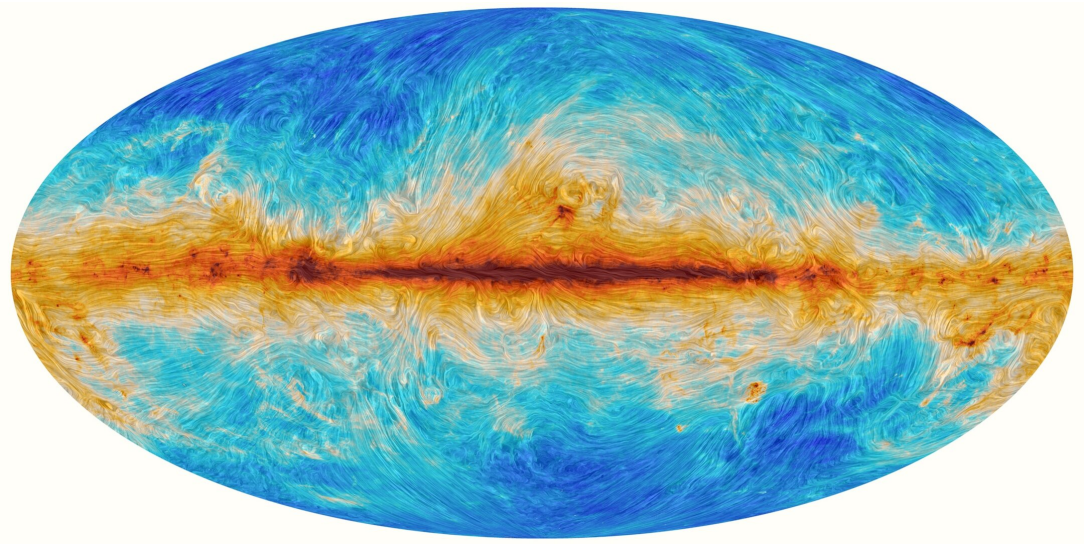

Figure 2.4: Sky map of the angle of polarisation of dust emission at 353 GHz caused by the Milky Way's magnetic fields. The colours represent intensity, and the view is rotated 90° to indicate the direction of the Galactic magnetic field projected onto the plane of the sky. From Adam et al. [28].

for a charged particle with charge e and mass m [9]. The particle oscillates at a frequency ν_0, such that the emitted dipole radiation is at the same frequency ν_0. The splitting of the emitted frequency is due to the Lorentz force, which we know will influence the charged particle in the presence of a magnetic field. One distinguishes between the *longitudinal* and *transverse* Zeeman effect, where the latter is much harder to observe. For the longitudinal case, the splitting becomes

$$\nu_{\pm} = \nu_0 \pm \frac{eB_{\parallel}}{4\pi mc}, \tag{2.2.9}$$

which it only depends on the magnetic field component parallel to the line-of-sight. The split components will be circularly polarised with opposite signs. For the transverse Zeeman effect one considers the magnetic field component perpendicular to the line-of-sight. However, the three lines are now all linearly polarised. No net polarisation is usually observed in this case [3].

2.3 Magnetohydrodynamic turbulence

In order to describe the turbulence in GMFs, we need to consider MHD turbulence. Magnetohydrodynamics is the study of electrically conducting fluids in magnetic fields [13]. In astrophysics, MHD is used to describe the dynamics of plasmas, which are gases consisting of positively charged ions and negatively charged electrons [29]. In many cases one can treat plasma as a continuous fluid, similarly to fluid dynamics. Plasma makes up most of the matter in the Universe, and the ISM can act like a plasma as there are free electrons in the interstellar space [29]. MHD can therefore be used to analyse the dynamics of the ISM and is important for understanding the structure of the GMF. In astrophysics, one uses a model of MHD by Alfvén proposed in 1942, which combines Maxwell's equations in Eq. (2.1.1) and fluid dynamics [13].

The field of MHD further leads to the field of MHD turbulence, which, as the name implies, deals with the turbulent flows of electrically conducting fluids in magnetic fields. Interstellar turbulence leads to a significant complication of the structure of the GMF. As turbulence is not well understood, the existence of turbulent GMFs thus leads to much more complex and difficult

analyses. Since the processes described in the previous section, such as Faraday rotation and synchrotron emission, are dependent on the magnetic field, it is important to better understand the concept of turbulence in the GMF.

To deal with MHD turbulence in the ISM, one relies heavily on numerical methods and computations. Simple models are generally not sufficient to create realistic descriptions [14]. There are several methods of simulating turbulence, e.g. methods based on well known theories on turbulence such as Kolmogorov's theory [13] which will be described in the next section.

To describe a fluid where friction is allowed and turbulence appears, the velocity field of the flow is split into two terms,

$$\mathbf{u}(\mathbf{x}, t) = \langle \mathbf{u}(\mathbf{x}) \rangle + \delta\mathbf{u}(\mathbf{x}, t), \tag{2.3.1}$$

known as the Reynolds decomposition [30]. As usual, $\mathbf{x}$ denotes the position and t denotes the time of the fluid element. The first term is the average of a (regular) velocity field[7], while the second is the turbulent term. We can describe the turbulent term by its spectral representation as the sum, or integral, of Fourier modes [30],

$$\delta\mathbf{u}(\mathbf{k}) = \int \mathrm{d}^3 x \delta\mathbf{u}(\mathbf{x}) \mathrm{e}^{-\mathrm{i}\mathbf{k}\cdot\mathbf{x}}. \tag{2.3.2}$$

Central in the field of fluid dynamics is the Reynolds number [30],

$$R_e = \frac{uL}{\nu}. \tag{2.3.3}$$

Here, u is the velocity of the fluid, L is the characteristic length and ν is the kinematic viscosity. The Reynolds number is a dimensionless quantity describing the degree of turbulence in a flow. We have laminar flow for R_e less than around 2300 and turbulent flow for R_e larger than around 4000. It is, however, worth noting that the onset of turbulence will happen in a range of Reynolds numbers, dependent on other parameters of the experiment. Most important is the fact that a higher R_e corresponds to a larger degree of turbulence. A simulation of a 2D flow past a cylinder is shown in Fig. 2.5 for different Reynolds numbers R_e in the range $10 - 250$. The figure demonstrates the disordering of the flow for increasing R_e.

2.4 Kolmogorov's theory

Kolmogorov introduced his theory based on developments made by Richardson in 1922 regarding the scales of turbulent motion [30]. In particular, Richardson used the notion of energy cascades. The kinetic energy will enter the turbulence at the largest scales, and is then transferred to smaller and smaller scales. In the end, the energy is dissipated due to viscosity. At each scale, turbulence consists of eddies of different sizes ℓ with velocity $u(\ell)$. The time scale of a given eddy is then $\tau(\ell) \equiv \ell/u(\ell)$. Thus the idea of energy cascades implies that larger eddies break down into smaller ones as the energy is transferred. Kolmogorov's theory assumes isotropic turbulence of the small-scale structure, which is what will be considered in the following.

The mean rate of energy transfer is given by [13]

$$\varepsilon_\ell \equiv \frac{\mathrm{d}E_\ell}{\mathrm{d}t} \propto \frac{u_\ell^3}{\ell}, \tag{2.4.1}$$

and the mean rate of energy dissipation is defined as

$$\varepsilon = -\lim_{\nu \to 0} \frac{\mathrm{d}E}{\mathrm{d}t}. \tag{2.4.2}$$

[7] This term is in fact the average of the whole velocity field, as the average of the turbulent component should be zero.

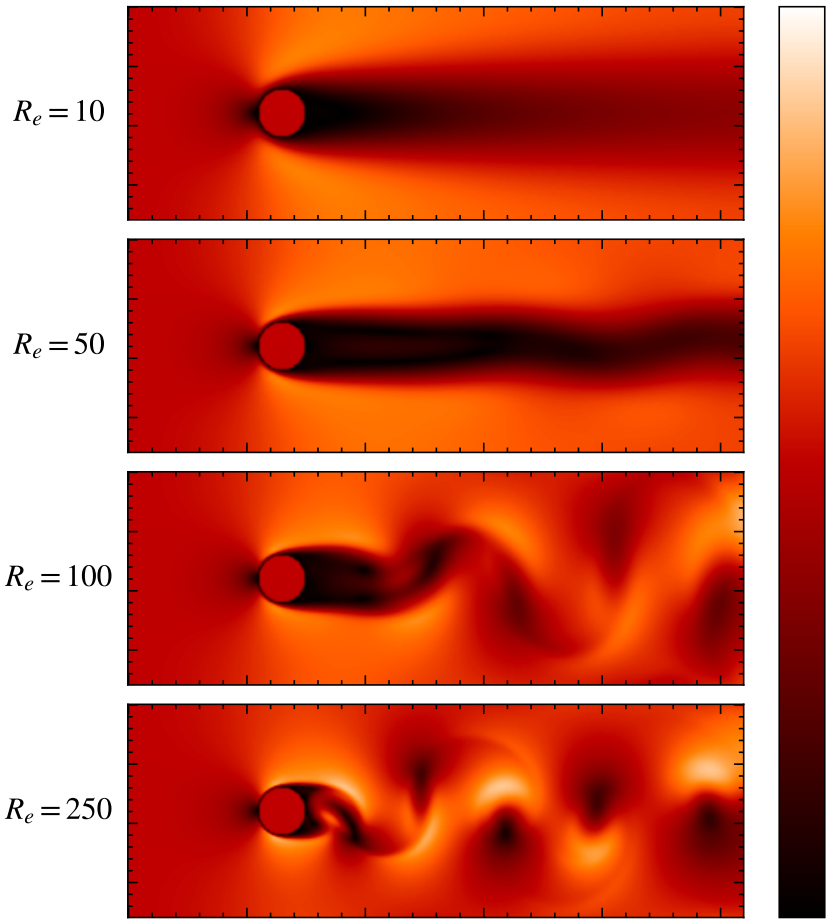

Figure 2.5: Simulation of a 2D flow past a cylinder for different Reynolds numbers R_e after the same time t. The colour indicates the velocity u of the fluid element, where darker colour corresponds to smaller u. Code adapted from [31].

Note that ε corresponds to flows with Reynolds number $R_e \to \infty$, which means highly turbulent flows. This is seen from the definition of the Reynolds number in Eq. (2.3.3) as the viscosity $\nu \to 0$.

We now define the dissipation scale L_{min} as the scale ℓ of energy dissipation and the injection scale L_{max} as the scale where energy is injected. Consequently, we distinguish between the dissipation range and the injection range. Scales with

$$L_{\text{min}} \ll \ell \ll L_{\text{max}}, \tag{2.4.3}$$

form the so-called inertial range [30]. Since no energy is injected or dissipated in this range, the mean rate of energy transfer ε_ℓ equals the mean rate of energy dissipation ε [13]. Hence,

$$\varepsilon\ell \propto u_\ell^3. \tag{2.4.4}$$

For a given length scale ℓ, the corresponding wavenumber is $k = 2\pi/\ell$ [30]. This means the inertial range is described by wavenumbers k such that $k_{\text{min}} \ll k \ll k_{\text{max}}$ with $k_{\text{min}} = 2\pi/L_{\text{max}}$ and $k_{\text{max}} = 2\pi/L_{\text{min}}$. The total energy of a system is

$$E = \int E(k)\mathrm{d}k, \tag{2.4.5}$$

where $E(k)$ denotes the energy spectrum. Given a spectral tensor of the velocity field in three dimensions $\Phi_{ii}(\mathbf{k})$, assuming the turbulence is homogeneous, the energy spectrum is defined as [13]

$$E(\mathbf{k}) \equiv \frac{1}{2}\Phi_{ii}(\mathbf{k}), \tag{2.4.6}$$

where

$$\Phi_{ij}(\mathbf{k}) \equiv \frac{1}{(2\pi)^3}\iiint R_{ij}(\boldsymbol{\ell})e^{-i\mathbf{k}\cdot\boldsymbol{\ell}}\mathrm{d}\boldsymbol{\ell}. \tag{2.4.7}$$

The term $R_{ij}(\boldsymbol{\ell}) \equiv \langle u_i(\mathbf{x})u_j(\mathbf{x}+\boldsymbol{\ell})\rangle$ is the second order velocity correlation tensor. For isotropic turbulence, we need to only consider the norm of the wavevector, i.e. the wavenumber k, in the spectral tensor. The energy spectrum becomes then

$$E(k) = 2\pi k^2 \Phi_{ii}(k), \tag{2.4.8}$$

where one integrates $E(\mathbf{k})$ over a sphere in Fourier space of radius $\mathbf{k}$. The spectral tensor is proportional to the velocity u_ℓ^2 through $R_{ij}(\boldsymbol{\ell})$, and the triple integral over $\boldsymbol{\ell}$ gives a proportionality factor k^3. Therefore, we arrive at

$$E(k)k \propto u_\ell^2 \propto (\varepsilon\ell)^{2/3} \propto \varepsilon^{2/3}k^{-2/3}. \tag{2.4.9}$$

Consequently, for a constant C, the so-called Kolmogorov $k^{-5/3}$ spectrum is given by

$$E(k) = C\varepsilon^{2/3}k^{-5/3}. \tag{2.4.10}$$

This spectrum is a power-law energy spectrum $E(k) \propto k^{-\gamma}$ with $\gamma = 5/3$. A diagram of the energy spectrum in a log-log plot is shown in Fig. 2.6, distinguishing between the different ranges. In the inertial range, the Kolmogorov $k^{-5/3}$ relation is therefore shown as a straight line with slope $-5/3$. In the injection range and dissipation range, the energy spectra cannot be described.

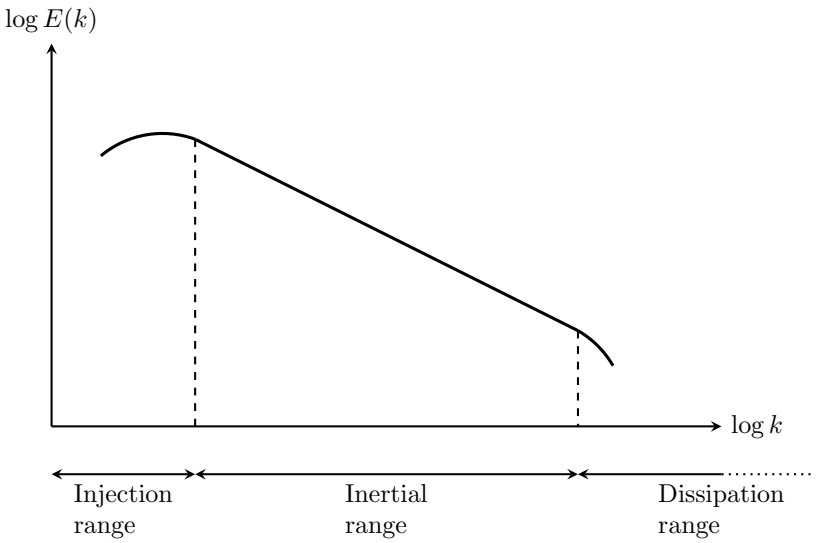

Figure 2.6: Illustration of the Kolmogorov energy spectrum. Energy is injected in the injection range, before it cascades through the inertial range, and finally dissipates in the dissipation range. The slope of the straight line in the inertial range is $-5/3$.

We finally define the correlation length L_c, sometimes called the coherence length, for a turbulent magnetic field with a power-law spectrum [32],

$$L_\mathrm{c} = \frac{L_\mathrm{max}}{2}\frac{\gamma-1}{\gamma}\frac{1-(L_\mathrm{min}/L_\mathrm{max})^\gamma}{1-(L_\mathrm{min}/L_\mathrm{max})^{\gamma-1}} \simeq \frac{L_\mathrm{max}}{2}\frac{\gamma-1}{\gamma}. \tag{2.4.11}$$

The approximation is valid for $L_{\max} \gg L_{\min}$ and $\gamma > 1$. For the case of Kolmogorov spectrum with $\gamma = 5/3$, the correlation length becomes $L_c \simeq L_{\max}/5$.

2.5 Numerical models

As we rely on numerical models to describe the GMF, several different programs have been made both for turbulent fields and the coherent GMF. In the following we will present two programs that provide frameworks for generating magnetic fields, `ELMAG` and `UF23` by [32] and [22], respectively.

2.5.1 Turbulent field from `ELMAG`

To generate a turbulent magnetic field according to Kolmogorov's theory discussed in 2.4, we use the numerical model in the program `ELMAG 3.01`[8] provided by [32]. The `ELMAG` program is a Monte Carlo program for simulating electromagnetic cascades, both on the extragalactic background light (EBL) and in magnetic fields, using `Fortran 90`. The turbulent magnetic field generated by `ELMAG` is an isotropic and divergence-free Gaussian random field, and is only a small part of the program itself. We will, however, refer to `ELMAG` as the magnetic field model, as this is our only application of the program.

The turbulent field model of `ELMAG` is based on algorithms described in [33] and [34], and assumes a magnetic field

$$\mathbf{B}(\mathbf{r}) = \sum_{j=1}^{n_k} B_j \left[\cos\alpha_j \hat{\mathbf{e}}_{x'} + \mathrm{i} h_j \sin\alpha_j \hat{\mathbf{e}}_{y'}\right] \mathrm{e}^{\mathrm{i}(k_j \hat{\mathbf{e}}_{z'} + \beta_j)}. \tag{2.5.1}$$

This is a superposition of transverse Fourier modes. For a given mode j, α_j and β_j are random phases with uniform distribution on $[0, 2\pi]$ and $h_j = \pm 1$ is the polarisation of the magnetic field. The helicity $\langle h \rangle$ is the expectation value of the polarisation, and gives a fully left- or right-helical field for $\langle h \rangle = 1$ and $\langle h \rangle = -1$, respectively. The strength of a magnetic field mode is given by

$$B_j = B_{\min} \left(\frac{k_j}{k_{\min}}\right)^{-\gamma/2}, \tag{2.5.2}$$

where $B_{\min}$ determines the magnetic field strength of the lowest Fourier mode, and $k_{\min}$ is its wavenumber. The sets of Cartesian unit vectors $\hat{\mathbf{e}}_{i'}$ in Eq. (2.5.1) are related to $\hat{\mathbf{e}}_i$ by the rotation $\mathbf{r}' = R\mathbf{r}$, with

$$R(\vartheta_j, \phi_j) = \begin{bmatrix} \cos\vartheta_j \cos\phi_j & \cos\vartheta_j \sin\phi_j & -\sin\vartheta_j \\ -\sin\phi_j & \cos\phi_j & 0 \\ \sin\vartheta_j \cos\phi_j & \sin\vartheta_j \sin\phi_j & \cos\vartheta_j \end{bmatrix}. \tag{2.5.3}$$

For an isotropic magnetic field, the rotation angle ϕ_j is uniformly distributed on $[0, 2\pi]$ and $\cos\vartheta_j$ is uniformly distributed on $[-1, 1]$.

By using the described numerical model, the magnetic field strength B in the xy-plane for $z = 0$ is plotted in Fig. 2.7. Four different correlation lengths L_c have been chosen; 50 pc, 100 pc, 150 pc and 200 pc, for x and y both ranging from 0 to 1 kpc. The field strength B is plotted as B/B_{rms} with $B_{\mathrm{rms}} = 3\,\mu\mathrm{G}$. The other parameters are constant. In particular, the number of turbulent nodes $n_k = 1000$, the helicity $\langle h \rangle = 0$ and $L_{\min}/L_c = 0.005$. Recall that

[8] The program may be used for any energy spectrum with slope γ, however we will focus on Kolmogorov's theory where $\gamma = 5/3$ unless otherwise stated.

for Kolmogorov turbulence $L_c \simeq L_{\max}/5$, and the injection scale $L_{\max}$ is therefore also changing with the correlation length. We see from Fig. 2.7 that the magnetic fields are turbulent on smaller scales for smaller correlation lengths L_c, as we would expect.

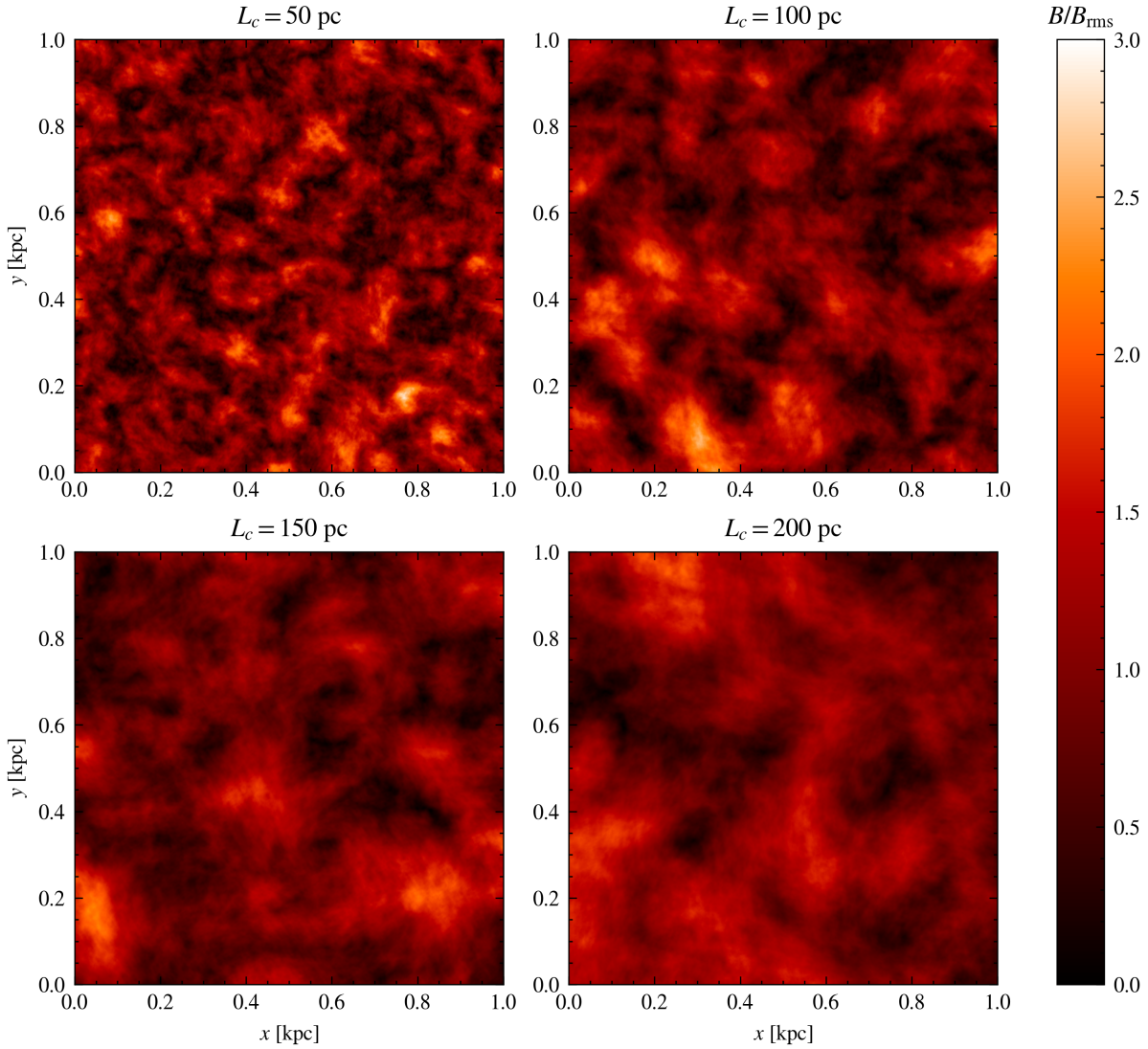

Figure 2.7: Magnetic field strength $B/B_{\rm rms}$ of generated turbulent fields in the xy-plane for four different correlation lengths L_c. Each field has $n_k = 1000$ turbulent modes, helicity $\langle h \rangle = 0$, $L_{\min}/L_c = 0.005$ and $B_{\rm rms} = 3\,\mu$G.

As we are interested in the GMF we should make some further adjustments to the model. We will assume that the mean strength of the field $B_{\rm rms}$ decreases with the z-coordinate. This is due to the fact that the strength of the magnetic field will tend towards zero as one exits the Galactic disk. As an example, we may choose the scaling function to be the Gaussian,

$$f(z) = \exp\left(-\frac{z^2}{2\sigma^2}\right), \tag{2.5.4}$$

which is normalised to 1 at $z = 0$, and σ is the root mean square (RMS) width, or standard deviation (SD). The generated turbulent magnetic field is scaled by multiplying the field strength with $f(z)$ at each point along z. As magnetic fields follow Maxwell's equations, the divergence should be zero by Gauss's law in Eq. (2.1.1b). The multiplication of a function with $\mathbf{B}$ may violate this. However, we will ignore the possible effects by the described scaling of the magnetic field, as it should not become problematic for our use case.

A plot of the strength along z for a generated turbulent magnetic field can be seen in Fig. 2.8a, while Fig. 2.8b shows a generated turbulent magnetic field scaled by $f(z)$ along with a Gaussian function normalised to B_{rms} at $z = 0$. The figure illustrates the scaling effect for increasing z-values.

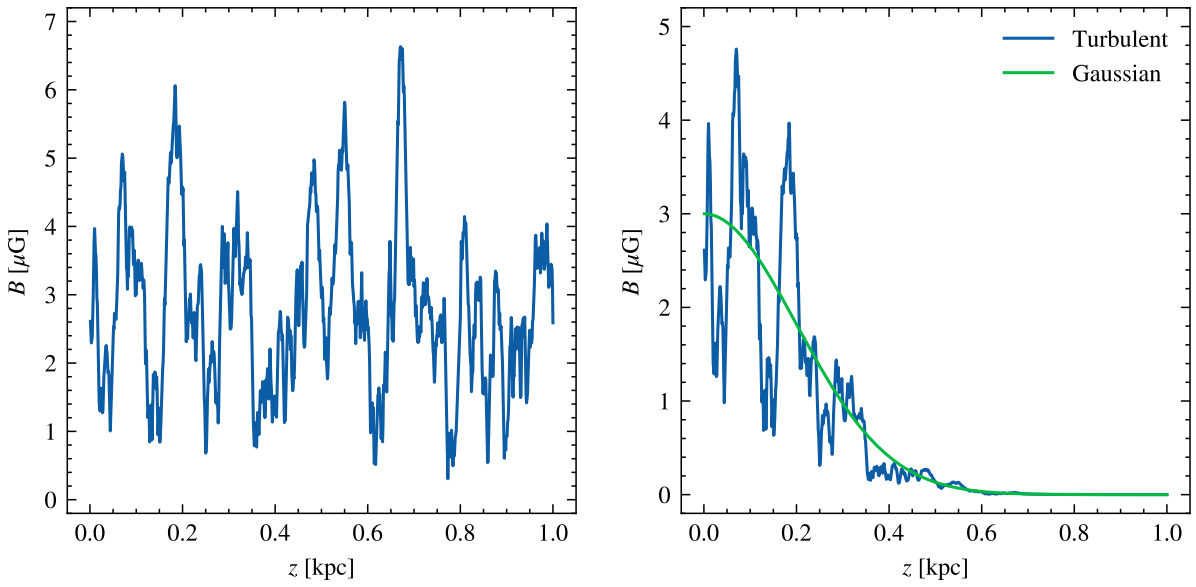

(a) **(b)**

Figure 2.8: The strength along z for (a) a generated turbulent magnetic field, and (b) a generated turbulent magnetic field scaled by a Gaussian together with a Gaussian function. The generated fields have $B_{\text{rms}} = 3\,\mu\text{G}$, $L_c = 20\,\text{pc}$, $L_{\text{min}}/L_c = 0.005$, $n_k = 1000$ and $\langle h \rangle = 0$, while the Gaussian function is normalised to B_{rms} at $z = 0$. Both the scaling function and the Gaussian function has a width of $\sigma = 200\,\text{pc}$.

In addition to using the function in Eq. (2.5.4) to scale the magnetic field, it is reasonable to assume that a similar function can be used to scale the electron density along z. As more free electrons should be present towards the centre of the Galactic disk, this should be taken into account later when the model is used to calculate different quantities.

2.5.2 `UF23` regular field models

While the `ELMAG` turbulent field model only generates turbulent magnetic fields according to a power-law energy spectrum such as Kolmogorov's theory, we wish to consider a more global description of the GMF. Unger and Farrar [22] provides a framework `UF23` with eight different models for the coherent magnetic field of the Galaxy. These models intent to give a realistic representation of the global structure of the GMF, that is a spiral coherent magnetic field. They are constructed using Faraday rotation measures of extragalactic sources as well as synchrotron intensity data. An overview of the ensemble of GMF models is shown in Tab. 2.1. The table includes the type of disk field; GD (grand-design spiral) or LS (local spur), the toroidal halo; explicit or twisted, the poloidal halo; CX-sigm or CX-expo, the electron density model; YMW16 or NE2001, and the synchrotron intensity data; W (WMAP), P (Planck), CG (Cosmoglobe) or a combination. For all the given models the CR diffusion equation is solved by using the `DRAGON` plain diffusion model [35]. In Fig. 2.9, the magnetic field strength in the xy- and xz-plane is plotted for the models `base`, `expX` and `nebCor`. Following is a more in-depth description of the components constituting the GMF models, however we refer to Unger and Farrar [22] for more detailed information.

Table 2.1: Ensemble of GMF models from the framework `UF23` showing the type of disk field, toroidal halo, poloidal halo, electron density model and synchrotron intensity data.

Model name	Disk	Toroidal halo	Poloidal halo	n_e model	QU
`base`	GD	explicit	CX-sigm	YMW16	(W+P)/2
`expX`	GD	explicit	CX-expo	YMW16	(W+P)/2
`spur`	LS	explicit	CX-sigm	YMW16	(W+P)/2
`neCL`	GD	explicit	CX-sigm	NE2001	(W+P)/2
`twistX`	GD	twisted	CX-sigm	NE2001	(W+P)/2
`nebCor`	GD	explicit	CX-sigm	YMW16	(W+P)/2
`cre10`	GD	explicit	CX-sigm	YMW16	(W+P)/2
`synCG`	GD	explicit	CX-sigm	YMW16	CG

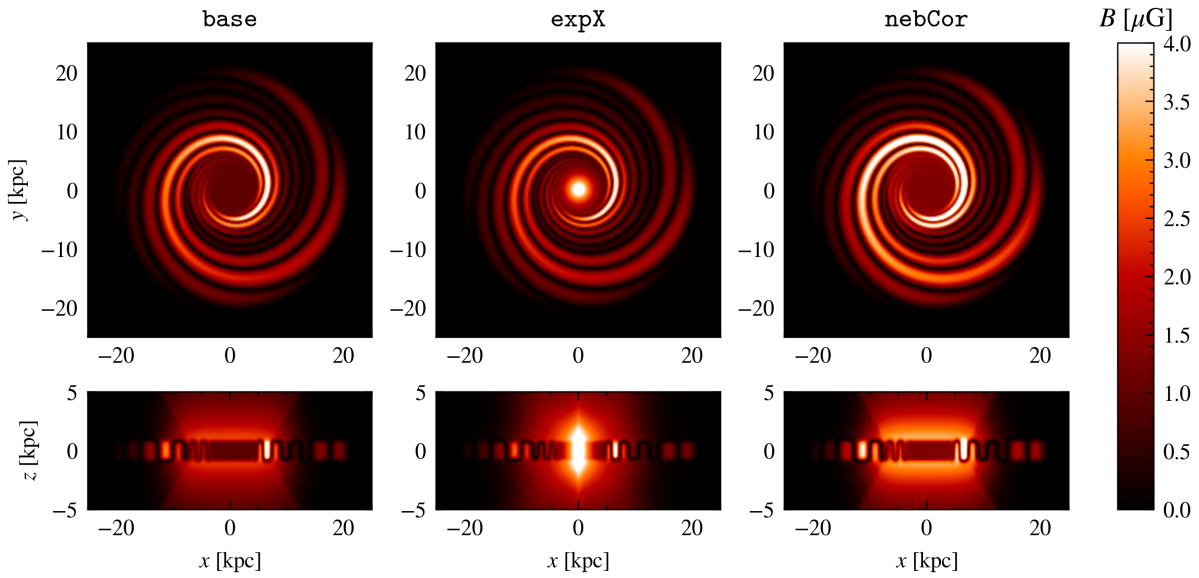

Figure 2.9: Magnetic field strength B of coherent magnetic fields in the xy- and xz-plane for three of the models from `UF23`.

Disk field

As the Milky Way is believed to to have a spiral coherent magnetic field close to the disk, `UF23` assumes a logarithmic spiral. This disk field is modelled by assuming a "pitch angle", defined for magnetic fields as [17]

$$\alpha = \arctan\left(\frac{B_r}{B_\phi}\right), \tag{2.5.5}$$

where B_r and B_ϕ are the radial and azimuthal components of the magnetic field, respectively. One also has to assume the arm width and angle at some radius, as well as the magnetic field strength. In each arm, the magnetic flux should be constant as function of radius. As the radius increases out of the disk, the magnetic field should become weak. This is true for the electron density as well. An outer radius of $r_2 = 20\,\mathrm{kpc}$ is therefore defined by [22], such that the disk

field is effectively zero for $r > r_2$. Furthermore, an inner radius of $r_1 = 5\,\mathrm{kpc}$ is chosen. For radii smaller than this, the magnetic field is expected to be weak, and no longer a logarithmic spiral. Compared to previous magnetic field models, the Fourier spiral of [22] provides a disk field without discontinuities.

The eighth models in Tab. 2.1 are either grand-design (GD) magnetic disk fields from the Fourier spiral, or a local spur (LS) which includes only a single arm (the Orion arm) of the GD spiral field. The `spur` model is the only one with a LS disk field, while the rest of the models are based on the GD disk field.

Toroidal and poloidal halo

The models are created by considering that the global structure of the GMF is a superposition of a logarithmic spiral field and a large-scale halo field, where the latter consists of a toroidal and/or poloidal field.

The toroidal magnetic field is a purely azimuthal field consisting only of the component B_ϕ of the magnetic field vector $\mathbf{B}$. On the other hand, the poloidal magnetic field consists of only the components B_r and B_z of $\mathbf{B}$. In [22], this halo field is an improved X-field from that introduced by Jansson and Farrar [36]. It is made either a power-function X-field or a coasting X-field (CX), where all the chosen models in Tab. 2.1 are of the type CX. The radial midplane dependence of the magnetic field strength is determined by a scaling function that is for the models either by an exponential or a logistic sigmoid function, giving the entries of either CX-sigm or CX-expo in Tab. 2.1.

Given a poloidal halo field, the differential rotation of the Galaxy implies the creation of toroidal fields. This twisting of the poloidal field leads to the unified halo by [22]. The explicit toroidal fields in Tab. 2.1 are modelled using a logistic sigmoid function, while the twisted toroidal halo field of the model `twistX` is the result of this unified halo model.

Electron density models

Two different thermal electron models are used by [22], the NE2001 by Cordes and Lazio [37] and YMW16 by Yao et al. [38] models. Both use data from Galactic pulsars and describe the dispersion measure (DM), that is the integral from Earth to the pulsar over the electron number density n_e. Hence the DM is similar to the RM defined in Sec. 2.2.1, but without the magnetic field dependence.

As mentioned, the `DRAGON` plain diffusion model [35] is used to describe the CR density distribution and energy spectrum by solving the diffusion equation.

Rotation measure and synchrotron intensity data

The `UF23` model uses a large set of RM data as well as synchrotron intensity data, however not self-consistently. For the polarised synchrotron intensity, one uses the Stokes parameters which will be detailed later in Sec. 5.3, and considers in particular the parameters Q and U. Through the quadratic addition of these parameters one obtains the (linear) polarised intensity,

$$I_{\mathrm{lin}}^2 = Q^2 + U^2. \tag{2.5.6}$$

The data providing these polarised intensities are given in the last column of Tab. 2.1. A combination of WMAP (W) [39] and Planck (P) [40] satellite data is used for most models, except the model `synCG`. This uses the alternative Cosmoglobe (CG) [41] data, which is a combined analysis of W and P. A comparison of the different data sets for the Stokes parameters Q and U are shown in figure 22 of [22].

2.5.3 Combining the models

A realistic model of the GMF should consist of a combination of a regular field and a turbulent field, that is

$$\mathbf{B}_{\text{tot}} = \mathbf{B}_{\text{reg}} + \mathbf{B}_{\text{turb}}. \tag{2.5.7}$$

The `UF23` model generates coherent magnetic fields, or regular fields, but does not consider the turbulent component. We therefore wish to combine this model with the `ELMAG` turbulent field model. In doing so, we need to preserve the overall global structure from `UF23` while introducing additional turbulent motion, similarly to scaling the turbulent magnetic field in Fig. 2.8b. Letting $\mathbf{B}_{\texttt{UF23}}$ denote the magnetic field generated by `UF23` and $\mathbf{B}_{\texttt{ELMAG}}$ denote the magnetic field generated by `ELMAG`, we define the total field at a position $\mathbf{x}$ in space as

$$\mathbf{B}_{\text{tot}}(\mathbf{x}) = \mathbf{B}_{\texttt{UF23}}(\mathbf{x}) + s(\mathbf{x})\mathbf{B}_{\texttt{ELMAG}}(\mathbf{x}). \tag{2.5.8}$$

Here, $s(\mathbf{x})$ is a scaling function also dependent on the position in space. We will define this scaling function as

$$s(\mathbf{x}) = \frac{B_{\texttt{UF23}}(\mathbf{x})}{B_{\text{rms}}}\beta, \tag{2.5.9}$$

such that β is the fraction of turbulent field strength to regular field strength,

$$\beta \equiv \frac{B_{\text{turb}}}{B_{\texttt{UF23}}}. \tag{2.5.10}$$

It is reasonable to assume that β is in the range 0 to a value not much larger than 1, as we expect the global structure of the magnetic field to be most significant. The total magnetic field strength in the xy and xz-plane can be seen in Fig. 2.10 for three different models, `base`, `expX` and `nebCor`. Here, the parameter β is chosen to be 0.5. It is clear that the combination of the models preserves the global coherent field from `UF23`, while it simultaneously includes turbulent motion.

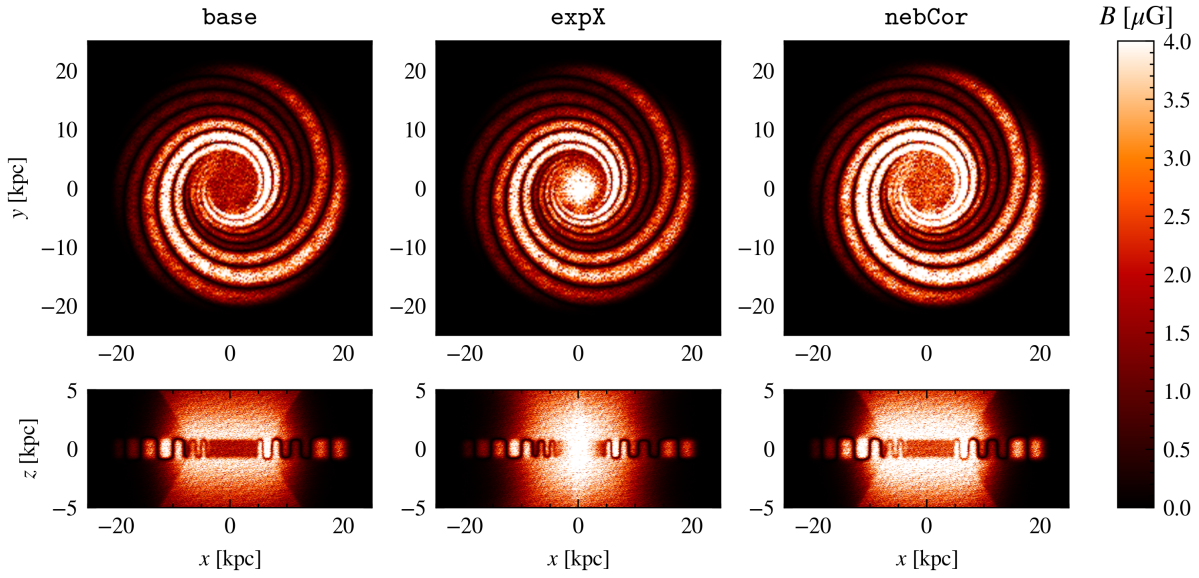

Figure 2.10: Total magnetic field strength B [μG] in the xy- and xz-plane with $\beta = 0.5$ for three of the models from `UF23`. The turbulent component of the fields have $B_{\text{rms}} = 3\,\mu\text{G}$, $L_c = 20\,\text{pc}$, $L_{\text{min}}/L_c = 0.005$, $n_k = 1000$ and $\langle h \rangle = 0$.

Chapter 3

Radiation of relativistic particles

When a charged particle is accelerated by a magnetic field, it produces electromagnetic radiation. This radiation is called cyclotron radiation if the particle is non-relativistic, and synchrotron radiation if the particle is ultra-relativistic [9]. To describe synchrotron radiation, our starting point is the essential discussion of how a relativistic particle moves in a magnetic and electric field. We want to analyse the case where there is no electric field present and simplify the equation of motion accordingly.

The following discussion is based on the books by Rybicki and Lightman [9] and Longair [10]. It is worth noting that the two books use different notations and systems of units. In particular, [9] uses Gaussian-cgs units while [10] uses SI units. We will follow the the notation of [9], and Gaussian-cgs units are assumed.

3.1 Motion of a particle

We consider a relativistic particle of mass m and charge q in an electric and magnetic field, $\mathbf{E}$ and $\mathbf{B}$, respectively. The total force $\mathbf{F}$ acting on the particle is then given by the Lorentz force law,

$$\mathbf{F} = q\left(\mathbf{E} + \frac{1}{c}\mathbf{v}\times\mathbf{B}\right). \tag{3.1.1}$$

Using the momentum $\mathbf{p}$ of the particle, we write the force as

$$\mathbf{F} = \frac{\mathrm{d}\mathbf{p}}{\mathrm{d}t} = \frac{\mathrm{d}}{\mathrm{d}t}(\gamma m\mathbf{v}) = m\frac{\mathrm{d}\gamma}{\mathrm{d}t}\mathbf{v} + m\gamma\frac{\mathrm{d}\mathbf{v}}{\mathrm{d}t}. \tag{3.1.2}$$

Here, $\mathbf{v}$ is the velocity of the particle and $\gamma = \left(1 - v^2/c^2\right)^{-1/2}$ is the Lorentz factor, given $v \equiv |\mathbf{v}| = \sqrt{\mathbf{v}\cdot\mathbf{v}}$ and the speed of light c. The combination of Eq. (3.1.1) and (3.1.2) gives us an expression for the equation of motion for the particle. We see however that Eq. (3.1.2) includes the time derivative of the Lorentz factor. We would like to show that this term only depends on the electric field $\mathbf{E}$. We therefore begin by expressing the time derivative of the Lorentz factor as

$$\frac{\mathrm{d}\gamma}{\mathrm{d}t} = \frac{\mathrm{d}}{\mathrm{d}t}\left(1 - \frac{v^2}{c^2}\right)^{-\frac{1}{2}} = \left(-\frac{1}{2}\right)\left(-\frac{2v}{c^2}\right)\left(1 - \frac{v^2}{c^2}\right)^{-\frac{3}{2}}\frac{\mathrm{d}v}{\mathrm{d}t} = \frac{v}{c^2}\gamma^3\frac{\mathrm{d}v}{\mathrm{d}t} = \frac{1}{c^2}\gamma^3\mathbf{v}\cdot\frac{\mathrm{d}\mathbf{v}}{\mathrm{d}t}. \tag{3.1.3}$$

The trick we will use is to calculate the dot product of the particle velocity $\mathbf{v}$ with the force $\mathbf{F}$ in Eq. (3.1.1), that is

$$\mathbf{v}\cdot\mathbf{F} = \mathbf{v}\cdot\left[q\left(\mathbf{E} + \frac{1}{c}\mathbf{v}\times\mathbf{B}\right)\right]. \tag{3.1.4}$$

Using that

$$\gamma^2 = \frac{1}{1-\frac{v^2}{c^2}} = \frac{1-\frac{v^2}{c^2}+\frac{v^2}{c^2}}{1-\frac{v^2}{c^2}} = 1 + \frac{\frac{v^2}{c^2}}{1-\frac{v^2}{c^2}} = 1 + \gamma^2 \frac{\mathbf{v}\cdot\mathbf{v}}{c^2}, \tag{3.1.5}$$

we evaluate the left-hand side (LHS) of Eq. (3.1.4). This gives

$$\begin{aligned}\mathbf{v}\cdot\mathbf{F} &= \mathbf{v}\cdot\left(m\frac{\mathrm{d}\gamma}{\mathrm{d}t}\mathbf{v} + m\gamma\frac{\mathrm{d}\mathbf{v}}{\mathrm{d}t}\right) = m\left(\frac{1}{c^2}\gamma^3\mathbf{v}\cdot\frac{\mathrm{d}\mathbf{v}}{\mathrm{d}t}\right)\mathbf{v}\cdot\mathbf{v} + m\gamma\mathbf{v}\cdot\frac{\mathrm{d}\mathbf{v}}{\mathrm{d}t} \\ &= m\gamma\left(\mathbf{v}\cdot\frac{\mathrm{d}\mathbf{v}}{\mathrm{d}t}\right)\left(\gamma^2\frac{\mathbf{v}\cdot\mathbf{v}}{c^2}+1\right) = m\gamma^3\left(\mathbf{v}\cdot\frac{\mathrm{d}\mathbf{v}}{\mathrm{d}t}\right) = mc^2\frac{\mathrm{d}\gamma}{\mathrm{d}t}.\end{aligned} \tag{3.1.6}$$

On the right-hand side (RHS) of Eq. (3.1.4) we are left with

$$\mathbf{v}\cdot\left[q\left(\mathbf{E}+\frac{1}{c}\mathbf{v}\times\mathbf{B}\right)\right] = q\mathbf{v}\cdot\mathbf{E}, \tag{3.1.7}$$

as $\mathbf{v}\cdot(\mathbf{v}\times\mathbf{B}) = (\mathbf{v}\times\mathbf{v})\cdot\mathbf{B} = 0$. Therefore,

$$mc^2\frac{\mathrm{d}\gamma}{\mathrm{d}t} = q\mathbf{v}\cdot\mathbf{E}. \tag{3.1.8}$$

In our treatment of the problem we assume there is no electric field $\mathbf{E}$ present. This means that the time derivative of the Lorentz factor is zero, that is $\gamma =$ constant and hence $v = |\mathbf{v}| =$ constant. Our equation of motion then simplifies significantly, and becomes

$$\gamma m\frac{\mathrm{d}\mathbf{v}}{\mathrm{d}t} = \frac{q}{c}\left(\mathbf{v}\times\mathbf{B}\right). \tag{3.1.9}$$

This is an ordinary differential equation that, together with a chosen initial value $\mathbf{v}_0 \equiv \mathbf{v}(t=0)$, can be solved numerically.

3.2 Total emitted power

A useful quantity is the total power emitted into synchrotron radiation, sometimes also called the total energy (or radiation) loss rate. For this we take into consideration Larmor's formula for the power emitted by a single, relativistic charge q,

$$P' = \frac{2q^2}{3c^3}|\mathbf{a}'|^2. \tag{3.2.1}$$

Here, the acceleration $\mathbf{a}'$ is the proper acceleration of the particle and the power P' is measured in the particle's instantaneous rest frame S'. In this frame the particle accelerates but will have zero velocity at a certain time. Relating the frame S that moves with the velocity $-v$ with respect to the particle, we have

$$\mathrm{d}W = \gamma\mathrm{d}W', \quad \mathrm{d}t = \gamma\mathrm{d}t'. \tag{3.2.2}$$

We therefore obtain

$$P = \frac{\mathrm{d}W}{\mathrm{d}t} = \frac{\mathrm{d}W'}{\mathrm{d}t'} = P'. \tag{3.2.3}$$

Hence, the total emitted power is a Lorentz invariant, and subsequently we can write

$$P = \frac{2q^2}{3c^3}a'^2, \tag{3.2.4}$$

defining $a' \equiv |\mathbf{a}'|$.

In our case of a particle moving in a magnetic field $\mathbf{B}$, we know that the acceleration is always perpendicular to the magnetic field direction, $a \equiv |\mathbf{a}| = |\mathbf{a}_\perp| \equiv a_\perp$. It is therefore convenient to express the acceleration in terms of its parallel and perpendicular components with respect to $\mathbf{B}$. We have that

$$a'_\parallel = \gamma^3 a_\parallel, \quad a'_\perp = \gamma^2 a_\perp, \tag{3.2.5}$$

such that

$$|\mathbf{a}|^2 = |\mathbf{a}_\parallel|^2 + |\mathbf{a}_\perp|^2 . \tag{3.2.6}$$

The total emitted power becomes

$$P = \frac{2q^2}{3c^3}\gamma^4 \left(a_\perp^2 + \gamma^2 a_\parallel^2\right) = \frac{2q^2}{3c^3}\gamma^4 a_\perp^2, \tag{3.2.7}$$

using that $a_\parallel = 0$. To obtain an expression for $a_\perp$ we begin by simplifying the equation of motion given by Eq. (3.1.9). As for the acceleration, we split the velocity into a component parallel and perpendicular to the magnetic field direction, $\mathbf{v} = \mathbf{v}_\parallel + \mathbf{v}_\perp$. Since $\mathbf{v}_\parallel \times \mathbf{B} = 0$, the equation of motion consists of

$$\frac{\mathrm{d}\mathbf{v}_\parallel}{\mathrm{d}t} = 0, \quad \frac{\mathrm{d}\mathbf{v}_\perp}{\mathrm{d}t} = \frac{q}{\gamma mc}\mathbf{v}_\perp \times \mathbf{B}. \tag{3.2.8}$$

The first equality implies that $\mathbf{v}_\parallel$ = constant, and as remarked previously in Sec. 3.1, the velocity $v = |\mathbf{v}|$ is also a constant quantity. Together this implies that $v_\perp \equiv |\mathbf{v}_\perp|$ = constant. Therefore, given a uniform field $\mathbf{B}$, the motion of the particle then becomes helical. Projected onto the normal plane, this motion is circular, as can be seen in Fig. 3.1.

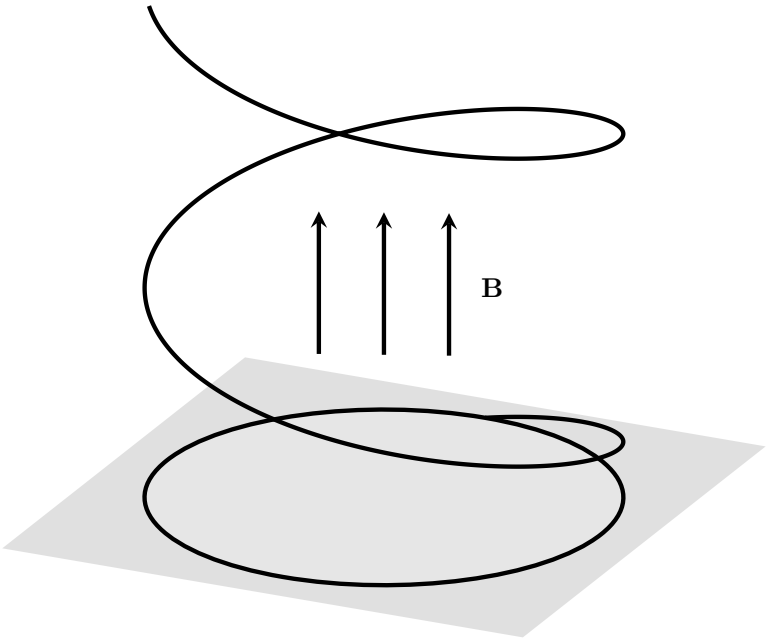

Figure 3.1: Helical motion of a charged particle in a uniform magnetic field $\mathbf{B}$. Projected onto a plane normal to $\mathbf{B}$, the motion is circular.

Since we have circular motion, it is a simple matter to calculate the radius of the circle r by equating the magnitude of the perpendicular Lorentz force $\mathbf{F}$ with the centripetal force $\mathbf{F}_c$. The centripetal acceleration is given by $a_c = v_\perp^2/r$, and we find

$$|\mathbf{F}_c| = |\gamma m \mathbf{a}_c| = \gamma m a_c = \gamma m \frac{v_\perp^2}{r}, \tag{3.2.9a}$$

$$|\mathbf{F}| = \left|\frac{q}{c}\mathbf{v}\times\mathbf{B}\right| = \frac{|q|}{c}v_\perp B, \tag{3.2.9b}$$

where $B \equiv |\mathbf{B}|$ is the strength of the magnetic field. This leads to

$$r = \frac{\gamma m c v_\perp}{|q|B}. \tag{3.2.10}$$

The period of the circular motion is $T = 2\pi r/v_\perp$, and we obtain the angular frequency of rotation, or gyration frequency,

$$\omega_B = 2\pi\nu_B = \frac{2\pi}{T} = \frac{v_\perp}{r} = \frac{|q|B}{\gamma m c}, \tag{3.2.11}$$

where $\nu_B = 1/T$ is the frequency. Revisiting the magnitude of our Lorentz force expression in Eq. (3.2.9),

$$\gamma m a_\perp = |\mathbf{F}| = \frac{|q|}{c}v_\perp B, \tag{3.2.12}$$

we obtain

$$a_\perp = \frac{|q|B}{\gamma m c}v_\perp = \omega_B v_\perp. \tag{3.2.13}$$

We can now find an expression for the total emitted power using the perpendicular velocity. Inserting Eq. (3.2.13) into Eq. (3.2.7),

$$P = \frac{2q^2}{3c^3}\gamma^4\frac{q^2B^2}{\gamma^2m^2c^2}v_\perp^2 = \frac{2}{3}\gamma^2\frac{q^4B^2}{m^2c^5}v_\perp^2. \tag{3.2.14}$$

This can further be simplified to

$$P = \frac{2}{3}r_0^2 c\beta_\perp^2\gamma^2B^2, \tag{3.2.15}$$

using the classical electron radius $r_0 \equiv q^2/(mc^2)$ and $\beta_\perp = v_\perp/c$. We would like an expression for the power dependent on β and not its perpendicular component. For this we take the angle α between the magnetic field $\mathbf{B}$ and the velocity $\mathbf{v}$, called the pitch angle[1], and average over all possible values. This is valid for an isotropic distribution of velocities, and gives

$$\langle\beta_\perp^2\rangle = \frac{\beta^2}{4\pi}\int\sin^2\alpha\mathrm{d}\Omega = \frac{2}{3}\beta^2, \tag{3.2.16}$$

using the solid angle $\mathrm{d}\Omega = \sin\alpha\mathrm{d}\alpha\mathrm{d}\varphi$. We then obtain our final expression for the total power emitted by the particle,

$$P = \left(\frac{2}{3}\right)^2 r_0^2 c\beta^2\gamma^2B^2. \tag{3.2.17}$$

It is also common to write the total emitted power in terms of the magnetic energy density $U_B = B^2/8\pi$ and the Thomson cross section $\sigma_T = 8\pi r_0^2/3$, which gives

$$P = \frac{4}{3}\sigma_T c\beta^2\gamma^2U_B. \tag{3.2.18}$$

For a fixed energy $E = \gamma mc^2$ of the relativistic particle, the total emitted power in Eq. (3.2.17) depends on the particle mass only through r_0 and γ, and we have that $P \propto 1/m^4$. This means that the smaller the mass of the particle, the higher is the contribution to synchrotron radiation. We can essentially disregard all particles except for the electron, due to its low mass compared to other charged particles. From now on, we will therefore assume that $m = m_e$ and write $q = -e$.

[1]Not to be confused with the pitch angle for magnetic fields defined in Eq. (2.5.5).

3.3 Relativistic beaming

When we have emission from a relativistic particle, an important consideration is that the radiation is beamed in the particle's direction of motion. We therefore do not have isotropic radiation when the velocity of the particle is close to the light speed c. For an observer at some position in space, the detected radiation will have a strong dependence on the angle between the particle's velocity and its position relative to the observer. In the following, we will study this so-called relativistic beaming in more detail.

We consider an observer at rest in a reference frame S and a charged particle in the reference frame S' moving at a velocity v in the x-direction relative to the observer. Then the Lorentz transformations for position and time are given by

$$\mathrm{d}t = \gamma\left(\mathrm{d}t' + \frac{v}{c^2}\mathrm{d}x'\right), \tag{3.3.1a}$$

$$\mathrm{d}x = \gamma\left(\mathrm{d}x' + v\mathrm{d}t'\right), \tag{3.3.1b}$$

$$\mathrm{d}y = \mathrm{d}y', \tag{3.3.1c}$$

$$\mathrm{d}z = \mathrm{d}z'. \tag{3.3.1d}$$

It is straightforward to find that

$$u_x = \frac{\mathrm{d}x}{\mathrm{d}t} = \frac{u'_x + v}{1 + vu'_x/c^2}, \tag{3.3.2a}$$

$$u_y = \frac{\mathrm{d}y}{\mathrm{d}t} = \frac{u'_y}{\gamma(1 + vu'_x/c^2)}, \tag{3.3.2b}$$

$$u_z = \frac{\mathrm{d}z}{\mathrm{d}t} = \frac{u'_z}{\gamma(1 + vu'_x/c^2)}. \tag{3.3.2c}$$

We may generalise these equations, assuming that the frame S' moves with velocity $\mathbf{v}$ in an arbitrary direction. Then, if a point has velocity $\mathbf{u}'$ in the frame S', we can express the parallel and perpendicular components of the velocity $\mathbf{u}$ with respect to $\mathbf{v}$ in the frame S as

$$u_\parallel = \frac{u'_\parallel + v}{\left(1 + vu'_\parallel/c^2\right)}, \quad u_\perp = \frac{u'_\perp}{\gamma\left(1 + vu'_\parallel/c^2\right)}. \tag{3.3.3}$$

From our choice of coordinates, the azimuthal angle $\phi = \phi'$ is unchanged. Given $u' \equiv |\mathbf{u}'|$, the polar angle θ changes according to the aberration formula,

$$\tan\theta = \frac{u_\perp}{u_\parallel} = \frac{u'\sin\theta'}{\gamma\left(u'\cos\theta' + v\right)}. \tag{3.3.4}$$

We now simplify by setting $\theta' = \pi/2$ corresponding to a photon emitted at right angles to v in the frame S'. The velocity of the photon is $u = u' = c$, and hence

$$\tan\theta = \frac{c}{\gamma v}. \tag{3.3.5}$$

When the particle moves at velocities v close to the speed of light, $\gamma \gg 1$ and θ becomes small. Then the approximation $\tan\theta \simeq \theta$ is valid, giving

$$\theta \simeq \frac{1}{\gamma}, \tag{3.3.6}$$

where we also set $v \simeq c$. We can therefore conclude that a fast moving source, such as an ultra-relativistic electron, emits photons mainly in the forward direction within a cone of opening

angle $\theta \simeq 1/\gamma$. An illustration of the beaming of the radiation is shown in Fig. 3.2. In the reference frame S' of the particle, the radiation is emitted isotropically, while it is beamed in the reference frame S of the observer. As an example, an electron with a Lorentz factor of 10^5, that is an energy of approximately 50 GeV, will emit photons beamed within a cone of opening angle $\theta = 10^{-5}$ rad $\simeq 2$ arcsec.

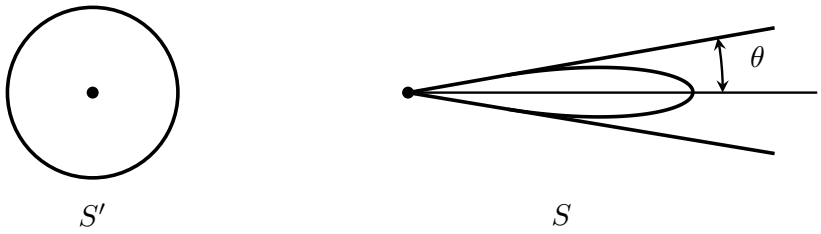

Figure 3.2: Relativistic beaming for a charged particle in its rest frame S' and in the reference frame S of the observer.

3.4 Geometry

We now intend to describe the geometry of polarisation for synchrotron radiation using Fig. 3.3 as a reference. For the instant $t = 0$, we define a coordinate system such that the particle is in the origin with velocity $\mathbf{v}$ along the x-axis. The unit vector $\mathbf{n}$ is pointing towards the observer and lies in the xz-plane, and the angle θ is defined as the angle between $-\mathbf{x}$ and $\mathbf{v}$. In Fig. 3.3 this corresponds to the angle between $\mathbf{n}$ and the x-axis. For this geometry, the magnetic field $\mathbf{B}$ lies along the z-axis, giving an instantaneous orbit in the xy-plane with radius of curvature

$$a \equiv |\mathbf{a}| = \frac{v}{\omega_B \sin\alpha}. \tag{3.4.1}$$

Here, α is the particle pitch angle, i.e. the angle between $\mathbf{B}$ and $\mathbf{v}$, introduced in Sec. 3.2. Another two unit vectors $\boldsymbol{\epsilon}_\perp$ and $\boldsymbol{\epsilon}_\parallel = \mathbf{n} \times \boldsymbol{\epsilon}_\perp$ are defined such that $\boldsymbol{\epsilon}_\parallel$ lies along the y-axis, that is in the acceleration direction, perpendicular to both the magnetic field $\mathbf{B}$ and to the velocity $\mathbf{v}$.

As seen in projection by the observer, the magnetic field $\mathbf{B}$ is perpendicular and parallel to the vectors $\boldsymbol{\epsilon}_\perp$ and $\boldsymbol{\epsilon}_\parallel$, respectively. This geometry allows us to describe the two polarisation states of synchrotron radiation that is observed.

3.5 Radiation field

The radiation field of an electron consists of the electric and magnetic field,

$$\mathbf{E}(\mathbf{r}, t) = \frac{e}{c}\left\{\frac{\mathbf{n}}{\kappa^3 R} \times [(\mathbf{n} - \boldsymbol{\beta}') \times \dot{\boldsymbol{\beta}}']\right\}, \tag{3.5.1a}$$

$$\mathbf{B}(\mathbf{r}, t) = \mathbf{n} \times \mathbf{E}. \tag{3.5.1b}$$

Here we have defined

$$\boldsymbol{\beta}' \equiv \frac{\mathbf{v}'}{c}, \quad \kappa \equiv 1 - \mathbf{n} \cdot \boldsymbol{\beta}', \quad \mathbf{n} \equiv \frac{\mathbf{R}}{R}, \tag{3.5.2}$$

where $R \equiv |\mathbf{R}|$ such that $\mathbf{n}$ defines a unit vector, and $\mathbf{E}$, $\mathbf{B}$ and $\mathbf{n}$ are mutually perpendicular. The primes refers to evaluation at the retarded time,

$$t' = t - \frac{R(t')}{c}, \tag{3.5.3}$$

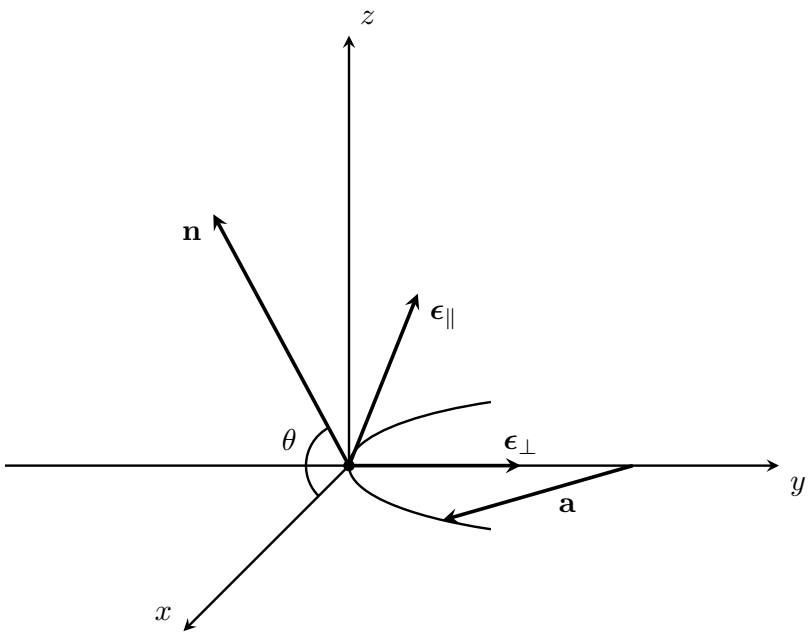

Figure 3.3: Polarisation geometry of synchrotron radiation. At $t = 0$, the particle is in the origin with velocity along the x-axis and $\mathbf{B}$ along the z-axis. The trajectory then lies in the xy-plane with radius of curvature a. The vector $\mathbf{n}$ points towards the observer.

where

$$\mathbf{R}(t') = \mathbf{r} - \mathbf{r}_1(t'), \quad R(t') \simeq r - \mathbf{n} \cdot \mathbf{r}_1(t'), \tag{3.5.4}$$

for the assumption that $r_1 \ll r$, where $r_1 \equiv |\mathbf{r}_1|$ and $r \equiv |\mathbf{r}|$. Differentiating the expression for the retarded time, we get the time-interval ratio

$$\frac{\partial t'}{\partial t} = \frac{1}{1 - \mathbf{n} \cdot \boldsymbol{\beta}'} = \frac{1}{\kappa}. \tag{3.5.5}$$

We can also write the time t in terms of the retarded time t' as

$$t = t' + \frac{R(t')}{c} = t' + \frac{r}{c} - \frac{\mathbf{n} \cdot \mathbf{r}_1}{c}. \tag{3.5.6}$$

The charged particle will follow a periodic motion with frequency of rotation ω_B. However, we should distinguish between the received and emitted power. The power received by an observer will be at a Doppler shifted frequency of rotation. The particle is therefore observed at a frequency of rotation ω_B/b, where b is a constant taking this Doppler effect into account, considering the difference in periods at the source and at the field point. Whether or not to include this factor depends on the situation. In most cases it is not necessary to include b as it will not contribute in a physical sense. This factor does in fact drop out in our calculations of the polarisation degree in chapter 5. For this reason we choose to not include the factor in the following calculations, essentially setting $b = 1$, but keeping track of the factor throughout the thesis to make the arguments as clear as possible.

Using the angular frequency of rotation ω_B, we can now write the particle's radiation field as a superposition of harmonics of frequency $2\pi/\omega_B$, that is [11]

$$\mathbf{E}(r, t) = \sum_{n=-\infty}^{\infty} E_n \exp\left(in\omega_B t\right), \tag{3.5.7}$$

where

$$\mathbf{E}_n(r) = \frac{\omega_B}{2\pi}\int_0^{\frac{2\pi}{\omega_B}} \mathbf{E}\exp\left(in\omega_B t\right)\mathrm{d}t. \tag{3.5.8}$$

Inserting Eq. (3.5.1a), we obtain

$$\mathbf{E}_n(r) = \frac{e}{2\pi cr}\omega_B\int_0^{\frac{2\pi}{\omega_B}} \frac{\mathbf{n}\times[(\mathbf{n}-\boldsymbol{\beta}')\times\dot{\boldsymbol{\beta}}']}{\kappa^3}\exp\left(in\omega_B t\right)\mathrm{d}t. \tag{3.5.9}$$

Since we need to evaluate the expressions with primes at the retarded time, we use Eq. (3.5.5) to write $\mathrm{d}t = \kappa\mathrm{d}t'$. Then using the expression for the time t in terms of the retarded time t' in Eq. (3.5.6), we can write

$$\begin{aligned}\exp(in\omega_B t) &= \exp\left[in\omega_B\left(t' + \frac{r}{c} - \frac{\mathbf{n}\cdot\mathbf{r}_1(t')}{c}\right)\right]\\ &= \exp\left(in\omega_B\frac{r}{c}\right)\exp\left[in\omega_B\left(t' - \frac{\mathbf{n}\cdot\mathbf{r}_1(t')}{c}\right)\right].\end{aligned} \tag{3.5.10}$$

Consequently, Eq. (3.5.9) becomes

$$\mathbf{E}_n(r) = \frac{e}{2\pi cr}\omega_B\exp\left(in\omega_B\frac{r}{c}\right)\int_0^{\frac{2\pi}{\omega_B}} \frac{\mathbf{n}\times[(\mathbf{n}-\boldsymbol{\beta}')\times\dot{\boldsymbol{\beta}}']}{\kappa^2}\exp\left[in\omega_B\left(t' - \frac{\mathbf{n}\cdot\mathbf{r}_1(t')}{c}\right)\right]\mathrm{d}t'. \tag{3.5.11}$$

Using the identity

$$\frac{\mathbf{n}\times[(\mathbf{n}-\boldsymbol{\beta}')\times\dot{\boldsymbol{\beta}}']}{\kappa^2} = \frac{\mathrm{d}}{\mathrm{d}t'}\left[\frac{\mathbf{n}\times(\mathbf{n}\times\boldsymbol{\beta}')}{\kappa}\right], \tag{3.5.12}$$

and integrating by parts, Eq. (3.5.11) simplifies to

$$\mathbf{E}_n(r) = \frac{e}{2\pi cr}\omega_B^2 in\exp\left(in\omega_B\frac{r}{c}\right)\int_{-\infty}^{\infty}\mathbf{n}\times(\mathbf{n}\times\boldsymbol{\beta}')\exp\left[in\omega_B\left(t' - \frac{\mathbf{n}\cdot\mathbf{r}_1(t')}{c}\right)\right]\mathrm{d}t'. \tag{3.5.13}$$

We are interested in rewriting Eq. (3.5.13) by splitting the electric field into perpendicular and parallel components. To do this we will use the coordinate system $(\mathbf{n}, \boldsymbol{\epsilon}_\perp, \boldsymbol{\epsilon}_\parallel)$ described in Sec. 3.4. As the particle moves in the orbit with radius of curvature a, the angular distance travelled after a time t' is vt'/a. This angle corresponds to the angle between the y-axis and $\mathbf{a}$ in Fig. 3.3. We find that

$$\mathbf{r}_1\left(t'\right) = 2a\sin\left(\frac{vt'}{2a}\right)\left[\boldsymbol{\epsilon}_\perp\sin\left(\frac{vt'}{2a}\right) + \mathbf{n}\cos\theta\cos\left(\frac{vt'}{2a}\right) - \boldsymbol{\epsilon}_\parallel\sin\theta\cos\left(\frac{vt'}{2a}\right)\right]. \tag{3.5.14}$$

The velocity is then given by

$$\mathbf{v}' = v\left[\boldsymbol{\epsilon}_\perp\sin\left(\frac{vt'}{a}\right) + \mathbf{n}\cos\theta\cos\left(\frac{vt'}{a}\right) - \boldsymbol{\epsilon}_\parallel\sin\theta\cos\left(\frac{vt'}{a}\right)\right]. \tag{3.5.15}$$

Using that $\mathbf{n}\times\boldsymbol{\epsilon}_\perp = \boldsymbol{\epsilon}_\parallel$, $\mathbf{n}\times\boldsymbol{\epsilon}_\parallel = -\boldsymbol{\epsilon}_\perp$ and $\mathbf{n}\times\mathbf{n} = 0$, we obtain

$$\mathbf{n}\times(\mathbf{n}\times\boldsymbol{\beta}') = \beta\left[-\sin\left(\frac{vt'}{a}\right)\boldsymbol{\epsilon}_\perp + \sin\theta\cos\left(\frac{vt'}{a}\right)\boldsymbol{\epsilon}_\parallel\right]. \tag{3.5.16}$$

One finds, by inserting the expression for $\mathbf{r}_1(t')$ from Eq. (3.5.14), that

$$t' - \frac{\mathbf{n}\cdot\mathbf{r}_1\left(t'\right)}{c} = t' - \frac{a}{c}\cos\theta\sin\left(\frac{vt'}{a}\right). \tag{3.5.17}$$

Making an expansion to third order gives us

$$t' - \frac{\mathbf{n}\cdot\mathbf{r}_1(t')}{c} = t'\left(1-\frac{v}{c}\right) + \frac{v}{c}\frac{\theta^2}{2}t' + \frac{v^3}{6ca^2}t'^3. \tag{3.5.18}$$

Here we have assumed that θ and vt'/c are small, and made the expansions

$$\cos\theta \simeq 1 - \frac{\theta^2}{2}, \tag{3.5.19}$$

$$\sin\left(\frac{vt'}{a}\right) \simeq \frac{vt'}{a} - \frac{v^3t'^3}{6a^3}. \tag{3.5.20}$$

We now write $(1-v/c) = 1/2\gamma^2$ since $v \simeq c$ and $\gamma \gg 1$. Using this approximation and setting $v = c$, Eq. (3.5.18) can be simplified to

$$t' - \frac{\mathbf{n}\cdot\mathbf{r}_1(t')}{c} \simeq \frac{1}{2\gamma^2}\left[t'\left(1+\gamma^2\frac{v}{c}\theta^2\right) + \frac{v^3\gamma^2t'^3}{3ca^2}\right] = \frac{1}{2\gamma^2}\left[t'\left(1+\gamma^2\theta^2\right) + \frac{c^2\gamma^2t'^3}{3a^2}\right]. \tag{3.5.21}$$

To simplify the term $\mathbf{n}\times(\mathbf{n}\times\boldsymbol{\beta}')$, we will use the result of Legg and Westfold [12] to evaluate the expression to the order of γ^{-2} instead of γ^{-1} as done by [9, 10]. In our notation, we get that

$$\mathbf{n}\times(\mathbf{n}\times\boldsymbol{\beta}') \simeq \left[-\frac{vt'}{a}\boldsymbol{\epsilon}_\perp + \left(\theta - \frac{1}{2}\left\{\frac{vt'}{a}\right\}^2\cot\alpha\right)\boldsymbol{\epsilon}_\parallel\right]. \tag{3.5.22}$$

We now introduce some convenient substitutions, defining

$$\theta_\gamma^2 \equiv 1+\gamma^2\theta^2, \quad y \equiv \frac{\gamma ct'}{a\theta_\gamma}, \quad \eta \equiv \frac{n\omega_B a\theta_\gamma^3}{3c\gamma^3}. \tag{3.5.23}$$

The expression in the exponential inside the integral in Eq. (3.5.13) can consequently be simplified to give

$$in\omega_B\left(t' - \frac{\mathbf{n}\cdot\mathbf{r}_1(t')}{c}\right) = \mathrm{i}\frac{3}{2}\eta\left(y+\frac{1}{3}y^3\right). \tag{3.5.24}$$

Changing the variable of integration from t' to y gives the differential $\mathrm{d}t' = (a\theta_\gamma/\gamma c)\mathrm{d}y$. We also see that $vt'/a = y\theta_\gamma/\gamma$, when $v = c$. With all the mentioned substitutions, the perpendicular and parallel components of $\mathbf{E}_n$ may be written as

$$\begin{aligned} E_\perp &= -\frac{e}{2\pi cr}\omega_B^2 in\exp\left(in\omega_B\frac{r}{c}\right)\int_{-\infty}^{\infty}\frac{\theta_\gamma}{\gamma}y\exp\left[\mathrm{i}\frac{3}{2}\eta\left(y+\frac{1}{3}y^3\right)\right]\frac{a\theta_\gamma}{\gamma c}\mathrm{d}y \\ &= -\frac{e}{2\pi cr}\omega_B^2 in\exp\left(in\omega_B\frac{r}{c}\right)\left(\frac{a\theta_\gamma^2}{\gamma^2 c}\right)\int_{-\infty}^{\infty}y\exp\left[\mathrm{i}\frac{3}{2}\eta\left(y+\frac{1}{3}y^3\right)\right]\mathrm{d}y, \end{aligned} \tag{3.5.25}$$

and

$$\begin{aligned} E_\parallel &= \frac{e}{2\pi cr}\omega_B^2 in\exp\left(in\omega_B\frac{r}{c}\right)\int_{-\infty}^{\infty}\left(\theta - \frac{\theta_\gamma^2}{2\gamma^2}y^2\cot\alpha\right)\exp\left[\mathrm{i}\frac{3}{2}\eta\left(y+\frac{1}{3}y^3\right)\right]\frac{a\theta_\gamma}{\gamma c}\mathrm{d}y \\ &= \frac{e}{2\pi cr}\omega_B^2 in\exp\left(in\omega_B\frac{r}{c}\right)\int_{-\infty}^{\infty}\left(\frac{a\theta\theta_\gamma}{\gamma c} - \frac{a\theta_\gamma^3}{2\gamma^3 c}y^2\cot\alpha\right)\exp\left[\mathrm{i}\frac{3}{2}\eta\left(y+\frac{1}{3}y^3\right)\right]\mathrm{d}y, \end{aligned} \tag{3.5.26}$$

respectively. Now it remains to calculate the integrals in Eq. (3.5.25) and (3.5.26). In appendix A.1 we present full derivations of integrals denoted $\mathcal{I}_{\gamma,s}$. Using these, it is straightforward to find that

$$\int_{-\infty}^{\infty}y^2\exp\left[\mathrm{i}\frac{3}{2}\eta\left(y+\frac{1}{3}y^3\right)\right]\mathrm{d}y = -\frac{2}{\sqrt{3}}K_{1/3}(\eta), \tag{3.5.27a}$$

$$\int_{-\infty}^{\infty} y \exp\left[\mathrm{i}\frac{3}{2}\eta\left(y+\frac{1}{3}y^3\right)\right]\mathrm{d}y = \mathrm{i}\frac{2}{\sqrt{3}}K_{2/3}(\eta), \tag{3.5.27b}$$

$$\int_{-\infty}^{\infty} \exp\left[\mathrm{i}\frac{3}{2}\eta\left(y+\frac{1}{3}y^3\right)\right]\mathrm{d}y = \frac{2}{\sqrt{3}}K_{1/3}(\eta). \tag{3.5.27c}$$

Here, $K_{2/3}$ and $K_{1/3}$ are the modified Bessel functions of order $2/3$ and $1/3$, respectively. These functions are plotted in Fig. 3.4 to illustrate their behaviour. The modified Bessel function $K_{2/3}(x)$ dominates over $K_{1/3}(x)$ for small values of x, while they both fast approach zero for larger values of x. For large values of x, one can obtain the asymptotic expansion of the modified Bessel function [42],

$$K_\nu(x) \simeq \left(\frac{\pi}{2}\right)^{1/2} \mathrm{e}^{-x} x^{-1/2}\left(1+\frac{4\nu^2-1}{8x}\right), \quad x \gg 1. \tag{3.5.28}$$

For the cases $\nu = 2/3$ and $\nu = 1/3$, we have that

$$K_{2/3}(x) \simeq \left(\frac{\pi}{2}\right)^{1/2} \mathrm{e}^{-x} x^{-1/2}\left(1+\frac{7}{72x}\right), \quad x \gg 1, \tag{3.5.29a}$$

$$K_{1/3}(x) \simeq \left(\frac{\pi}{2}\right)^{1/2} \mathrm{e}^{-x} x^{-1/2}\left(1-\frac{5}{72x}\right), \quad x \gg 1. \tag{3.5.29b}$$

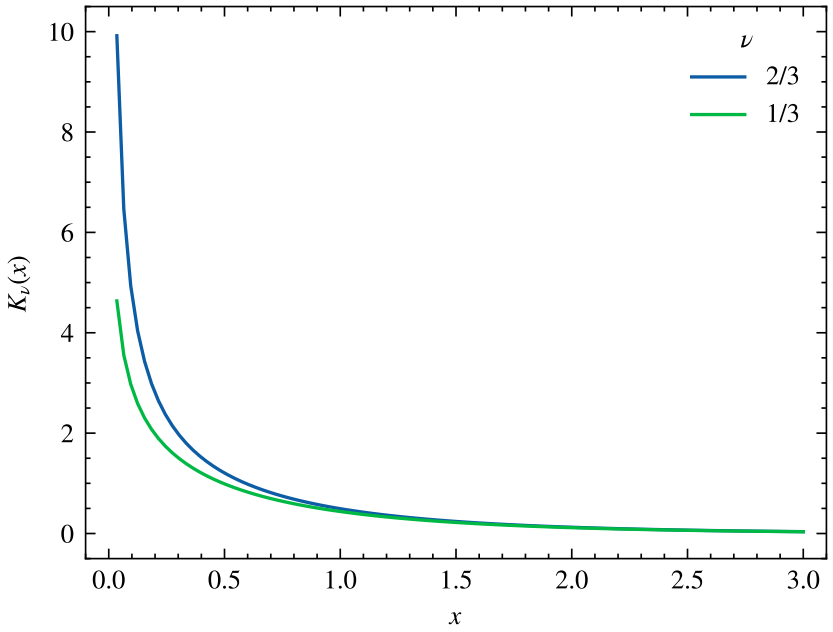

Figure 3.4: Modified Bessel functions $K_\nu(x)$ of order $\nu = 2/3$ and $\nu = 1/3$.

Using now the integrals in Eq. (3.5.27), the expressions in Eq. (3.5.25) and (3.5.26) finally become

$$E_\perp = -\frac{e}{\sqrt{3}\pi c r}\omega_B^2 n \exp\left(\mathrm{i}n\omega_B\frac{r}{c}\right)\left(\frac{a\theta_\gamma^2}{\gamma^2 c}\right)K_{2/3}(\eta), \tag{3.5.30a}$$

$$E_\parallel = \frac{e}{\sqrt{3}\pi c r}\omega_B^2 \mathrm{i}n \exp\left(\mathrm{i}n\omega_B\frac{r}{c}\right)\left(\frac{a\theta\theta_\gamma}{\gamma c}+\frac{a\theta_\gamma^3}{2\gamma^3 c}\cot\alpha\right)K_{1/3}(\eta). \tag{3.5.30b}$$

The obtained components of the radiation field depend strongly on the argument of the modified Bessel functions. From Fig. 3.4, it is clear that the radiation field becomes small for increasing

η as K_ν approaches zero. The variable η is in turn proportional to θ_γ^3. By keeping the other variables constant, we see that this dependence leads to a stronger radiation field for smaller angles θ. This is what we would expect from our discussion of relativistic beaming in Sec. 3.3.

We note that in keeping the factor b, corresponding to taking the Doppler shift into account for the observed frequency, only would correspond to substituting ω_B for ω_B/b in the obtained equations. The components of the radiation field in Eq. (3.5.30) would therefore depend on b if this factor was considered. However, what we are interested in are the polarisation degrees, and as mentioned, the factor will disappear once these are calculated in chapter 5.

Chapter 4

Spectrum of synchrotron radiation

We now intend to describe the spectrum of synchrotron radiation. We will begin by looking at the intensity spectrum of a single electron, and then extend the treatment to a power-law electron distribution. The intensity spectrum can be found as a special case of the discussion of the polarisation degree in chapter 5. However, the treatment in chapter 5 is more complicated. We therefore choose to follow the approach of the books by Rybicki and Lightman [9] and Longair [10] in this chapter. This serves to familiarise ourselves with the calculations, and the behaviour of the intensity spectrum. In the final section of this chapter we will consider the conditions for when classical electrodynamics is valid.

4.1 Intensity spectrum

We consider the two polarisation states determined by the unit vectors $\boldsymbol{\epsilon}_\perp$ and $\boldsymbol{\epsilon}_\parallel$ as shown in Fig. 3.3. Then the total intensity spectrum, or energy per angular frequency ω per solid angle Ω, is defined as

$$\frac{\mathrm{d}W}{\mathrm{d}\omega\mathrm{d}\Omega} = \frac{c}{4\pi^2}\left|\int R\mathbf{E}(t)\mathrm{e}^{\mathrm{i}\omega t}\mathrm{d}t\right|^2 = \frac{e^2}{4\pi^2 c}\left|\int\left[\mathbf{n}\times\{(\mathbf{n}-\boldsymbol{\beta}')\times\dot{\boldsymbol{\beta}}'\}\kappa^{-3}\right]\mathrm{e}^{\mathrm{i}\omega t}\mathrm{d}t\right|^2. \tag{4.1.1}$$

We can split the intensity spectrum into a sum of the perpendicular and parallel spectra, that is

$$\frac{\mathrm{d}W}{\mathrm{d}\omega\mathrm{d}\Omega} \equiv \frac{\mathrm{d}W_\perp}{\mathrm{d}\omega\mathrm{d}\Omega} + \frac{\mathrm{d}W_\parallel}{\mathrm{d}\omega\mathrm{d}\Omega}. \tag{4.1.2}$$

We have already calculated the components of the nth harmonic of the electric field in Sec. 3.5, so we can reuse many of the arguments presented there to find the intensity spectrum. In Sec. 3.5, we denoted the angular frequency of rotation ω_B, which in this section becomes ω, since we are considering an arbitrary angular frequency. We also want to consider the total radiation field $\mathbf{E}$, not the nth harmonic $\mathbf{E}_n$. We will essentially replace the summation by an integral, assuming a continuous distribution of modes. By the same assumptions made leading to Eq. (3.5.11), we obtain

$$\frac{\mathrm{d}W}{\mathrm{d}\omega\mathrm{d}\Omega} = \frac{e^2\omega^2}{4\pi^2 c}\left|\int\mathbf{n}\times(\mathbf{n}\times\boldsymbol{\beta}')\exp\left[\mathrm{i}\omega\left(t'-\frac{\mathbf{n}\cdot\mathbf{r}_1(t')}{c}\right)\right]\mathrm{d}t'\right|^2. \tag{4.1.3}$$

The term $\mathbf{n}\times(\mathbf{n}\times\boldsymbol{\beta}')$ is split into a perpendicular and parallel component according to Eq. (3.5.22), however we omit the second order approximation in $1/\gamma$ and write as in [9] and [10],

$$\mathbf{n}\times\left(\mathbf{n}\times\boldsymbol{\beta}'\right) \simeq \left(-\frac{vt'}{a}\boldsymbol{\epsilon}_\perp + \theta\boldsymbol{\epsilon}_\parallel\right). \tag{4.1.4}$$

We also recall the third order approximation made in Eq. (3.5.21). The perpendicular and parallel components of the intensity spectrum can then be written as

$$\frac{\mathrm{d}W_\perp}{\mathrm{d}\omega\mathrm{d}\Omega} = \frac{e^2\omega^2}{4\pi^2 c}\left|\int \frac{ct'}{a}\exp\left[\frac{\mathrm{i}\omega}{2\gamma^2}\left(\theta_\gamma^2 t' + \frac{c^2\gamma^2 t^3}{3a^2}\right)\right]\mathrm{d}t'\right|^2, \tag{4.1.5a}$$

$$\frac{\mathrm{d}W_\parallel}{\mathrm{d}\omega\mathrm{d}\Omega} = \frac{e^2\omega^2\theta^2}{4\pi^2 c}\left|\int \exp\left[\frac{\mathrm{i}\omega}{2\gamma^2}\left(\theta_\gamma^2 t' + \frac{c^2\gamma^2 t^3}{3a^2}\right)\right]\mathrm{d}t'\right|^2. \tag{4.1.5b}$$

We again introduce some convenient substitutions,

$$\theta_\gamma^2 \equiv 1 + \gamma^2\theta^2, \quad y \equiv \frac{\gamma c t'}{a\theta_\gamma}, \quad \eta \equiv \frac{\omega a \theta_\gamma^3}{3c\gamma^3}. \tag{4.1.6}$$

θ_γ and y are the same variables as defined in Sec. 3.5, but η is slightly different. The only change is that ω_B has become ω and $n = 1$. These substitutions allow us to write Eq. (4.1.5a) and (4.1.5b) as

$$\frac{\mathrm{d}W_\perp}{\mathrm{d}\omega\mathrm{d}\Omega} = \frac{e^2\omega^2}{4\pi^2 c}\left(\frac{a\theta_\gamma^2}{\gamma^2 c}\right)^2\left|\int_{-\infty}^{\infty} y\exp\left[\frac{3}{2}\mathrm{i}\eta\left(y + \frac{1}{3}y^3\right)\right]\mathrm{d}y\right|^2, \tag{4.1.7a}$$

$$\frac{\mathrm{d}W_\parallel}{\mathrm{d}\omega\mathrm{d}\Omega} = \frac{e^2\omega^2\theta^2}{4\pi^2 c}\left(\frac{a\theta_\gamma}{\gamma c}\right)^2\left|\int_{-\infty}^{\infty} \exp\left[\frac{3}{2}\mathrm{i}\eta\left(y + \frac{1}{3}y^3\right)\right]\mathrm{d}y\right|^2. \tag{4.1.7b}$$

Using Eq. (3.5.27b) and (3.5.27c), we obtain the intensity spectrum in the two polarisation states,

$$\frac{\mathrm{d}W_\perp}{\mathrm{d}\omega\mathrm{d}\Omega} = \frac{e^2\omega^2}{3\pi^2 c}\left(\frac{a\theta_\gamma^2}{\gamma^2 c}\right)^2 K_{2/3}^2(\eta), \tag{4.1.8a}$$

$$\frac{\mathrm{d}W_\parallel}{\mathrm{d}\omega\mathrm{d}\Omega} = \frac{e^2\omega^2\theta^2}{3\pi^2 c}\left(\frac{a\theta_\gamma}{\gamma c}\right)^2 K_{1/3}^2(\eta). \tag{4.1.8b}$$

It is convenient to define the critical angular frequency,

$$\omega_c \equiv \frac{3}{2}\gamma^3\omega_B\sin\alpha, \tag{4.1.9}$$

which corresponds to the frequency at which the electron emits most strongly. Above this frequency, the power spectrum is expected to fall of rapidly. We will comment further on this at the end of this section.

A plot of the angular variation of the intensity of synchrotron radiation given a constant pitch angle $\alpha = 90°$ is shown in Fig. 4.1. Both the perpendicular components (solid lines) and parallel components (dashed lines) are plotted using Eq. (4.1.8a) and (4.1.8b), respectively. Four different values of constant $x = \omega/\omega_c$ are plotted and the intensities are normalised to the peak value for each x, that is the perpendicular component for $\theta = 0$. Although the perpendicular intensity is maximum for $\theta = 0$, the parallel component is maximum at some angle $\theta > 0$. It is clear that large values of x lead to a total intensity much more concentrated around $\theta = 0$.

We have not yet discussed the polarisation, however we can still make some conclusions based on Fig. 4.1. We see that the radiation is linearly polarised in the plane perpendicular to the magnetic field direction at $\theta = 0$, since the parallel component of the intensity is zero. For increasing θ we get an increase in the parallel intensity, which means that the polarisation increases in the parallel plane [43].

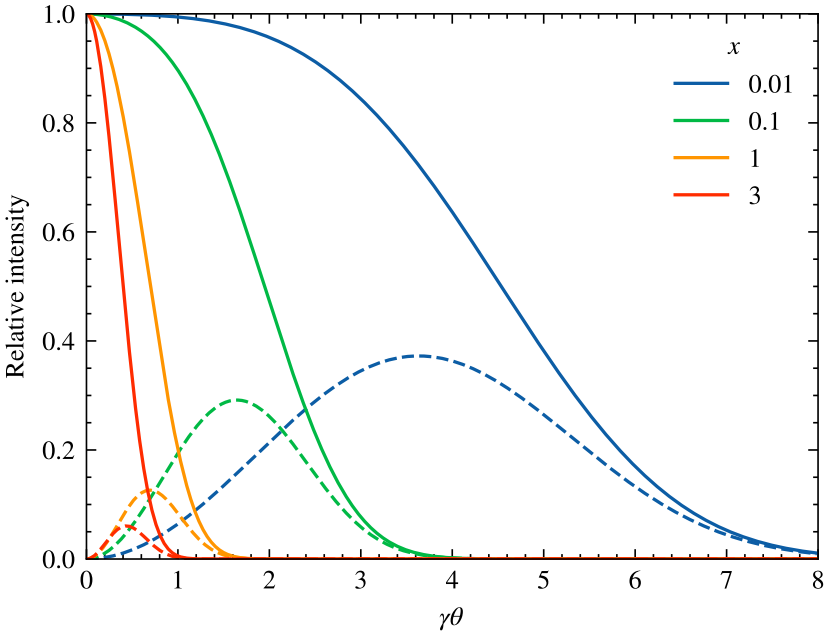

Figure 4.1: Relative intensity of synchrotron radiation as a function of $x = \omega/\omega_c$ given pitch angle $\alpha = 90°$ for the perpendicular component (solid lines) and the parallel component (dashed lines).

We now wish to get rid of the solid angle dependence of the intensity spectrum. From Sec. 3.3 we know that the radiation will be almost completely confined to the shaded area in Fig. 4.2, that is the area within an angle $1/\gamma$ of a cone of half-angle equal to the pitch angle α. We are therefore able to take the element of solid angle $\mathrm{d}\Omega = 2\pi \sin\alpha \mathrm{d}\theta$, and the integration limits can be taken to be from $-\infty$ to ∞ as the radiation is concentrated to small angles around α. Integrating Eq. (4.1.8a) and (4.1.8b) over Ω gives then

$$I_\perp(\omega) = \frac{\mathrm{d}W_\perp}{\mathrm{d}\omega} = \frac{2e^2\omega^2 a^2 \sin\alpha}{3\pi c^3\gamma^4} \int_{-\infty}^{\infty} \theta_\gamma^4 K_{2/3}^2(\eta)\mathrm{d}\theta, \tag{4.1.10a}$$

$$I_\parallel(\omega) = \frac{\mathrm{d}W_|}{\mathrm{d}\omega} = \frac{2e^2\omega^2 a^2 \sin\alpha}{3\pi c^3\gamma^2} \int_{-\infty}^{\infty} \theta_\gamma^2\theta^2 K_{1/3}^2(\eta)\mathrm{d}\theta. \tag{4.1.10b}$$

By noting that we can write $\eta = \frac{1}{2}\theta_\gamma^3 x$ for $x = \omega/\omega_c$, these integrals can be solved using the integrals in Eq. (A.2.6) and (A.2.3) in appendix A. After some reduction, we have that

$$I_\perp(\omega) = \frac{\mathrm{d}W_\perp}{\mathrm{d}\omega} = \frac{\sqrt{3}e^2\gamma \sin\alpha}{2c}[F(x) + G(x)], \tag{4.1.11a}$$

$$I_\parallel(\omega) = \frac{\mathrm{d}W_\parallel}{\mathrm{d}\omega} = \frac{\sqrt{3}e^2\gamma \sin\alpha}{2c}[F(x) - G(x)], \tag{4.1.11b}$$

for $x = \omega/\omega_c$ and

$$F(x) \equiv x \int_x^{\infty} K_{5/3}(\xi)\mathrm{d}\xi, \tag{4.1.12a}$$

$$G(x) \equiv xK_{2/3}(x). \tag{4.1.12b}$$

The behaviour of these two functions is shown in Fig. 4.3, as a normal plot and a log-log plot. One usually considers the asymptotic forms of $F(x)$ and $G(x)$ for large values of x, which are given by [11]

$$F(x) \simeq \left(\frac{\pi}{2}\right)^{1/2} \mathrm{e}^{-x} x^{1/2} \left(1 + \frac{55}{72x}\right), \quad x \gg 1, \tag{4.1.13a}$$

$$G(x) \simeq \left(\frac{\pi}{2}\right)^{1/2} \mathrm{e}^{-x} x^{1/2} \left(1 + \frac{7}{72x}\right), \quad x \gg 1. \tag{4.1.13b}$$

One can also obtain these relations using the expression for the asymptotic behaviour of the modified Bessel functions presented in Eq. (3.5.28). To the lowest order, the functions obtained are the same for large x, as Fig. 4.3 also might suggest. On the other hand, for small values of x one can obtain for $F(x)$ [9],

$$F(x) \simeq \frac{4\pi}{\sqrt{3}\Gamma(\frac{1}{3})} \left(\frac{x}{2}\right)^{1/3}, \quad x \ll 1. \tag{4.1.14}$$

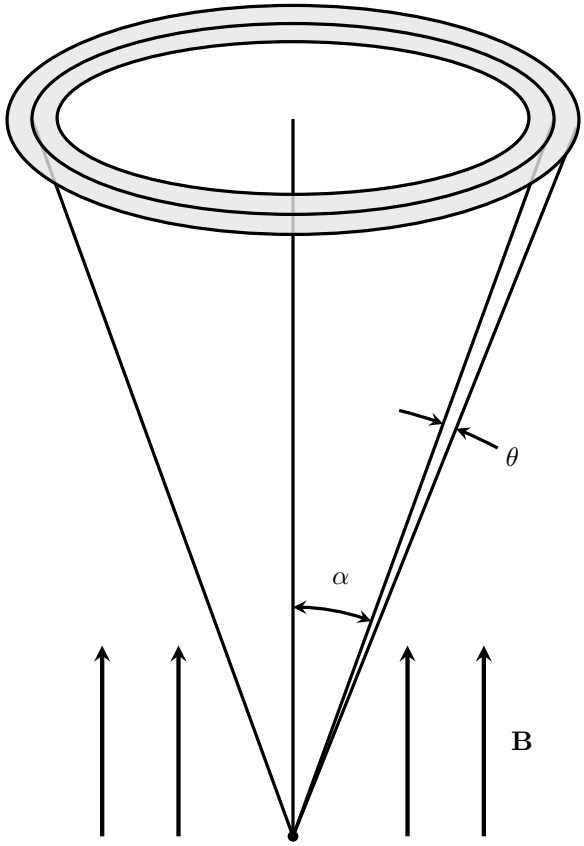

Figure 4.2: Synchrotron emission from a particle in a magnetic field **B** with pitch angle α. The shaded area is where most of the radiation is confined.

The results in Eq. (4.1.11a) and (4.1.11b) are expressions for the energy per frequency range radiated per orbit in the projected normal plane. By dividing these equations by the orbital period of the charge, that is $T = 2\pi/\omega_B$, we get expressions for the emitted power per frequency,

$$P_\perp(\omega) = \frac{\sqrt{3}e^3 B \sin\alpha}{4\pi mc^2}[F(x) + G(x)], \tag{4.1.15a}$$

$$P_\parallel(\omega) = \frac{\sqrt{3}e^3 B \sin\alpha}{4\pi mc^2}[F(x) - G(x)]. \tag{4.1.15b}$$

The total emitted power per frequency is then given by the sum of the two components,

$$P(\omega) = \frac{\sqrt{3}e^3 B \sin\alpha}{2\pi mc^2} F(x). \tag{4.1.16}$$

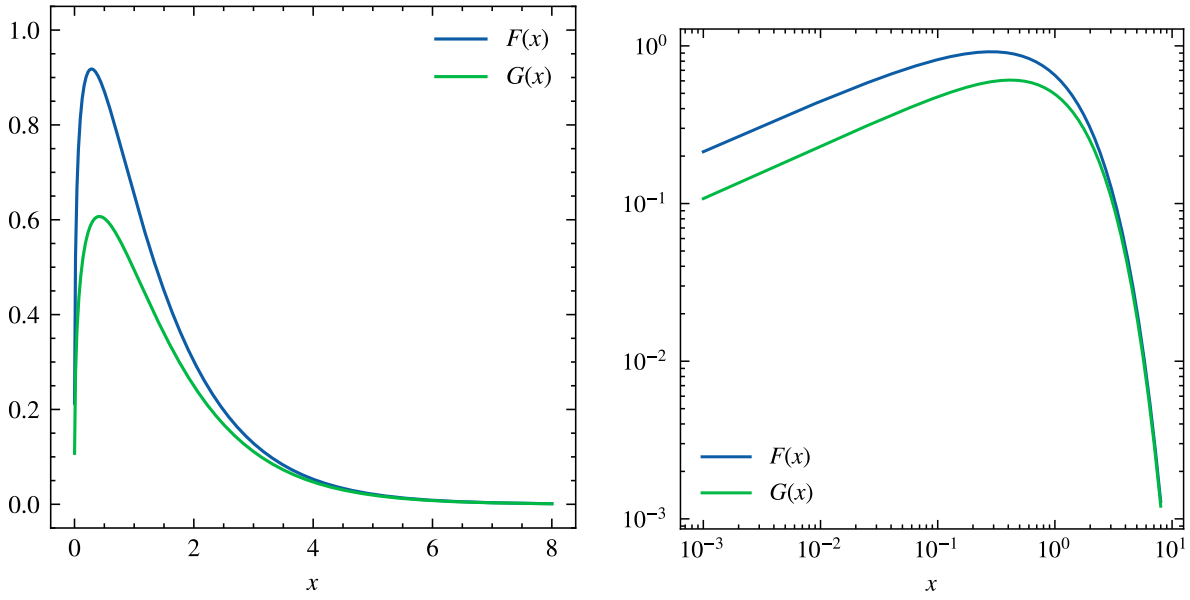

Figure 4.3: The functions $F(x)$ and $G(x)$ in terms of $x = \omega/\omega_c$ as (a) a normal plot and (b) a log-log plot.

To analyse the spectrum of synchrotron radiation, that is the behaviour of the total emitted power per frequency, we need to look at the function $F(x)$, shown in Fig. 4.3. The electron should emit more strongly around ω_c, that is for values of x around 1. In particular, half of the emitted power should come from frequencies $\omega < \omega_c$ and half from $\omega > \omega_c$. This means that the area under the function $F(x)$ in Fig. 4.3 should be equally divided to the left and right of $x = 1$.

4.2 Spectrum of a power-law electron distribution

We now want to look at the power per frequency for a power-law distribution of energies,

$$n_e(E)\mathrm{d}E = C' E^{-p}\mathrm{d}E, \tag{4.2.1}$$

for a constant C' and the particle distribution index p. The term $n_e(E)\mathrm{d}E$ represents the number density of electrons with energies in the interval E to $E + \mathrm{d}E$. The minimum energy of an electron is given by its rest mass energy, $E_0 = mc^2$, while the relativistic electron energy is $E = \gamma mc^2$. We can therefore write $\gamma = E/E_0$, and the power-law distribution can be written as

$$n_e(\gamma)\mathrm{d}\gamma = C\gamma^{-p}\mathrm{d}\gamma. \tag{4.2.2}$$

The constant C is different to the constant C' in Eq. (4.2.1). Note also that C must have units of cm^{-3}. Consequently, the power per frequency per unit volume is given by

$$\mathcal{P}(\omega) = C \int P(x)\gamma^{-p}\mathrm{d}\gamma. \tag{4.2.3}$$

Here we have expressed the power per frequency P in terms of $x = \omega/\omega_c$. We will in the following assume a fixed pitch angle α and integrate contributions of electrons for different energies to a fixed x. For a relativistic electron, we find that

$$x = \frac{\omega}{\omega_c} = \frac{\omega}{\frac{3}{2}\gamma^3\omega_B \sin\alpha} = \frac{2\omega}{3\gamma^3 \sin\alpha}\frac{\gamma mc}{eB} = \frac{1}{\gamma^2}\frac{2\omega mc}{3eB\sin\alpha} \equiv \frac{A}{\gamma^2}. \tag{4.2.4}$$

We have used that the critical angular frequency is $\omega_c = \frac{3}{2}\gamma^3\omega_B \sin\alpha$ and that the angular frequency of rotation is $\omega_B = eB/\gamma mc$. Now the integral in Eq. (4.2.3) can be rewritten using the total power per frequency in Eq. (4.1.16). Since $\gamma = (A/x)^{1/2}$,

$$\mathrm{d}\gamma = -\frac{1}{2}A^{1/2}x^{-3/2}\mathrm{d}x, \tag{4.2.5}$$

and the limits of integration have changed to ∞ to 0, we get

$$\begin{aligned}\mathcal{P}(\omega) &= -C\frac{\sqrt{3}e^3B\sin\alpha}{2\pi mc^2}\int_\infty^0 F(x)\left(\frac{A}{x}\right)^{-p/2}\frac{1}{2}A^{1/2}x^{-3/2}\mathrm{d}x \\ &= C\frac{\sqrt{3}e^3B\sin\alpha}{4\pi mc^2}A^{-(p-1)/2}\int_0^\infty x^{(p-3)/2}F(x)\mathrm{d}x.\end{aligned} \tag{4.2.6}$$

The following relations for the integrals over the functions F and G can be derived[1] [9],

$$\int_0^\infty x^\mu F(x)\mathrm{d}x = \frac{2^{\mu+1}}{\mu+2}\Gamma\left(\frac{\mu}{2}+\frac{7}{3}\right)\Gamma\left(\frac{\mu}{2}+\frac{2}{3}\right), \tag{4.2.7a}$$

$$\int_0^\infty x^\mu G(x)\mathrm{d}x = 2^\mu\Gamma\left(\frac{\mu}{2}+\frac{4}{3}\right)\Gamma\left(\frac{\mu}{2}+\frac{2}{3}\right), \tag{4.2.7b}$$

where Γ is the gamma function. For $\mu = (p-3)/2$ this leads to

$$\mathcal{P}(\omega) = C\frac{\sqrt{3}e^3B\sin\alpha}{2\pi mc^2(p+1)}\left(\frac{\omega mc}{3eB\sin\alpha}\right)^{-(p-1)/2}\Gamma\left(\frac{p}{4}+\frac{19}{12}\right)\Gamma\left(\frac{p}{4}-\frac{1}{12}\right), \tag{4.2.8}$$

where we have also inserted for the quantity A defined earlier. Converting from angular frequency to frequency by $\omega = 2\pi\nu$ gives

$$\mathcal{P}(\nu) = C\frac{\sqrt{3}e^3B\sin\alpha}{2\pi mc^2(p+1)}\left(\frac{2\pi mc}{3eB\sin\alpha}\right)^{-(p-1)/2}\Gamma\left(\frac{p}{4}+\frac{19}{12}\right)\Gamma\left(\frac{p}{4}-\frac{1}{12}\right)\nu^{-(p-1)/2}. \tag{4.2.9}$$

The pitch angles α are likely to be isotropic and we therefore use that the probability distribution is $\frac{1}{2}\sin\alpha\mathrm{d}\alpha$. Then integrating over α gives

$$\frac{1}{2}\int_0^\pi(\sin\alpha)^{(p+3)/2}\mathrm{d}\alpha = \frac{\sqrt{\pi}}{2}\frac{\Gamma\left(\frac{p+5}{4}\right)}{\Gamma\left(\frac{p+7}{4}\right)}. \tag{4.2.10}$$

Finally, the power per frequency per unit volume is

$$\mathcal{P}(\nu) = C\frac{\sqrt{3\pi}e^3B}{4\pi mc^2(p+1)}\left(\frac{2\pi mc}{3eB}\right)^{-(p-1)/2}\frac{\Gamma\left(\frac{p}{4}+\frac{19}{12}\right)\Gamma\left(\frac{p}{4}-\frac{1}{12}\right)\Gamma\left(\frac{p+5}{4}\right)}{\Gamma\left(\frac{p+7}{4}\right)}\nu^{-(p-1)/2}. \tag{4.2.11}$$

4.3 Synchrotron self-absorption

The ultra-relativistic particles emitting synchrotron radiation will also be able to absorb photons. This process is called *synchrotron self-absorption*, and in this section we will intend to calculate the total absorption coefficient. It can be shown that this coefficient is given by[2]

$$\alpha_\nu = -\frac{c^2}{8\pi\nu^2}\int \mathrm{d}E P(\nu,E)E^2\frac{\partial}{\partial E}\left[\frac{n_e(E)}{E^2}\right], \tag{4.3.1}$$

[1] These integrals will also be presented in chapter 5, with derivations in appendix A.3.
[2] See Rybicki and Lightman [9] for the derivation of this formula.

for $P(\nu, E) = 2\pi P(\omega)$ where $P(\omega)$ is the total emitted power per frequency in Eq. (4.1.16). For a power-law electron distribution, we have that

$$\frac{\partial}{\partial E}\left[\frac{n_e(E)}{E^2}\right] = \frac{\partial}{\partial E}\left[C' E^{-(p+2)}\right] = -(p+2)C' E^{-(p+1)} = -(p+2)\frac{n_e(E)}{E}. \tag{4.3.2}$$

It follows that the absorption coefficient is given by

$$\alpha_\nu = \frac{(p+2)c^2}{8\pi\nu^2}\int P(\nu, E)\frac{n_e(E)}{E}\mathrm{d}E = \frac{(p+2)c^2}{8\pi\nu^2}\int P(\nu, E)E^{-1}C' E^{-p}\mathrm{d}E. \tag{4.3.3}$$

In terms of the Lorentz factor, we get that

$$\alpha_\nu = \frac{(p+2)c^2}{8\pi\nu^2}\int P(\nu, E)E_0^{-1}C\gamma^{-(p+1)}\mathrm{d}\gamma = C\frac{(p+2)}{8\pi m\nu^2}\int P(\nu, E)\gamma^{-(p+1)}\mathrm{d}\gamma, \tag{4.3.4}$$

where we have used that $E = \gamma mc^2 = \gamma E_0$. As in the previous section, we use Eq. (4.2.5) to change the integration variable from γ to x, and obtain

$$\begin{aligned}
\alpha_\nu &= C\frac{(p+2)}{8\pi m\nu^2}\frac{\sqrt{3}e^3 B\sin\alpha}{mc^2}\int F(x)\gamma^{-(p+1)}\mathrm{d}\gamma \\
&= -C\frac{\sqrt{3}(p+2)e^3 B\sin\alpha}{8\pi m^2c^2\nu^2}\frac{1}{2}A^{1/2}A^{-(p+1)/2}\int_\infty^0 F(x)x^{-3/2}x^{(p+1)/2}\mathrm{d}x \\
&= C\frac{\sqrt{3}(p+2)e^3 B\sin\alpha}{16\pi m^2c^2\nu^2}A^{-p/2}\int_0^\infty x^{(p-2)/2}F(x)\mathrm{d}x \\
&= C\frac{\sqrt{3}(p+2)e^3 B\sin\alpha}{16\pi m^2c^2\nu^2}\left(\frac{3eB\sin\alpha}{4\pi\nu mc}\right)^{p/2}\frac{2^{p/2+1}}{p+2}\Gamma\left(\frac{3p+22}{12}\right)\Gamma\left(\frac{3p+2}{12}\right) \\
&= C\frac{\sqrt{3}e^3}{8\pi m^2c^2}\left(\frac{3e}{2\pi mc}\right)^{p/2}(B\sin\alpha)^{p/2+1}\Gamma\left(\frac{3p+22}{12}\right)\Gamma\left(\frac{3p+2}{12}\right)\nu^{-p/2-2}.
\end{aligned} \tag{4.3.5}$$

As we did for the total emitted power per frequency per unit volume, we assume that the pitch angles α are isotropic with probability distribution $\frac{1}{2}\sin\alpha\mathrm{d}\alpha$. Using that

$$\frac{1}{2}\int_0^\pi(\sin\alpha)^{p/2+2}\mathrm{d}\alpha = \frac{\sqrt{\pi}}{2}\frac{\Gamma\left(\frac{p+6}{4}\right)}{\Gamma\left(\frac{p+8}{4}\right)}, \tag{4.3.6}$$

we obtain

$$\alpha_\nu = C\frac{\sqrt{3\pi}e^3}{16\pi m^2c^2}\left(\frac{3e}{2\pi mc}\right)^{p/2}B^{p/2+1}\frac{\Gamma\left(\frac{3p+22}{12}\right)\Gamma\left(\frac{3p+2}{12}\right)\Gamma\left(\frac{p+6}{4}\right)}{\Gamma\left(\frac{p+8}{4}\right)}\nu^{-p/2-2}. \tag{4.3.7}$$

We have that $\alpha_\nu \propto \nu^{-p/2-2}$ and from Eq. (4.2.11), $\mathcal{P} \propto \nu^{-(p-1)/2}$. We can compare the emitted power per frequency and the absorption coefficient by finding that

$$\frac{\alpha_\nu}{\mathcal{P}} \propto \nu^{-5/2}. \tag{4.3.8}$$

It is clear that the electrons emit far more radiation than they absorb above some critical frequency, which will be an important consideration in chapter 6.

4.4 Restrictions to classical electrodynamics

In this chapter and the previous, we have provided an in-depth description of synchrotron radiation. However, we have not considered the regimes in which our treatment no longer is valid, and therefore restricts our theory. In strong magnetic fields, non-linear quantum effects become important [44]. In these cases, particle interactions and electromagnetic fields enters the radiation-dominated regime, and we are in the field of high-intensity particle physics. An extensive description of these quantum effects is beyond the scope of this thesis, but we proceed to present the relevant restrictions.

Strong electromagnetic fields are characterised through the comparison with a critical field. In quantum electrodynamics (QED), the critical magnetic field is given by [44]

$$B_{\text{cr}} = \frac{m^2 c^3}{e\hbar} \simeq 4.41 \times 10^{13}\,\text{G}. \tag{4.4.1}$$

Here, $\hbar$ is the reduced Planck's constant, and m, c and e is the electron mass, speed of light and electron charge, respectively. One can similarly obtain the critical electric field by $E_{\text{cr}} = cB_{\text{cr}}$, which is often called the Schwinger field. In classical electrodynamics, it is possible to define equivalent critical magnetic and electric fields. These fields are a few orders of magnitude higher, in fact they differ only by a factor of $1/\alpha$, where $\alpha \simeq 1/137$ is the fine-structure constant [44]. As the classical critical fields are higher, they are less relevant, and we consider the QED critical field in the following. In particular, from Sec. 2.1, we know that astrophysical objects such as neutron stars and magnetars can have magnetic fields stronger than B_{cr} in Eq. (4.4.1). The non-linear quantum effects become important in these cases.

We may define the quantum non-linearity parameter for electrons [44],

$$\chi \equiv \frac{|p_\perp|}{mc}\frac{B}{B_{\text{cr}}}. \tag{4.4.2}$$

For relativistic electrons, the momentum is given by $p = \gamma mc$, and so we instead write

$$\chi \simeq \gamma \frac{B}{B_{\text{cr}}}. \tag{4.4.3}$$

We therefore restrict the classical theory to hold in the case of $\chi \ll 1$. In the cases when χ approaches or exceeds 1, we are in the regime of where the non-linear quantum effects should be considered.

We can now rewrite the parameter x defined previously in this chapter, to include the parameter χ. Using that $\omega_B = eB/\gamma mc$, we first get

$$x = \frac{\omega}{\omega_c} = \frac{2\omega}{3\gamma^3 \omega_B \sin\alpha} = \frac{2\omega mc}{3\gamma^2 eB \sin\alpha}. \tag{4.4.4}$$

Inserting $B = \chi B_{\text{cr}}/\gamma$ and B_{cr} from Eq. (4.4.1), and simplifying gives

$$x = \frac{2\hbar\omega}{3\chi\gamma mc^2 \sin\alpha}. \tag{4.4.5}$$

We can correct this expression for quantum effects, which to first order in $\hbar$ corresponds to the substitution $\omega \to \omega(1 + \hbar\omega/\gamma mc^2)$. Defining

$$f_c = \frac{\hbar\omega}{\gamma mc^2}, \tag{4.4.6}$$

as the fraction of the electron energy that is transferred to the photon during the emission process [44], the parameter x becomes

$$x \to x_q = \frac{2\hbar\omega\left(1+\frac{\hbar\omega}{\gamma mc^2}\right)}{3\chi\gamma mc^2\sin\alpha} = \frac{2f_c}{3\chi\sin\alpha}(1+f_c) = \frac{2f_c}{3\chi\sin\alpha(1-f_c)}(1-f_c^2)$$
$$\simeq \frac{2f_c}{3\chi\sin\alpha(1-f_c)} = \frac{x}{1-f_c}. \tag{4.4.7}$$

By substituting x with x_q, we are introducing a quantum correction that will lead to a reduction in the total emitted power. The first order correction used corresponds to a recoil effect for $\chi \gtrsim 1$, while spin effects only appear if one includes the second order term in $\hbar$. As discussed in Sec. 4.1, in the classical description, half the emitted power should correspond to values $x > 1$. For strong magnetic fields where $\chi \gtrsim 1$, we would have that most of the radiation is carried away by photons, in which each photon has an energy greater than the energy of the electron [44]. In this case, the quantum correction becomes very important.

As we have seen, the function $F(x)$ defined by Eq. (4.1.12a) determines the spectrum of synchrotron radiation. This function is plotted in Fig. 4.3 for increasing x. In Fig. 4.4 one can see the quantum-corrected spectrum of synchrotron radiation emitted by an electron in solid lines compared to the classical spectrum in dashed lines. In particular, we have plotted the function $F(\tilde{x}(f_c))$ in terms of f_c, that is $\tilde{x}(f_c) = x_q$ in solid lines and $\tilde{x}(f_c) = x$ in dashed lines. Four different values of χ have been chosen. As can be seen, the quantum-corrected spectrum differs substantially from the classical spectrum as χ and f_c increases.

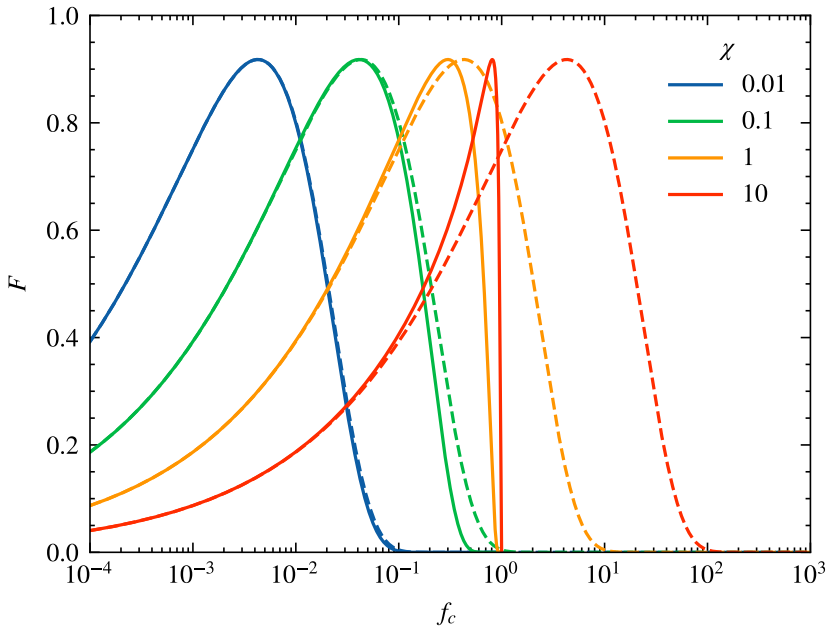

Figure 4.4: The function $F(\tilde{x}(f_c))$ in terms of f_c for $\tilde{x}(f_c) = x_q$ (solid lines) and $\tilde{x}(f_c) = x$ (dashed lines).

Chapter 5

Polarisation

We would now like to study the degree of polarisation for synchrotron radiation, which describes to which extent the radiation emitted is polarised. For this we want to use the emission-polarisation tensor and the Stokes parameters.

The following discussion uses the book by Rybicki and Lightman [9] to some extent, but the articles by Westfold [11] and Legg and Westfold [12] are the main sources.

5.1 Emission-polarisation tensor

We begin by studying the average power radiated over a period $2\pi/\omega_B$. Here we have also set the factor b discussed in chapter 3 equal to 1. Introducing the Poynting vector [9],

$$\mathbf{S} = \frac{c}{4\pi}\mathbf{E}\times\mathbf{B}, \tag{5.1.1}$$

we should have that $\langle\mathbf{S}\rangle\cdot\mathbf{n}\mathrm{d}S$ is the average power through a surface element $\mathrm{d}S$. Following the procedure of Westfold [11], the average of $\mathbf{S}$ can be calculated as

$$\langle\mathbf{S}\rangle = \frac{\omega_B}{2\pi}\int_0^{\frac{2\pi}{\omega_B}}\mathbf{S}\mathrm{d}t = \frac{\omega_B}{2\pi}\frac{c}{4\pi}\mathbf{n}\int_0^{\frac{2\pi}{\omega_B}}E^2\mathrm{d}t = \frac{c}{4\pi}\mathbf{n}\left(E_0^2+2\sum_{n=1}^{\infty}|E_n|^2\right), \tag{5.1.2}$$

where we have used the radiation field in Eq. (3.5.1b). Consider now the average power radiated into the solid angle $\mathrm{d}\Omega(\mathbf{n})$, denoted by $\langle P(\mathbf{n})\rangle\mathrm{d}\Omega(\mathbf{n})$. We have that

$$\langle P(\mathbf{n})\rangle = \frac{1}{2}P_0(\mathbf{n})+\sum_{n=1}^{\infty}\langle P_n(\mathbf{n})\rangle, \tag{5.1.3}$$

where

$$\langle P_n(\mathbf{n})\rangle = \frac{cr^2}{2\pi}|E_n|^2, \tag{5.1.4}$$

for the distance from the origin r. Therefore, for the nth harmonic, the average power radiated into the solid angle $\mathrm{d}\Omega(\mathbf{n})$ is given by $\langle P_n(\mathbf{n})\rangle\mathrm{d}\Omega(\mathbf{n})$.

We can now define the emission-polarisation tensor for a single electron [12][1],

$$\rho = \frac{cr^2}{2\pi}\mathbf{E}_n\mathbf{E}_n^*. \tag{5.1.5}$$

[1] Legg and Westfold [12] use SI units and define the tensor as $\rho = (2r^2/\mu c)\mathbf{E}_n\mathbf{E}_n^*$. In Gaussian-cgs units we have the relation $\mu_0 = 1/\epsilon_0 c^2$, where $\epsilon_0 = 1/4\pi$ is dimensionless. Using $\mu = \mu_0$ we obtain the desired result.

Here n corresponds to the normal vector $\mathbf{n}$, not the nth harmonic. The convenience of working with polarisation tensors will become clear in Sec. 5.3 when we define the Stokes parameters. For now we proceed to obtain expressions for the components of the tensor.

Because the average power in the nth harmonic consists of contributions from $\mathbf{E}_n$ in any two orthogonal directions transverse to $\mathbf{n}$, we take the perpendicular and parallel components of the electric field given by Eq. (3.5.30a) and (3.5.30b), respectively. We can therefore write the emission-polarisation tensor as

$$\rho = \begin{bmatrix} \rho_{11} & \rho_{12} \\ \rho_{21} & \rho_{22} \end{bmatrix} = \frac{cr^2}{2\pi} \begin{bmatrix} E_\perp E_\perp^* & E_\perp E_\parallel^* \\ E_\parallel E_\perp^* & E_\parallel E_\parallel^* \end{bmatrix}. \tag{5.1.6}$$

The entries of the tensor are consequently

$$\rho_{11} = \frac{e^2}{6\pi^3 c}\omega_B^4 n^2 \left(\frac{a^2\theta_\gamma^4}{\gamma^4 c^2}\right) K_{2/3}^2(\eta), \tag{5.1.7a}$$

$$\rho_{12} = -\frac{e^2}{6\pi^3 c}\omega_B^4 \mathrm{i}n^2 \left(\frac{a^2\theta\theta_\gamma^3}{\gamma^3 c^2} + \frac{a^2\theta_\gamma^5}{2\gamma^5 c^2}\cot\alpha\right) K_{2/3}(\eta)K_{1/3}(\eta), \tag{5.1.7b}$$

$$\rho_{21} = \frac{e^2}{6\pi^3 c}\omega_B^4 \mathrm{i}n^2 \left(\frac{a^2\theta\theta_\gamma^3}{\gamma^3 c^2} + \frac{a^2\theta_\gamma^5}{2\gamma^5 c^2}\cot\alpha\right) K_{2/3}(\eta)K_{1/3}(\eta), \tag{5.1.7c}$$

$$\rho_{22} = \frac{e^2}{6\pi^3 c}\omega_B^4 n^2 \left(\frac{a^2\theta^2\theta_\gamma^2}{\gamma^2 c^2} + \frac{a^2\theta\theta_\gamma^4}{\gamma^4 c^2}\cot\alpha + \frac{a^2\theta_\gamma^6}{4\gamma^6 c^2}\cot^2\alpha\right) K_{1/3}^2(\eta). \tag{5.1.7d}$$

We now wish to convert the emission-polarisation tensor of Eq. (5.1.6) into a continuous function of frequency. This is possible for large-order harmonics, as the spectrum becomes quasi-continuous [12]. We consider the average power in a frequency[2] band of width $\mathrm{d}\nu$, that is $\langle P_\nu(\mathbf{n})\rangle \mathrm{d}\nu \mathrm{d}\Omega(\mathbf{n})$ received within the solid angle $\mathrm{d}\Omega(\mathbf{n})$. The frequency is, for $\nu_B = \omega_B/2\pi$,

$$\nu = n\nu_B = \frac{n\omega_B}{2\pi}, \tag{5.1.8}$$

and we can write

$$\langle P_\nu(\mathbf{n})\rangle = \langle P_n(\mathbf{n})\rangle \frac{1}{\nu_B} = \frac{1}{\nu_B}\frac{cr^2}{2\pi}|E_n|^2. \tag{5.1.9}$$

We make the substitution

$$x = \frac{\nu}{\nu_c}, \tag{5.1.10}$$

which gives us a dimensionless variable. Note that this is exactly the same variable as used in the previous chapter, i.e. $x = \omega/\omega_c$. For the radius of curvature $a = c/(\omega_B \sin\alpha)$ by the assumption that $v \simeq c$, the critical frequency is

$$\nu_c = \frac{\omega_c}{2\pi} = \frac{\frac{3}{2}\gamma^3\omega_B \sin\alpha}{2\pi} = \frac{3c\gamma^3}{4\pi a}. \tag{5.1.11}$$

Substituting Eq. (5.1.8) and (5.1.11) into the expression for x and solving for n, we get

$$x = \frac{4\pi a}{3c\gamma^3}\nu = \frac{4\pi a}{3c\gamma^3}\frac{n\omega_B}{2\pi} = \frac{2a\omega_B n}{3c\gamma^3}, \tag{5.1.12}$$

$$n = \frac{3c\gamma^3}{2a\omega_B}x. \tag{5.1.13}$$

[2]The frequency is denoted f by the articles [11, 12], but for consistency in notation we denote the frequency by ν.

Finally, the frequency polarisation tensor in terms of x is written as

$$\rho_x = \frac{1}{\nu_B}\rho = \frac{2\pi}{\omega_B}\rho = \begin{bmatrix} \rho_{x_{11}} & \rho_{x_{12}} \\ \rho_{x_{21}} & \rho_{x_{22}} \end{bmatrix}. \tag{5.1.14}$$

Using the expression for n, writing η as

$$\eta = \frac{n\omega_B a\theta_\gamma^3}{3c\gamma^3} = \frac{3c\gamma^3}{2a\omega_B}x\frac{\omega_B a\theta_\gamma^3}{3c\gamma^3} = \frac{1}{2}\theta_\gamma^3 x, \tag{5.1.15}$$

allows us to calculate the components of Eq. (5.1.14). For $\rho_{x_{11}}$ we get

$$\begin{aligned}\rho_{x_{11}} &= \frac{2\pi}{\omega_B}\rho_{11} = \frac{2\pi}{\omega_B}\frac{e^2}{6\pi^3 c}\omega_B^4 n^2\left(\frac{a^2\theta_\gamma^4}{\gamma^4 c^2}\right)K_{2/3}^2(\eta) \\ &= \frac{e^2}{3\pi^2 c}\omega_B^3\left(\frac{3c\gamma^3}{2a\omega_B}x\right)^2\left(\frac{a^2\theta_\gamma^4}{\gamma^4 c^2}\right)K_{2/3}^2\left(\frac{1}{2}\theta_\gamma^3 x\right) \\ &= \frac{3e^2}{4\pi^2 c}\omega_B x^2\gamma^2\theta_\gamma^4 K_{2/3}^2\left(\frac{1}{2}\theta_\gamma^3 x\right),\end{aligned} \tag{5.1.16}$$

and similarly we obtain the other three components. The result is

$$\rho_{x_{11}} = \frac{3e^2}{4\pi^2 c}\omega_B x^2\gamma^2\theta_\gamma^4 K_{2/3}^2\left(\frac{1}{2}\theta_\gamma^3 x\right), \tag{5.1.17a}$$

$$\rho_{x_{12}} = -\frac{3e^2}{4\pi^2 c}\omega_B \mathrm{i}x^2\gamma^3\left(\theta\theta_\gamma^3 + \frac{\theta_\gamma^5}{2\gamma^2}\cot\alpha\right)K_{2/3}\left(\frac{1}{2}\theta_\gamma^3 x\right)K_{1/3}\left(\frac{1}{2}\theta_\gamma^3 x\right), \tag{5.1.17b}$$

$$\rho_{x_{21}} = \frac{3e^2}{4\pi^2 c}\omega_B \mathrm{i}x^2\gamma^3\left(\theta\theta_\gamma^3 + \frac{\theta_\gamma^5}{2\gamma^2}\cot\alpha\right)K_{2/3}\left(\frac{1}{2}\theta_\gamma^3 x\right)K_{1/3}\left(\frac{1}{2}\theta_\gamma^3 x\right), \tag{5.1.17c}$$

$$\rho_{x_{22}} = \frac{3e^2}{4\pi^2 c}\omega_B x^2\gamma^4\left(\theta^2\theta_\gamma^2 + \frac{\theta\theta_\gamma^4}{\gamma^2}\cot\alpha + \frac{\theta_\gamma^6}{4\gamma^4}\cot^2\alpha\right)K_{1/3}^2\left(\frac{1}{2}\theta_\gamma^3 x\right). \tag{5.1.17d}$$

The components of the frequency polarisation tensor in Eq. (5.1.17) are all proportional to ω_B, and thus inverse proportional to b, if this factor was included.

Since the obtained frequency polarisation tensor only describes one electron, it is necessary to expand the model to describe a distribution of electrons. To stay consistent with the approximation made by [12], including terms to $\mathcal{O}(\gamma^{-2})$ within the brackets, we will neglect the last term of $\rho_{x_{22}}$ in this calculation.

5.2 Polarisation tensor for a power-law electron distribution

We will assume a power-law distribution of electrons. For a constant C and the particle distribution index p, the number density of electrons $n_e(\gamma)$ of a given Lorentz factor γ, satisfies Eq. (4.2.2), that is

$$n_e(\gamma)\mathrm{d}\gamma = C\gamma^{-p}\mathrm{d}\gamma. \tag{5.2.1}$$

We define the emission-polarisation tensor in the frequency domain for a population of electrons satisfying this power-law as

$$j = \frac{1}{2\pi}\int n_e(\gamma)\int \phi(\alpha)\rho_x \mathrm{d}\Omega\mathrm{d}\gamma. \tag{5.2.2}$$

The reason for the division of 2π, which differs from the definition used in [12], will become clear in Sec. 5.3. The particle pitch angle distribution is denoted $\phi(\alpha)$ and the solid angle is $\mathrm{d}\Omega(\mathbf{n}) = 2\pi \sin\alpha \mathrm{d}\alpha$. In Sec. 5.1, we denoted $\langle P_\nu(\mathbf{n})\rangle \mathrm{d}\nu\mathrm{d}\Omega(\mathbf{n})$ as the average power *received* within the solid angle $\mathrm{d}\Omega(\mathbf{n})$. However, the factor b must be included if we consider the average power *emitted* into the solid angle $\mathrm{d}\Omega(\mathbf{n})$, which gives $b\langle P_\nu(\mathbf{n})\rangle \mathrm{d}\nu\mathrm{d}\Omega(\mathbf{n})$. Hence, the factor b should appear in Eq. (5.2.2), however we have set $b = 1$. It is clear that the product of the frequency polarisation tensor obtained in Eq. (5.1.17) with the factor b in the definition of j will give us an expression independent of b.

To simplify the first integral in Eq. (5.2.2), we define a new angle ψ such that $\alpha = \psi + \theta$, which we call the pitch angle deviation[3]. The solid angle then becomes $\mathrm{d}\Omega(\mathbf{n}) = 2\pi \sin\alpha \mathrm{d}\theta$. We still have that α and θ is the pitch angle and the angle between $-\mathbf{x}$ and $\mathbf{v}$, respectively. We want to expand $\phi(\alpha)\sin\alpha$ to the first order around ψ, and define functions f and g such that

$$f(\alpha) \equiv \phi(\alpha)\sin\alpha, \tag{5.2.3a}$$
$$g(\alpha) \equiv f'(\alpha) = \phi'(\alpha)\sin\alpha + \phi(\alpha)\cos\alpha. \tag{5.2.3b}$$

Then to first order[4],

$$\phi(\alpha)\sin\alpha = f(\alpha) = f(\psi) + f'(\psi)(\alpha - \psi) = f(\psi) + g(\psi)\theta. \tag{5.2.4}$$

Now Eq. (5.2.2) becomes

$$j = \int_0^\infty n_e(\gamma) \int_{-\infty}^\infty [f(\psi) + g(\psi)\theta]\, \rho_x \mathrm{d}\theta \mathrm{d}\gamma = \int_0^\infty I_x n_e(\gamma) \mathrm{d}\gamma, \tag{5.2.5}$$

where we have taken the range of θ between $-\infty$ and ∞, and defined the integral

$$I_x \equiv \int_{-\infty}^\infty [f(\psi) + g(\psi)\theta]\, \rho_x \mathrm{d}\theta. \tag{5.2.6}$$

We note already now that the interval $-\infty$ to ∞ is symmetric, and therefore the odd terms in θ will cancel upon integration. We will have a sum of integrals of the form

$$I_{abcd} \propto \int_{-\infty}^\infty \theta^a \theta_\gamma^b K_{1/3}^c \left(\frac{1}{2}\theta_\gamma^3 x\right) K_{2/3}^d \left(\frac{1}{2}\theta_\gamma^3 x\right) \mathrm{d}\theta, \tag{5.2.7}$$

for some integers a, b, c, d. Since $\theta_\gamma^2 = 1 + \gamma^2\theta^2$ depends on the angle θ only through θ^2, we have that θ_γ is always greater than zero. As the Bessel functions are always positive, the integer a being odd is sufficient to conclude that $I_{abcd} = 0$.

The emission-polarisation tensor obtained with entries in Eq. (5.1.17) is written in terms of the parameter x. Since Eq. (5.2.5) includes the term $n_e(\gamma)\mathrm{d}\gamma$, it is convenient to also express γ in terms of x and change the differential from $\mathrm{d}\gamma$ to $\mathrm{d}x$. The frequency of a non-relativistic electron is given by $\nu_{B_0} = eB/2\pi mc$, only a factor γ different from the frequency in the relativistic case. Hence, we can write $\nu_{B_0} = \gamma\nu_B$, where $\nu_B = \omega_B/2\pi$. The angular frequency of rotation can therefore be written in terms of the constant non-relativistic frequency and the Lorentz factor, that is $\omega_B = 2\pi\nu_{B_0}/\gamma$. The critical angular frequency at the angle ψ becomes

$$\nu_c = \frac{\frac{3}{2}\gamma^3\omega_B \sin\psi}{2\pi} = \frac{3}{2}\gamma^2\nu_{B_0}\sin\psi. \tag{5.2.8}$$

[3]This angle is denoted $\theta = \alpha - \psi$ by [11, 12], where α is the pitch angle and ψ the angle between $-\mathbf{x}$ and $\mathbf{v}$.

[4]Note that Legg and Westfold [12] writes the first order approximation (which they call second order) as $\phi(\alpha)\sin\alpha = \phi(\psi)\sin\psi[1 + g(\psi)\theta\cot\psi]$, where they have defined $g(\psi) = 1 + [\phi'(\psi)/\phi(\psi)]\tan\psi$. This is exactly the same as writing $\phi(\alpha)\sin\alpha = f(\psi) + g(\psi)\theta$, corresponding to our expression for the first order approximation.

We now have everything necessary to express γ in terms of x. We get that

$$x = \frac{\nu}{\nu_c} = \frac{2}{3}\frac{\nu}{\nu_{B_0}\sin\psi}\frac{1}{\gamma^2}, \tag{5.2.9}$$

and solving for γ gives

$$\gamma = \left(\frac{2}{3}\right)^{1/2}\frac{\nu^{1/2}}{(\nu_{B_0}\sin\psi)^{1/2}}x^{-1/2}, \tag{5.2.10}$$

$$\mathrm{d}\gamma = -\frac{1}{2}\left(\frac{2}{3}\right)^{1/2}\frac{\nu^{1/2}}{(\nu_{B_0}\sin\psi)^{1/2}}x^{-3/2}\mathrm{d}x. \tag{5.2.11}$$

The power-law distribution of energies can now be expressed as function of x, inserting the expression for γ into the power-law,

$$n_e(\gamma) = C\gamma^{-p} = C\left(\frac{3}{2}\right)^{p/2}\frac{(\nu_{B_0}\sin\psi)^{p/2}}{\nu^{p/2}}x^{p/2}. \tag{5.2.12}$$

Upon changing the variable of integration, the limits change from 0 to ∞ to ∞ to 0. Hence we omit the minus sign from the expression of $\mathrm{d}\gamma$ in Eq. (5.2.11), setting the limits again to 0 to ∞, and finally have that

$$n_e(\gamma)\mathrm{d}\gamma = C\frac{1}{\sqrt{6}}\left(\frac{3}{2}\right)^{p/2}\frac{(\nu_{B_0}\sin\psi)^{(p-1)/2}}{\nu^{(p-1)/2}}x^{(p-3)/2}\mathrm{d}x. \tag{5.2.13}$$

Solving for the components of j in Eq. (5.2.5) are lengthy calculations, so we need a careful approach. The calculations contain several integrals which are given in appendix A, where we also include derivations. In the following, it is useful to introduce the functions from appendix A.3,

$$\mathcal{J}_n = \int_0^\infty x^{n-2}F(x)\mathrm{d}x = \int_0^\infty x^{n-1}\int_x^\infty K_{5/3}(\xi)\mathrm{d}\xi\mathrm{d}x = \frac{\frac{2}{3}+n}{n}\mathcal{L}_n, \tag{5.2.14a}$$

$$\mathcal{L}_n = \int_0^\infty x^{n-2}G(x)\mathrm{d}x = \int_0^\infty x^{n-1}K_{2/3}(x)\mathrm{d}x = 2^{n-2}\Gamma\left(\frac{n}{2}-\frac{1}{3}\right)\Gamma\left(\frac{n}{2}+\frac{1}{3}\right), \tag{5.2.14b}$$

$$\mathcal{R}_n = \int_0^\infty x^{n-2}H(x)\mathrm{d}x = \int_0^\infty x^{n-1}K_{1/3}(x)\mathrm{d}x = 2^{n-2}\Gamma\left(\frac{n}{2}-\frac{1}{6}\right)\Gamma\left(\frac{n}{2}+\frac{1}{6}\right). \tag{5.2.14c}$$

The first two functions, $\mathcal{J}_n$ and $\mathcal{L}_n$, are valid for $n > \frac{2}{3}$, while $\mathcal{R}_n$ is valid for $n > \frac{1}{3}$. The functions $F(x)$ and $G(x)$ are defined in Eq. (4.1.12a) and (4.1.12b), respectively, and we have also defined

$$H(x) \equiv xK_{1/3}(x). \tag{5.2.15}$$

This function is shown in Fig. 5.1 along with $F(x)$ and $G(x)$, as a normal plot and a log-log plot. The contribution from $H(x)$ upon integration is smaller than that of $F(x)$ and $G(x)$.

Calculation of j_{11}

We consider now the first component j_{11}. Inserting Eq. (5.1.17a) into Eq. (5.2.6) gives

$$I_{x_{11}} = \frac{3e^2}{4\pi^2 c}\omega_B x^2\gamma^2\int_{-\infty}^{\infty}\left[f(\psi)+g(\psi)\theta\right]\theta_\gamma^4 K_{2/3}^2\left(\frac{1}{2}\theta_\gamma^3 x\right)\mathrm{d}\theta. \tag{5.2.16}$$

As discussed earlier, since the integral is taken between $-\infty$ and ∞, the odd terms in θ will cancel. In the case of $I_{x_{11}}$, this means the term proportional to $g(\psi)$. Hence,

$$I_{x_{11}} = \frac{3e^2}{4\pi^2 c}\omega_B x^2\gamma^2 f(\psi)\int_{-\infty}^{\infty}\theta_\gamma^4 K_{2/3}^2\left(\frac{1}{2}\theta_\gamma^3 x\right)\mathrm{d}\theta$$

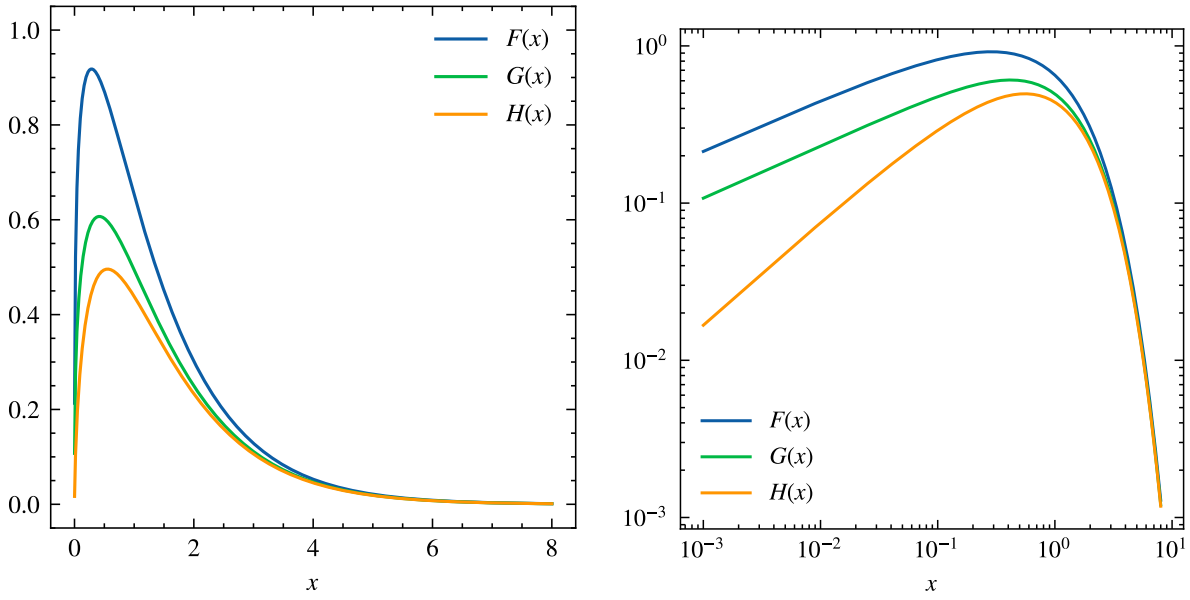

Figure 5.1: The functions $F(x)$, $G(x)$ and $H(x)$ in terms of $x = \omega/\omega_c$ as (a) a normal plot and (b) a log-log plot.

$$
\begin{aligned}
&= \frac{3e^2}{4\pi^2 c}\frac{eB}{\gamma mc}x^2\gamma^2 f(\psi)\frac{\pi}{\sqrt{3}\gamma x^2}\left[F(x)+G(x)\right] \\
&= \frac{\sqrt{3}e^3 B}{4\pi mc^2} f(\psi)\left[F(x)+G(x)\right], \qquad (5.2.17)
\end{aligned}
$$

where we have used Eq. (A.2.6) and that $\omega_B = eB/\gamma mc$. Inserting into Eq. (5.2.5) gives

$$
\begin{aligned}
j_{11} &= \int_0^\infty I_{x_{11}} n_e(\gamma)\mathrm{d}\gamma \\
&= \int_0^\infty \frac{\sqrt{3}e^3 B}{4\pi mc^2} f(\psi)\left[F(x)+G(x)\right] C\frac{1}{\sqrt{6}}\left(\frac{3}{2}\right)^{p/2}\frac{(\nu_{B_0}\sin\psi)^{(p-1)/2}}{\nu^{(p-1)/2}}x^{(p-3)/2}\mathrm{d}x \\
&= C\frac{e^3 B}{4\sqrt{2}\pi mc^2}\left(\frac{3}{2}\right)^{p/2}(\sin\psi)^{(p+1)/2}\left(\frac{\nu_{B_0}}{\nu}\right)^{(p-1)/2}\phi(\psi)\int_0^\infty x^{(p-3)/2}\left[F(x)+G(x)\right]\mathrm{d}x \\
&= C\frac{e^3 B}{4\sqrt{2}\pi mc^2}\left(\frac{3}{2}\right)^{p/2}(\sin\psi)^{(p+1)/2}\left(\frac{\nu_{B_0}}{\nu}\right)^{(p-1)/2}\phi(\psi)\left[\mathcal{J}_{(p+1)/2}+\mathcal{L}_{(p+1)/2}\right], \qquad (5.2.18)
\end{aligned}
$$

using that $f(\psi) = \phi(\psi)\sin\psi$, and the functions $\mathcal{L}_n$ and $\mathcal{J}_n$ defined in Eq. (5.2.14a) and (5.2.14b), respectively.

Calculation of j_{22}

For the other diagonal component j_{22} of the emission-polarisation tensor, we need

$$
I_{x_{22}} = \frac{3e^2}{4\pi^2 c}\omega_B x^2\gamma^4\int_{-\infty}^{\infty}\left[f(\psi)+g(\psi)\theta\right]\left(\theta^2\theta_\gamma^2+\frac{\theta\theta_\gamma^4}{\gamma^2}\cot\psi\right)K_{1/3}^2\left(\frac{1}{2}\theta_\gamma^3 x\right)\mathrm{d}\theta. \qquad (5.2.19)
$$

As before, we may remove the terms odd in θ, and using Eq. (A.2.3) and (A.2.18) in appendix A.2 we get that

$$
I_{x_{22}} = \frac{3e^2}{4\pi^2 c}\omega_B x^2\gamma^4\int_{-\infty}^{\infty}\left(f(\psi)\theta^2\theta_\gamma^2+g(\psi)\frac{\theta^2\theta_\gamma^4}{\gamma^2}\cot\psi\right)K_{1/3}^2\left(\frac{1}{2}\theta_\gamma^3 x\right)\mathrm{d}\theta
$$

$$= \frac{3e^2}{4\pi^2 c}\frac{eB}{\gamma mc}x^2\gamma^4\frac{\pi}{\sqrt{3}\gamma^3x^2}\left[f(\psi)\left\{F(x)-G(x)\right\}+g(\psi)\frac{\cot\psi}{4\gamma^2}\left\{\frac{2}{x}H(x)-G(x)+F(x)\right\}\right]$$
$$= \frac{\sqrt{3}e^3B}{4\pi mc^2}f(\psi)\left[F(x)-G(x)\right]. \tag{5.2.20}$$

In the last line we have removed the higher order term in $1/\gamma$, that is the term proportional to $g(\psi)$. We get the exact same expression as for $I_{x_{11}}$ in Eq. (5.2.17) except for a negative sign in front of $G(x)$. The calculation of j_{22} proceeds by replacing $\mathcal{L}_{(p+1)/2}$ with $-\mathcal{L}_{(p+1)/2}$ in Eq. (5.2.18), and we obtain the result

$$j_{22} = C\frac{e^3B}{4\sqrt{2}\pi mc^2}\left(\frac{3}{2}\right)^{p/2}(\sin\psi)^{(p+1)/2}\left(\frac{\nu_{B_0}}{\nu}\right)^{(p-1)/2}\phi(\psi)\left[\mathcal{J}_{(p+1)/2}-\mathcal{L}_{(p+1)/2}\right]. \tag{5.2.21}$$

Calculation of j_{12} and j_{21}

The components $\rho_{x_{12}}$ and $\rho_{x_{21}}$ in Eq. (5.1.17b) and (5.1.17c), respectively, are equal except for the sign. We will therefore consider the positive $\rho_{x_{21}}$ component and know that $j_{12} = -j_{21}$. We have that

$$I_{x_{21}} = \mathrm{i}\frac{3e^2}{4\pi^2 c}\omega_B x^2\gamma^3\int_{-\infty}^{\infty}\left[f(\psi)+g(\psi)\theta\right]\left(\theta\theta_\gamma^3+\frac{\theta_\gamma^5}{2\gamma^2}\cot\psi\right)K_{2/3}\left(\frac{1}{2}\theta_\gamma^3x\right)K_{1/3}\left(\frac{1}{2}\theta_\gamma^3x\right)\mathrm{d}\theta$$
$$= \mathrm{i}\frac{3e^2}{4\pi^2 c}\omega_B x^2\gamma^3\int_{-\infty}^{\infty}\left(g(\psi)\theta^2\theta_\gamma^3+f(\psi)\frac{\theta_\gamma^5}{2\gamma^2}\cot\psi\right)K_{2/3}\left(\frac{1}{2}\theta_\gamma^3x\right)K_{1/3}\left(\frac{1}{2}\theta_\gamma^3x\right)\mathrm{d}\theta. \tag{5.2.22}$$

Noting that $g(\psi) = [\phi'(\psi)\tan\psi+\phi(\psi)]\cos\psi$ and $f(\psi)\cot\psi = \phi(\psi)\cos\psi$ we can write

$$g(\psi)\theta^2\theta_\gamma^3+f(\psi)\frac{\theta_\gamma^5}{2\gamma^2}\cot\psi = \cos\psi\left([\phi'(\psi)\tan\psi+\phi(\psi)]\theta^2\theta_\gamma^3+\phi(\psi)\frac{\theta_\gamma^5}{2\gamma^2}\right). \tag{5.2.23}$$

The integral becomes

$$I_{x_{21}} = \mathrm{i}\frac{3e^2}{4\pi^2 c}\omega_B x^2\gamma^3\cos\psi\left\{[\phi'(\psi)\tan\psi+\phi(\psi)]T_4+\phi(\psi)\frac{1}{2\gamma^2}T_5\right\}$$
$$= \mathrm{i}\frac{e^3B\cos\psi}{4\sqrt{3}\pi mc^2}\frac{1}{\gamma x}\left\{[\phi'(\psi)\tan\psi+\phi(\psi)]\left[4G(x)-2F(x)\right]+\phi(\psi)\left[3xH(x)+2G(x)-F(x)\right]\right\}, \tag{5.2.24}$$

where we have used the integrals T_4 and T_5 in Eq. (A.2.11) and (A.2.14), respectively. Using that

$$\frac{1}{\gamma x} = \sqrt{\frac{3}{2}}\frac{(\nu_{B_0}\sin\psi)^{1/2}}{\nu^{1/2}}x^{-1/2}, \tag{5.2.25}$$

and integrating over γ gives

$$j_{21} = \mathrm{i}C\frac{e^3B}{8\sqrt{3}\pi mc^2}\left(\frac{3}{2}\right)^{p/2}\cot\psi(\sin\psi)^{p/2+1}\left(\frac{\nu_{B_0}}{\nu}\right)^{p/2}$$
$$\times\left\{[\phi'(\psi)\tan\psi+\phi(\psi)]\left[4\mathcal{L}_{p/2}-2\mathcal{J}_{p/2}\right]+\phi(\psi)\left[3\mathcal{R}_{p/2+1}+2\mathcal{L}_{p/2}-\mathcal{J}_{p/2}\right]\right\}. \tag{5.2.26}$$

Isotropic velocity distribution

Summarising this section, we have obtained the emission-polarisation tensor by calculations, and its components are given by Eq. (5.2.18), (5.2.26) and (5.2.21). Considering now an isotropic velocity distribution, we have that $\phi'(\psi) = 0$ [12]. The components of j are then given by

$$j_{11} = C\frac{e^3B}{4\sqrt{2}\pi mc^2}\left(\frac{3}{2}\right)^{p/2}(\sin\psi)^{(p+1)/2}\left(\frac{\nu_{B_0}}{\nu}\right)^{(p-1)/2}\phi(\psi)\left[\mathcal{J}_{(p+1)/2}+\mathcal{L}_{(p+1)/2}\right], \tag{5.2.27a}$$

$$j_{12} = -\mathrm{i}C\frac{\sqrt{3}e^3B}{8\pi mc^2}\left(\frac{3}{2}\right)^{p/2}\cot\psi(\sin\psi)^{p/2+1}\left(\frac{\nu_{B_0}}{\nu}\right)^{p/2}\phi(\psi)\left[\mathcal{R}_{p/2+1}+2\mathcal{L}_{p/2}-\mathcal{J}_{p/2}\right], \quad (5.2.27b)$$

$$j_{21} = \mathrm{i}C\frac{\sqrt{3}e^3B}{8\pi mc^2}\left(\frac{3}{2}\right)^{p/2}\cot\psi(\sin\psi)^{p/2+1}\left(\frac{\nu_{B_0}}{\nu}\right)^{p/2}\phi(\psi)\left[\mathcal{R}_{p/2+1}+2\mathcal{L}_{p/2}-\mathcal{J}_{p/2}\right], \quad (5.2.27c)$$

$$j_{22} = C\frac{e^3B}{4\sqrt{2}\pi mc^2}\left(\frac{3}{2}\right)^{p/2}(\sin\psi)^{(p+1)/2}\left(\frac{\nu_{B_0}}{\nu}\right)^{(p-1)/2}\phi(\psi)\left[\mathcal{J}_{(p+1)/2}-\mathcal{L}_{(p+1)/2}\right]. \quad (5.2.27d)$$

5.3 Stokes parameters

Now that we have all the components of the emission-polarisation tensor for both the single electron and the power-law electron distribution, we want to calculate the degree of circular and linear polarisation. As we have seen, a general polarisation tensor can be constructed from the radiation field components such that

$$\mathcal{N} = \langle E_i E_j^* \rangle, \quad (5.3.1)$$

for $i, j = 1, 2$. That is

$$\mathcal{N} = \begin{bmatrix} \mathcal{N}_{11} & \mathcal{N}_{12} \\ \mathcal{N}_{21} & \mathcal{N}_{22} \end{bmatrix} = \begin{bmatrix} E_1E_1^* & E_1E_2^* \\ E_2E_1^* & E_2E_2^* \end{bmatrix}. \quad (5.3.2)$$

It is then convenient to define the Stokes parameters in terms of the general polarisation tensor $\mathcal{N}$,

$$I = \mathcal{N}_{11}+\mathcal{N}_{22}, \quad Q = \mathcal{N}_{11}-\mathcal{N}_{22}, \quad U = \mathcal{N}_{12}+\mathcal{N}_{21}, \quad V = \mathrm{i}(\mathcal{N}_{12}-\mathcal{N}_{21}). \quad (5.3.3)$$

This means that we can write

$$\mathcal{N}_{11} = \frac{1}{2}(I+Q), \quad \mathcal{N}_{12} = \frac{1}{2}(U-\mathrm{i}V), \quad \mathcal{N}_{21} = \frac{1}{2}(U+\mathrm{i}V), \quad \mathcal{N}_{22} = \frac{1}{2}(I-Q). \quad (5.3.4)$$

However, any linear combination of Stokes parameters can also be treated as Stokes parameters [45]. The parameter I is proportional to the intensity (or total energy flux) of the wave [9]. This means we can write $\mathcal{N}_{ij} = I_{ij}/I_{\mathrm{tot}}$, where I_{tot} denotes the total intensity. The parameter V is the circularity parameter such that $V = 0$ would imply linear polarisation. In the case of $Q = U = 0$ we would have circular polarisation. Lastly, the case of $Q = U = V = 0$ implies no polarisation at all.

We now conveniently define the Stokes vector as

$$\begin{bmatrix} I \\ Q \\ U \\ V \end{bmatrix} = \begin{bmatrix} E_1E_1^*+E_2E_2^* \\ E_1E_1^*-E_2E_2^* \\ E_1E_2^*+E_2E_1^* \\ \mathrm{i}(E_1E_2^*-E_2E_1^*) \end{bmatrix}. \quad (5.3.5)$$

It is possible to write the Stokes parameters as an incoherent superposition of two waves, in which the first wave is unpolarised and the second completely polarised,

$$\begin{bmatrix} I \\ Q \\ U \\ V \end{bmatrix} = \begin{bmatrix} I_{\mathrm{u}} \\ 0 \\ 0 \\ 0 \end{bmatrix} + \begin{bmatrix} I_{\mathrm{p}} \\ Q \\ U \\ V \end{bmatrix}. \quad (5.3.6)$$

Here, $I_\mathrm{p} = \sqrt{Q^2 + U^2 + V^2}$, and the degree of elliptical polarisation is then defined as [45]

$$\Pi = \frac{I_\mathrm{p}}{I} = \frac{\sqrt{Q^2 + U^2 + V^2}}{I}. \tag{5.3.7}$$

In the case of a monochromatic wave, $I_\mathrm{u} = 0$ and we have pure elliptical polarisation. In this case,

$$I^2 = Q^2 + U^2 + V^2. \tag{5.3.8}$$

In the case of quasi-monochromatic waves, $I_\mathrm{p} \leq I$ and we instead have that

$$I^2 \geq Q^2 + U^2 + V^2. \tag{5.3.9}$$

Since we are interested not only in the elliptical polarisation, or total polarisation, but also the circular and linear polarisation, we further split the wave into a superposition of three waves,

$$\begin{bmatrix} I \\ Q \\ U \\ V \end{bmatrix} = \begin{bmatrix} I_\mathrm{u} \\ 0 \\ 0 \\ 0 \end{bmatrix} + \begin{bmatrix} I_\mathrm{circ} \\ 0 \\ 0 \\ V \end{bmatrix} + \begin{bmatrix} I_\mathrm{lin} \\ Q \\ U \\ 0 \end{bmatrix}. \tag{5.3.10}$$

The first term still corresponds to a completely unpolarised wave, while the second term corresponds to a circularly polarised wave and the the third term corresponds to a linearly polarised wave. Furthermore, we have that $I_\mathrm{circ} = \sqrt{V^2}$ and $I_\mathrm{lin} = \sqrt{Q^2 + U^2}$. This leads to the definition of the degree of circular and linear polarisation,

$$\Pi_\mathrm{circ} = \frac{I_\mathrm{circ}}{I} = \frac{\sqrt{V^2}}{I}, \tag{5.3.11}$$

$$\Pi_\mathrm{lin} = \frac{I_\mathrm{lin}}{I} = \frac{\sqrt{Q^2 + U^2}}{I}, \tag{5.3.12}$$

respectively. The possible polarisation states for $I = \pm Q, \pm U, \pm V$ are shown in Fig. 5.2. The representation shows the polarisation in the plane perpendicular to the direction of propagation, defined by any two perpendicular basis vectors of the electric field. Note that the parameter I is always positive, while the parameters Q, U and V can be negative.

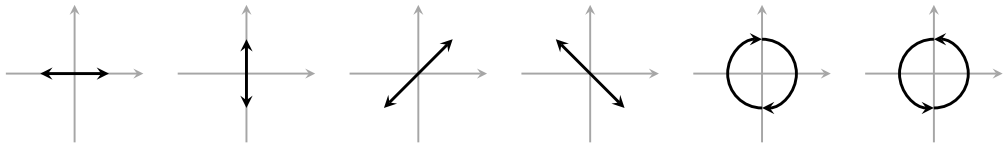

Figure 5.2: Representation of possible pure polarisation states and their relation to the Stokes parameters.

We would now like to calculate the Stokes parameters for the two cases considered, that is for a single electron using the polarisation tensor ρ_x and for a power-law electron distribution using the polarisation tensor j. We note already now that the off-diagonal components of our emission-polarisation tensors are imaginary and equal except for the sign. This means that the parameter $U = 0$ in both cases, and the degree of circular and linear polarisation is

$$\Pi_\mathrm{circ} = \frac{\sqrt{V^2}}{I} \quad \text{and} \quad \Pi_\mathrm{lin} = \frac{\sqrt{Q^2}}{I}, \tag{5.3.13}$$

respectively. We also recall that the I parameter should be proportional to the total intensity, which would be the sum of the perpendicular and parallel component of the intensity obtained in Eq. (4.1.8a) and (4.1.8b).

Single electron

Using the emission-polarisation tensor ρ_x with components given in Eq. (5.1.17), we obtain the Stokes parameters

$$\rho_{x,I} = \frac{3e^2}{4\pi^2 c}\omega_B x^2 \gamma^2 \theta_\gamma^2 \left[\theta_\gamma^2 K_{2/3}^2\left(\frac{1}{2}\theta_\gamma^3 x\right) + \gamma^2\left(\theta^2 + \frac{\theta\theta_\gamma^2}{\gamma^2}\cot\alpha + \frac{\theta_\gamma^4}{4\gamma^4}\cot^2\alpha\right) K_{1/3}^2\left(\frac{1}{2}\theta_\gamma^3 x\right)\right], \tag{5.3.14a}$$

$$\rho_{x,Q} = \frac{3e^2}{4\pi^2 c}\omega_B x^2 \gamma^2 \theta_\gamma^2 \left[\theta_\gamma^2 K_{2/3}^2\left(\frac{1}{2}\theta_\gamma^3 x\right) - \gamma^2\left(\theta^2 + \frac{\theta\theta_\gamma^2}{\gamma^2}\cot\alpha + \frac{\theta_\gamma^4}{4\gamma^4}\cot^2\alpha\right) K_{1/3}^2\left(\frac{1}{2}\theta_\gamma^3 x\right)\right], \tag{5.3.14b}$$

$$\rho_{x,U} = 0, \tag{5.3.14c}$$

$$\rho_{x,V} = \frac{3e^2}{2\pi^2 c}\omega_B x^2 \gamma^3 \left(\theta\theta_\gamma^3 + \frac{\theta_\gamma^5}{2\gamma^2}\cot\alpha\right) K_{2/3}\left(\frac{1}{2}\theta_\gamma^3 x\right) K_{1/3}\left(\frac{1}{2}\theta_\gamma^3 x\right). \tag{5.3.14d}$$

Considering only the first order approximation in γ^{-1}, all the terms in Eq. (5.3.14) proportional to $\cot\alpha$ are zero. In this case, as we have remarked previously in the analysis of the intensity spectrum in Sec. 4.1, the condition $\theta = 0$ implies linear polarisation, since the V parameter becomes zero. For any value $\theta > 0$, we also have that $V > 0$, which implies some degree of circular polarisation. It is also clear from Eq. (5.3.14a) that the I parameter in this approximation is proportional to the total intensity when comparing with the results of Sec. 4.1.

Recall that for the single electron case, the factor b should still appear in the emission-polarisation tensor ρ_x, as opposed to the power-law electron distribution case where the factor dropped out. However, in any case, the polarisation degrees defined by Eq. (5.3.13) are quotients of the Stokes parameters, and the factor b drops out.

Power-law electron distribution

For the power-law electron distribution, we find that the Stokes parameters for an isotropic velocity distribution are given by

$$j_I = C\frac{e^3 B}{2\sqrt{2}\pi mc^2}\left(\frac{3}{2}\right)^{p/2}(\sin\psi)^{(p+1)/2}\left(\frac{\nu_{B_0}}{\nu}\right)^{(p-1)/2}\phi(\psi)\mathcal{J}_{(p+1)/2}, \tag{5.3.15a}$$

$$j_Q = C\frac{e^3 B}{2\sqrt{2}\pi mc^2}\left(\frac{3}{2}\right)^{p/2}(\sin\psi)^{(p+1)/2}\left(\frac{\nu_{B_0}}{\nu}\right)^{(p-1)/2}\phi(\psi)\mathcal{L}_{(p+1)/2}, \tag{5.3.15b}$$

$$j_U = 0, \tag{5.3.15c}$$

$$j_V = C\frac{\sqrt{3}e^3 B}{4\pi mc^2}\left(\frac{3}{2}\right)^{p/2}\cot\psi(\sin\psi)^{p/2+1}\left(\frac{\nu_{B_0}}{\nu}\right)^{p/2}\phi(\psi)\left[\mathcal{R}_{p/2+1} + 2\mathcal{L}_{p/2} - \mathcal{J}_{p/2}\right]. \tag{5.3.15d}$$

The expression for j_I is exactly the same as Eq. (4.2.9) for the power per frequency derived in Sec. 4.2 for the case of $\phi(\psi) = 1$ and $\psi = \alpha$. This can be seen by expressing

$$\mathcal{J}_{(p+1)/2} = \frac{2^{(p+1)/2}}{p+1}\Gamma\left(\frac{p}{4} - \frac{1}{12}\right)\Gamma\left(\frac{p}{4} + \frac{19}{12}\right), \tag{5.3.16}$$

using Eq. (5.2.14a) and (5.2.14b). The division of 2π in Eq. (5.2.2) therefore becomes clear. We have defined the polarisation tensor such that the Stokes parameter j_I is not only proportional to the power per frequency per unit volume in Eq. (4.2.9), but equal to it. Working with polarisation degrees, this makes no difference, but this equality will be useful for chapter 6.

Note that our calculated expression for j_V is a factor of 4/3 off from that of [12]. This may be due to a difference in assumptions, some error in either calculation or choice of approximation. However, j_V appears only in the expression for the circular polarisation degree, which we will see that in all practical cases can be neglected. We therefore proceed with our calculated value of j_V in Eq. (5.3.15d).

5.4 Degree of circular polarisation

We defined the degree of circular polarisation in Eq. (5.3.13) given that the parameter U is zero. Now we will use the Stokes parameters obtained in the previous section to find the circular polarisation degree for a single electron and electrons with a power-law distribution. Once these are obtained, we will also provide plots to see the behaviour of the polarisation degree for increasing magnetic field strength.

Single electron

Using the Stokes parameters in Eq. (5.3.14), the degree of circular polarisation is

$$\Pi_{\text{circ}} = \frac{\rho_{x,V}}{\rho_{x,I}} = \frac{2\gamma\left(\theta\theta_\gamma + \frac{\theta_\gamma^3}{2\gamma^2}\cot\alpha\right) K_{2/3}\left(\frac{1}{2}\theta_\gamma^3 x\right) K_{1/3}\left(\frac{1}{2}\theta_\gamma^3 x\right)}{\theta_\gamma^2 K_{2/3}^2\left(\frac{1}{2}\theta_\gamma^3 x\right) + \gamma^2\left(\theta^2 + \frac{\theta\theta_\gamma^2}{\gamma^2}\cot\alpha + \frac{\theta_\gamma^4}{4\gamma^4}\cot^2\alpha\right) K_{1/3}^2\left(\frac{1}{2}\theta_\gamma^3 x\right)}. \tag{5.4.1}$$

For the lower order approximation $\mathcal{O}(\gamma^{-1})$, that is for very large γ, the terms proportional to $\cot\alpha$ are negligible and the circular polarisation can be written as

$$\Pi_{\text{circ}} = \frac{2\gamma\theta\theta_\gamma K_{2/3}\left(\frac{1}{2}\theta_\gamma^3 x\right) K_{1/3}\left(\frac{1}{2}\theta_\gamma^3 x\right)}{\theta_\gamma^2 K_{2/3}^2\left(\frac{1}{2}\theta_\gamma^3 x\right) + \gamma^2\theta^2 K_{1/3}^2\left(\frac{1}{2}\theta_\gamma^3 x\right)}. \tag{5.4.2}$$

This approximation also is correct for pitch angles α around 90°, as $\cot\alpha$ then becomes very small. Let us try to reason how the function in Eq. (5.4.2) behaves in terms of the magnetic field strength. The argument of the Bessel functions scales as

$$z \equiv \frac{1}{2}\theta_\gamma^3 x \propto \frac{1}{B}, \tag{5.4.3}$$

since $x \propto a \propto 1/\omega_B$ and $\omega_B \propto B$. For increasing magnetic field strength B, the Bessel functions will thus also increase, as is easily seen from the plot of the modified Bessel functions in Fig. 3.4. Since $K_{2/3}(z)$ increases faster than $K_{1/3}(z)$, we should expect that keeping every parameter constant and varying B, will lead to a decrease of the circular polarisation when B becomes very large. Furthermore, for large values of z, that is for small values of B, the modified Bessel functions $K_{2/3}(z)$ and $K_{1/3}(z)$ can by approximated by the asymptotic expressions in Eq. (3.5.29a) and (3.5.29b), respectively. For very large z, we ignore the second term in both cases and hence $K_{2/3}(z) \simeq K_{1/3}(z)$. The circular polarisation degree should therefore become constant for small values of B. This can be seen in dashed lines in Fig. 5.3 for some selected frequencies ν. In particular, the fixed values chosen are the velocity $v = 0.9999c$ and $\theta = 1/(2\gamma)$. The angle θ is chosen to lie well within the cone of half angle $1/\gamma$, to ensure that we are considering an angle where radiation is emitted.

In solid lines in Fig. 5.3, we see the case of a small pitch angle $\alpha = 1°$. Here, the higher order approximation in γ^{-1} is necessary to include, and the circular polarisation degree changes

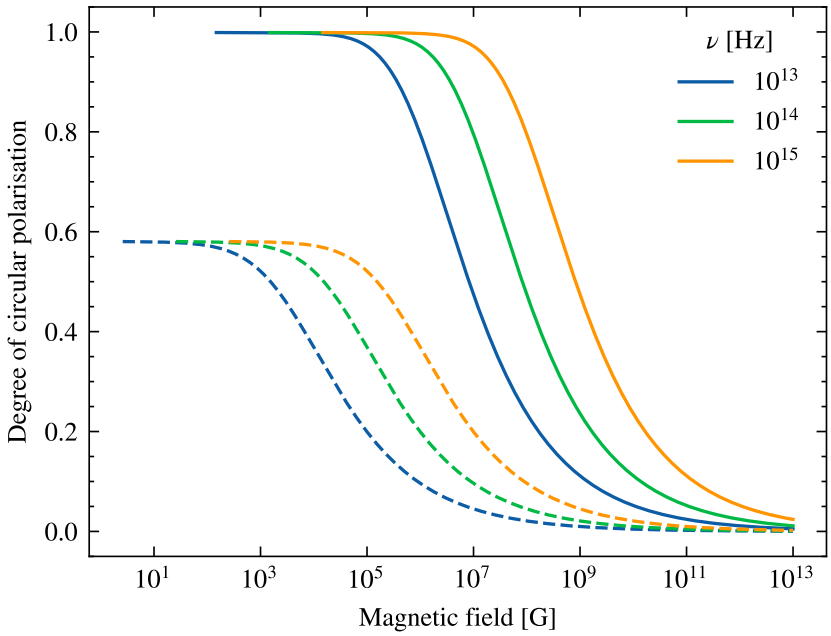

Figure 5.3: Degree of circular polarisation for a single electron as function of magnetic field strength B for different frequencies ν. The pitch angle α is 90° for the dashed lines and 1° for the solid lines. The other parameters are fixed, with velocity $v = 0.9999c$ and $\theta = 1/(2\gamma)$.

behaviour significantly. In fact, the circular polarisation degree is 1 for lower magnetic field strengths before it decreases to zero.

We can compare this result with the degree of linear polarisation in the next section. However, first we consider the power-law electron distribution.

Power-law electron distribution

Using Eq. (5.3.15a) and (5.3.15d), we get that the circular polarisation degree for a power-law electron distribution can be written as

$$\Pi_{\text{circ}} = \frac{j_V}{j_I} = 2\sqrt{\frac{2}{3}} \cot\psi (\sin\psi)^{1/2} \left(\frac{\nu_{B_0}}{\nu}\right)^{1/2} \frac{\mathcal{J}_{(p+1)/2}}{\mathcal{R}_{p/2+1} + 2\mathcal{L}_{p/2} - \mathcal{J}_{p/2}}. \tag{5.4.4}$$

Using Eq. (5.2.14) one can rewrite the last fraction. This does not yield a nice answer, so we leave the expression as it is.

It is clear that the circular polarisation degree only depends on the magnetic field through ν_{B_0}, and we have that $\Pi_{\text{circ}} \propto B^{1/2}$. The circular polarisation degree will increase with B, and eventually exceed 1, which is physically impossible. This can be seen in Fig. 5.4. Here we have plotted the degree of circular polarisation for a power-law electron distribution for different values of the pitch angle deviation ψ, while keeping $\nu = 5 \times 10^{14}$ Hz and $p = 1.4$ fixed. The impossible behaviour of the polarisation degree will be discussed in Sec. 8.1.

5.5 Degree of linear polarisation

We now move from circular polarisation to linear polarisation. The degree of linear polarisation is the only polarisation degree considered in the discussion of synchrotron radiation in the books by Rybicki and Lightman [9] and Longair [10]. Their approach considers the power per

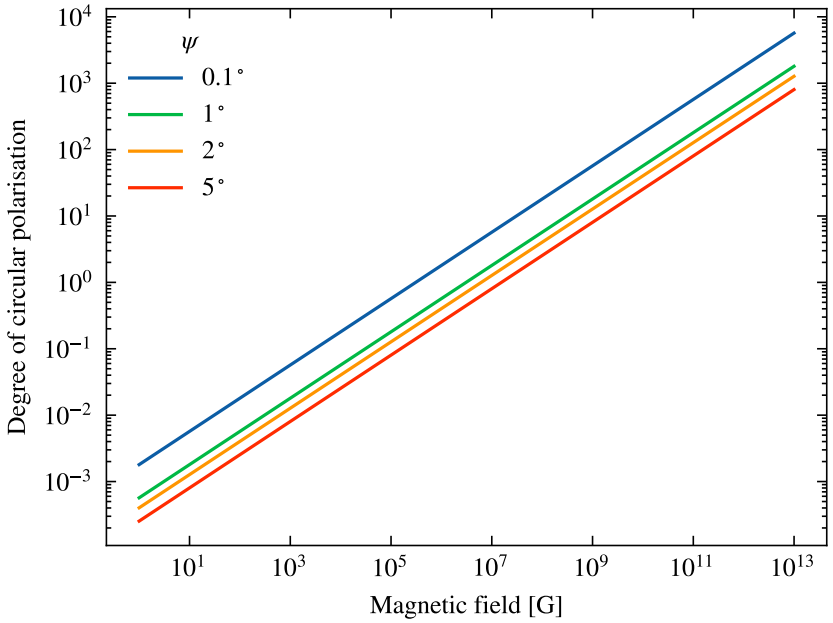

Figure 5.4: Degree of circular polarisation for a power-law electron distribution as function of magnetic field strength B for different pitch angle deviations ψ. The other parameters are fixed, with frequency $\nu = 5 \times 10^{14}$ Hz and particle distribution index $p = 1.4$.

frequency discussed in chapter 4. In this section we will follow both their treatments, as well as the approach using Stokes parameters, such that comparisons can be made.

Single electron

For particles with the same velocity, i.e. the same γ, the degree of linear polarisation is defined by Rybicki and Lightman [9] and Longair [10] as

$$\Pi_{\text{lin}}(\omega) = \frac{P_\perp(\omega) - P_\parallel(\omega)}{P_\perp(\omega) + P_\parallel(\omega)} = \frac{G(x)}{F(x)}, \tag{5.5.1}$$

where $P_\perp$ and $P_\parallel$ denote the perpendicular and parallel components of the power per frequency defined in Eq. (4.1.15a) and (4.1.15b), respectively. Furthermore, $F(x)$ and $G(x)$ are the functions defined in Eq. (4.1.12a) and (4.1.12b) for $x = \omega/\omega_c$. A plot of the linear polarisation degree using the functions $F(x)$ and $G(x)$ is shown in Fig. 5.5. We see that the linear polarisation degree increases from a value of 0.50, and approaches 1 for large values of x.

We can also use the Stokes parameters in Eq. (5.3.14) to calculate the linear polarisation degree. This gives the expression

$$\Pi_{\text{lin}} = \frac{\rho_{x,Q}}{\rho_{x,I}} = \frac{\theta_\gamma^2 K_{2/3}^2\left(\frac{1}{2}\theta_\gamma^3 x\right) - \gamma^2\left(\theta^2 + \frac{\theta\theta_\gamma^2}{\gamma^2}\cot\alpha + \frac{\theta_\gamma^4}{4\gamma^4}\cot^2\alpha\right) K_{1/3}^2\left(\frac{1}{2}\theta_\gamma^3 x\right)}{\theta_\gamma^2 K_{2/3}^2\left(\frac{1}{2}\theta_\gamma^3 x\right) + \gamma^2\left(\theta^2 + \frac{\theta\theta_\gamma^2}{\gamma^2}\cot\alpha + \frac{\theta_\gamma^4}{4\gamma^4}\cot^2\alpha\right) K_{1/3}^2\left(\frac{1}{2}\theta_\gamma^3 x\right)}. \tag{5.5.2}$$

In the lower order approximation, which we recall is the order of approximation made in Sec. 4.1,

$$\Pi_{\text{lin}} = \frac{\theta_\gamma^2 K_{2/3}^2\left(\frac{1}{2}\theta_\gamma^3 x\right) - \gamma^2\theta^2 K_{1/3}^2\left(\frac{1}{2}\theta_\gamma^3 x\right)}{\theta_\gamma^2 K_{2/3}^2\left(\frac{1}{2}\theta_\gamma^3 x\right) + \gamma^2\theta^2 K_{1/3}^2\left(\frac{1}{2}\theta_\gamma^3 x\right)}. \tag{5.5.3}$$

This is the same as Eq. (5.5.1), except that we have not integrated over the solid angle $\mathrm{d}\Omega$ as we did with the intensity spectrum in Sec. 4.1. Hence Eq. (5.5.3) still includes the θ dependence.

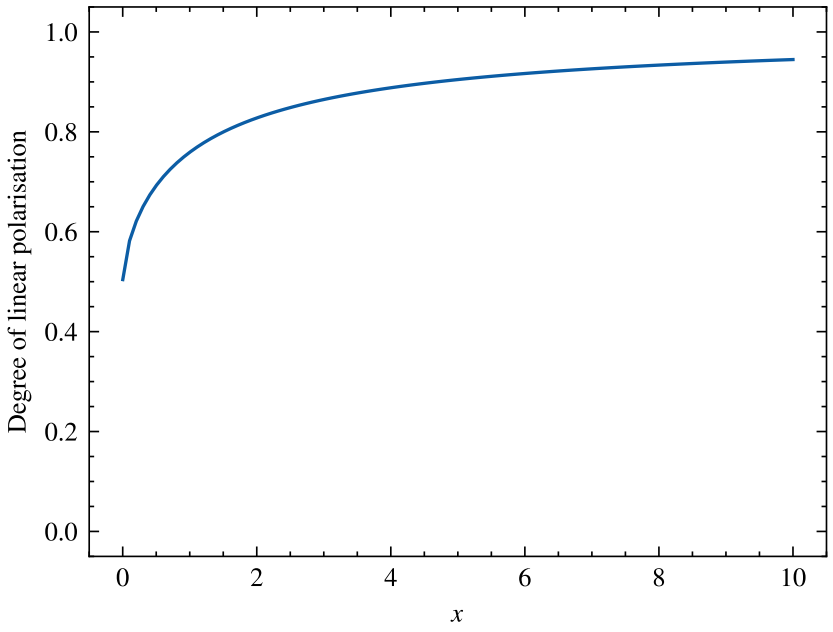

Figure 5.5: Linear polarisation degree as function of $x = \omega/\omega_c$ for a single electron using the functions $F(x)$ and $G(x)$.

We plot the degree of linear polarisation as function of the magnetic field strength B, fixing the values of $v = 0.9999c$ and $\theta = 1/(2\gamma)$. The result is seen in Fig. 5.6 for different frequencies ν and for pitch angle α of 90° (dashed lines) and 1° (solid lines). We see that the linear polarisation degree approaches 1 for stronger magnetic fields. This is consistent with the result for the circular polarisation degree seen in Fig. 5.3. For smaller values of B, the degree of linear polarisation decreases, while the degree of circular polarisation increases. As for the circular polarisation degree, the dependence on the pitch angle is significant.

Power-law electron distribution

Following the procedure of [9, 10], we integrate the perpendicular and parallel power per frequency, $P_\perp$ and $P_\parallel$, over the power-law distribution of electrons defined by Eq. (4.2.2). Using Eq. (4.1.15a) and (4.1.15b), we obtain

$$C\int_0^\infty P_\perp(\omega)\gamma^{-p}\mathrm{d}\gamma = C\frac{\sqrt{3}e^3B\sin\alpha}{4\pi mc^2}\int_0^\infty [F(x)+G(x)]\gamma^{-p}\mathrm{d}\gamma, \tag{5.5.4a}$$

$$C\int_0^\infty P_\parallel(\omega)\gamma^{-p}\mathrm{d}\gamma = C\frac{\sqrt{3}e^3B\sin\alpha}{4\pi mc^2}\int_0^\infty [F(x)-G(x)]\gamma^{-p}\mathrm{d}\gamma. \tag{5.5.4b}$$

Inserting these two equations into the definition of the linear polarisation degree in Eq. (5.5.1) gives

$$\Pi_{\mathrm{lin}} = \frac{\int_0^\infty G(x)\gamma^{-p}\mathrm{d}\gamma}{\int_0^\infty F(x)\gamma^{-p}\mathrm{d}\gamma}. \tag{5.5.5}$$

Recall from Eq. (5.2.10) that $\gamma \propto x^{-1/2}$ and consequently that $\mathrm{d}\gamma \propto x^{-3/2}\mathrm{d}x$. Hence, the linear polarisation degree in terms of x becomes

$$\Pi_{\mathrm{lin}} = \frac{\int_0^\infty G(x)x^{(p-3)/2}\mathrm{d}x}{\int_0^\infty F(x)x^{(p-3)/2}\mathrm{d}x}, \tag{5.5.6}$$

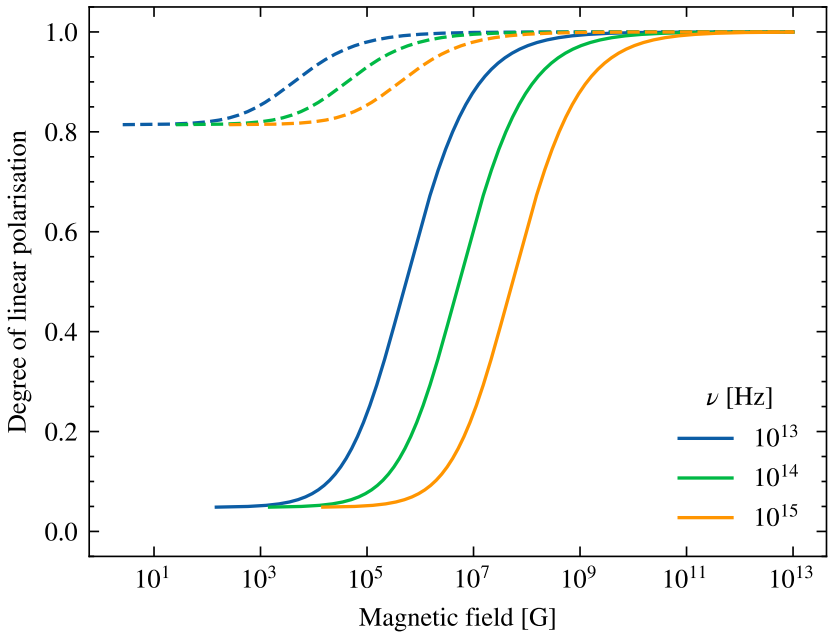

Figure 5.6: Degree of linear polarisation for a single electron as function of magnetic field strength B for different frequencies ν. The pitch angle α is 90° for the dashed lines and 1° for the solid lines. The other parameters are fixed, with velocity $v = 0.9999c$ and $\theta = 1/(2\gamma)$.

as all the other factors cancel. Using Eq. (4.2.7a) and (4.2.7b) we have that $\mu = (p-3)/2$ and obtain

$$\Pi_{\rm lin} = \frac{2^{\mu}(\mu+1)}{2^{\mu+1}} \frac{\Gamma\left(\frac{\mu}{2}+\frac{4}{3}\right)}{\Gamma\left(\frac{\mu}{2}+\frac{7}{3}\right)} = \frac{p+1}{4} \frac{\Gamma\left(\frac{p-3}{4}+\frac{4}{3}\right)}{\Gamma\left(\frac{p-3}{4}+\frac{7}{3}\right)}. \tag{5.5.7}$$

Setting $z = \frac{p-3}{4} + \frac{4}{3}$ and using the recurrence relation of the gamma function from Abramovitz and Stegun [46], $\Gamma(z+1) = z\Gamma(z)$, we can write

$$\frac{\Gamma\left(\frac{p-3}{4}+\frac{4}{3}\right)}{\Gamma\left(\frac{p-3}{4}+\frac{7}{3}\right)} = \frac{\Gamma\left(\frac{p-3}{4}+\frac{4}{3}\right)}{\left(\frac{p-3}{4}+\frac{4}{3}\right)\Gamma\left(\frac{p-3}{4}+\frac{4}{3}\right)} = \frac{12}{3p+7}. \tag{5.5.8}$$

Inserting this expression into Eq. (5.5.7) and simplifying yields

$$\Pi_{\rm lin} = \frac{p+1}{p+\frac{7}{3}}. \tag{5.5.9}$$

We have found a very simple expression for the linear polarisation degree in terms of only the particle distribution index p. The polarisation degree will be minima[5] at $p = 0$, that is $\Pi_{\rm lin} = 3/7 \simeq 0.43$, and it will approach 1 for increasing p.

For the frequency integrated radiation, we have that $\omega \propto x$ and we can write

$$\Pi_{\rm lin} = \frac{\int_0^\infty G(x)\mathrm{d}x}{\int_0^\infty F(x)\mathrm{d}x}. \tag{5.5.10}$$

Comparing this with Eq. (5.5.6), it is clear that $p = 3$ gives equality. Inserting this into Eq. (5.5.9), we obtain

$$\Pi_{\rm lin} = \frac{4}{3+\frac{7}{3}} = 0.75. \tag{5.5.11}$$

[5]We only consider power-law distributions with positive particle distribution index p.

Hence, the frequency integrated linear polarisation of synchrotron radiation is 75%, which is quite high.

We can also calculate the degree of linear polarisation by using the Stokes parameters, and compare with the result in Eq. (5.5.9). By using Eq. (5.3.15), it is simple to find that

$$\Pi_{\rm lin} = \frac{j_Q}{j_I} = \frac{\mathcal{L}_{(p+1)/2}}{\mathcal{J}_{(p+1)/2}} = \frac{\mathcal{L}_{(p+1)/2}}{\frac{2/3+(p+1)/2}{(p+1)/2}\mathcal{L}_{(p+1)/2}} = \frac{\frac{p+1}{2}}{\frac{2}{3}+\frac{p+1}{2}} = \frac{p+1}{p+\frac{7}{3}}. \tag{5.5.12}$$

Here we have also used the relation in Eq. (5.2.14a), and the result is exactly Eq. (5.5.9). For a given particle distribution index p, the linear polarisation degree is constant for any value of the magnetic field strength B, frequency ν and pitch angle α. From Eq. (5.4.4) we have that $\Pi_{\rm circ} \propto B^{1/2}$, and we saw in Fig. 5.4 that the degree of circular polarisation is very small for weak magnetic fields. For field strengths of the order of μG, as expected from the GMF, the degree of linear polarisation is clearly dominant.

Chapter 6

Radiative transfer

We have already seen the properties of synchrotron radiation and calculated the most important quantities such as the emission-polarisation tensor and its Stokes parameters. However, to get a more complete picture of the process we need to take a small step back to consider radiative transfer, as well as diffusion.

6.1 Radiative transfer equation

When radiation passes through a medium, it can interact by absorption, emission or scattering processes, which leads to an increase or decrease in intensity, or energy. To describe these processes, the radiative transfer equation (RTE) [9],

$$\frac{\mathrm{d}I_\nu}{\mathrm{d}s} = -\alpha_\nu I_\nu + j_\nu, \tag{6.1.1}$$

is used. Here, I_ν is the (specific) intensity such that $\mathrm{d}I_\nu/\mathrm{d}s$ describes the change in intensity for propagation over a distance $\mathrm{d}s$. Furthermore, α_ν is the absorption coefficient and j_ν is the emissivity, or emission coefficient, in units power per frequency per unit volume. Since we have described the polarised radiation through use of the Stokes parameters, we wish to rewrite the RTE in terms of Stokes vectors. This gives [47]

$$\frac{\mathrm{d}}{\mathrm{d}s}\begin{bmatrix} I \\ Q \\ U \\ V \end{bmatrix} = \begin{bmatrix} j_I \\ j_Q \\ j_U \\ j_V \end{bmatrix} - \begin{bmatrix} \alpha_I & \alpha_Q & \alpha_U & \alpha_V \\ \alpha_Q & \alpha_I & \rho_V & \rho_U \\ \alpha_U & -\rho_V & \alpha_I & \rho_Q \\ \alpha_V & -\rho_U & -\rho_Q & \alpha_I \end{bmatrix}\begin{bmatrix} I \\ Q \\ U \\ V \end{bmatrix}, \tag{6.1.2}$$

where j_I, j_Q, j_U and j_V are the emission coefficients, α_I, α_Q, α_U and α_V are the emissivities, and ρ_I, ρ_Q, ρ_U and ρ_V are the Faraday rotation coefficients. We can define

$$\mathbf{I} \equiv \begin{bmatrix} I \\ Q \\ U \\ V \end{bmatrix} \quad \text{and} \quad \mathbf{j}_I \equiv \begin{bmatrix} j_I \\ j_Q \\ j_U \\ j_V \end{bmatrix} \tag{6.1.3}$$

as the Stokes vector and the emissivity vector, respectively. Expressions for the components of $\mathbf{j}_I$ are already given in Sec. 5.3, and in particular we have that $j_U = 0$. This was the result of

choosing basis vectors parallel and perpendicular to the magnetic field. This choice aligns the magnetic field with the Stokes parameter U, which means that we also have $\alpha_U = \rho_U = 0$.

We found in Sec. 4.3 that electrons following a power-law distribution of energies emit far more radiation than they absorb. The relationship scales with the frequency through $\mathcal{P} \propto \nu^{5/2}\alpha_\nu$. As absorption will contribute much less than emission, we will make the assumption that $\alpha_I = \alpha_Q = \alpha_U = \alpha_V = 0$ to simplify the RTE.

Furthermore, in Sec. 2.2.1 we presented the Faraday rotation measure defined by Eq. (2.2.2). Setting a constant electron density $n_e(s) = 1\,\mathrm{cm}^{-3}$ and a constant magnetic field strength $B_\parallel(s) = 3\,\mu\mathrm{G}$ and integrating over a distance of 1 kpc, we obtain RM $\simeq 2400\,\mathrm{rad\,m}^{-2}$. The rotation angle is $\Phi = \lambda^2\mathrm{RM}$, and since $\lambda \propto \nu^{-1}$, the rotation angle is very small given the calculated RM and high frequencies ν. We will in chapter 7 use the frequency $\nu = 408\,\mathrm{MHz}$ and the electron number density $n_e(0) \sim 10^{-5}\,\mathrm{cm}^{-3}$. Assuming the number density is constant over the distance of 1 kpc, we find that RM $\simeq 0.024$ and $\Phi \simeq 0.01$ rad. As a typical value of the GMF is $B = 3\,\mu\mathrm{G}$, we would expect even smaller values of $B_\parallel(s)$ as the direction of the magnetic field changes, and the RM should realistically be even smaller. We can therefore reasonably assume that Faraday rotation contributes little to the radiative transfer, and set all the Faraday rotation coefficients $\rho_I = \rho_Q = \rho_U = \rho_V = 0$.

With only the emission coefficients left to consider, the RTE simplifies significantly, and can be written as

$$\frac{\mathrm{d}}{\mathrm{d}s}\mathbf{I} = \mathbf{j}_I. \tag{6.1.4}$$

6.2 Line-of-sight integral

We will in this section use the method of calculating the line-of-sight (LoS) integral. This will be done for the polarisation as well as the total intensity from synchrotron radiation received at Earth.

6.2.1 Polarisation

We would like to calculate the circular and linear polarisation degree received by an observer at Earth using the radiative transfer equation in Eq. (6.1.4). We already have the expressions for the components of $\mathbf{j}_I$ from Sec. 5.3. However, since the emissivity vector is calculated in the local frame of the electron, the coefficients must be transformed to the observed polarisation basis. This is done by rotating the emissivity vector by multiplication with the matrix [47][1]

$$R(\chi) = \begin{bmatrix} 1 & 0 & 0 & 0 \\ 0 & \cos 2\chi & -\sin 2\chi & 0 \\ 0 & \sin 2\chi & \cos 2\chi & 0 \\ 0 & 0 & 0 & 1 \end{bmatrix}. \tag{6.2.1}$$

The angle χ is defined to lie between the projected magnetic field $\mathbf{B}$ and the polarisation basis. The factor of 2 in the arguments of the cosine and sine functions is due to the fact that χ is periodic in π. That is, there is no difference in polarisation for the angles χ and $\chi + \pi$. We can now write the RTE as

$$\frac{\mathrm{d}}{\mathrm{d}s}\mathbf{I} = R(\chi)\mathbf{j}. \tag{6.2.2}$$

[1] Dexter [47] also takes into account general relativity, which is not considered in this thesis.

To solve Eq. (6.2.2), we consider a line-of-sight integral in the z-direction, that is taking $\hat{\mathbf{s}} = \hat{\mathbf{z}}$. The geometry of the LoS integral is shown in Fig. 6.1, where Fig. 6.1a illustrates along which line $\hat{\mathbf{s}}$ we wish to integrate. We choose a coordinate system with the observer situated at the origin $(x, y, z) = (0, 0, 0)$, and the polarisation basis consists of the unit vectors $\hat{\mathbf{x}}$ and $\hat{\mathbf{y}}$. The angle χ is then the angle between the magnetic field vector projected onto the xy-plane and the x-axis, as can be seen in Fig. 6.1b.

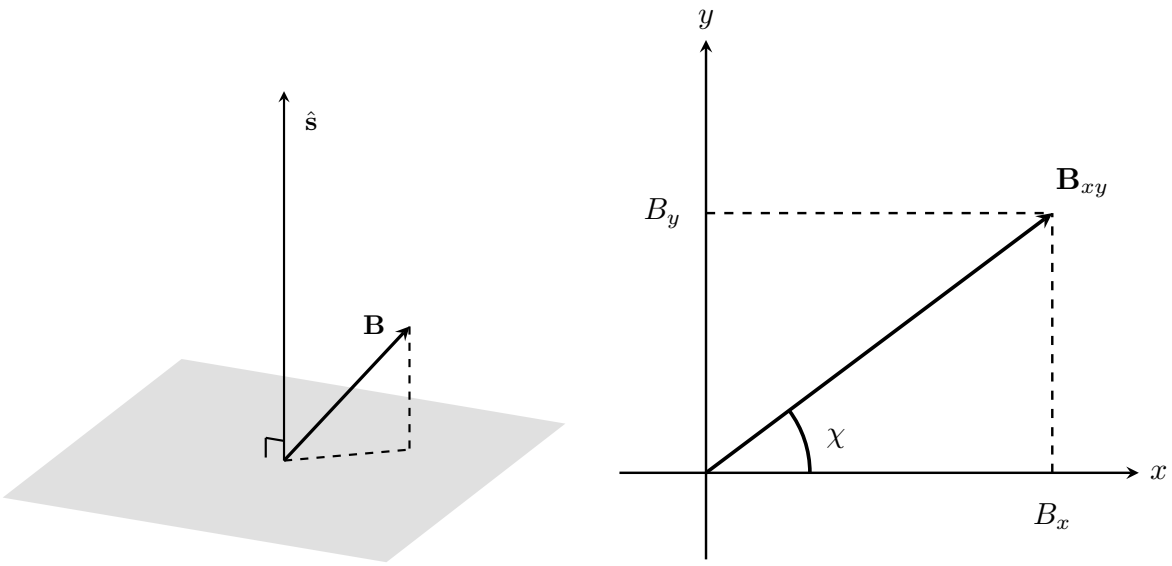

(a) Line-of-sight direction $\hat{\mathbf{s}}$, its perpendicular plane and an arbitrary magnetic field vector.

(b) Projected magnetic field vector $\mathbf{B}$ onto the xy-plane, where χ is the angle between $\mathbf{B}_{xy}$ and $\hat{\mathbf{x}}$.

Figure 6.1: Geometry for the line-of-sight integral. The plane in (a) is chosen to be the xy-plane in (b) such that $\hat{\mathbf{s}} = \hat{\mathbf{z}}$.

We now wish to calculate

$$\mathbf{I} = \int R(\chi)\mathbf{j}\mathrm{d}z \tag{6.2.3}$$

by summing up all the contributions of the emissivity $R(\chi)\mathbf{j}$ for N particles with z-values in the range $[0, z_{\max}]$, where $z_{\max}$ is some maximum value of z. The contributions to the emissivity is consequently multiplied with the step size Δz used in the numerical integration. We recall that the emission from ultra-relativistic electrons is mainly in the forward direction, and lies within a cone of opening angle $\theta \simeq 1/\gamma$. As the angle θ is very small, it is reasonable to assume that an observer at Earth only receives contributions from electrons moving right towards them. Therefore, we will assume that each particle has a velocity along $-\hat{\mathbf{z}}$ and given the magnetic field direction, it is possible to calculate the pitch angle α at each point. It is clear that both α and χ are constant at each point in the case of a uniform magnetic field. This means that given a frequency ν, the contribution of $R(\chi)\mathbf{j}$ to the Stokes vector $\mathbf{I}$ is constant along the LoS. The more interesting case is when the magnetic field vector changes magnitude and direction along the LoS, e.g. for a turbulent magnetic field.

6.2.2 Intensity

We would also like to perform a LoS integral to calculate the synchrotron intensity

$$I_\nu = \frac{\mathrm{d}E}{\mathrm{d}A\mathrm{d}t\mathrm{d}\Omega\mathrm{d}\nu}. \tag{6.2.4}$$

In this case, the geometry is much more simple as we do not need to consider the polarisation angle or transform our coefficients into the polarisation basis. At each point along the LoS, we

simply need to add up all the contributions to the intensity from electrons emitting towards the observer. We will consider the (differential) number density of electrons[2] with energy E,

$$n(z, E) = \frac{\mathrm{d}N}{\mathrm{d}E\mathrm{d}V}, \tag{6.2.5}$$

and assume the electrons follow a power-law distribution, that is $\mathrm{d}N/\mathrm{d}E \propto E^{-p}$, and that we choose the line-of-sight $\hat{\mathbf{s}} = \hat{\mathbf{z}}$. The power-law distribution in Eq. (4.2.1) becomes

$$n(z, E)\mathrm{d}E = n_0' E^{-p}\mathrm{d}E. \tag{6.2.6}$$

Here, n_0' is the normalisation constant. By choosing a reference energy E_{ref}, we can write the power-law as

$$n(z, E) = n(z, E_{\mathrm{ref}}) \left(\frac{E}{E_{\mathrm{ref}}}\right)^{-p} = n(z, E_{\mathrm{ref}}) \left(\frac{\gamma}{\gamma_{\mathrm{ref}}}\right)^{-p}, \tag{6.2.7}$$

where $\gamma_{\mathrm{ref}} = E_{\mathrm{ref}}/E_0$ for the rest mass energy E_0. We wish to consider the number density

$$n(z, \gamma) = \frac{\mathrm{d}N}{\mathrm{d}\gamma\mathrm{d}V} = \frac{\mathrm{d}N}{\mathrm{d}E\mathrm{d}V}\frac{\mathrm{d}E}{\mathrm{d}\gamma} = n(z, E)E_0. \tag{6.2.8}$$

In terms of the Lorentz factor, we therefore obtain the power-law

$$n(z, \gamma) = n(z, E_{\mathrm{ref}})E_0 \left(\frac{\gamma}{\gamma_{\mathrm{ref}}}\right)^{-p} = n(z, E_{\mathrm{ref}})E_0\gamma_{\mathrm{ref}}^{p}\gamma^{-p} = n(z, E_{\mathrm{ref}})\frac{E_{\mathrm{ref}}^{p}}{E_0^{p-1}}\gamma^{-p}. \tag{6.2.9}$$

Hence, the new normalisation constant becomes

$$n_\gamma(z) \equiv n(z, E_{\mathrm{ref}})\frac{E_{\mathrm{ref}}^{p}}{E_0^{p-1}} = n_0 g(z), \tag{6.2.10}$$

such that

$$n(z, \gamma)\mathrm{d}\gamma = n_\gamma(z)\gamma^{-p}\mathrm{d}\gamma. \tag{6.2.11}$$

Here we have assumed that $n(z, E_{\mathrm{ref}}) = n(0, E_{\mathrm{ref}})g(z)$, where $g(z)$ is some scaling function dependent on z, the distance along the line-of-sight. Therefore n_0 becomes a normalisation constant independent of this distance.

Now, the LoS integral is given by

$$I_\nu = \int j_\nu \mathrm{d}z, \tag{6.2.12}$$

where j_ν is the emissivity at some point in space given by

$$j_\nu = \frac{\mathrm{d}E}{\mathrm{d}V\mathrm{d}t\mathrm{d}\Omega\mathrm{d}\nu} = \frac{1}{4\pi}\int P(\nu)n(z, \gamma)\mathrm{d}\gamma = \frac{1}{4\pi}\mathcal{P}(\nu). \tag{6.2.13}$$

Here, $\mathcal{P}(\nu)$ denotes the total power per frequency per unit volume found in Eq. (4.2.9) with $C = n_\gamma(z)$. As for the LoS integral in the previous section, we will assume that the particles have velocity along $-\hat{\mathbf{z}}$, towards the observer. This means that the angle θ is zero and consequently the pitch angle deviation ψ is equal to the pitch angle α. Therefore, we have that the emissivity, or power per frequency per unit volume, corresponds to j_I in Eq. (5.3.15a) for $\psi = \alpha$ and $\phi(\psi) = \phi(\alpha) = 1$. Hence, we write

$$j_\nu = n_\gamma(z)\frac{e^3 B}{8\sqrt{2}\pi^2 mc^2}\left(\frac{3}{2}\right)^{p/2}(\sin\alpha)^{(p+1)/2}\left(\frac{\nu_{B_0}}{\nu}\right)^{(p-1)/2}\mathcal{J}_{(p+1)/2}. \tag{6.2.14}$$

[2]For simplicity, we will from now on write the electron number density as n instead of n_e, dropping the subscript.

6.2.3 Angular resolution

When performing the LoS integral given a generated turbulent magnetic field with a (finite) correlation length[3] L_c, we need to consider the angular resolution, or angular field of view (FOV), if we wish to compare with measurements. We therefore have to average over the FOV at each point along the LoS. Given the angular FOV ϑ, at a distance s from the observer the area is

$$A \simeq \pi \left[s \tan\left(\frac{\vartheta}{2}\right) \right]^2 . \tag{6.2.15}$$

We assume that ϑ is small, e.g. 1°, such that we are able to approximate the area on the sphere of radius s as a circle in the plane perpendicular to $\hat{\mathbf{s}}$. As can be seen from Fig. 6.2, the area A_2 is larger than A_1 given that its distance s_2 is greater than s_1. We consider that the turbulent magnetic field consists of boxes of area L_c^2, and will therefore have to average the intensity over the number of boxes fitting within the observed area A.

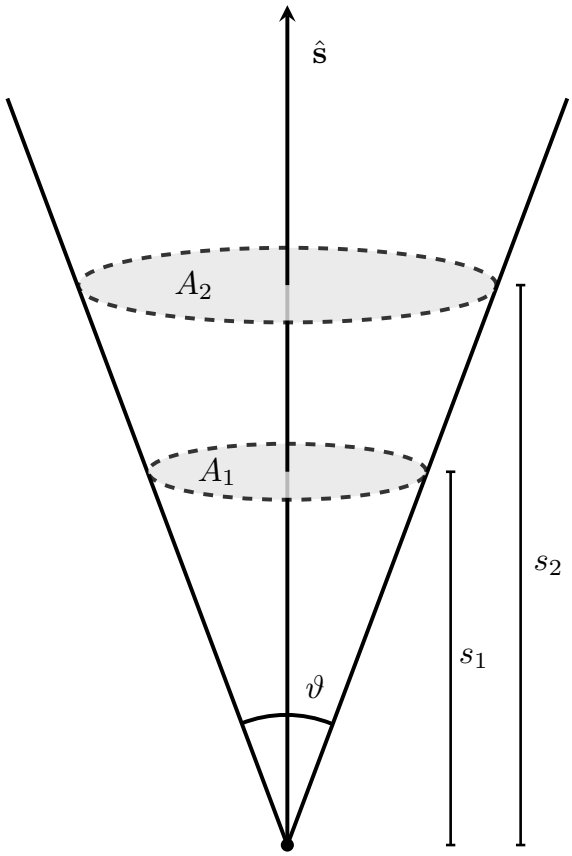

Figure 6.2: Geometry of the field of view, including the angular FOV ϑ and the observed areas A_1 and A_2 at the two distances from the observer s_1 and s_2, respectively.

Given the correlation length of the magnetic field L_c, we may estimate the number of points contributing within the area A at a distance s from the observer as

$$N \simeq \left\lfloor \frac{A}{L_c^2} \right\rfloor . \tag{6.2.16}$$

The intensity should consequently be calculated N times, and the average of these contributions should account for the intensity at the point s along the LoS. In the case of $N = 0$, no averaging is done, and only one contribution to the intensity is made.

[3] A regular field essentially has infinite correlation length.

In many cases we will perform a large number of simulations and average over the results to obtain mean values of intensity. If the number of simulations is large enough, it is expected that the process of averaging over the FOV is redundant, as the fluctuations around the mean are already removed. We therefore keep in mind that considering the angular resolution only amounts to a longer computation time in many cases. Similarly, at very large distances s, the number of points contributing within the area A may be very large. To avoid unnecessary extra computation time, one can set an upper bound on N as well.

6.3 Diffusion

We have seen in Sec. 2.4 that Kolmogorov's theory is based on a slope $\gamma = 5/3$, however other energy spectra may be considered. An example is the Iroshnikov–Kraichnan theory where $\gamma = 3/2$ [13]. In either case, the parameter γ may be related to the diffusion coefficient. In addition, the diffusion coefficient can also be used in estimating the electron number density.

6.3.1 Random walk

We will consider the case of a pure isotropic turbulent field and derive the diffusion coefficient accordingly. For this, we will use the method of a random walk in three dimensions. The random walk describes the random path of particles interacting and diffusing within the ISM. One assumes that an electron takes N steps in a random direction, where each step has length L, known as the mean free path. After N steps, the particle will have a net vector displacement

$$\mathbf{d} = \sum_{i=1}^{N} \mathbf{L}_i. \tag{6.3.1}$$

We wish to find the norm of this displacement, and therefore calculate

$$d^2 = \mathbf{d} \cdot \mathbf{d} = \sum_{i=1}^{N} \sum_{j=1}^{N} \mathbf{L}_i \cdot \mathbf{L}_j. \tag{6.3.2}$$

As each of the steps $\mathbf{L}_i$ has length equal to the mean free path L, we get that

$$d^2 = NL^2 + L^2 \sum_{i=1}^{N} \sum_{\substack{j=1 \\ j \neq i}}^{N} \cos\theta_{ij}, \tag{6.3.3}$$

where θ_{ij} is the angle between $\mathbf{L}_i$ and $\mathbf{L}_j$. Since the steps are chosen at random, the angles are isotropically distributed and the sum of the cosine terms should approach zero. The displacement can therefore be estimated as

$$d = \sqrt{N} L. \tag{6.3.4}$$

This displacement is a RMS distance, while the expected value of the distance from the origin after N steps is a different quantity. This value is smaller than the RMS distance and may be expressed, in one dimension, as [48]

$$\langle |d| \rangle = L \sqrt{\frac{2N}{\pi}}. \tag{6.3.5}$$

While the RMS distance d is related to the SD with zero mean, the expected value of the distance $\langle |d| \rangle$ is related to the mean absolute deviation (MAD).

We now consider the diffusion coefficient. The diffusion equation combines Fick's law and the continuity equation [49],

$$\mathbf{j} = -D\boldsymbol{\nabla} n, \tag{6.3.6}$$

$$\boldsymbol{\nabla} \cdot \mathbf{j} = -\frac{\partial n}{\partial t}, \tag{6.3.7}$$

respectively. Here, $\mathbf{j}$ is the current, n is the number density and D is the diffusion coefficient. For an isotropic medium, this gives the diffusion equation

$$\frac{\partial n}{\partial t} = \boldsymbol{\nabla} \cdot (D\boldsymbol{\nabla} n)\,. \tag{6.3.8}$$

This partial differential equation (PDE) is analogous to the heat equation, and its fundamental solution may be found as [50]

$$n(r,t) = \frac{1}{(4\pi Dt)^{m/2}} \exp\left(-\frac{r^2}{4Dt}\right), \tag{6.3.9}$$

given that $n(r,0) = \delta(r)$. The variable m is the number of dimensions, in our case three. The solution is therefore a Gaussian function where the mean distance travelled by the particle is $d = \sqrt{2Dt}$, that is the standard deviation usually denoted by σ in statistics. As the particle has travelled a total distance of NL according to our random walk model, we estimate the velocity to be $v = NL/t$. Equating Eq. (6.3.4) with the mean distance from the fundamental solution of the diffusion equation, we get that

$$D \propto \frac{NL^2}{t} = vL. \tag{6.3.10}$$

By more precise analyses, the diffusion coefficient is estimated to be $D = vL/3$ [51]. The key point, however, is that the diffusion coefficient depends on the mean free path L of the particle.

For the propagation of CRs, the diffusion coefficient is dependent on the energy through [25]

$$D(E) \propto E^{\beta}, \tag{6.3.11}$$

for some spectral index β. On the other hand, the diffusion coefficient scales with the Larmor radius R_L as

$$D(E) \propto R_L^{2-\gamma}, \tag{6.3.12}$$

and as the Larmor radius is proportional to E/B, we get the relationship $\beta = 2 - \gamma$. Hence, for Kolmogorov turbulence, the diffusion coefficient scales with $E^{1/3}$ and $B^{-1/3}$, and for Iroshnikov–Kraichnan turbulence it scales with $E^{1/2}$ and $B^{-1/2}$.

6.3.2 Stationary case

Let us now consider the stationary case of the diffusion equation in Eq. (6.3.8) in one dimension. The stationary condition means that the time derivative on the LHS is zero. We have that

$$\frac{\mathrm{d}}{\mathrm{d}z}\left(D(z)\frac{\mathrm{d}n}{\mathrm{d}z}\right) = 0. \tag{6.3.13}$$

Equivalently, we may write

$$D(z)\frac{\mathrm{d}n}{\mathrm{d}z} = \text{const.} \equiv -j_0, \tag{6.3.14}$$

where j_0 is some constant. We are left with a much simpler ordinary differential equation (ODE) than that of Eq. (6.3.8), and the solution can be expressed as

$$n(z) = n_0 - j_0 \int_0^z \frac{\mathrm{d}z'}{D(z')}, \tag{6.3.15}$$

given the condition that $n_0 \equiv n(0)$. Assuming that the diffusion coefficient changes with distance z, we cannot simplify the equation further without considering the expression for D. We expect the number density n to decrease for increasing z, as we assume the number of particles should be larger towards the centre of the Galaxy. We may therefore take the diffusion coefficient,

$$D(z) = D_0 \exp\left(\frac{z}{z_0}\right), \tag{6.3.16}$$

as an example, where $D_0 \equiv D(0)$ and z_0 is some constant parameter. It is a simple calculation to show that

$$n(z) = n_0 + \frac{j_0 z_0}{D_0}\left[\exp\left(-\frac{z}{z_0}\right) - 1\right]. \tag{6.3.17}$$

Depending on the physical constants, it is important to note that this expression can be negative. This happens for some values of z when $j_0 z_0 / D_0 n_0 > 1$. As a negative number density is physically impossible, we must impose a cut-off at some z_c where $n(z_c) = n_c$ and set $n(z) = n_c$ for all $z > z_c$. Here n_c represents some constant "background" number density, which should be small, but could be non-zero. For the case when $j_0 z_0 / D_0 n_0 < 1$, the number density will decrease and approach a constant positive value.

Chapter 7

Numerical simulations and results

In this chapter we will present our numerical simulations and their results. The focus will lie on testing the numerical models from Sec. 2.5 in terms of intensity and polarisation of synchrotron radiation. In addition, we will consider an alternative simplified magnetic field model.

In most of the numerical simulations we use the frequency $\nu = 408\,\mathrm{MHz}$, due to the physical data we will use for comparisons. We note that for this frequency we are well within the region where synchrotron radiation dominates the Galactic emission spectrum, as seen in Fig. 1.1. We therefore do not have to take into account processes such as free-free and dust emission.

7.1 Pure turbulent fields

The pure turbulent fields are generated using the `ELMAG` program. However, this program is dependent on several input parameters, and it is therefore necessary to investigate the effects of varying these.

7.1.1 Number of turbulent modes

The number of turbulent modes n_k should be looked into to ensure that the turbulence generated by `ELMAG` is sufficiently irregular. We know that the polarisation degree should decrease for increasing distances, as the turbulence ensures additions in random polarisation directions according to the pitch angle α. In comparison, the polarisation degree for a uniform field stays constant as the pitch angle does not change over distance. As a simplified view on the `ELMAG` turbulent field model, we can assume that it generates boxes of side lengths equal to the correlation length L_c where the magnetic field is uniform. In each box, the direction of the uniform field should be random. By performing a LoS integral over a number of N boxes, we therefore have a case of a random walk as discussed in Sec. 6.3.1, and the polarisation degree should approximately decrease with length $z = NL_c$ as $1/\sqrt{N}$.

The number of turbulent modes determines the "degree" of turbulence, and we may expect that for fewer turbulent modes, the polarisation degree will saturate and stabilise at higher values. In Fig. 7.1 we see this behaviour. Using the method from Sec. 6.2.1, we have simulated 500 different turbulent fields using `ELMAG` and performed a LoS integral for polarisation, for the number of turbulent modes $n_k = 10, 100, 1000$. The correlation length is $L_c = 20\,\mathrm{pc}$, the RMS strength of the magnetic field is $B_{\mathrm{rms}} = 3\,\mu\mathrm{G}$, the particle distribution index is $p = 2.4$ and the frequency is $\nu = 50\,\mathrm{MHz}$. The figure shows the mean polarisation degree as a function of distance z and the expected behaviour of $1/\sqrt{N}$ is plotted in dashed lines. The stabilisation in polarisation degree happens at values of $\Pi \approx 0.32, 0.10, 0.03$ for $n_k = 10, 100, 1000$, respectively.

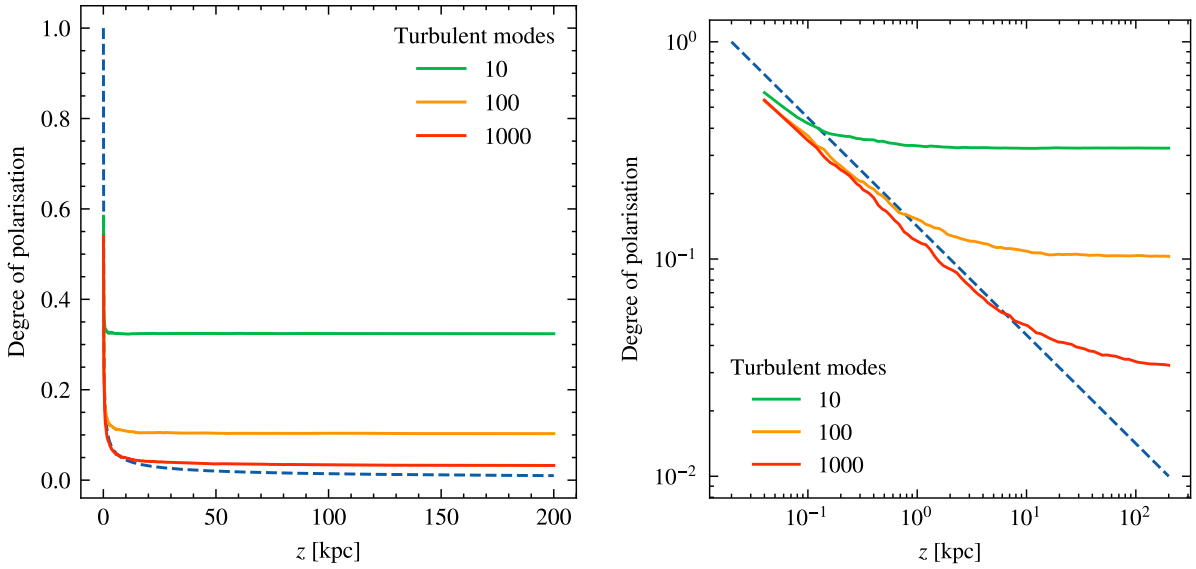

Figure 7.1: Mean degree of polarisation as function of distance z for three different numbers of turbulent modes $n_k = 10, 100, 1000$ as (a) a normal plot and (b) a log-log plot. The parameters used are $L_c = 20\,\mathrm{pc}$, $B_{\mathrm{rms}} = 3\,\mu\mathrm{G}$, $p = 2.4$ and $\nu = 50\,\mathrm{MHz}$. The function $1/\sqrt{N}$ is plotted in dashed lines over distances $z = NL_c$.

We see from Fig. 7.1 that a LoS integral over a distance of more than approximately 6 kpc requires a larger amount of turbulent modes than each of the cases considered to ensure the randomness of the field. However, increasing n_k leads to a significant increase of computation time and one should therefore be careful in choosing the necessary number of turbulent modes for each specific simulation.

7.1.2 Normalisation

We would like to consider the synchrotron intensity using the turbulent magnetic field model of `ELMAG`. Unlike the treatment of polarisation, we are now required to consider the normalisation of our relevant expressions.

In chapter 6 we discussed the LoS integral over intensities. The last step missing is finding the constant n_0 and the function $g(z)$ to obtain an expression for the normalisation $n_\gamma(z) \equiv n_0 g(z)$ in Eq. (6.2.14). For this we will use data from the Alpha Magnetic Spectrometer (AMS), a particle detector on the International Space Station (ISS) [52]. The AMS has since 2011 provided data on CRs in the range of MeV to TeV. We use the AMS-02 data for the combined electron and positron spectrum measured [53]. The energy spectrum is seen in Fig. 7.2a, in units of $\mathrm{eV\,cm^{-1}\,s^{-1}\,sr^{-1}}$. The dashed lines indicate the energy of an electron given the magnetic field strengths $10\,\mu\mathrm{G}$ and $1\,\mu\mathrm{G}$. Here we have used that most radiation is emitted at the critical frequency, in which the average is given by

$$\langle \nu_c \rangle = \frac{\langle \omega_c \rangle}{2\pi} = \frac{3eB\gamma^2}{4\pi mc} \langle \sin\alpha \rangle. \tag{7.1.1}$$

We have that $\langle \sin\alpha \rangle = \pi/4$ by averaging over the solid angle $\mathrm{d}\Omega = \sin\alpha \mathrm{d}\alpha \mathrm{d}\varphi$. Furthermore, we use that $\langle \nu_c \rangle = 408\,\mathrm{MHz}$ and the energy is then obtained through $E = \gamma mc^2$. In Fig. 7.2b, we show the number density spectrum in units of $\mathrm{eV^{-1}\,cm^{-3}}$, where the conversion from the energy spectrum is done by

$$n(E) = \frac{4\pi}{c} I(E). \tag{7.1.2}$$

For high-energy electrons and positrons, we see that the number density follows an approximate power-law,

$$n(E)\mathrm{d}E = E^{-p}\mathrm{d}E, \tag{7.1.3}$$

as we have assumed throughout the thesis in the calculation of emissivities. By performing a fit, we obtain a particle distribution index and a normalisation constant of

$$p = 2.98 \quad \text{and} \quad n_0 \simeq 2.74 \times 10^{-5}\,\mathrm{cm}^{-3}, \tag{7.1.4}$$

respectively. This very simple analysis of the CR electron and positron spectrum serves as a starting point for investigating the possible parameters defining our problem.

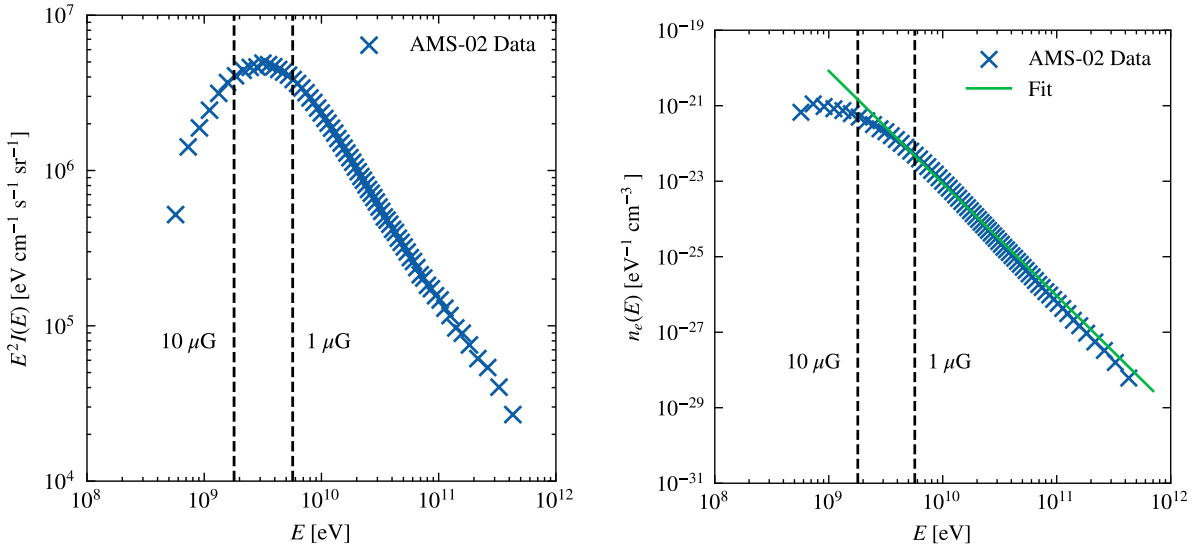

(a) **(b)**

Figure 7.2: The electron and positron spectrum measured by AMS-02 for (a) energy and (b) number density. In the case of number density, a power-law fit has been made. The dashed lines indicate the energy of an electron with an average critical frequency $\langle \nu_c \rangle = 408\,\mathrm{MHz}$ in magnetic fields of strengths $10\,\mu\mathrm{G}$ and $1\,\mu\mathrm{G}$.

Note that for low-energy electrons and positrons, the shape of the spectrum bends and no longer follows the power-law. This is likely due to solar modulation effects on the CRs. As CRs enter the heliosphere, they interact with the turbulent solar wind including its magnetic field, which leads to variations in energy and intensity [54]. The spectrum for low-energy electrons and positrons therefore appears different than that of high-energy electrons and positrons. In Fig. 7.3 we show the computed electron local interstellar spectra (LIS) along with the modulated electron spectrum at Earth from Bisschoff et al. [55]. The V1 electron observations[1] from [56] are done at 122 AU, while the PAMELA observations[2] from [57] are done at 1 AU. For low-energy electrons, we therefore expect that the spectrum bends less than that in Fig. 7.2. However, a power-law fit should yield a somewhat lower particle distribution index p in this region, as well as a lower electron density normalisation constant n_0.

It now remains to determine the scaling function $g(z)$. In addition, we also wish to determine how the magnetic field strength scales with the position. That means finding $f(z)$ such that $B = f(z)B_{\mathrm{rms}}$, thus redefining the function in Eq. (2.5.4). We will use the method of [58], which uses the numerical model `DRAGON` [35] to compute CR propagation, in order to model the

[1] Voyager 1 (V1) is a space probe which has been observing the LIS from Galactic CRs since 2012.

[2] This electron spectrum was measured by the Payload for Antimatter Matter Exploration and Light-nuclei Astrophysics (PAMELA) from 2006 to 2009, and fitted with a solar modulation model.

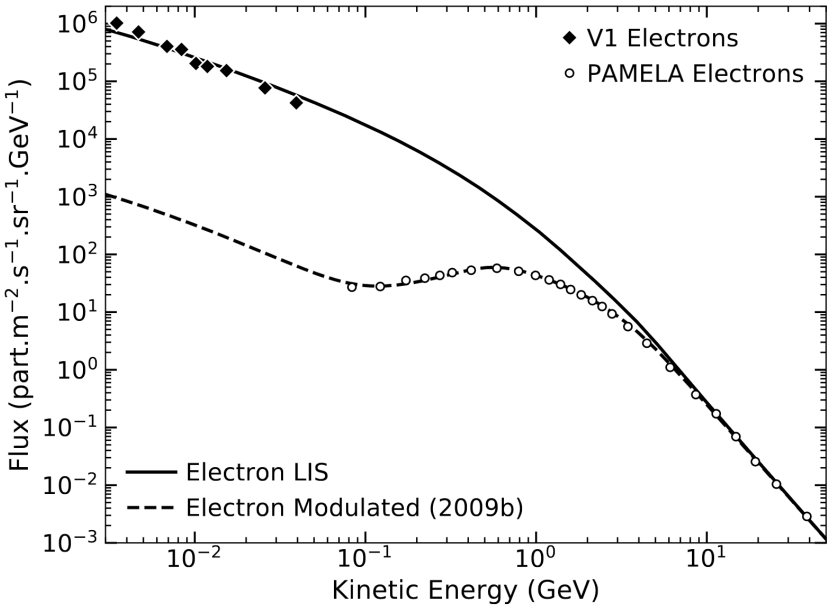

Figure 7.3: Computed electron LIS and modulated electron spectrum at Earth. From Bisschoff et al. [55].

$e^{\pm}$ spectra. It is there shown that the turbulent component of the GMF dominates over the regular component for the desired setup. Hence, we consider only the turbulent component of the GMF in this section as well. The model also assumes a diffusive halo, and we define its effective scale height z_t, such that the diffusion coefficient scales as

$$D(z)^{-1} \propto \exp\left(-\frac{|z|}{z_t}\right). \tag{7.1.5}$$

The values of z_t in kpc considered by [58] are $\{1, 2, 4, 8, 16\}$ and we will proceed with the same values. Furthermore, from the same article, the magnetic field strength B of the random component scales with $D(z)^{-1}$. However, from Sec. 6.3, we know that this implies turbulence with an energy spectrum with $\gamma = 1$, i.e. not Kolmogorov turbulence. Upon using the `ELMAG` program, this must therefore be taken into consideration as γ is an input parameter. We can now define our magnetic field scaling function as

$$f(z) = \exp\left(-\frac{|z|}{z_t}\right). \tag{7.1.6}$$

As for the scaling of the number density of electrons, we consider the vertical profile with

$$g(z) = \exp\left(-a\frac{|z|}{z_t}\right), \tag{7.1.7}$$

where we set the constant $a = 2$ in our simulations. This profile can be seen in Fig. 7.4, which corresponds to an approximation of the vertical profile in the article by [58], that is the bottom panel of their figure 5.

Furthermore, [58] provides a normalisation for the RMS magnetic field strength in terms of the scale height. For B_{rms} in μG and z_t in kpc, we use that

$$B_{\text{rms}} = \sqrt{\frac{148.06}{z_t} + 19.12}. \tag{7.1.8}$$

The set of scale heights considered along with their corresponding approximate values of B_{rms} are given in Tab. 7.1. For smaller scale heights, the intensity observed at Earth should decrease

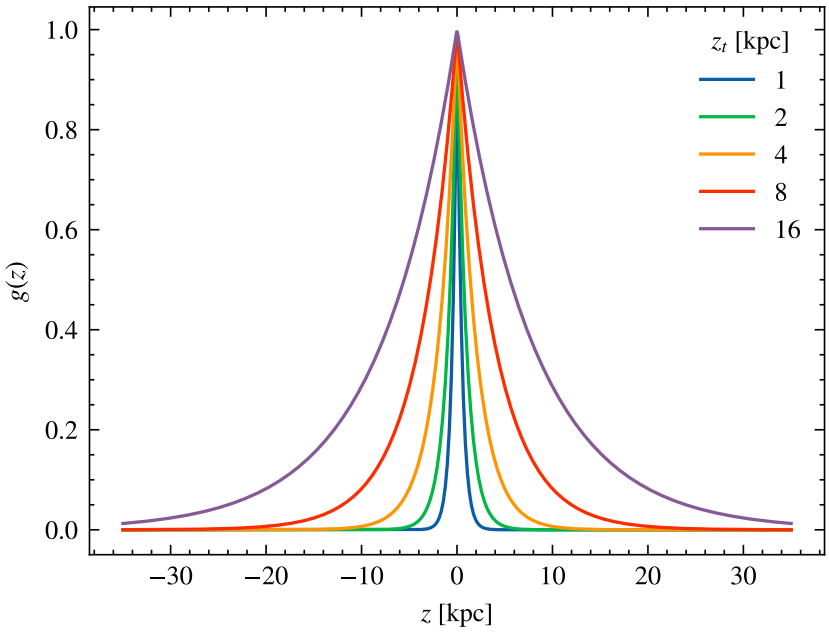

Figure 7.4: Scaling function $g(z)$ for the electron number density in terms of the vertical distance z.

as we get less contribution for larger distance z. However, as is clear from the normalisation of B_{rms}, the magnetic field strength increases in this case, which should assure that the intensity also increases due to a larger contribution of intensity at each point along z.

Table 7.1: Approximate normalisation values for the RMS magnetic field strength B_{rms} given the scale height z_t.

Scale height z_t [kpc]	Magnetic field strength B_{rms} [μG]
1	12.93
2	9.65
4	7.49
8	6.13
16	5.33

7.1.3 Intensity latitude profiles

With the normalisation from the previous section, we now have all the necessary parameters to perform the LoS integral over intensities. We will look at the latitude profile of the synchrotron emission, and compare with figure 7 of [58]. We consider the latitude to be 0° in the centre of the disk of the Galaxy, 90° in the direction $\hat{\mathbf{z}}$ and −90° in the direction $-\hat{\mathbf{z}}$. Our intention is to calculate the intensity received at Earth for different latitudes, that is different line-of-sights. It is therefore important to distinguish the z-value in the scaling functions $f(z)$ and $g(z)$ to the s-value of the LoS. It is clear the intensity along the LoS where $z = 0$ will keep increasing with distance, as there is no scaling into the Galactic disk. The result of the LoS integral in the central region, around latitude 0°, is not accurate. As in [58], we will therefore exclude the region of latitudes $[-10°, 10°]$. The result is given in Fig. 7.5a for the different values of the

scale height z_t. The frequency is chosen as $\nu = 408\,\mathrm{MHz}$ and the integral is performed over a distance of 50 kpc. The plot does not show the intensity I_ν, but $T \times \nu^{2.5}$ in units of $\mathrm{K\,MHz^{2.5}}$, however we will still call the plots "intensity" latitude profiles in the following. The conversion to temperature is done using the Rayleigh-Jeans law,

$$T = \frac{I_\nu c^2}{2\nu^2 k_B}, \tag{7.1.9}$$

where k_B is Boltzmann's constant and c is the light speed as usual. The number of turbulent modes is $n_k = 100$, and the correlation length L_c is chosen to be 2×10^{-3} pc, which is very small. We note however that smaller correlation lengths only ensure the smoothness of the lines, it will not change the overall tendency.

The result in Fig. 7.5 also shows the radio data with uncertainties taken from figure 7 of [58]. These data are derived from [59] which provides a global sky model of the diffuse Galactic radio emission. At 408 MHz, this data is in turn derived from the Haslam map [60]. Comparing Fig. 7.5a with figure 7 of [58], we see that our result resembles theirs, but our temperature, and hence intensity, is smaller by approximately one order of magnitude. The overall shape of the latitude profiles correlate well, however there is a wider spread in intensity over scale heights in our results. The differences could be due to the different models used in [58] and this thesis, but the choice in parameters and normalisation should be the biggest uncertainty. In particular, the intensity is proportional to the normalisation constant n_0, and it is clear that increasing this parameter will shift the latitude profiles vertically in the plot.

Choosing a power-law with a slightly less steep slope of $p = 2.8$ and the same number density normalisation constant as before gives the result of Fig. 7.5b. The plot demonstrates the sensitivity to the parameter p, as the intensity is now in a range closer to that of the results in [58] as well as the radio data. When performing the normalisation on the AMS-02 data, we know that our fit is not accurate for the low-energy electrons and positrons around $10^9 - 10^{10}$ eV. To assume the spectrum is more accurately modelled by a power-law with a less steep slope as indicated by Fig. 7.3 is therefore reasonable.

7.2 Regular fields

We will now consider the regular fields from the `UF23` model described in Sec. 2.5.2, and look at both the polarisation degree as well as intensity. In all the simulations we assume that the Earth is located at the coordinates $x = -8\,\mathrm{kpc}$ and $y = z = 0$.

7.2.1 Polarisation

The regular fields from `UF23` do not contain any turbulent field, and we expect that this leads to high polarisation degrees. This is seen in Fig. 7.6. As the circular polarisation degree contributes little to the total degree of polarisation, we consider here only the degree of linear polarisation. In Fig. 7.6a, the particle distribution index is $p = 2.98$ and in Fig. 7.6b it is $p = 2.8$. The plots show the contribution to the linear polarisation degree considering LoS integrals over lengths z on the x-axis. The magnetic field is zero beyond approximately 30 kpc in the `UF23` models, and hence the polarisation degree stays constant for any distance larger than this. We see that the polarisation degree decreases slightly with the particle distribution index p, however the linear polarisation is very high.

7.2.2 Intensity latitude profiles

Using the same normalisation constant $n_0 = 2.74 \times 10^{-5}\,\mathrm{cm^{-3}}$ as before, we set the value of the electron number density constant along z, that is $n(z) = n_0$. Using the models of `UF23`, we get

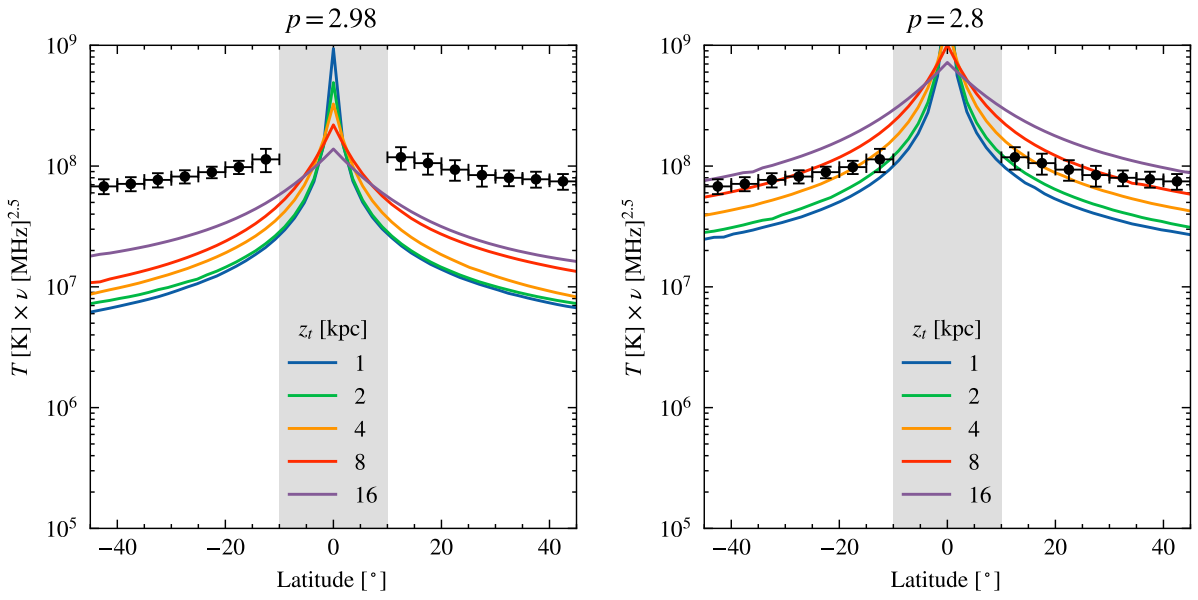

Figure 7.5: Latitude profiles of synchrotron emission for different scale heights z_t, with normalisation taken from the AMS-02 fit, with (a) particle distribution index $p = 2.98$ and (b) a reduced particle distribution index of $p = 2.8$. The electron number density normalisation constant is $n_0 = 2.74 \times 10^{-5}\,\mathrm{cm}^{-3}$ and the frequency is $\nu = 408\,\mathrm{MHz}$.

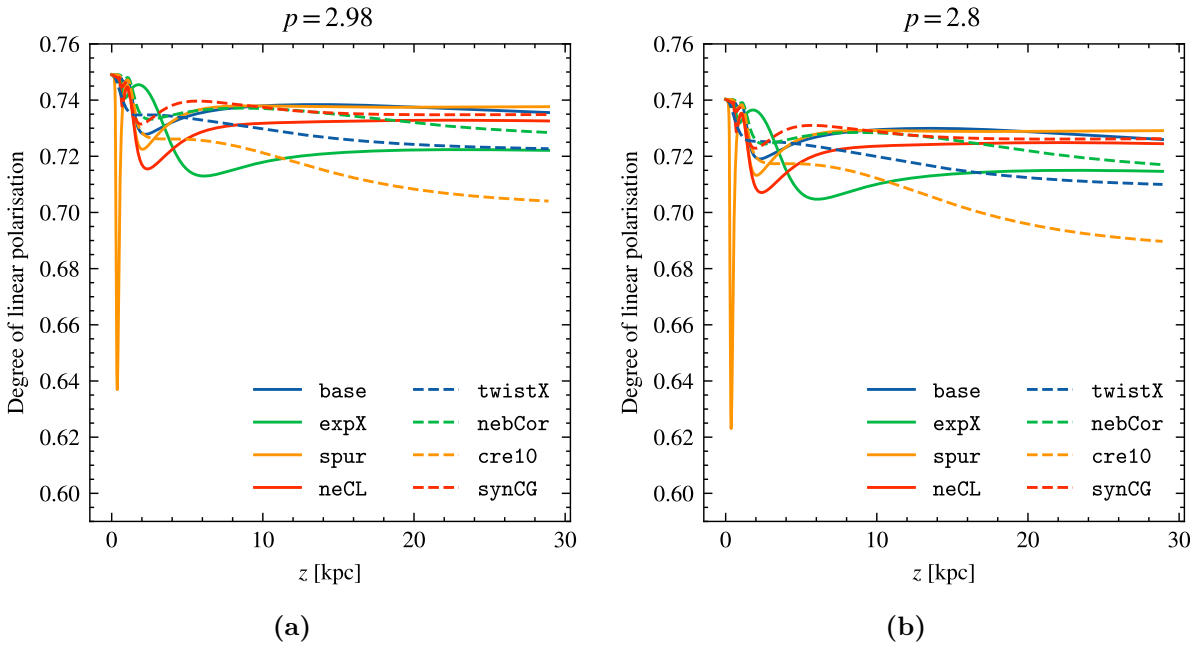

Figure 7.6: Degree of linear polarisation for the eight different regular magnetic field models of `UF23` for (a) particle distribution index $p = 2.98$ and (b) a reduced particle distribution index of $p = 2.7$. The frequency is $\nu = 408\,\mathrm{MHz}$.

intensity latitude profiles as shown in Fig. 7.7 for the particle distribution indices $p = 2.98$ and $p = 2.8$. Compared with the radio data, we see that the intensity in both cases is much too low using only the regular fields. It is also clear that a non-constant and decreasing electron

number density will further decrease the intensity, but we note that decreasing p or increasing n_0 will lead to an increase in the intensity.

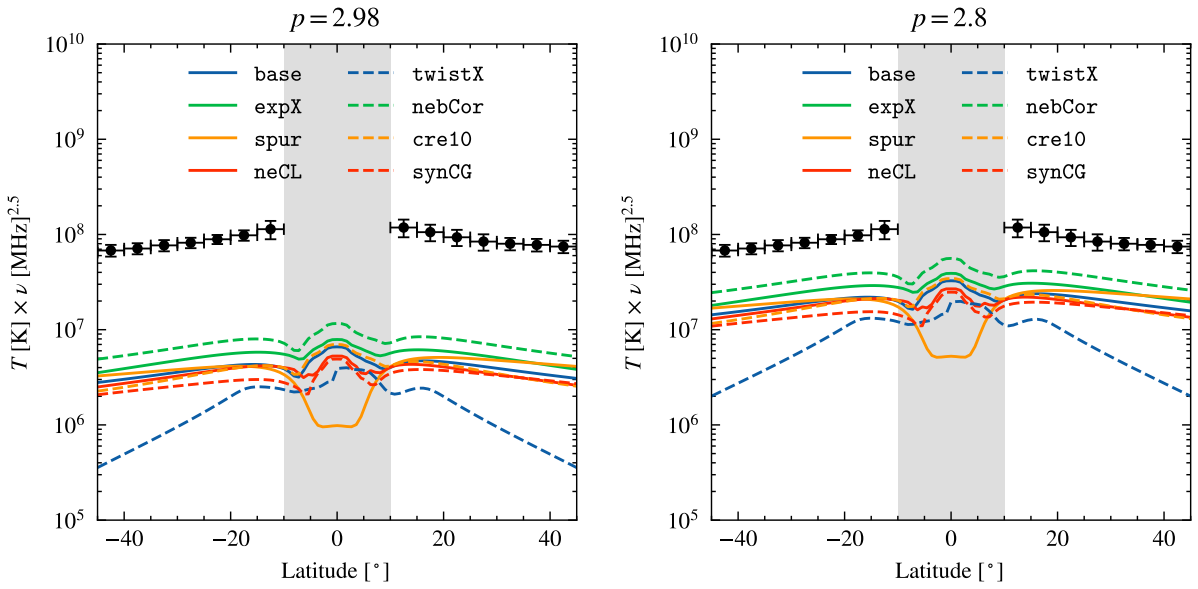

Figure 7.7: Latitude profiles of synchrotron emission for the eight different regular field models of `UF23` for (a) particle distribution index $p = 2.98$ and (b) a reduced particle distribution index of $p = 2.7$. The electron number density normalisation constant is $n_0 = 2.74 \times 10^{-5}\,\mathrm{cm}^{-3}$ and the frequency is $\nu = 408\,\mathrm{MHz}$.

7.3 Combination of `ELMAG` and `UF23`

The combination of the models from `ELMAG` and `UF23` was described in Sec. 2.5.3. We will now look at the polarisation degree and latitude profiles of the resulting fields.

7.3.1 Polarisation

For the combination the turbulent fields generated by `ELMAG` and regular fields generated by the eight models of `UF23`, we find the mean degree of linear polarisation for different values of β and p using the LoS integral along $\hat{\mathbf{z}}$. The results are summarised in Tab. 7.2 for a selection of parameters. The polarisation values are calculated by taking the average of the linear polarisation degree for $N = 10^4$ independent runs for each of the eight models. As usual, the circular polarisation degree is negligible.

As an example, the `base` and `expX` models are taken with $\beta = 0.5$ and $p = 2.8$, giving the plots for the linear polarisation degrees in Fig. 7.8. Here, we have included the confidence intervals 1σ and 2σ, as each realisation of the turbulent field gives different magnetic fields. That is, for the N runs, about 68% lies within the darker shaded region and 95% lies within the lighter shaded region. In all the simulations, we have chosen the frequency $\nu = 408\,\mathrm{MHz}$, the number of turbulent modes $n_k = 1000$ and the correlation length $L_c = 20\,\mathrm{pc}$ of the turbulent component.

Recall that we defined the parameter β to be the fraction of turbulent to regular magnetic field strength, and expect a realistic model of the GMF to have β in the range 0 to a value not much larger than 1 to preserve the large-scale regular field structure. However, the results show much too high polarisation degrees in any of the cases in Tab. 7.2. It is clear that increasing β or decreasing the particle distribution index p implies a decrease in Π_{lin}, but no combination of

Table 7.2: Mean degree of linear polarisation for the combination of ELMAG and the eight models of UF23 for different values of β and p. All simulations have frequency $\nu = 408\,\mathrm{MHz}$, number of turbulent modes $n_k = 1000$ and correlation length $L_c = 20\,\mathrm{pc}$.

Parameters		Degree of linear polarisation							
β	p	base	neCL	expX	spur	cre10	synCG	twistX	nebCor
0.5	2	0.52	0.55	0.54	0.56	0.45	0.56	0.49	0.49
0.5	2.4	0.56	0.58	0.56	0.59	0.51	0.59	0.55	0.54
0.5	2.8	0.59	0.6	0.59	0.61	0.55	0.61	0.58	0.58
1	2	0.3	0.32	0.31	0.34	0.24	0.35	0.28	0.27
1	2.4	0.33	0.35	0.34	0.37	0.29	0.37	0.33	0.32
1	2.8	0.37	0.38	0.36	0.39	0.33	0.39	0.36	0.35
1.5	2	0.18	0.19	0.18	0.21	0.14	0.21	0.17	0.16
1.5	2.4	0.2	0.22	0.21	0.23	0.18	0.23	0.20	0.19
1.5	2.8	0.23	0.24	0.23	0.24	0.2	0.25	0.23	0.22
10	2.0	0.1	0.09	0.09	0.09	0.09	0.09	0.1	0.1
10	2.4	0.11	0.11	0.1	0.1	0.11	0.11	0.11	0.11
10	2.8	0.12	0.12	0.12	0.12	0.12	0.12	0.12	0.12
100	2	0.1	0.1	0.1	0.09	0.1	0.1	0.1	0.1
100	2.4	0.11	0.11	0.11	0.11	0.11	0.11	0.11	0.11
100	2.8	0.12	0.12	0.12	0.12	0.12	0.12	0.12	0.12

variables in the realistic range produce average polarisation degrees lower than 0.1. It should be kept in mind that a larger turbulent component will increase the uncertainties and widen the 1σ and 2σ intervals.

We also included large values of β, specifically $\beta = 10$ and $\beta = 100$, in Tab. 7.2. Very high values of β means the magnetic field strength of the turbulent component is very large, and the regular field may be neglected. However, since we have a set correlation length and a field that is zero beyond approximately 30 kpc, we still do not expect that the polarisation degree approaches zero. We see that the mean polarisation degree stabilises at values around 0.1 for the given parameters. Therefore, in addition to being unrealistic, larger values of β does not necessarily solve the issue with the low measured polarisation degrees.

7.3.2 Intensity latitude profiles

Seeing that the polarisation degree is too high for the combination of ELMAG and UF23, we know that it not sufficient as a description of the GMF. Nevertheless, we still look into the intensity latitude profiles.

The addition of a turbulent field component to the regular field, should amount to an addition of intensity along the LoS. This is because we are adding the term $s(\mathbf{x})\mathbf{B}_{\texttt{ELMAG}}(\mathbf{x})$ in Eq. (2.5.8), increasing the total field strength. Taking the average of 100 simulations for the combined field with the base and expX models for different values of β gives the results in Fig. 7.9. We have

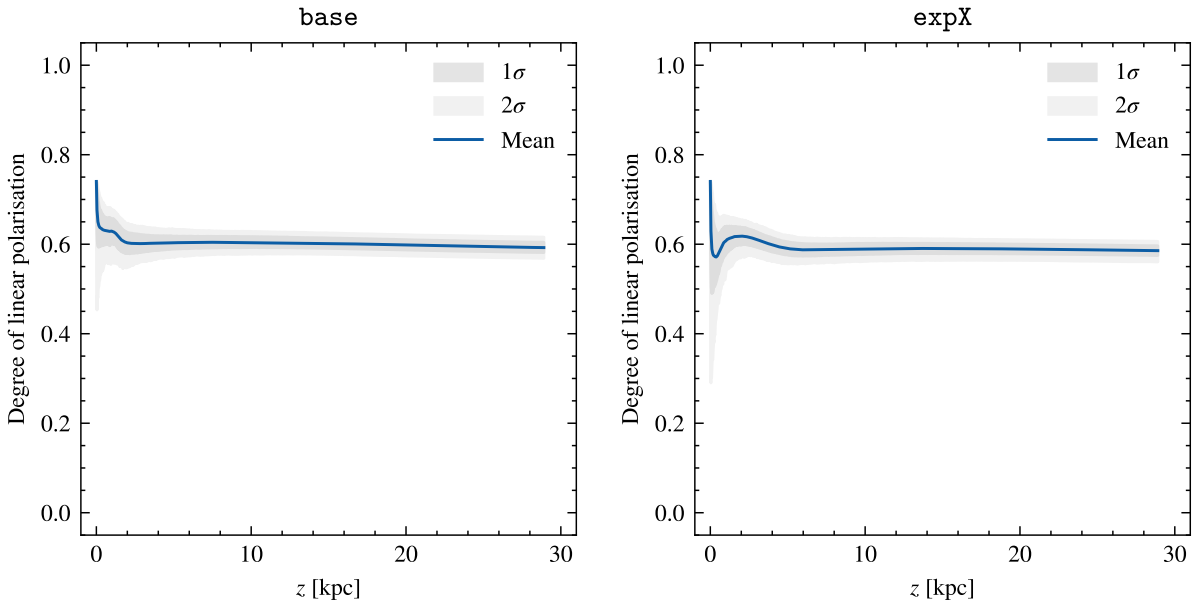

Figure 7.8: Mean degree of linear polarisation for the combination of `ELMAG` and the regular magnetic field models (a) `base` and (b) `expX` of `UF23` with confidence intervals 1σ and 2σ, given $\beta = 0.5$ and $p = 2.8$. The frequency, number of turbulent modes and correlation length is $\nu = 408\,\mathrm{MHz}$, $n_k = 1000$ and $L_c = 20\,\mathrm{pc}$, respectively.

used the particle distribution index $p = 2.8$, the frequency $\nu = 408\,\mathrm{MHz}$ and the correlation length $L_c = 20\,\mathrm{pc}$. For $\beta = 0$, we get the same regular field latitude profiles as in Fig. 7.7, while increasing the parameter β increases the intensity. The shape of the profiles do not change significantly as we are taking the average of many simulations. For a single simulation, we might get more skewed profiles depending on the behaviour of the turbulent field.

For the given parameters, we need very high values of β to get intensity profiles in the region of the physical data. Hence, high values of β are required both for realistic polarisation degrees and intensity profiles.

7.4 Simplified total field model

It is clear from the previous section that by combining the turbulent magnetic field model of `ELMAG` and the regular magnetic field models of `UF23`, we were not able to produce satisfactory fields for the polarisation of synchrotron radiation. We intend to investigate a possible simplified magnetic field model to see for which geometry and set of parameters we can reproduce the expected intensity latitude profiles and low polarisation degrees.

From the discussion of the different components of the GMF in Sec. 2.1, we will assume the Galaxy is divided into three regions; the disk, halo and corona. The magnetic field in the disk and corona will be assumed to be random, where the strength should be stronger in the disk. In the halo we will assume a coherent field that is near uniform except for some small fluctuations.

As a starting point, we will consider the setup defined by Tab. 7.3. For each component, the size in the z-direction is denoted by l such that the total size of the Galaxy becomes $l_{\mathrm{tot}} = l_{\mathrm{disk}} + l_{\mathrm{halo}} + l_{\mathrm{corona}}$. Each component has a different correlation length L_c, where the halo field correlation length is the same as the halo size l_{halo}. The scale heights for both the magnetic field strength and the electron number density are also included in the table. In the

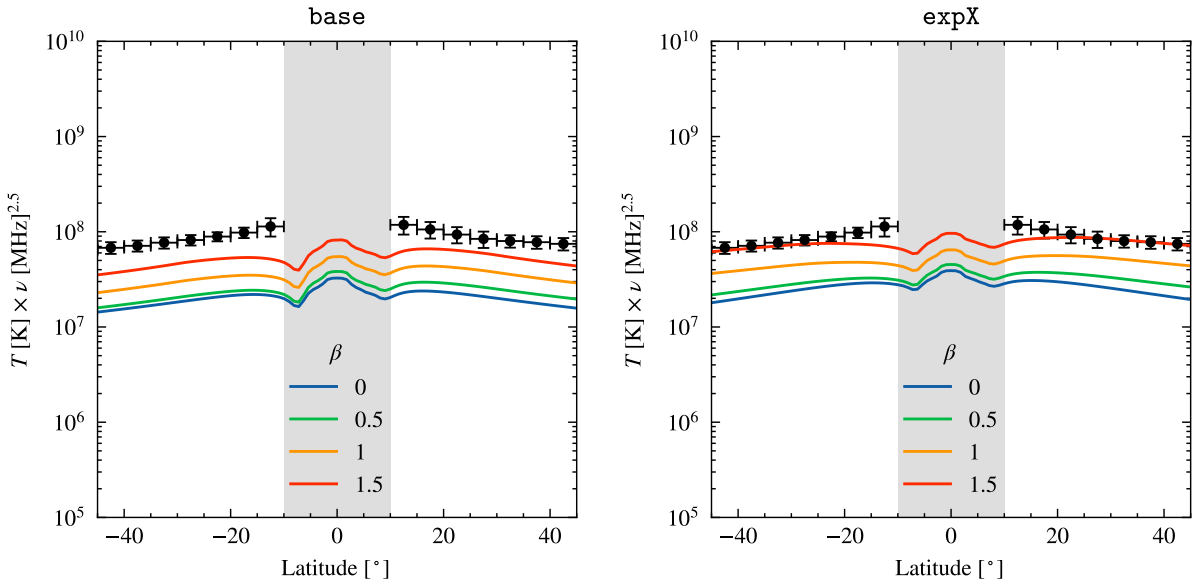

Figure 7.9: Latitude profiles of synchrotron emission for the combination of `ELMAG` and the (a) `base` and (b) expX model of `UF23` for different values of β. The particle distribution index is $p = 2.8$, the frequency is $\nu = 408\,\mathrm{MHz}$, the number of turbulent modes $n_k = 1000$ and the correlation length is $L_c = 20\,\mathrm{pc}$.

disk we assume that the magnetic field is constant with $B_0 \equiv 4\,\mu\mathrm{G}$. The field then decreases outwards once $z > l_{\mathrm{disk}}$, with a minimum value of $B_{\mathrm{min}} \equiv 0.5\,\mu\mathrm{G}$. That is, once the magnetic field reaches this value for some z_*, we keep it constant for $z > z_*$. We assume that the electron number density decreases with a constant scale height $z_{t,n}$ throughout the entire Galaxy, with a minimum value of $n_{\mathrm{min}} = n(z_c)/n_0 = 0.1$.

Table 7.3: Setup for the simplified total magnetic field model, including the size, correlation length and scale heights of the different components of the GMF.

Component	l [kpc]	L_c [kpc]	$z_{t,B}$ [kpc]	$z_{t,n}$ [kpc]
Disk	0.2	5×10^{-3}	∞	5
Halo	10	10	5/3	5
Corona	250	50×10^{-3}	5/3	5

We recall Eq. (6.3.17), and using the scale height $z_0 = z_{t,n}$ and normalising the equation gives

$$\frac{n(z)}{n_0} = 1 + \frac{j_0 z_{t,n}}{D_0 n_0}\left[\exp\left(-\frac{z}{z_{t,n}}\right) - 1\right]. \tag{7.4.1}$$

We approximate the constant

$$\frac{j_0 z_{t,n}}{D_0 n_0} \simeq 2.0. \tag{7.4.2}$$

Upon changing e.g. the electron number density n_0, we will still assume that the constant in Eq. (7.4.2) stays the same, essentially modifying the other parameters accordingly. This is to assure a somewhat realistic electron number density profile that decreases fast outwards from the disk and stays constant at a minimum value once this is reached. The scale height $z_{t,n}$ is still an important parameter, determining the rate of the decrease.

Obtaining Eq. (6.3.17), we made the assumption that the diffusion coefficient D scales with $\exp(z/z_{t,n})$, and we know from Sec. 6.3.1 that $B \propto D^{-1/3}$ for Kolmogorov turbulence. Although we will generate uniform random magnetic field directions, we will still use this relationship, assuming that the turbulence follows a power-law with $\gamma = 5/3$. Therefore, we have that the magnetic field scale height must be $z_{t,B} = z_{t,n}/3$.

To generate an isotropic unit vector for the magnetic field in the disk and corona, one chooses the azimuthal angle uniformly on $[0, 2\pi]$ and the cosine of the polar angle $\cos\vartheta$ uniformly on $[-1, 1]$. Then the magnetic field direction is generated by

$$\frac{\mathbf{B}}{B} = \begin{bmatrix} \sin\vartheta\cos\phi \\ \sin\vartheta\sin\phi \\ \cos\vartheta \end{bmatrix}. \tag{7.4.3}$$

At each step in the halo, which we have assumed to be a regular field, we will take the same angles ϕ and ϑ as the previous step, but introduce some small fluctuations. By denoting the step by k, we choose

$$\phi_{k+1} = \phi_k + \frac{\pi}{6}u, \tag{7.4.4a}$$

$$\vartheta_{k+1} = \vartheta_k + \frac{\pi}{12}v, \tag{7.4.4b}$$

where u and v are random numbers uniformly distributed on $[-1, 1]$. The difference in the factors $\pi/6$ and $\pi/12$ is chosen due to the fact that $\phi \in [0, 2\pi]$ while $\vartheta \in [0, \pi]$.

Upon performing the LoS integral, we will take the step size L_c in the turbulent disk and corona, while in the halo we will choose $L_c/10$. This is because the regular field essentially has infinite correlation length. As we have defined $l_{\text{halo}} = L_{c,\text{halo}}$, we instead take 10 steps within this correlation length to make sure the small fluctuations are included.

In the following, we will consider both polarisation and intensity, as well as Faraday RM. We should keep in mind that over large distances, regular fields should contribute to both intensity and polarisation, while pure turbulent random fields should only contribute to the intensity. As discussed in Sec. 7.1.1, this is because the random magnetic field vectors implies additions in random polarisation directions, and the polarisation degree should decrease as $1/\sqrt{N}$ for $N = z/L_c$. This means that over large enough distances, the regular fields should be dominant component that determines the polarisation degree measured. However, we might get contributions from the turbulent fields in the disk and corona in the case that l_{disk} and l_{corona} are not large enough, given the magnetic field strength and electron number density, or that the scale heights are too small. To obtain low polarisation degrees, we therefore expect that the regular field cannot be too large. In addition, we need to have a combination of the components and parameters that also fits the total intensity. The existence of both a regular and turbulent component of the GMF is therefore expected.

7.4.1 Polarisation

Performing 10^4 independent simulations of the simplified total field model with the initial setup gives the density of polarisation in Fig. 7.10 for three selected particle distribution indices p. The average polarisation is approximately $\Pi = 0.19, 0.17, 0.15$ for $p = 3, 2.8, 2.6$, respectively. For e.g. $p = 2.6$, there is 0% chance for any polarisation greater than 0.23.

For the case of $p = 2.6$, Fig. 7.11 shows the degree of polarisation as function of distance for the whole Galaxy, including the disk, halo and corona, as well as for the region around the division

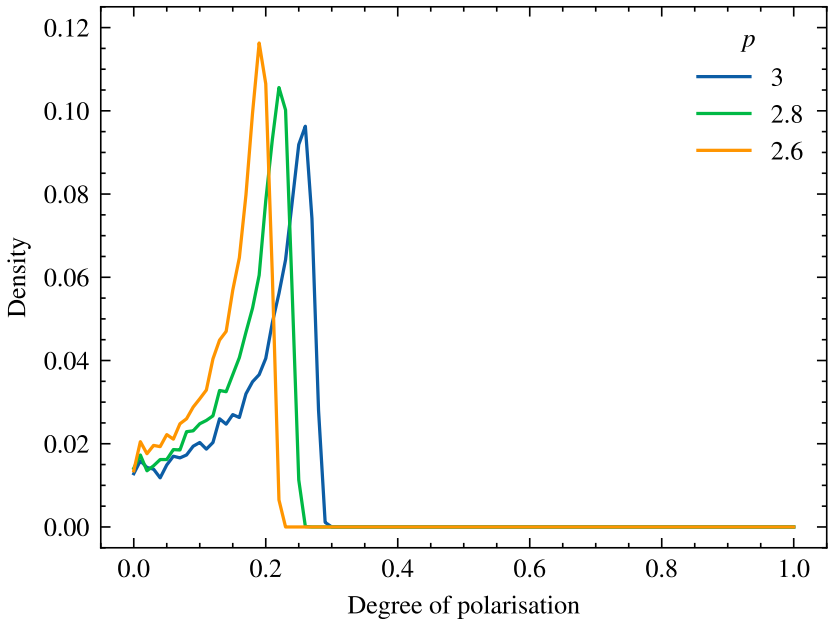

Figure 7.10: Density of polarisation for the simplified total field model for 10^4 independent simulations, for different particle distribution indices. The frequency is $\nu = 408\,\mathrm{MHz}$.

of the disk and halo. The dashed lines indicate the division of the components. At $z = l_{\mathrm{tot}}$, the mean degree of polarisation is approximately 0.15, as we also found earlier this section. The confidence intervals are greater below the mean, which corresponds to the results from Fig. 7.10. At $z = l_{\mathrm{tot}}$ there is no polarisation greater than 0.23 but obtaining a polarisation below the mean, in the range $[0, 0.15]$, is non-zero.

We see the large change in polarisation going from the disk to the halo in Fig. 7.11b. In the disk, the turbulent field gives a decreasing polarisation degree as the magnetic field directions are chosen at random. In the halo, the magnetic field direction is coherent, with small fluctuations. The intensity in almost equal directions are added up, so the decrease is not very fast in this region as the polarisation directions do not cancel each other as effectively. The large "jump" in polarisation degree in the division of the disk and halo is due to their large difference in correlation length L_c. Since the step size in the LoS integral is chosen to be $L_{c,\mathrm{disk}} = 0.005\,\mathrm{kpc}$ in the disk and $L_{c,\mathrm{halo}}/10 = 1\,\mathrm{kpc}$ in the halo, the contribution from the halo will dominate. If we had chosen a smaller step size, the change in polarisation from the disk to the halo should be more smooth.

7.4.2 Relative intensity

From the setup in Tab. 7.3, we have defined the disk to be very thin compared to the halo and corona. However the magnetic field is much stronger and the electron number density much higher in the disk. We wish to investigate the contribution to intensity in the different regions. We know from the polarisation in Fig. 7.11b that there is a significant jump in polarisation from the disk to halo. In Fig. 7.12 we have plotted the relative intensity as function of distance z for some particle distribution indices p. The dashed lines indicate the division of the components of the disk, halo and corona. The plot is made by averaging over the intensity from 10^4 independent simulations, and normalising.

It is clear that around 20% of the intensity is due to the disk field, around $20 - 30\%$ is due to the halo field and the rest is due to the corona field. From our parameters we have that the

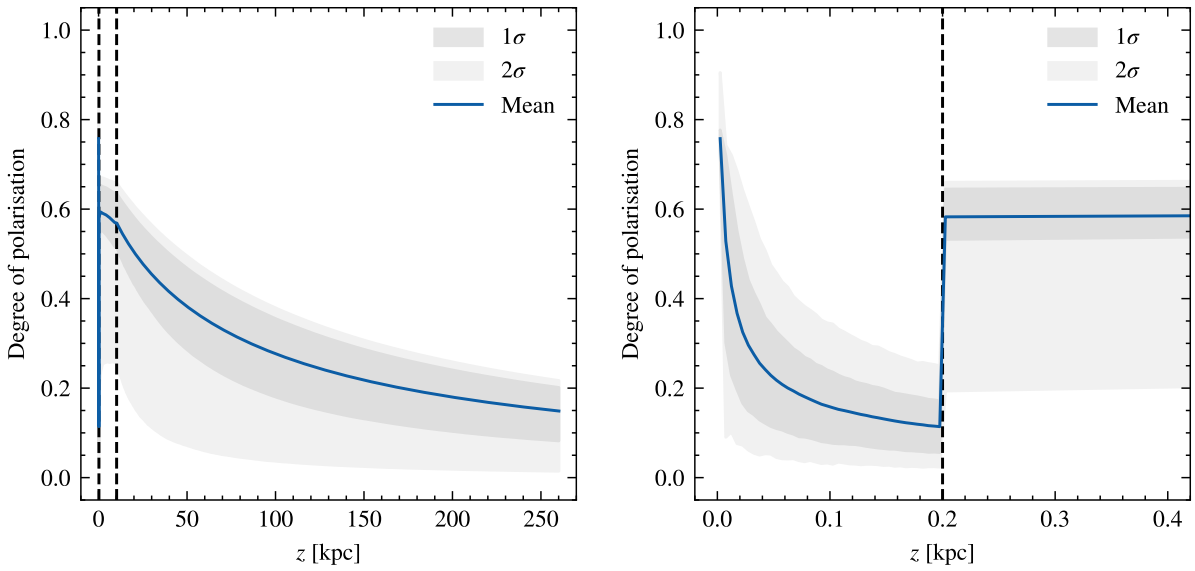

(a) **(b)**

Figure 7.11: Mean degree of polarisation for the simplified total field model for (a) the entire Galaxy and (b) the region around the division of the disk and halo. Confidence intervals 1σ and 2σ are included, and the dashed lines indicate the division of the components of the Galaxy; the disk, halo and corona. The particle distribution index is $p = 2.5$ and the frequency is $\nu = 408\,\mathrm{MHz}$.

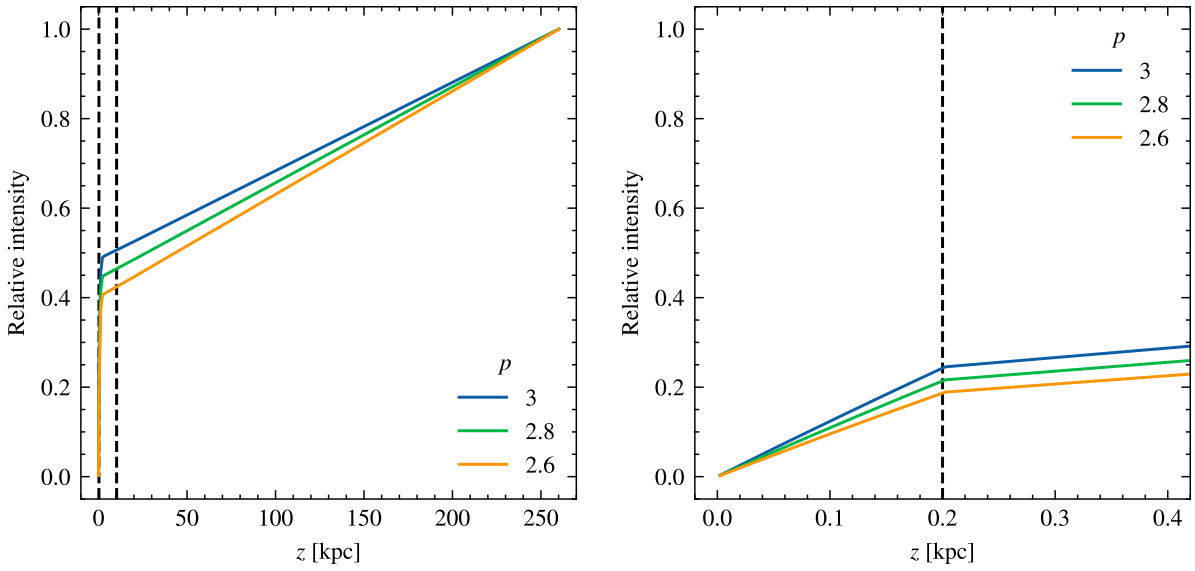

(a) **(b)**

Figure 7.12: Relative intensity for the simplified total field model for (a) the entire Galaxy and (b) the region around the division of the disk and halo, for different particle distribution indices p. The dashed lines indicate the division of the components of the Galaxy; the disk, halo and corona. The frequency is $\nu = 408\,\mathrm{MHz}$.

disk field strength is $B_0 = 4\,\mu\mathrm{G}$. The field then decreases in the halo and corona through

$$B = B_0 \exp\left(-\frac{z - l_{\mathrm{disk}}}{z_{t,n}/3}\right), \tag{7.4.5}$$

for $z_{t,n} = 5\,\mathrm{kpc}$. The magnetic field strength reaches its minimum value $B_{\mathrm{min}} = 0.5\,\mu\mathrm{G}$ at $z_* \simeq 3.7\,\mathrm{kpc}$, and stays constant at B_{min} for all $z > z_*$. From Eq. (7.4.1), the normalised electron number density reaches its minimum value $n_{\mathrm{min}} = 0.1$ at $z_c \simeq 3\,\mathrm{kpc}$ and stays constant at n_{min} for all $z > z_c$. This means that at distances $z > z_* > z_c$, both the magnetic field strength and the electron number density is constant. This leads to the linear increase of the average intensity in the halo and corona in Fig. 7.12a.

7.4.3 Faraday rotation and energy losses

As our model is very simple, we should look into whether or not the model is reasonable with respect to the Faraday RM and the energy loss of ultra-relativistic electrons.

The Faraday RM was defined in Eq. (2.2.2), and performing 10^5 simulations of the RM for the initial setup in Tab. 7.3 with $n_0 = 2.74 \times 10^{-5}\,\mathrm{cm}^{-3}$, gives RMs fairly uniform in the approximate range $[-0.13, 0.13]\,\mathrm{rad\,m}^{-2}$. As an example, three arbitrary initialisations of the magnetic field gives the relative RMs in Fig. 7.13. As to be expected, most of the contribution to the RM comes from the halo where the field is regular. In the turbulent disk and corona, the contributions to the RM from positive and negative values of $B_{\parallel}$ along the LoS should cancel each other out. The argument for the large change in RM from the disk to the halo is the same as that for the polarisation in Fig. 7.11. That is, the step size in the halo is much larger than that in the disk.

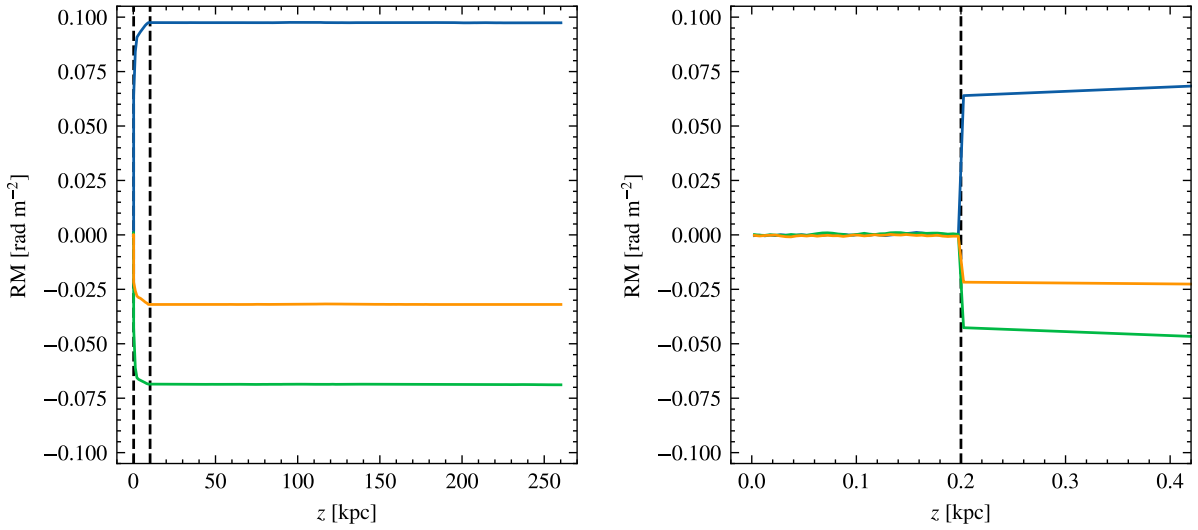

Figure 7.13: Relative Faraday RM for the simplified total field model for (a) the entire Galaxy and (b) the division of the disk and halo, for three arbitrary initialisations of the magnetic field. The dashed lines indicate the division of the components of the Galaxy; the disk, halo and corona.

From Eq. (2.2.1), the extrema $\mathrm{RM} = \pm 0.13\,\mathrm{rad\,m}^{-2}$ give rotation angles $\Phi \simeq \pm 0.07\,\mathrm{rad}$. That is a maximum 4° rotation. This rotation is small enough to assume that we may neglect Faraday rotation effects on our results. From [61] we have that the excess in residual rotation measure (RRM)[3] from nearby galaxies at low frequencies is $|\mathrm{RRM}| \simeq 3.7\,\mathrm{rad\,m}^{-2}$ with uncertainty up to $\pm 1.3\,\mathrm{rad\,m}^{-2}$. This is much higher than our maximum RM, indicating that the model does not produce too high RMs for our Galaxy compared to external galaxies.

[3]The RRM is the RM where the Galactic component has been removed, that is RRM = RM − GRM, where GRM is the Galactic rotation measure. This is the only way to study the RM from extragalactic sources.

Another consideration to make is the energy loss of the ultra-relativistic electrons. The total power emitted by a single particle is given by Eq. (3.2.17). For $\beta \simeq 1$, that is

$$P = -\frac{\mathrm{d}E}{\mathrm{d}t} = \left(\frac{2}{3}\right)^2 r_0^2 c \gamma^2 B^2. \tag{7.4.6}$$

We solve this ODE by integrating over the energy $E = \gamma mc^2$ from E_0 to E, and over the time t from t_0 to t, assuming that the energy at time t_0 and t is E_0 and E, respectively. Hence,

$$\Delta t \equiv t - t_0 = \left(\frac{3}{2}\right)^2 \frac{(mc^2)^2}{r_0^2 c B^2} \left(\frac{1}{E} - \frac{1}{E_0}\right). \tag{7.4.7}$$

This expression is the time t it takes for the particle to loose the energy E given that it has an initial energy E_0. We will consider the half-life $t_{1/2}$ of the electron, that is the time it takes for its energy to be reduced to half the initial energy. Setting $t_0 = 0$ and $E = E_0/2$, this leads to the expression

$$t_{1/2} = \Delta t\,(E = E_0/2) = \left(\frac{3}{2}\right)^2 \frac{mc}{r_0^2 B^2} \frac{1}{\gamma_0}, \tag{7.4.8}$$

for $\gamma_0 = E_0/mc^2$. In Fig. 7.14 we show the half-life in terms of the age of the Galaxy[4] as function of the Lorentz factor γ_0 for given magnetic field strengths. We have included the maximum and minimum magnetic field strength of the simplified total field model $B_0 = 4\,\mu$G and $B_{\min} = 0.5\,\mu$G, corresponding to the disk and most of the corona. Similarly to the analysis leading to the dashed lines in Fig. 7.2 for the energy, we include the Lorentz factor of an electron emitted at the average critical frequency $\langle \nu_c \rangle = 408\,$MHz in dashed lines for the two magnetic field strengths.

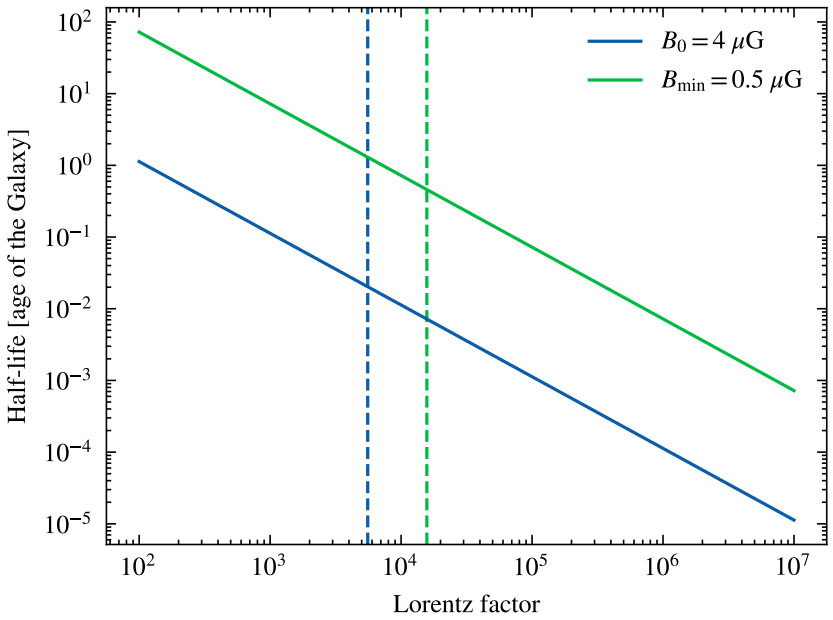

Figure 7.14: Half-life of an electron in terms of the age of the Galaxy as function of the Lorentz factor γ_0, for different magnetic field strengths. The dashed lines indicate the Lorentz factor of an electron with an average critical frequency $\langle \nu_c \rangle = 408\,$MHz in magnetic fields of the same strengths.

Given a power-law distribution of electrons, we assume more electrons with lower energies, or Lorentz factors, than electrons with higher energies. Additionally, in the corona, we expect that

[4] The age of the Milky Way is estimated to be approximately 13.6×10^9 years.

the half-lives of most of the electrons are comparable to the age of the Galaxy as indicated by the intersection of the solid and dashed green lines. As electrons will spend considerable time in the corona, we may therefore proceed by ignoring the effects of energy losses.

7.4.4 Intensity latitude profiles

For the simplified total field model with the setup in Tab. 7.3, the intensity latitude profiles for $p = 2.8$ and $p = 2.98$ are calculated and shown in Fig. 7.15. The same normalisation constant $n_0 = 2.74 \times 10^{-5}\,\mathrm{cm}^{-3}$ for the electron number density is used and the frequency is $\nu = 408\,\mathrm{MHz}$ as usual. We have done the simulation 10^3 times and taken the average of the results. It is clear that the intensity is too low in the considered cases of the particle distribution index, and that the profile needs a slight adjustment to fit the shape of the physical data.

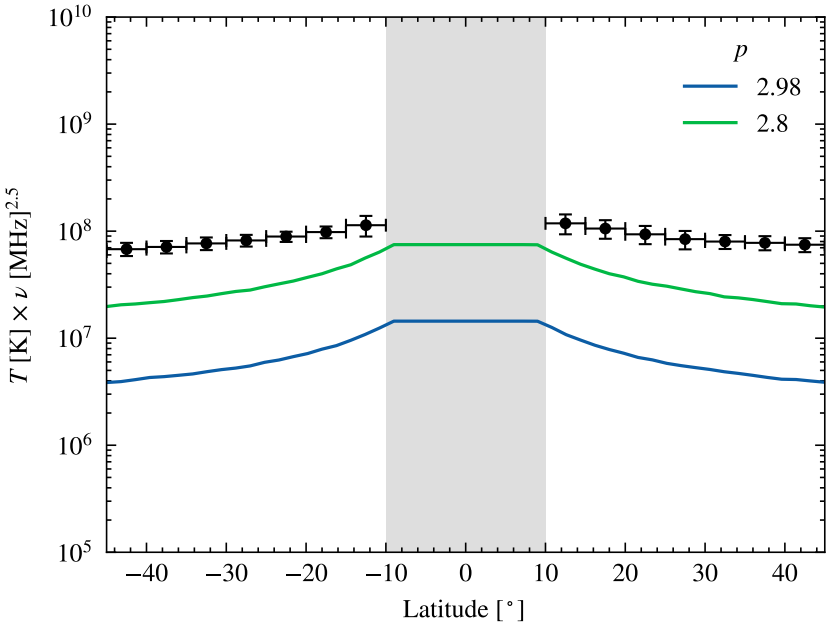

Figure 7.15: Latitude profiles of synchrotron emission for the simplified total field model for two different particle distribution indices. The electron number density normalisation constant is $n_0 = 2.74 \times 10^{-5}\,\mathrm{cm}^{-3}$ and the frequency is $\nu = 408\,\mathrm{MHz}$.

We have a set of free parameters that we wish to optimise to obtain a good fit for the intensity latitude profile. These are given in Tab. 7.4.

7.4.5 Chi-square test

To find a better fit for the parameters in Tab. 7.4, we consider a goodness-of-fit test. The data points provided by [58] contain errors $\sigma_\pm$ at each given latitude. As the errors are asymmetrical, we define σ_+ to be the error in positive intensity and σ_- to be the error in negative intensity. We use the chi-square statistic

$$\chi^2 = \sum_{i=1}^{N} \frac{(O_i - C_i)^2}{\sigma_i^2}, \tag{7.4.9}$$

where

$$\sigma_i = \begin{cases} \sigma_{i,+} & \text{if } O_i - C_i \geq 0, \\ \sigma_{i,-} & \text{if } O_i - C_i < 0. \end{cases} \tag{7.4.10}$$

Each data point is denoted by $i = 1, 2, \ldots, N$, where we have $N = 14$ in our case. The quantity O_i is the observed value of point i, while C_i is the calculated value of this point dependent on

Table 7.4: List of free parameters for the simplified total field model.

Parameter	Symbol
Correlation length of corona	$L_{c,\text{corona}}$
Correlation length of disk	$L_{c,\text{disk}}$
Correlation length of halo	$L_{c,\text{halo}}$
Disk field strength	B_0
Electron number density normalisation constant	n_0
Electron number density scale height	$z_{t,n}$
Magnetic field strength scale height	$z_{t,B}$
Minimum electron number density fraction	n_{min}
Minimum magnetic field strength	B_{min}
Particle distribution index	p
Size of corona	l_{corona}
Size of disk	l_{disk}
Size of halo	l_{halo}

the free parameters. The best fit for our parameters is the case that minimises χ^2. For our application, there is no need to take into account overfitting. We must keep in mind, however, that a good fit for the intensity latitude profiles may give a much too high polarisation.

Effectively we have 13 different variables in Tab. 7.4 to optimise using the chi-square test. However, this is not only computationally heavy, but also of little use, as we are considering a very simplified model based on relatively weak assumptions. We will therefore begin by choosing a subset of the parameters.

Recall that the energy spectrum in Fig. 7.2 bends in the μG range of the magnetic field strength as indicated by the dashed lines. As this is the region we are interested in, we expect a lower normalisation constant n_0. However, the effect of changing the electron number density normalisation constant n_0 amounts to a vertical shift in the intensity profile. We have seen that this is also the case for the particle distribution index p. We will therefore assume that n_0 is constant at the calculated value from the AMS-02 data, that is $n_0 = 2.74 \times 10^{-5}\,\text{cm}^{-3}$, and optimise p accordingly. Furthermore, we assume that the size and correlation length of each component is constant and given by Tab. 7.3, and that we consider a Kolmogorov energy spectrum, which means that $z_{t,B} = z_{t,n}/3$ in the halo and corona.

For our first chi-square test, we assume that both the minimum electron number density $n_{\text{min}} = 0.1$ and the minimum magnetic field strength $B_{\text{min}} = 0.5\,\mu\text{G}$ are constant. This leaves us with three free parameters; p, $z_{t,n}$ and B_0. We choose 7 equally spaced values for $p \in [2.4, 3]$, and 5 equally spaced values for $z_{t,n} \in [2, 6]\,\text{kpc}$ and $B_0 \in [3, 7]\,\mu\text{G}$. At each latitude with data point O_i we average over 10^3 simulations of the intensity to obtain our value for C_i. The chi-square values at each point are added up according to Eq. (7.4.9), and the five best results of the test are summarised in Tab. 7.5. The last column of the table also includes the mean degree of polarisation for the given parameters, calculated by the LoS integral along $\hat{\mathbf{z}}$.

Table 7.5: Chi-square values and mean degree of polarisation for the five best set of parameters for varying p, $z_{t,n}$ and B_0 of the simplified total field model. The parameters $n_{\min}$ and $B_{\min}$ are fixed.

p	$z_{t,n}$ [kpc]	B_0 [μG]	$n_{\min}$	$B_{\min}$ [μG]	χ^2	$\langle\Pi\rangle$
2.7	2	6	0.1	0.5	0.22	0.15
2.7	4	5	0.1	0.5	0.41	0.17
2.7	3	5	0.1	0.5	0.47	0.15
2.7	6	4	0.1	0.5	0.63	0.17
2.7	3	6	0.1	0.5	0.67	0.17

Values of p around 2.7 are clearly favoured for this test. The choice of $z_{t,n}$ and B_0 may vary more, and we see that the best χ^2 value corresponds to a disk field strength B_0 larger than that of the initial guess of 4 μG and an electron number density scale height $z_{t,n}$ smaller than that of the initial guess of 5 kpc. For the three best fits of the parameters, Fig. 7.16 shows the intensity latitude profiles.

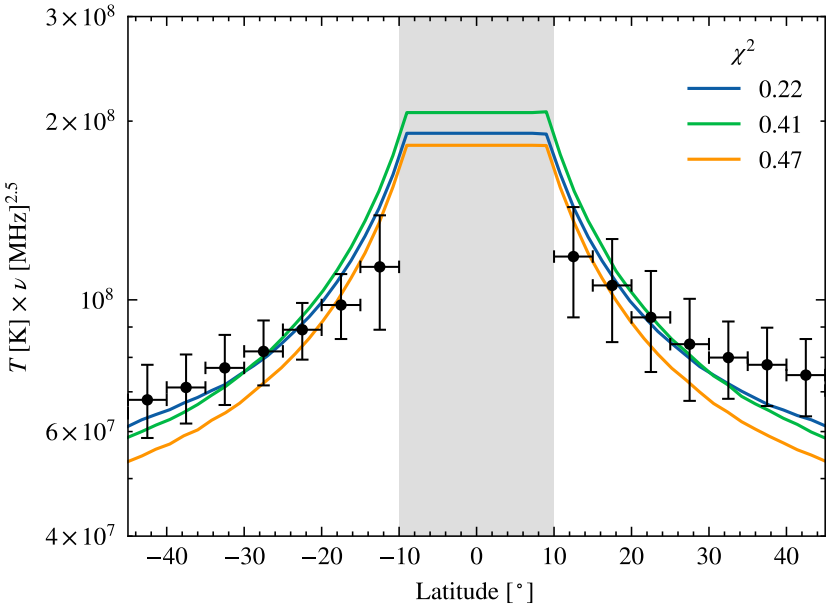

Figure 7.16: Latitude profiles of synchrotron emission for the simplified total field model for the three best results from Tab. 7.5.

We see that the best fits for this model give mean polarisation degrees around 0.16, which is still quite high. We therefore consider the parameters $n_{\min}$ and $B_{\min}$ next. As one would expect low values of the electron number density and magnetic field strength in the corona, we will intend to decrease these values in our model. However, decreasing either of these parameters should increase the polarisation degree and decrease the intensity, due to the smaller contribution from the turbulent corona. On the other hand, from Fig. 7.10 and 7.15 we know that a smaller value of the particle distribution index p corresponds to a higher intensity and lower polarisation. We will therefore fix the disk field strength $B_0 = 6\,\mu$G and the electron density scale height $z_{t,n} = 2$ kpc, and decrease $n_{\min}$ and $B_{\min}$, as well as decrease p.

Choosing 6 equally spaced values for $p \in [2.65, 2.7]$ and $n_{\min} \in [0.05, 0.1]$, and 3 equally spaced values for $B_{\min} \in [0.3, 0.5]\,\mu$G, gives us the results of the chi-square test in Tab. 7.6. In Tab. 7.6a we show the five best intensity latitude fits, while in Tab. 7.6b we have sorted the mean polarisation degree values given that the test yields a chi-square value less than 0.5.

Table 7.6: Chi-square values and mean degree of polarisation for varying p, $n_{\min}$ and $B_{\min}$ of the simplified total field model for (a) the ten best set of parameters and (b) the ten best set of parameters with $\chi^2 < 0.5$ and lowest degree of polarisation. The parameters $z_{t,n}$ and B_0 are fixed.

(a) Sorted by χ^2.

p	$z_{t,n}$ [kpc]	B_0 [μG]	$n_{\min}$	$B_{\min}$ [μG]	χ^2	$\langle\Pi\rangle$
2.66	2	6	0.1	0.1	0.09	0.3
2.66	2	6	0.05	0.1	0.09	0.39
2.66	2	6	0.09	0.1	0.09	0.32
2.66	2	6	0.07	0.1	0.09	0.35
2.66	2	6	0.06	0.1	0.1	0.37
2.66	2	6	0.08	0.1	0.1	0.34
2.66	2	6	0.06	0.2	0.1	0.3
2.66	2	6	0.05	0.2	0.11	0.33
2.67	2	6	0.05	0.3	0.12	0.28
2.67	2	6	0.07	0.3	0.12	0.24

(b) Sorted by $\langle\Pi\rangle$, given that $\chi^2 < 0.5$.

p	$z_{t,n}$ [kpc]	B_0 [μG]	$n_{\min}$	$B_{\min}$ [μG]	χ^2	$\langle\Pi\rangle$
2.69	2	6	0.1	0.5	0.37	0.15
2.69	2	6	0.09	0.5	0.27	0.15
2.7	2	6	0.1	0.5	0.22	0.15
2.69	2	6	0.1	0.4	0.19	0.16
2.7	2	6	0.09	0.5	0.22	0.16
2.67	2	6	0.09	0.4	0.5	0.17
2.68	2	6	0.08	0.5	0.43	0.17
2.69	2	6	0.08	0.5	0.21	0.17
2.68	2	6	0.1	0.4	0.26	0.17
2.7	2	6	0.1	0.4	0.35	0.17

The best parameters for the intensity latitude profiles are those with reduced values of $n_{\min}$ and $B_{\min}$. These fits are very good, and Fig. 7.17 shows the latitude profile for the best case, $\chi^2 = 0.09$. However, the parameters of Tab. 7.6a give high mean degrees of polarisation. From the good fits with $\chi^2 < 0.5$, the lowest polarisation degrees corresponds to values of $n_{\min}$ and

$B_{\min}$ in our defined upper bounds of the test. The test shows that, given the fixed parameters, decreasing the particle distribution index p cannot balance the decrease of $n_{\min}$ and $B_{\min}$ to keep the mean degree of polarisation from increasing. These results point to the existence of a relatively significant corona field in our simple model.

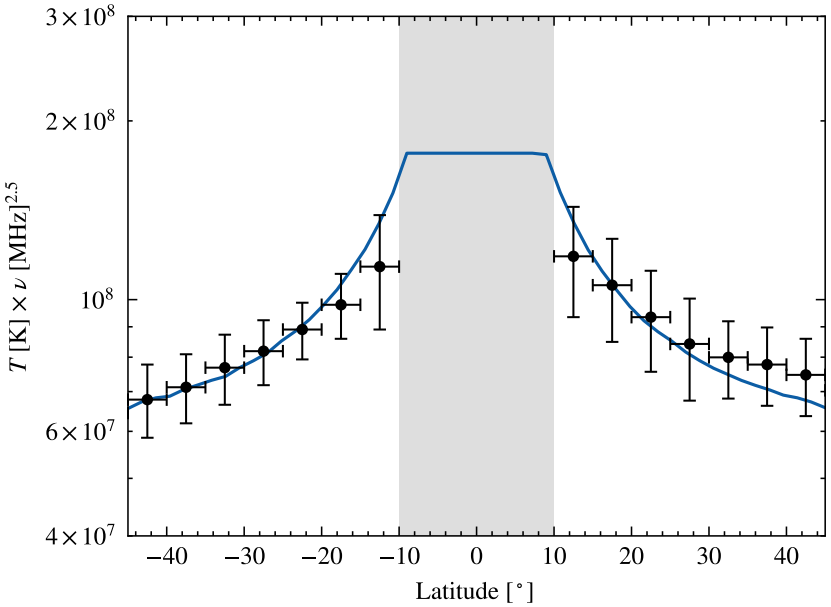

Figure 7.17: Latitude profiles of synchrotron emission for the simplified total field model for the best result from Tab. 7.6a, with a chi-square value of $\chi^2 = 0.09$.

Chapter 8

Discussion

Both from the theoretical part of the thesis, as well as from the numerical simulations, we have presented results that require further comments. We will begin the discussion by considering the polarisation degrees derived in chapter 5, and then move on to the results of chapter 7.

8.1 Theory of polarisation

From Sec. 5.4 there are several points to be discussed. In particular, we wish to further analyse the difference from the single electron case to the power-law electron distribution case, as well as the behaviour of the polarisation degrees for strong magnetic fields.

8.1.1 From a single electron to a power-law electron distribution

As already mentioned in Sec. 5.3, the Stokes parameter j_V for the power-law electron distribution was found to be a factor of $4/3$ off from the derived quantity by Legg and Westfold [12]. For any practical application, the degree of circular polarisation is negligible as argued by [9, 10]. The radiation of the electron will be elliptically polarised when viewed at any angle, however we recall that the radiation of an ultra-relativistic electron is almost completely confined within an angle $\theta \simeq 1/\gamma$. The observed radiation therefore only consists of electrons whose trajectory lies within this angle of the LoS. Considering now a distribution of pitch angles $\phi(\alpha)$, all the electrons contributing to the intensity observed will be elliptically polarised. As long as the pitch angle distribution ϕ varies smoothly with the pitch angle α, the elliptical components will cancel. We will have an equal contribution of emission cones from both sides of the line-of-sight. Therefore, the radiation should be characterised by the degree of linear polarisation. As j_V only appears in the expression for the circular polarisation degree, the factor of $4/3$ should not significantly affect any of our results in chapter 7. As an example, we show the density of linear and total polarisation for the simplified total field model in Fig. 8.1. The linear polarisation degree is clearly dominant in relation to the circular polarisation degree, as it seems to be equal to the total polarisation degree. In fact, the average degree of circular polarisation for this simulation is of the order of 10^{-5}.

It is, however, still interesting to consider the behaviour of the circular polarisation degree. Both the degree of circular and linear polarisation change significantly from the single electron case to the power-law electron distribution case. The circular polarisation degree of the single electron overall *decreases* (Fig. 5.3), while for a power-law electron distribution it *increases* (Fig. 5.4) as function of the magnetic field strength B. Similarly, the linear polarisation degree overall *increases* (Fig. 5.6) for a single electron, while for a power-law electron distribution it stays *constant* (Eq. (5.5.9)) as function of the magnetic field strength B. We would expect

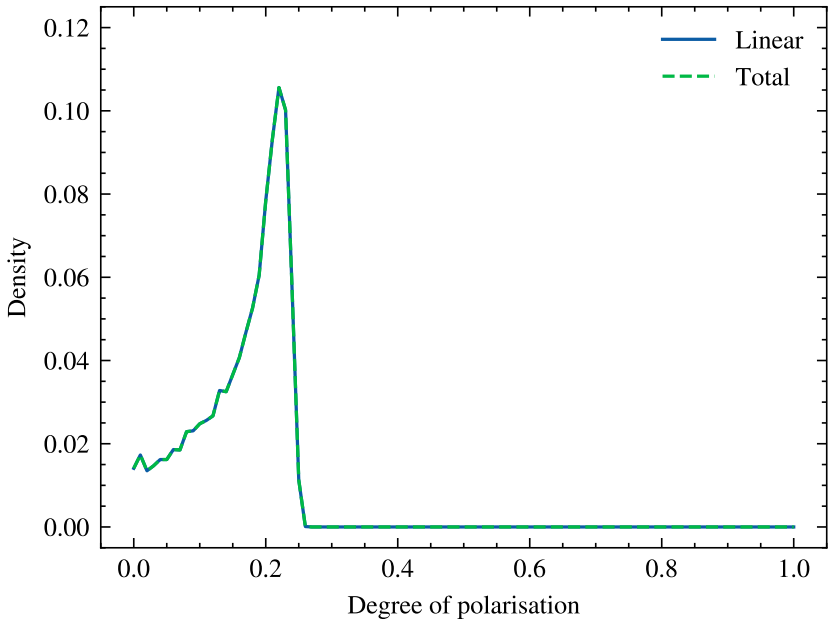

Figure 8.1: Density of linear and total degree of polarisation for the simplified total field model for 10^4 independent simulations. The parameters $p = 2.7$, $z_{t,n} = 2\,\mathrm{kpc}$, $B_0 = 6\,\mu\mathrm{G}$, $n_{\min} = 0.1$ and $B_{\min} = 0.5\,\mu\mathrm{G}$ are chosen, and the frequency is $\nu = 408\,\mathrm{MHz}$.

the same behaviour of the polarisation degrees going from a single electron to a collection of electrons.

One should note the errors that might appear due to the integration over energies. The limits of integration are taken between 0 and ∞ and this energy range may be unrealistic. In general, it is difficult to know the effect of such an approximation, but it should be kept in mind.

Furthermore, from the discussion of the Stokes parameters in Sec. 5.3, we know that the general polarisation tensor $\mathcal{N}$ consists of components of the form $E_i E_j^*$. This structure means the circular polarisation degree can be written as

$$\Pi_{\mathrm{circ}} = \frac{V}{I} = \frac{2\sqrt{uv}}{u+v}, \tag{8.1.1}$$

for some u and v. This is true in the case of $U = 0$, that is $E_1 E_2^* = E_2 E_1^*$. Hence the factor of 2 appears since $V = 2\mathrm{i} E_1 E_2^*$. In the case of the single electron we would have

$$u \equiv C_1 K_{2/3}(z), \quad v \equiv C_2 K_{1/3}(z), \tag{8.1.2}$$

where $z = \frac{1}{2}\theta_\gamma^3 x$ and where we have defined constants C_1 and C_2 that are independent of $x \propto 1/B$. The maximum of Eq. (8.1.1) is 1, which corresponds to the diagonal where $u = v$. The circular polarisation degree is therefore correctly normalised, and Eq. (8.1.1) should hold for any perpendicular and parallel intensity. The form of the equation should not change upon integration over energies, however, this is not true for the integration over pitch angle. In this case we are making an expansion and pick out the even and odd terms in θ. Thus, this procedure violates the form of Eq. (8.1.1). The situation is the same for the degree of linear polarisation. Here, for the same u and v defined above,

$$\Pi_{\mathrm{lin}} = \frac{Q}{I} = \frac{u-v}{u+v}. \tag{8.1.3}$$

This has a maximum of 1 along $v = 0$, and also provides a correctly normalised expression. Upon integration over pitch angle, the form of Eq. (8.1.3) is violated. It is clear that the violations of Eq. (8.1.1) and (8.1.3) might lead to the strange behaviour of the polarisation degrees for a power-law electron distribution. A possible solution should be to evaluate the integral over pitch angle numerically in Eq. (5.2.2) for the emission-polarisation tensor j.

8.1.2 Degree of polarisation for strong magnetic fields

In Sec. 5.4 we found that the degree of circular polarisation for a power-law distribution is proportional to $B^{1/2}$ and therefore exceeds 1 for strong magnetic fields. In Fig. 5.4 we see that this happens for magnetic field strengths around $10^5 - 10^8$ G for the given choices of ψ. We note that values of B in this interval do not correspond to the critical magnetic field in Eq. (4.4.1) which is of the order 10^{13} G, and hence $B \ll B_{\rm cr}$. However, we require $\chi \simeq \gamma B/B_{\rm cr} \ll 1$ to conclude that the change in behaviour is not due to the quantum effects discussed in Sec. 4.4. We can write $\gamma \ll B_{\rm cr}/B$, and for e.g. $B = 10^7$ G, this corresponds to a Lorentz factor $\gamma \ll 10^6$. As B increases, the Lorentz factor have to decrease to satisfy this requirement, and at some point γ will be too small for the electrons to be considered ultra-relativistic. To make an estimate of the Lorentz factor for the parameters in Fig. 5.4, we use the fact that most of the emission happens at the critical frequency $\nu_c = \omega_c/2\pi$ where ω_c is defined by Eq. (4.1.9). This means that

$$\gamma = \left(\frac{4\pi\nu_c mc}{3eB\sin\alpha}\right)^{1/2}. \tag{8.1.4}$$

The Lorentz factor is proportional to $B^{-1/2}$, and will decrease for increasing magnetic field strength. For $\nu_c = 5 \times 10^{14}$ Hz, Fig. 8.2 shows the Lorentz factor γ as a function of magnetic field strength B for different pitch angle deviations ψ. We see that γ decreases with both B and ψ. The figure shows results that are clearly within our requirement that $\gamma \ll B_{\rm cr}/B$, however for ultra-relativistic electrons we expect higher γ-factors for values of B higher than $\sim 10^5$ G. As the electrons no longer stay in the ultra-relativistic regime, we are not considering synchrotron radiation. We may therefore conclude that the results for the circular polarisation degree only are valid for weaker magnetic fields, and not in the region where it exceeds 1.

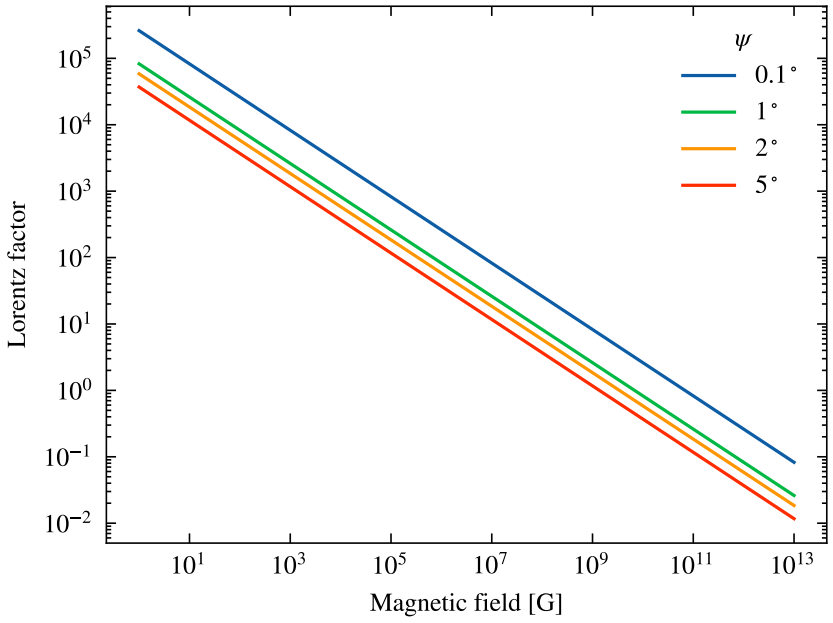

Figure 8.2: Lorentz factor γ as function of magnetic field strength B for different pitch angle deviations ψ. The frequency is $\nu = 5 \times 10^{14}$ Hz.

In appendix B we comment on the proposed solution by [62] of considering the second order pitch angle distribution approximation. The results of that analysis show that the second order approximation does not affect the circular polarisation degree for the valid weaker magnetic field strengths, and is therefore not relevant in the ultra-relativistic synchrotron regime.

8.2 Galactic magnetic field models

The results of the numerical simulations in chapter 7 show the difficulties in describing the GMF by use of numerical models. We may summarise the main results as the following.

(i) The `ELMAG` turbulent field model produces sufficiently turbulent magnetic fields only up to a certain distance dependent on the number of turbulent modes.

(ii) Generating pure turbulent magnetic fields using `ELMAG` can reproduce intensity latitude profiles similar to those in [58], dependent on the electron number density normalisation.

(iii) Neither the `UF23` model nor the combination of `UF23` and the `ELMAG` turbulent field model can reproduce the low polarisation degree values measured by the C-BASS project for realistic parameters. In both cases, the intensity profiles are too low given the calculated electron number density normalisation.

(iv) The simplified total field model may fit the low polarisation degrees as well as the intensity latitude profiles for optimised parameters. There are, however, many free parameters.

8.2.1 `ELMAG` and `UF23`

We start by looking at the first three points concerning the pure turbulent field from `ELMAG` and the combination of `ELMAG` and the `UF23` models.

Number of turbulent modes

The number of turbulent modes n_k for the `ELMAG` turbulent magnetic field model considered in Sec. 7.1.1 has a significant effect on the polarisation degree. We note that the polarisation degree will stabilise at higher values of z for an increase of the particle distribution index p. Furthermore, for increasing number of turbulent modes n_k, the computation time[1] increases linearly as in Fig. 8.3. For each number of modes n_k, one simulation of the turbulent field is done with $L_c = 20\,\mathrm{pc}$, $B_{\mathrm{rms}} = 3\,\mu\mathrm{G}$, $p = 2.4$ and $\nu = 50\,\mathrm{MHz}$.

We do not expect that the number of turbulent modes n_k to significantly influence the intensity latitude profiles, given that n_k is not "too small". As long as we have relatively random field vectors, the averaging over many simulations should make sure that any effects from the number of turbulent modes are unnoticeable. However, this could be looked further into.

The problems with the number of turbulent modes for `ELMAG` may therefore only influence the results of the polarisation degrees, that is Tab. 7.2 and Fig. 7.8 for the total field. Since the magnetic field is zero beyond 30 kpc in the `UF23` models, we know that the distance of the LoS integral should be much larger than the distance where the polarisation degree starts to saturate as shown in Fig. 7.1. However, the magnetic field should also be much weaker at larger distances, and the effect of the number of turbulent modes on the polarisation degree in the combined `ELMAG` and `UF23` model may be minimal, which is what we see from Fig. 8.4. Here we have plotted the degree of linear polarisation for the combined `ELMAG` and `UF23` model `base` with the setup in Tab. 7.2 as function of the number of turbulent modes n_k. The case

[1] We define the computation time as the CPU elapsed time, which is calculated in `Fortran 90` by using the function `cpu_time`.

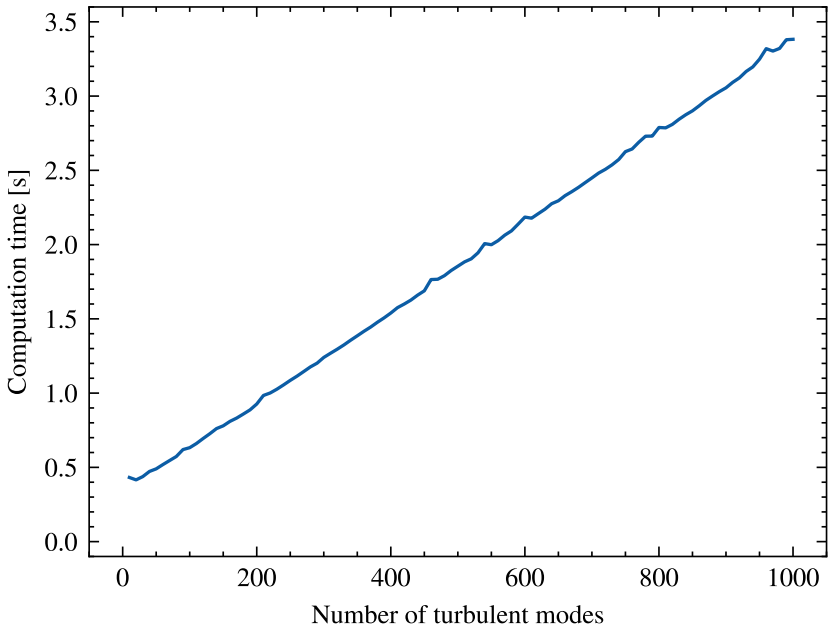

Figure 8.3: Computation time as function of the number of turbulent modes n_k for calculation of polarisation degrees using the `ELMAG` turbulent magnetic field model.

of $\beta = 10$ from Tab. 7.2 is not included as it is approximately the same as for $\beta = 100$. For high values of β, we see that more turbulent modes are required. However, as the polarisation degree approaches a constant value as a function of n_k, the number of turbulent modes should not be an issue for the results in Sec. 7.3. Choosing n_k around 1000 should be sufficient.

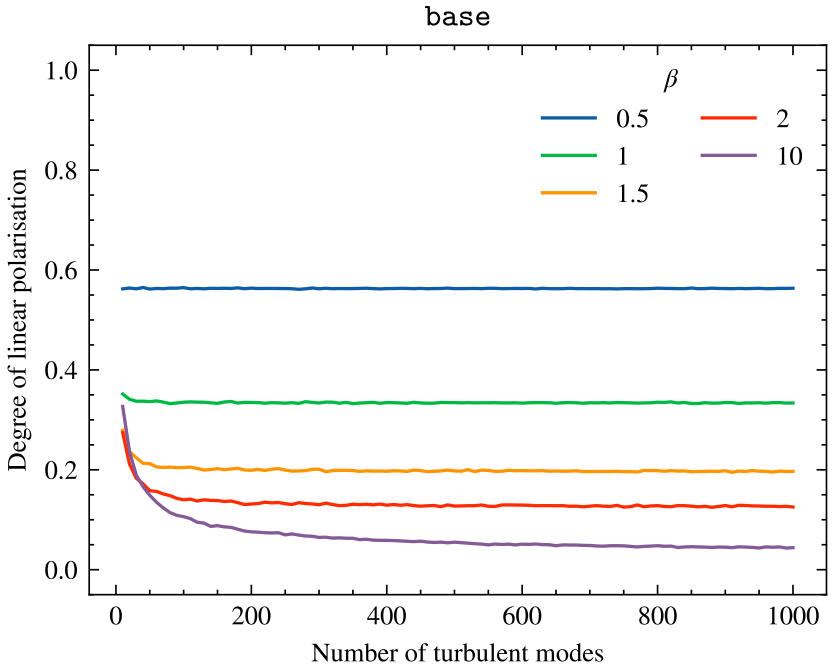

Figure 8.4: Degree of linear polarisation as function of the number of turbulent modes n_k for the combined `ELMAG` and `UF23` model `base` for different values of β. The frequency is $\nu = 408\,\mathrm{MHz}$, the particle distribution index is $p = 2.4$ and the correlation length is $L_c = 20\,\mathrm{pc}$.

Normalisation

The normalisation done in Sec. 7.1.2 gave us the approximate particle distribution index $p = 2.98$ and electron number density normalisation constant $n_0 \simeq 2.74 \times 10^{-5}\,\mathrm{cm}^{-3}$. Upon calculating intensity latitude profiles and polarisation degrees, we have assumed that n_0 is constant at this value, and varied p some small amounts. It is important to keep in mind that these values are the result of a very simple analysis and that we have not considered any uncertainties. Furthermore, we made a power-law fit for high-energy electrons, although for magnetic field strengths in the range $1 - 10\,\mu\mathrm{G}$, the electrons are expected to have energies in the region where the spectrum starts to bend. A more detailed analysis should include uncertainties and take into consideration the bend in the spectrum for low-energy electrons.

We also considered the assumption by [58] that $B \propto D(z)^{-1}$ which corresponds to an energy spectrum with slope $\gamma = 1$. However, in their simulations, [58] have used an Iroshnikov–Kraichnan, or "KRA", setup. As we have mentioned, Iroshnikov–Kraichnan turbulence implies an energy spectrum with slope $\gamma = 3/2$ and not $\gamma = 1$. This inconsistency is not expected to be an issue, as the assumptions of the normalisation are loosely based on the analysis of the stationary case of the diffusion equation discussed in Sec. 6.3.2.

A comment should also be made on the radio data with uncertainties taken directly from [58]. We have not made any attempt to reproduce the analysis leading to these data points, and it may be of interest to take this analysis into consideration. The radio data are derived from [59] which uses the Haslam map [60]. An improved all-sky 408 MHz temperature map from [63] is reconstructed[2] in Fig. 8.5.

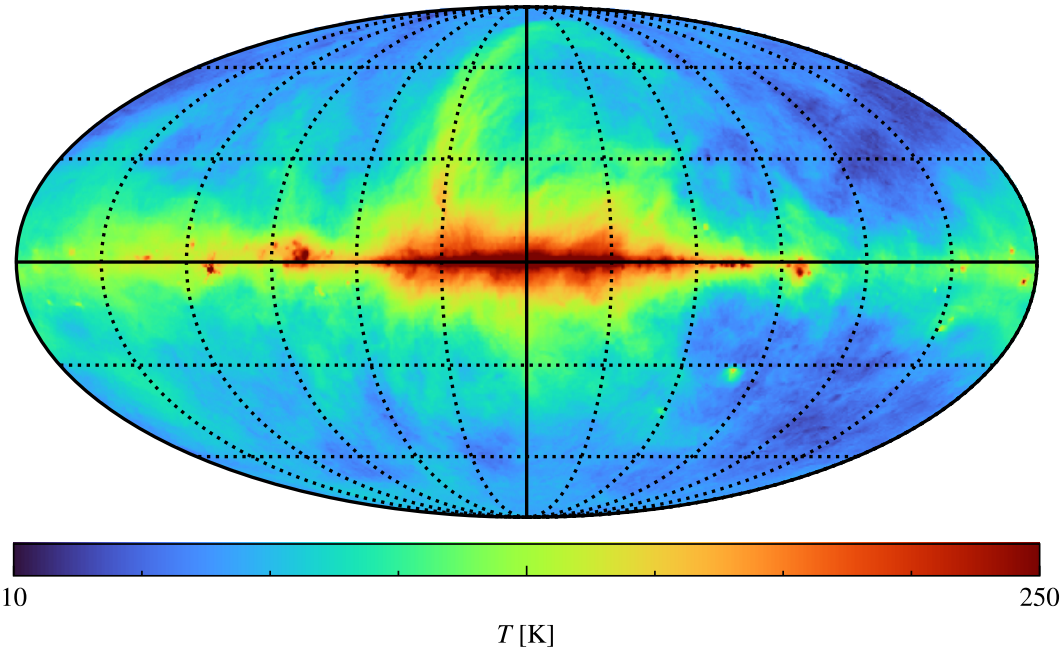

Figure 8.5: All-sky 408 MHz temperature map with a logarithmic colour scale. Constructed from the improved Haslam all-sky map of Remazeilles et al. [63].

To consider the latitude profile of the brightness temperature from the Haslam data, the points along the vertical central line in Fig. 8.5 are extracted. Visualising the latitude profile from the extracted data gives the plot in Fig. 8.6. Here we have also included the radio data from [58], and the plot gives us an indication that the analysis of the article provides data points in

[2]The data is provided in a FITS file, commonly used in astronomy for storing large datasets. This can easily be read using the `HEALPix` framework [64] which provides a structure for the pixelisation of data on the sphere.

some agreement with the all-sky map. The exact analysis of [58] should still be investigated, especially as the data points include uncertainties.

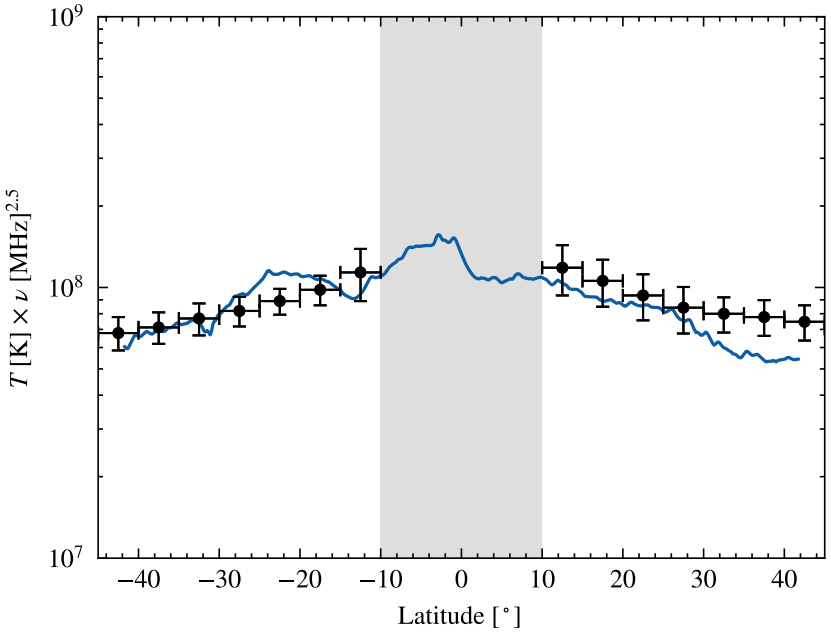

Figure 8.6: Latitude profile of the 408 MHz temperature data along with radio data. Constructed from the improved Haslam all-sky map of Remazeilles et al. [63].

Other uncertainties of the normalisation for the intensity latitude profiles in Fig. 7.5 are the scaling function $g(z)$ and the magnetic field normalisation by [58] in Eq. (7.1.8). We have simply made an approximation to the $g(z)$ profile and as in the article, assumed that the synchrotron spectrum is reproduced by the described setup in Sec. 7.1.2. However, the intensity latitude profiles in Fig. 7.5 indicate that our assumptions and normalisation of the AMS-02 data provides profiles that agree relatively well with the results of [58].

Inconsistency with intensity and polarisation data

We have already seen that we were not able to reproduce the intensity and polarisation data using the `UF23` models or the combination of `ELMAG` and `UF23`. For the polarisation, it is evident that the `UF23` models alone are not sufficient as they describe the large-scale regular GMF and do not include the small-scale turbulent component. Therefore, the polarisation degrees are much too high compared with the results of the C-BASS project. Additionally, the intensity is too low for our given normalisation, but there are several uncertainties around this procedure.

The introduction of a turbulent component using the `ELMAG` turbulent field model gives lower polarisation degrees, however not sufficiently. The results in Tab. 7.2 show that the mean degrees of linear polarisation are still very high. For these simulations, Fig. 8.7 shows the density of linear polarisation for the model `base`, for different values of β. Given $L_c = 20\,\mathrm{pc}$ (solid lines) and $\beta = 2$, which means the turbulent component is twice as strong as the regular component, close to 30% of the simulations give polarisation degrees below 0.1. This is a relatively reasonable result, however $\beta = 2$ is arguably too high considering what one would expect to be realistic. In the case of $\beta = 1.5$, less than 0.5% of the simulations give polarisation degrees below 0.1, and for the last two cases, the percentage is zero. For realistic values of β in the range $[0, 1]$, we would never obtain a polarisation degree low enough to fit the measured data with this model.

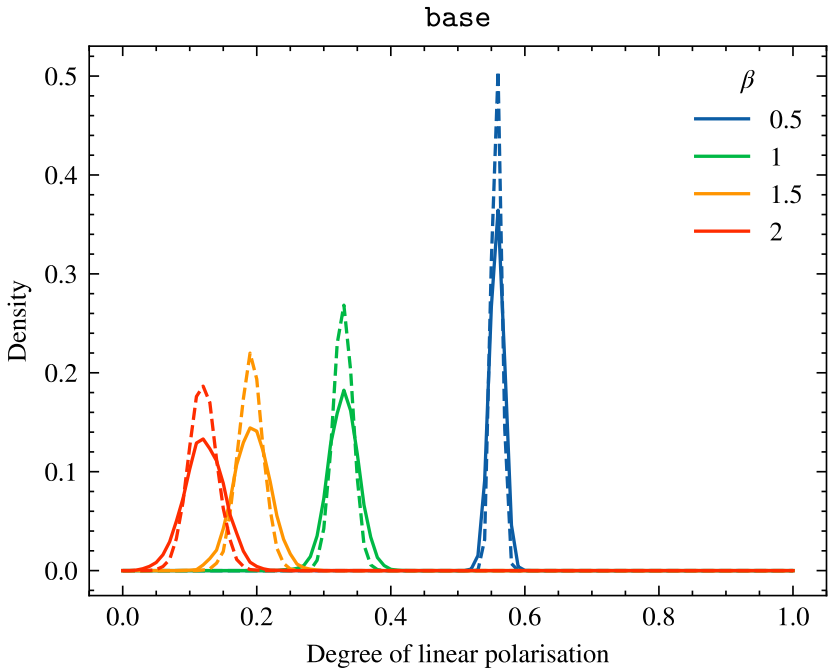

Figure 8.7: Density of linear polarisation for the combined `ELMAG` and `UF23` model `base` for 10^4 independent simulations, for different values of β. The correlation length is $L_c = 20\,\mathrm{pc}$ (solid lines) and $L_c = 2\,\mathrm{pc}$ (dashed lines). The frequency is $\nu = 408\,\mathrm{MHz}$, the particle distribution index is $p = 2.4$ and the number of turbulent modes is $n_k = 1000$.

A comment should be made on the correlation length L_c. In Fig. 8.7 we have also included the case with $L_c = 2\,\mathrm{pc}$ in dashed lines. Upon using the combined field model we have effectively considered a LoS integral with step size L_c, and calculated the Stokes parameters given both the regular and turbulent field at each point. Decreasing the correlation length L_c should therefore not change the mean degree of polarisation, as additional contributions from the turbulent field are balanced by additional contributions from the regular field. However, in this case, we expect that the density is more concentrated around the mean, as can be seen in Fig. 8.7. This is because the number of steps increase for decreasing L_c, and more of the turbulent contributions cancel each other out.

One possible solution to the combined `ELMAG` and `UF23` model is to introduce a turbulent corona field as in the simplified total field model described in Sec. 7.4. Depending on the strength, extent and correlation length of this field, it may reduce the polarisation degree substantially as well as increase the intensity.

8.2.2 Simplified total field model

The simplified total field model produces the magnetic field by using random field vectors, either chosen isotropically or through Eq. (7.4.4). From e.g. the case of $p = 2.8$ in Fig. 7.10, around 20% of the simulations give polarisation degrees lower than or equal to 0.1. For the given parameters, the model therefore implies that in about 20% of cases, we get a choice of magnetic field vectors that will give low polarisation degrees similar to the measured values of the C-BASS project.

The parameters listed in Tab. 7.4, as well as Eq. (7.4.1) along with Eq. (7.4.2) and the assumptions following, are large uncertainties. In particular, we note the value of 2 chosen for

the expression $j_0 z_{t,n}/D_0 n_0$ and the method of generating the regular halo field in Eq. (7.4.4). In both these cases, we have simply made assumptions that "seem" reasonable, but without any further comments or explanations.

By assuming that we may divide the GMF into a disk, halo and corona, we have little detailed knowledge of the most realistic values of the parameters. As we have seen, varying the free parameters in Tab. 7.4 may lead to several possible fits for the intensity latitude profiles. The effect of these parameters on our relevant quantities, the intensity and polarisation, is summarised in Tab. 8.1. Here, "↑" corresponds to an increase in the parameter or quantity, "↓" a decrease and "–" no change. We look at how the intensity and polarisation degree change by increasing each parameter, while keeping everything else constant. It is important to note that this is an average effect on the quantities, and depending on the random magnetic field vectors, the quantities may not behave according to Tab. 8.1 for a single simulation.

Table 8.1: The effect on the intensity and polarisation degree by increasing each value of the free parameters for the simplified total field model.

Parameter	Value	Intensity	Polarisation
$L_{c,\text{corona}}$	↑	–	↑
$L_{c,\text{disk}}$	↑	–	↑
$L_{c,\text{halo}}$	↑[3]	↑	↑
B_0	↑	↑	↑
n_0	↑	↑	–
$z_{t,n}$	↑	↑	↑
$z_{t,B}$	↑	↑	↑
n_{min}	↑	↑	↓
B_{min}	↑	↑	↓
p	↑	↓	↑
l_{corona}	↑	↑	↓
l_{disk}	↑	↑	↓
l_{halo}	↑	↑	↑

The overview in Tab. 8.1 may give us an idea of how the parameters should be varied to fit both the intensity and polarisation. However, as already mentioned, there are many free parameters and consequently many choices that will give reasonable results. We cannot conclude on a single set of parameters as there is not enough information to accurately determine the right choice. Furthermore, we should not forget the simplicity of the model. We cannot expect the model to be anything but an approximation to the structure of the GMF, that may or may not be based on the sufficiently "correct" assumptions.

[3] Increasing $L_{c,\text{halo}}$ in our simulations corresponds to also increasing l_{halo}, as we have defined the regular field to have $L_{c,\text{halo}} = l_{\text{halo}}$. We still always take 10 steps in the halo.

Chapter 9

Conclusion

In this thesis we have provided an in depth description of the theory of synchrotron radiation and its polarisation effects, as well as investigated different possible Galactic magnetic field models. The theory of synchrotron radiation was mainly based on the books by Rybicki and Lightman [9] and Longair [10], and the theory of polarisation on the classical treatments in the articles by Westfold [11] from 1959 and Westfold and Legg [12] from 1968.

In chapter 2 we discussed turbulent magnetic fields, with a focus on the GMF. As magnetic fields are present everywhere, they are important in the study of the structure and dynamics of our Universe. Their existence and characteristics can be analysed through different processes, and we introduced measurement techniques including Faraday rotation, synchrotron radiation, dust emission and the Zeeman effect. A few comments on MHD and MHD turbulence, in particular Kolmogorov's theory, was also provided. The chapter was ended by introducing two magnetic field models, the turbulent field model of the `ELMAG` [32] program and the regular field model `UF23` [22], as well as a method for combining these.

In chapter 3 we began the theoretical treatment of synchrotron radiation, which was continued in chapter 4. The important result of relativistic beaming was obtained for ultra-relativistic electrons. That is, the radiation emitted by an electron is confined within a cone of opening angle $\theta \simeq 1/\gamma$. We also provided expressions for the perpendicular and parallel component of the radiation field and used this to describe the intensity spectra of synchrotron radiation. Finally, we commented on the restrictions of synchrotron radiation, in particular the non-linear quantum effects that appear for strong magnetic fields.

Following the basic theory of synchrotron radiation, chapter 5 discussed polarisation in which our main equations were derived. We followed the treatments in [11, 12] to find expressions for the emission-polarisation tensor ρ_x for a single electron and j for a power-law electron distribution. The derivation leads to a circular polarisation degree $\Pi_{\text{circ}} \propto B^{1/2}$, which consequently will exceed 1 for large values of the magnetic field strength B. Therefore, as intended by [62], in appendix B the calculation of j is extended to include the approximation to second order in the pitch angle distribution function. However, in Sec. 8.1, we discuss this behaviour further and conclude that electrons cease to be ultra-relativistic in strong magnetic fields where the polarisation degree exceeds 1. In these cases we may no longer consider the process to be synchrotron emission. We also argued that the linear polarisation degree is dominant and the circular polarisation degree may be ignored for any practical application. Furthermore, we discuss that the expansion over the pitch angle in the calculation of the emission-polarisation tensor j should not be performed, as this violates the form of the circular and linear polarisation degree upon integration. A solution may be to evaluate the integral numerically.

A brief introduction to radiative transfer was presented in chapter 6, where the LoS integral frequently used in the numerical simulations also was introduced. The discussion of the LoS integral included descriptions of the method of how both the intensity and polarisation of synchrotron radiation is calculated, as well as the consideration of angular resolution. In the last section we considered diffusion, in particular we looked at its relation to the random walk model and solved the stationary case of the diffusion equation. The end of this chapter marked the conclusion of the theoretical part of the thesis.

The numerical simulations and results were presented in chapter 7. We began by considering pure turbulent fields using the magnetic fields generated by the `ELMAG` program in Sec. 7.1. Most important was the electron number density normalisation. We obtained this by using data from AMS-02, and the result was given in Eq. (7.1.4). This normalisation was used as the standard in most of the following simulations, with some variation. However, there are large uncertainties for this normalisation, considering the spectrum does not follow a perfect power-law. We also considered the treatment by Di Bernardo et al. [58] in Sec. 7.1. Using their approach, we found intensity latitude profiles of synchrotron radiation using the `ELMAG` turbulent field model which were reasonable compared with radio data.

Further comments on the pure turbulent fields was provided in Sec. 8.2.1. The fact that the `ELMAG` program may only produce sufficiently turbulent fields up to a certain distance dependent on the number of turbulent modes was discussed. It was shown, however, that none of the results of the simulations were likely affected by this. We may conclude that the number of turbulent modes is an important consideration upon using the `ELMAG` turbulent field, but the described issue is not problematic for our application. Additionally, we discussed the normalisation procedure and the uncertainties around this. By using our assumptions on the magnetic field dependence on the diffusion coefficient and the slope of the energy spectrum, the article [58] gave an inconsistent description of their model. The derived radio data provided may also be favourable to look into.

In Sec. 7.2 and 7.3 we looked at the models of `UF23` in relation to intensity and polarisation, both alone and in combination with the turbulent field of the `ELMAG` program. We provided both intensity latitude profiles and calculation of polarisation degrees. The GMF models did not provide good fits for the intensity radio data given the calculated normalisation or the measured polarisation from the C-BASS project, and this was further discussed in Sec. 8.2.1. The greatest issue is the polarisation degrees which are much too high. Even when considering a strong turbulent component along with the regular fields of `UF23`, the degree of polarisation is not low enough to match the C-BASS data. A possible solution, however, is to introduce an extended turbulent magnetic field beyond the regular field.

The last GMF model we investigated was the simplified total field model described in Sec. 7.4. In this model we divided the Galaxy into three regions; the disk, halo and corona. In the disk and corona, the magnetic field direction was assumed to be isotropic random, while in the halo it was assumed to be regular, or constant with small random fluctuations. We made simple approximations and assumptions on the diffusion equation and magnetic field strength, and were left with a set of free parameters listed in Tab. 7.4. We tested the model for a chosen set of parameters, and obtained polarisation and intensity plots. The polarisation degrees were much lower than for the previous tested models, but the intensity latitude profiles were too low. We therefore intended to optimise the free parameters to fit the profiles, however because of the large number of parameters, we performed a chi-square test by varying only a few at a time. The results of the tests gave good fits for many sets of parameters, while the best combinations of chi-square value and mean degree of polarisation were around 0.22 and 0.15, respectively. A mean degree of polarisation around 0.15 means a significant amount of the simulations with the given parameters gave polarisation degrees low enough to be in agreement with the measured

values of the C-BASS project. The simplified total field model was further commented on in the discussion in Sec. 8.2.2. Here we presented an overview of the effect on the intensity and polarisation in Tab. 8.1 of changing each parameter, and we commented on the uncertainties of the approximations and assumptions made.

In summary, we conclude that the GMF models of `UF23`, alone or in combination with a turbulent magnetic field generated by the `ELMAG` program, do not produce magnetic fields in agreement with the low measured synchrotron polarisation by the C-BASS project. A possible solution is to include an extended turbulent magnetic field. The properties of this field, such as the strength, extent and correlation length, could be looked into. Furthermore, a simplified total field model consisting of a turbulent disk and corona field, and a regular halo field, may be used to describe the measured radio intensity data and the low polarisation degrees. However, the model is very simple and based on weak assumptions, as well as it includes many free parameters. Without further knowledge or data, we cannot know to which extent this model is a sufficiently realistic description of the structure of the GMF.

Appendix A

Useful integrals

Several integrals without derivations have been used throughout the thesis as well as in appendix B. Here we present all the relevant integrals along with derivations.

A.1 Airy functions

The Airy function $\mathrm{Ai}(x)$ along with the function $\mathrm{Bi}(x)$ are defined as linearly independent solutions to the differential equation [46]

$$\frac{\mathrm{d}^2x}{\mathrm{d}y^2} - xy = 0. \tag{A.1.1}$$

By using the properties from Abramowitz and Stegun [46] we may express the Airy function through the integral

$$\mathrm{Ai}(x) = \frac{1}{2\pi}\int_{-\infty}^{\infty} \exp\left[\mathrm{i}\left(xz + \frac{1}{3}z^3\right)\right]\mathrm{d}z. \tag{A.1.2}$$

Additionally, one can relate the Airy function to the modified Bessel functions $K_{1/3}$ and $K_{2/3}$ by the properties

$$K_{1/3}\left(\frac{2}{3}x^{3/2}\right) = \pi\sqrt{\frac{3}{x}}\mathrm{Ai}(x), \tag{A.1.3a}$$

$$K_{2/3}\left(\frac{2}{3}x^{3/2}\right) = -\pi\frac{\sqrt{3}}{x}\mathrm{Ai}'(x). \tag{A.1.3b}$$

In particular, we find that

$$\mathrm{Ai}'(x) = \mathrm{i}\frac{1}{2\pi}\int_{-\infty}^{\infty} z\exp\left[\mathrm{i}\left(xz + \frac{1}{3}z^3\right)\right]\mathrm{d}z, \tag{A.1.4a}$$

$$\mathrm{Ai}''(x) = -\frac{1}{2\pi}\int_{-\infty}^{\infty} z^2\exp\left[\mathrm{i}\left(xz + \frac{1}{3}z^3\right)\right]\mathrm{d}z = x\mathrm{Ai}(x), \tag{A.1.4b}$$

where we have used the differential equation in Eq. (A.1.1) in the last equality for the double derivative. As the Airy function is related to the modified Bessel functions, we present some of their general properties. It is known that the modified Bessel functions satisfy $K_{-n}(x) = K_n(x)$ and the following recurrence relations [46],

$$K_{n+1}(x) = K_{n-1}(x) + \frac{2n}{x}K_n(x), \tag{A.1.5a}$$

$$\frac{\mathrm{d}}{\mathrm{d}x}K_n(x) = -\frac{1}{2}\left[K_{n-1}(x) + K_{n+1}(x)\right], \tag{A.1.5b}$$

for $n = 1/2, 3/2, \ldots$, as well as the fact that

$$\lim_{x\to\infty} K_n(x) = 0. \tag{A.1.6}$$

We now wish to find solutions to the integral[1]

$$\mathcal{I}_{\gamma,s} \equiv \int_{-\infty}^{\infty} \exp\left[\mathrm{i}\gamma\left(\mu y + \frac{1}{3}y^3\right)\right] y^s \mathrm{d}y, \tag{A.1.7}$$

for $s = -3, -2, -1, 0, 1, 2$. Most of these are presented in [12], but we will also provide derivations here. We should first recall the definitions of the functions F, G and H in Eq. (4.1.12a), (4.1.12b) and (5.2.15), respectively. That is

$$F(x) \equiv x\int_x^{\infty} K_{5/3}(\xi)\mathrm{d}\xi, \tag{A.1.8a}$$

$$G(x) \equiv xK_{2/3}(x), \tag{A.1.8b}$$

$$H(x) \equiv xK_{1/3}(x). \tag{A.1.8c}$$

Integral $\mathcal{I}_{\gamma,0}$

$$\mathcal{I}_{\gamma,0} \equiv \int_{-\infty}^{\infty} \exp\left[\mathrm{i}\gamma\left(\mu y + \frac{1}{3}y^3\right)\right] \mathrm{d}y = \frac{\sqrt{3}}{\gamma\mu} H\left(\frac{2}{3}\gamma\mu^{3/2}\right) \tag{A.1.9}$$

Derivation. We will use the substitution $z = \gamma^{1/3}y$, which corresponds to $\mathrm{d}y = \gamma^{-1/3}\mathrm{d}z$. We obtain

$$\begin{aligned}
\mathcal{I}_{\gamma,0} &= \gamma^{-1/3}\int_{-\infty}^{\infty} \exp\left[\mathrm{i}\left(\left\{\mu\gamma^{2/3}\right\} z + \frac{1}{3}z^3\right)\right] \mathrm{d}z \\
&= \gamma^{-1/3} 2\pi \mathrm{Ai}\left(\mu\gamma^{2/3}\right) = 2\pi\gamma^{-1/3}\frac{1}{\sqrt{3}\pi}\left(\mu\gamma^{2/3}\right)^{1/2} K_{1/3}\left(\frac{2}{3}\left\{\mu\gamma^{2/3}\right\}^{3/2}\right) \\
&= \frac{2}{\sqrt{3}}\mu^{1/2}K_{1/3}\left(\frac{2}{3}\gamma\mu^{3/2}\right) = \frac{\sqrt{3}}{\gamma\mu}H\left(\frac{2}{3}\gamma\mu^{3/2}\right).
\end{aligned} \tag{A.1.10}$$

Integral $\mathcal{I}_{\gamma,1}$

$$\mathcal{I}_{\gamma,1} \equiv \int_{-\infty}^{\infty} \exp\left[\mathrm{i}\gamma\left(\mu y + \frac{1}{3}y^3\right)\right] y\mathrm{d}y = \mathrm{i}\frac{\sqrt{3}}{\gamma\mu^{1/2}} G\left(\frac{2}{3}\gamma\mu^{3/2}\right) \tag{A.1.11}$$

Derivation. Using the same substitution as before,

$$\begin{aligned}
\mathcal{I}_{\gamma,1} &= \gamma^{-2/3}\int_{-\infty}^{\infty} \exp\left[\mathrm{i}\left(\left\{\mu\gamma^{2/3}\right\} z + \frac{1}{3}z^3\right)\right] z\mathrm{d}z \\
&= -\gamma^{-2/3} 2\pi\mathrm{i}\mathrm{Ai}'\left(\mu\gamma^{2/3}\right) = 2\pi\mathrm{i}\gamma^{-2/3}\frac{1}{\sqrt{3}\pi}\mu\gamma^{2/3}K_{2/3}\left(\frac{2}{3}\left\{\mu\gamma^{2/3}\right\}^{3/2}\right) \\
&= \mathrm{i}\frac{2}{\sqrt{3}}\mu K_{2/3}\left(\frac{2}{3}\gamma\mu^{3/2}\right) = \mathrm{i}\frac{\sqrt{3}}{\gamma\mu^{1/2}}G\left(\frac{2}{3}\gamma\mu^{3/2}\right).
\end{aligned} \tag{A.1.12}$$

[1] The variable γ should not be confused with the Lorentz factor.

Integral $\mathcal{I}_{\gamma,2}$

$$\mathcal{I}_{\gamma,2} \equiv \int_{-\infty}^{\infty} \exp\left[\mathrm{i}\gamma\left(\mu y + \frac{1}{3}y^3\right)\right] y^2 \mathrm{d}y = -\frac{\sqrt{3}}{\gamma} H\left(\frac{2}{3}\gamma\mu^{3/2}\right) \tag{A.1.13}$$

Derivation. Once again, defining $z = \gamma^{1/3} y$ gives

$$\begin{aligned}
\mathcal{I}_{\gamma,2} &= \gamma^{-1} \int_{-\infty}^{\infty} \exp\left[\mathrm{i}\left(\left\{\mu\gamma^{2/3}\right\} z + \frac{1}{3}z^3\right)\right] z^2 \mathrm{d}z \\
&= -\gamma^{-1} 2\pi\mu\gamma^{2/3} \mathrm{Ai}\left(\mu\gamma^{2/3}\right) = -2\pi\mu\gamma^{-1/3} \frac{1}{\sqrt{3}\pi} \left(\mu\gamma^{2/3}\right)^{1/2} K_{1/3}\left(\frac{2}{3}\left\{\mu\gamma^{2/3}\right\}^{3/2}\right) \\
&= -\frac{2}{\sqrt{3}}\mu^{3/2} K_{1/3}\left(\frac{2}{3}\gamma\mu^{3/2}\right) = -\frac{\sqrt{3}}{\gamma} H\left(\frac{2}{3}\gamma\mu^{3/2}\right).
\end{aligned} \tag{A.1.14}$$

Integral $\mathcal{I}_{\gamma,-1}$

$$\mathcal{I}_{\gamma,-1} \equiv \int_{-\infty}^{\infty} \exp\left[\mathrm{i}\gamma\left(\mu y + \frac{1}{3}y^3\right)\right] y^{-1} \mathrm{d}y = -\mathrm{i}\frac{\sqrt{3}}{\gamma\mu^{3/2}} \left[2G\left(\frac{2}{3}\gamma\mu^{3/2}\right) - F\left(\frac{2}{3}\gamma\mu^{3/2}\right)\right] \tag{A.1.15}$$

Derivation. This derivation is a little more complicated, and we will use a trick, seeing that

$$\begin{aligned}
\frac{\mathrm{d}}{\mathrm{d}\mu}\mathcal{I}_{\gamma,-1} &= \int_{-\infty}^{\infty} \frac{\mathrm{d}}{\mathrm{d}\mu} \exp\left[\mathrm{i}\gamma\left(\mu y + \frac{1}{3}y^3\right)\right] y^{-1} \mathrm{d}y = \mathrm{i}\gamma\mathcal{I}_{\gamma,0} = \mathrm{i}\frac{\sqrt{3}}{\mu} H\left(\frac{2}{3}\gamma\mu^{3/2}\right) \\
&= \mathrm{i}\frac{\sqrt{3}}{\mu}\frac{2}{3}\gamma\mu^{3/2} K_{1/3}\left(\frac{2}{3}\gamma\mu^{3/2}\right) = \mathrm{i}\frac{2}{\sqrt{3}}\gamma\mu^{1/2} K_{1/3}\left(\frac{2}{3}\gamma\mu^{3/2}\right) \\
&= \mathrm{i}\frac{2}{\sqrt{3}}\gamma\left(\frac{3}{2}\gamma^{-1}\right)^{1/3} x^{1/3} K_{1/3}(x),
\end{aligned} \tag{A.1.16}$$

for $x \equiv \frac{2}{3}\gamma\mu^{3/2}$, or $\mu = \left(\frac{3}{2}\gamma^{-1}x\right)^{2/3}$. It is possible to write

$$\frac{\mathrm{d}x}{\mathrm{d}\mu} = \gamma\mu^{1/2} = \gamma\left(\frac{3}{2}\gamma^{-1}x\right)^{1/3} \gamma\left(\frac{3}{2}\gamma^{-1}\right)^{1/3} x^{1/3}. \tag{A.1.17}$$

Now we can use the property of the Bessel in Eq. (A.1.5b), writing

$$\frac{\mathrm{d}}{\mathrm{d}x} K_{2/3}(x) = -\frac{1}{2}\left[K_{1/3}(x) + K_{5/3}(x)\right]. \tag{A.1.18}$$

Integrating Eq. (A.1.16) gives therefore

$$\begin{aligned}
\mathcal{I}_{\gamma,-1} &= \mathrm{i}\frac{2}{\sqrt{3}}\gamma\left(\frac{3}{2}\gamma^{-1}\right)^{1/3} \int_{\mu}^{\infty} x^{1/3} K_{1/3}(x)\mathrm{d}\mu = \mathrm{i}\frac{2}{\sqrt{3}} \int_{\frac{2}{3}\gamma\mu^{3/2}}^{\infty} K_{1/3}(x)\mathrm{d}x \\
&= \mathrm{i}\frac{2}{\sqrt{3}}\left[-2K_{2/3}\left(\frac{2}{3}\gamma\mu^{3/2}\right) - \int_{\frac{2}{3}\gamma\mu^{3/2}}^{\infty} K_{5/3}(x)\mathrm{d}x\right] \\
&= -\mathrm{i}\frac{2}{\sqrt{3}}\left(\frac{2}{3}\gamma\mu^{3/2}\right)^{-1}\left[2G\left(\frac{2}{3}\gamma\mu^{3/2}\right) - F\left(\frac{2}{3}\gamma\mu^{3/2}\right)\right] \\
&= -\mathrm{i}\frac{\sqrt{3}}{\gamma\mu^{3/2}}\left[2G\left(\frac{2}{3}\gamma\mu^{3/2}\right) - F\left(\frac{2}{3}\gamma\mu^{3/2}\right)\right].
\end{aligned} \tag{A.1.19}$$

Integral $\mathcal{I}_{\gamma,-2}$

$$\mathcal{I}_{\gamma,-2} \equiv \int_{-\infty}^{\infty} \exp\left[\mathrm{i}\gamma\left(\mu y + \frac{1}{3}y^3\right)\right] y^{-2}\mathrm{d}y = \frac{\sqrt{3}}{\mu^{1/2}}\left[G\left(\frac{2}{3}\gamma\mu^{3/2}\right) - F\left(\frac{2}{3}\gamma\mu^{3/2}\right)\right] \tag{A.1.20}$$

Derivation. Here, we will use integration by parts, utilising the integrals already found. Setting $u = \exp\left[\mathrm{i}\gamma\left(\mu y + \frac{1}{3}y^3\right)\right]$, that is $\mathrm{d}u = \mathrm{i}\gamma\exp\left[\mathrm{i}\gamma\left(\mu y + \frac{1}{3}y^3\right)\right](\mu + y^2)$, and $\mathrm{d}v = y^{-2}$, that is $v = -y^{-1}$, we get

$$\begin{aligned}
\mathcal{I}_{\gamma,-2} &= \mathrm{i}\gamma\int_{-\infty}^{\infty}\exp\left[\mathrm{i}\gamma\left(\mu y + \frac{1}{3}y^3\right)\right](\mu y^{-1} + y)\mathrm{d}y \\
&= \mathrm{i}\gamma\left(\mu\mathcal{I}_{\gamma,-1} + \mathcal{I}_{\gamma,1}\right) \\
&= \mathrm{i}\gamma\left\{-\mathrm{i}\frac{\sqrt{3}}{\gamma\mu^{1/2}}\left[2G\left(\frac{2}{3}\gamma\mu^{3/2}\right) - F\left(\frac{2}{3}\gamma\mu^{3/2}\right)\right] + \mathrm{i}\frac{\sqrt{3}}{\gamma\mu^{1/2}}G\left(\frac{2}{3}\gamma\mu^{3/2}\right)\right\} \\
&= \frac{\sqrt{3}}{\mu^{1/2}}\left[G\left(\frac{2}{3}\gamma\mu^{3/2}\right) - F\left(\frac{2}{3}\gamma\mu^{3/2}\right)\right].
\end{aligned} \tag{A.1.21}$$

We have used that the expression $\left\{-y^{-1}\exp\left[\mathrm{i}\gamma\left(\mu y + \frac{1}{3}y^3\right)\right]\right\}_{-\infty}^{\infty}$ is zero.

Integral $\mathcal{I}_{\gamma,-3}$

$$\begin{aligned}
\mathcal{I}_{\gamma,-3} &\equiv \int_{-\infty}^{\infty}\exp\left[\mathrm{i}\gamma\left(\mu y + \frac{1}{3}y^3\right)\right] y^{-3}\mathrm{d}y \\
&= \mathrm{i}\frac{\sqrt{3}}{2}\left\{\gamma\mu^{1/2}\left[G\left(\frac{2}{3}\gamma\mu^{3/2}\right) - F\left(\frac{2}{3}\gamma\mu^{3/2}\right)\right] + \mu^{-1}H\left(\frac{2}{3}\gamma\mu^{3/2}\right)\right\}
\end{aligned} \tag{A.1.22}$$

Derivation. Once again we use integration by parts. It follows that

$$\begin{aligned}
\mathcal{I}_{\gamma,-3} &= \mathrm{i}\gamma\frac{1}{2}\int_{-\infty}^{\infty}\exp\left[\mathrm{i}\gamma\left(\mu y + \frac{1}{3}y^3\right)\right](\mu y^{-2} + 1)\mathrm{d}y \\
&= \mathrm{i}\gamma\frac{1}{2}\left(\mu\mathcal{I}_{\gamma,-2} + \mathcal{I}_{\gamma,0}\right) \\
&= \mathrm{i}\gamma\frac{1}{2}\left\{\sqrt{3}\mu^{1/2}\left[G\left(\frac{2}{3}\gamma\mu^{3/2}\right) - F\left(\frac{2}{3}\gamma\mu^{3/2}\right)\right] + \frac{\sqrt{3}}{\gamma\mu}H\left(\frac{2}{3}\gamma\mu^{3/2}\right)\right\} \\
&= \mathrm{i}\frac{\sqrt{3}}{2}\left\{\gamma\mu^{1/2}\left[G\left(\frac{2}{3}\gamma\mu^{3/2}\right) - F\left(\frac{2}{3}\gamma\mu^{3/2}\right)\right] + \mu^{-1}H\left(\frac{2}{3}\gamma\mu^{3/2}\right)\right\}.
\end{aligned} \tag{A.1.23}$$

A.2 Theta integrals

The Airy function can be used to calculate relevant θ-integrals. We will now demonstrate a set of these integrals used throughout the thesis in the calculations of emissivities. Before we begin, we note a few useful integrals,

$$\int_{-\infty}^{\infty}\exp\left(\mathrm{i}ay^2\right)\mathrm{d}y = \sqrt{\pi}\mathrm{e}^{\mathrm{i}\frac{\pi}{4}}a^{-1/2}, \tag{A.2.1a}$$

$$\int_{-\infty}^{\infty} y\exp\left(\mathrm{i}ay^2\right)\mathrm{d}y = 0, \tag{A.2.1b}$$

$$\int_{-\infty}^{\infty} y^2\exp\left(\mathrm{i}ay^2\right)\mathrm{d}y = -\frac{\sqrt{\pi}}{2}\mathrm{e}^{-\mathrm{i}\frac{\pi}{4}}a^{-3/2}, \tag{A.2.1c}$$

$$\int_{-\infty}^{\infty} y^4 \exp\left(\mathrm{i}ay^2\right) \mathrm{d}y = \frac{3\sqrt{\pi}}{4} \mathrm{e}^{-\mathrm{i}\frac{3\pi}{4}} a^{-5/2}, \tag{A.2.1d}$$

where a is a constant. The results of the integrals $\mathcal{I}_{\gamma,s}$ from the previous section will also be used heavily in the following calculations, and with that, it is convenient to define

$$\mu \equiv \left(\frac{3}{4}x\right)^{2/3}. \tag{A.2.2}$$

Integral T_1

$$T_1 = \int_{-\infty}^{\infty} \theta_\gamma^2 \theta^2 K_{1/3}^2\left(\frac{1}{2}\theta_\gamma^3 x\right) \mathrm{d}\theta = \frac{\pi}{\sqrt{3}\gamma^3 x^2} \left[F(x) - G(x)\right] \tag{A.2.3}$$

Derivation. We begin by writing the Bessel functions in terms of Airy functions, finding

$$\begin{aligned}
K_{1/3}^2\left(\frac{1}{2}\theta_\gamma^3 x\right) &= K_{1/3}^2\left(\frac{2}{3}\left\{\mu\theta_\gamma^2\right\}^{3/2}\right) = \frac{3\pi^2}{\mu\theta_\gamma^2}\mathrm{Ai}^2(\mu\theta_\gamma^2) \\
&= \frac{3}{4\mu\theta_\gamma^2}\int_{-\infty}^{\infty} \exp\left[\mathrm{i}\left(\mu\theta_\gamma^2 u + \frac{1}{3}u^3\right)\right]\mathrm{d}u \int_{-\infty}^{\infty} \exp\left[\mathrm{i}\left(\mu\theta_\gamma^2 v + \frac{1}{3}v^3\right)\right]\mathrm{d}v \\
&= \frac{3}{4\mu\theta_\gamma^2}\int_{-\infty}^{\infty}\int_{-\infty}^{\infty} \exp\left[\mathrm{i}\left(\mu\theta_\gamma^2\{u-v\} + \frac{1}{3}\{u^3 - v^3\}\right)\right]\mathrm{d}u\mathrm{d}v \\
&= \frac{3}{2\mu\theta_\gamma^2}\int_{-\infty}^{\infty}\int_{-\infty}^{\infty} \exp\left[2\mathrm{i}\left(\mu\theta_\gamma^2 y + \frac{1}{3}\{y^3 + 3yz^2\}\right)\right]\mathrm{d}y\mathrm{d}z \\
&= \frac{3}{2\mu\theta_\gamma^2}\int_{-\infty}^{\infty} \exp\left[2\mathrm{i}\left(\mu\theta_\gamma^2 y + \frac{1}{3}y^3\right)\right]\int_{-\infty}^{\infty} \exp\left[2\mathrm{i}yz^2\right]\mathrm{d}z\mathrm{d}y \\
&= \frac{3\sqrt{\pi}}{2\sqrt{2}\mu\theta_\gamma^2}\mathrm{e}^{\mathrm{i}\frac{\pi}{4}}\int_{-\infty}^{\infty} \exp\left[2\mathrm{i}\left(\mu\theta_\gamma^2 y + \frac{1}{3}y^3\right)\right] y^{-1/2}\mathrm{d}y.
\end{aligned} \tag{A.2.4}$$

In the third line we have substituted v for $-v$, while in the fourth line we have defined $2y = u - v$ and $2z = u + v$. This gives $u = y + z$ and $v = z - y$, and $\mathrm{d}u\mathrm{d}v = 2\mathrm{d}y\mathrm{d}z$. In the final line we have used Eq. (A.2.1a). We now integrate over θ, recalling the definition of $\theta_\gamma^2 \equiv 1 + \gamma^2\theta^2$,

$$\begin{aligned}
T_1 &= \frac{3\sqrt{\pi}}{2\sqrt{2}\mu}\mathrm{e}^{\mathrm{i}\frac{\pi}{4}}\int_{-\infty}^{\infty} y^{-1/2}\int_{-\infty}^{\infty} \theta^2 \exp\left[2\mathrm{i}\left(\mu\theta_\gamma^2 y + \frac{1}{3}y^3\right)\right]\mathrm{d}\theta\mathrm{d}y \\
&= \frac{3\sqrt{\pi}}{2\sqrt{2}\mu}\mathrm{e}^{\mathrm{i}\frac{\pi}{4}}\int_{-\infty}^{\infty} y^{-1/2}\int_{-\infty}^{\infty} \theta^2 \exp\left[2\mathrm{i}\left(\mu\{1+\gamma^2\theta^2\}y + \frac{1}{3}y^3\right)\right]\mathrm{d}\theta\mathrm{d}y \\
&= \frac{3\sqrt{\pi}}{2\sqrt{2}\mu}\mathrm{e}^{\mathrm{i}\frac{\pi}{4}}\int_{-\infty}^{\infty} y^{-1/2}\int_{-\infty}^{\infty} \theta^2 \exp\left[2\mathrm{i}\mu\gamma^2 y\theta^2\right]\mathrm{d}\theta \exp\left[2\mathrm{i}\left(\mu y + \frac{1}{3}y^3\right)\right]\mathrm{d}y \\
&= -\frac{3\pi}{4\sqrt{2}\mu}(2\mu\gamma^2)^{-3/2}\int_{-\infty}^{\infty} y^{-2}\exp\left[2\mathrm{i}\left(\mu y + \frac{1}{3}y^3\right)\right]\mathrm{d}y \\
&= \frac{3\sqrt{3}\pi}{16\mu^3\gamma^3}\left[F(x) - G(x)\right] = \frac{\pi}{\sqrt{3}\gamma^3 x^2}\left[F(x) - G(x)\right].
\end{aligned} \tag{A.2.5}$$

In the fourth line, Eq. (A.2.1c) has been used, and the integral $\mathcal{I}_{2,-2}$ in the following line. In the last equation we have inserted the expression for μ and the derivation is concluded.

Integral T_2

$$T_2 = \int_{-\infty}^{\infty} \theta_\gamma^4 K_{2/3}^2\left(\frac{1}{2}\theta_\gamma^3 x\right)\mathrm{d}\theta = \frac{\pi}{\sqrt{3}\gamma x^2}\left[F(x) + G(x)\right] \tag{A.2.6}$$

Derivation. Similarly to the previous integral, we write the Bessel functions in terms of Airy functions, or in this case the derivatives of the Airy function. We get

$$\begin{aligned}
K_{2/3}^2\left(\frac{1}{2}\theta_\gamma^3 x\right) &= K_{2/3}^2\left(\frac{2}{3}\left\{\mu\theta_\gamma^2\right\}^{3/2}\right) = \frac{3\pi^2}{\mu^2\theta_\gamma^4}\mathrm{Ai}'^2(\mu\theta_\gamma^2) \\
&= -\frac{3}{4\mu^2\theta_\gamma^4}\int_{-\infty}^{\infty} u\exp\left[\mathrm{i}\left(\mu\theta_\gamma^2 u + \frac{1}{3}u^3\right)\right]\mathrm{d}u\int_{-\infty}^{\infty} v\exp\left[\mathrm{i}\left(\mu\theta_\gamma^2 v + \frac{1}{3}v^3\right)\right]\mathrm{d}v \\
&= \frac{3}{4\mu^2\theta_\gamma^4}\int_{-\infty}^{\infty}\int_{-\infty}^{\infty} uv\exp\left[\mathrm{i}\left(\mu\theta_\gamma^2\{u-v\} + \frac{1}{3}\{u^3-v^3\}\right)\right]\mathrm{d}u\mathrm{d}v \\
&= \frac{3}{2\mu^2\theta_\gamma^4}\int_{-\infty}^{\infty}\int_{-\infty}^{\infty} (z^2-y^2)\exp\left[2\mathrm{i}\left(\mu\theta_\gamma^2 y + \frac{1}{3}\{y^3+3yz^2\}\right)\right]\mathrm{d}y\mathrm{d}z \\
&= -\frac{3}{2\mu^2\theta_\gamma^4}\int_{-\infty}^{\infty}\exp\left[2\mathrm{i}\left(\mu\theta_\gamma^2 y + \frac{1}{3}y^3\right)\right]\int_{-\infty}^{\infty}(y^2-z^2)\exp\left[2\mathrm{i}yz^2\right]\mathrm{d}z\mathrm{d}y \\
&= -\frac{3\sqrt{\pi}}{2\sqrt{2}\mu^2\theta_\gamma^4}\int_{-\infty}^{\infty}\exp\left[2\mathrm{i}\left(\mu\theta_\gamma^2 y + \frac{1}{3}y^3\right)\right]\left(\mathrm{e}^{\mathrm{i}\frac{\pi}{4}}y^{3/2} + \mathrm{e}^{-\mathrm{i}\frac{\pi}{4}}\frac{1}{4}y^{-3/2}\right)\mathrm{d}y. \quad \text{(A.2.7)}
\end{aligned}$$

We have used the same substitutions as before. Now performing the integral over θ gives

$$\begin{aligned}
T_2 &= -\frac{3\sqrt{\pi}}{2\sqrt{2}\mu^2}\int_{-\infty}^{\infty}\left(\mathrm{e}^{\mathrm{i}\frac{\pi}{4}}y^{3/2} + \mathrm{e}^{-\mathrm{i}\frac{\pi}{4}}\frac{1}{4}y^{-3/2}\right)\int_{-\infty}^{\infty}\exp\left[2\mathrm{i}\left(\mu\theta_\gamma^2 y + \frac{1}{3}y^3\right)\right]\mathrm{d}\theta\mathrm{d}y \\
&= -\frac{3\sqrt{\pi}}{2\sqrt{2}\mu^2}\int_{-\infty}^{\infty}\left(\mathrm{e}^{\mathrm{i}\frac{\pi}{4}}y^{3/2} + \mathrm{e}^{-\mathrm{i}\frac{\pi}{4}}\frac{1}{4}y^{-3/2}\right)\int_{-\infty}^{\infty}\exp\left[2\mathrm{i}\mu\gamma^2 y\theta^2\right]\mathrm{d}\theta\exp\left[2\mathrm{i}\left(\mu y + \frac{1}{3}y^3\right)\right]\mathrm{d}y \\
&= -\frac{3\pi}{4\mu^{5/2}\gamma}\int_{-\infty}^{\infty}\left(\mathrm{i}y + \frac{1}{4}y^{-2}\right)\exp\left[2\mathrm{i}\left(\mu y + \frac{1}{3}y^3\right)\right]\mathrm{d}y \\
&= -\frac{3\pi}{4\mu^{5/2}\gamma}\left\{-\frac{\sqrt{3}}{2}\mu^{-1/2}G(x) + \frac{\sqrt{3}}{4}\mu^{-1/2}\left[G(x)-F(x)\right]\right\} \\
&= \frac{3\sqrt{3}\pi}{16\mu^3\gamma}\left[F(x)+G(x)\right] = \frac{\pi}{\sqrt{3}\gamma x^2}\left[F(x)+G(x)\right]. \quad \text{(A.2.8)}
\end{aligned}$$

Integral T_3

$$T_3 = \int_{-\infty}^{\infty}\theta_\gamma^4\theta^2 K_{2/3}^2\left(\frac{1}{2}\theta_\gamma^3 x\right)\mathrm{d}\theta = \frac{\pi}{4\sqrt{3}\gamma^3 x^2}\left[\frac{10}{3x}H(x) + G(x) - F(x)\right] \quad \text{(A.2.9)}$$

Derivation. As we already know the integral expression for the square of the Bessel function from the derivation of integral T_2, we find that

$$\begin{aligned}
T_3 &= -\frac{3\sqrt{\pi}}{2\sqrt{2}\mu^2}\int_{-\infty}^{\infty}\left(\mathrm{e}^{\mathrm{i}\frac{\pi}{4}}y^{3/2} + \mathrm{e}^{-\mathrm{i}\frac{\pi}{4}}\frac{1}{4}y^{-3/2}\right)\int_{-\infty}^{\infty}\theta^2\exp\left[2\mathrm{i}\left(\mu\theta_\gamma^2 y + \frac{1}{3}y^3\right)\right]\mathrm{d}\theta\mathrm{d}y \\
&= -\frac{3\sqrt{\pi}}{2\sqrt{2}\mu^2}\int_{-\infty}^{\infty}\left(\mathrm{e}^{\mathrm{i}\frac{\pi}{4}}y^{3/2} + \mathrm{e}^{-\mathrm{i}\frac{\pi}{4}}\frac{1}{4}y^{-3/2}\right)\int_{-\infty}^{\infty}\theta^2\exp\left[2\mathrm{i}\mu\gamma^2 y\theta^2\right]\mathrm{d}\theta\exp\left[2\mathrm{i}\left(\mu y + \frac{1}{3}y^3\right)\right]\mathrm{d}y \\
&= \frac{3\pi}{16\mu^{7/2}\gamma^3}\int_{-\infty}^{\infty}\left(1 - \mathrm{i}\frac{1}{4}y^{-3}\right)\exp\left[2\mathrm{i}\left(\mu y + \frac{1}{3}y^3\right)\right]\mathrm{d}y \\
&= \frac{3\pi}{16\mu^{7/2}\gamma^3}\left[\frac{\sqrt{3}}{2}\mu^{-1}H(x) + \frac{\sqrt{3}}{8}\left\{2\mu^{1/2}\left[G(x)-F(x)\right] + \mu^{-1}H(x)\right\}\right] \\
&= \frac{3\sqrt{3}\pi}{64\mu^3\gamma^3}\left[\frac{5}{2}\mu^{-3/2}H(x) + G(x) - F(x)\right] \\
&= \frac{\pi}{4\sqrt{3}\gamma^3 x^2}\left[\frac{10}{3x}H(x) + G(x) - F(x)\right]. \quad \text{(A.2.10)}
\end{aligned}$$

Integral T_4

$$T_4 = \int_{-\infty}^{\infty} \theta_\gamma^3 \theta^2 K_{1/3}\left(\frac{1}{2}\theta_\gamma^3 x\right) K_{2/3}\left(\frac{1}{2}\theta_\gamma^3 x\right) \mathrm{d}\theta = \frac{2\pi}{3\sqrt{3}\gamma^3 x^3}\left[2G(x) - F(x)\right] \tag{A.2.11}$$

Derivation. For this integral, we need to find an integral expression for the product of the two Bessel functions. We get that

$$\begin{aligned}
K_{1/3}\left(\frac{1}{2}\theta_\gamma^3 x\right) K_{2/3}\left(\frac{1}{2}\theta_\gamma^3 x\right) &= K_{1/3}\left(\frac{2}{3}\left\{\mu\theta_\gamma^2\right\}^{3/2}\right) K_{2/3}\left(\frac{2}{3}\left\{\mu\theta_\gamma^2\right\}^{3/2}\right) \\
&= -\frac{3\pi^2}{(\mu\theta_\gamma^2)^{3/2}} \mathrm{Ai}(\mu\theta_\gamma^2)\mathrm{Ai}'(\mu\theta_\gamma^2) \\
&= -\mathrm{i}\frac{3}{4(\mu\theta_\gamma^2)^{3/2}} \int_{-\infty}^{\infty} \exp\left[\mathrm{i}\left(\mu\theta_\gamma^2 u + \frac{1}{3}u^3\right)\right] \mathrm{d}u \int_{-\infty}^{\infty} v \exp\left[\mathrm{i}\left(\mu\theta_\gamma^2 v + \frac{1}{3}v^3\right)\right] \mathrm{d}v \\
&= \mathrm{i}\frac{3}{4(\mu\theta_\gamma^2)^{3/2}} \int_{-\infty}^{\infty}\int_{-\infty}^{\infty} v \exp\left[\mathrm{i}\left(\mu\theta_\gamma^2\{u-v\} + \frac{1}{3}\{u^3 - v^3\}\right)\right] \mathrm{d}u\mathrm{d}v \\
&= \mathrm{i}\frac{3}{2(\mu\theta_\gamma^2)^{3/2}} \int_{-\infty}^{\infty}\int_{-\infty}^{\infty} (z-y) \exp\left[2\mathrm{i}\left(\mu\theta_\gamma^2 y + \frac{1}{3}\{y^3 + 3yz^2\}\right)\right] \mathrm{d}y\mathrm{d}z \\
&= \mathrm{i}\frac{3}{2(\mu\theta_\gamma^2)^{3/2}} \int_{-\infty}^{\infty} \exp\left[2\mathrm{i}\left(\mu\theta_\gamma^2 y + \frac{1}{3}y^3\right)\right] \int_{-\infty}^{\infty} (z-y)\exp\left[2\mathrm{i}yz^2\right] \mathrm{d}z\mathrm{d}y \\
&= -\mathrm{i}\frac{3\sqrt{\pi}}{2\sqrt{2}(\mu\theta_\gamma^2)^{3/2}} e^{\mathrm{i}\frac{\pi}{4}} \int_{-\infty}^{\infty} \exp\left[2\mathrm{i}\left(\mu\theta_\gamma^2 y + \frac{1}{3}y^3\right)\right] y^{1/2}\mathrm{d}y.
\end{aligned} \tag{A.2.12}$$

As usual, we now perform the integral over θ and get

$$\begin{aligned}
T_4 &= -\mathrm{i}\frac{3\sqrt{\pi}}{2\sqrt{2}\mu^{3/2}} e^{\mathrm{i}\frac{\pi}{4}} \int_{-\infty}^{\infty} y^{1/2} \int_{-\infty}^{\infty} \theta^2 \exp\left[2\mathrm{i}\left(\mu\theta_\gamma^2 y + \frac{1}{3}y^3\right)\right] \mathrm{d}\theta\mathrm{d}y \\
&= -\mathrm{i}\frac{3\sqrt{\pi}}{2\sqrt{2}\mu^{3/2}} e^{\mathrm{i}\frac{\pi}{4}} \int_{-\infty}^{\infty} y^{1/2} \int_{-\infty}^{\infty} \theta^2 \exp\left[2\mathrm{i}\mu\gamma^2 y\theta^2\right] \mathrm{d}\theta \exp\left[2\mathrm{i}\left(\mu y + \frac{1}{3}y^3\right)\right] \mathrm{d}y \\
&= \mathrm{i}\frac{3\pi}{4\sqrt{2}\mu^{3/2}} (2\mu\gamma^2)^{-3/2} \int_{-\infty}^{\infty} y^{-1} \exp\left[2\mathrm{i}\left(\mu y + \frac{1}{3}y^3\right)\right] \mathrm{d}y \\
&= \frac{3\sqrt{3}\pi}{32\mu^{9/2}\gamma^3}\left[2G(x) - F(x)\right] = \frac{2\pi}{3\sqrt{3}\gamma^3 x^3}\left[2G(x) - F(x)\right].
\end{aligned} \tag{A.2.13}$$

Integral T_5

$$T_5 = \int_{-\infty}^{\infty} \theta_\gamma^5 K_{1/3}\left(\frac{1}{2}\theta_\gamma^3 x\right) K_{2/3}\left(\frac{1}{2}\theta_\gamma^3 x\right) \mathrm{d}\theta = \frac{2\pi}{3\sqrt{3}\gamma x^3}\left[3xH(x) + 2G(x) - F(x)\right] \tag{A.2.14}$$

Derivation. Using the result from integral T_4, we get

$$\begin{aligned}
T_5 &= -\mathrm{i}\frac{3\sqrt{\pi}}{2\sqrt{2}\mu^{3/2}} e^{\mathrm{i}\frac{\pi}{4}} \int_{-\infty}^{\infty} y^{1/2} \int_{-\infty}^{\infty} \theta_\gamma^2 \exp\left[2\mathrm{i}\left(\mu\theta_\gamma^2 y + \frac{1}{3}y^3\right)\right] \mathrm{d}\theta\mathrm{d}y \\
&= -\mathrm{i}\frac{3\sqrt{\pi}}{2\sqrt{2}\mu^{3/2}} e^{\mathrm{i}\frac{\pi}{4}} \int_{-\infty}^{\infty} y^{1/2} \int_{-\infty}^{\infty} (1+\gamma^2\theta^2) \exp\left[2\mathrm{i}\left(\mu\theta_\gamma^2 y + \frac{1}{3}y^3\right)\right] \mathrm{d}\theta\mathrm{d}y \\
&= -\mathrm{i}\frac{3\sqrt{\pi}}{2\sqrt{2}\mu^{3/2}} e^{\mathrm{i}\frac{\pi}{4}} \int_{-\infty}^{\infty} y^{1/2} \int_{-\infty}^{\infty} (1+\gamma^2\theta^2) \exp\left[2\mathrm{i}\mu\gamma^2 y\theta^2\right] \mathrm{d}\theta \exp\left[2\mathrm{i}\left(\mu y + \frac{1}{3}y^3\right)\right] \mathrm{d}y \\
&= \frac{3\pi}{2\sqrt{2}\mu^{3/2}} (2\mu\gamma^2)^{-1/2} \int_{-\infty}^{\infty} \exp\left[2\mathrm{i}\left(\mu y + \frac{1}{3}y^3\right)\right] \mathrm{d}y + \gamma^2 T_4
\end{aligned}$$

$$= \frac{3\sqrt{3}\pi}{8\mu^3\gamma} H(x) + \gamma^2 T_4 = \frac{2\pi}{\sqrt{3}\gamma x^2} H(x) + \gamma^2 T_4$$
$$= \frac{2\pi}{3\sqrt{3}\gamma x^3} \left[3xH(x) + 2G(x) - F(x)\right]. \tag{A.2.15}$$

Integral T_6

$$T_6 = \int_{-\infty}^{\infty} \theta_\gamma^2 \theta^4 K_{1/3}^2 \left(\frac{1}{2}\theta_\gamma^3 x\right) \mathrm{d}\theta = \frac{3\pi}{4\sqrt{3}\gamma^5 x^2} \left[\frac{2}{3x} H(x) + G(x) - F(x)\right] \tag{A.2.16}$$

Derivation. In this case we also know the expression for $K_{1/3}^2$ from the derivation of integral T_1. Therefore, we get that

$$\begin{aligned} T_6 &= \frac{3\sqrt{\pi}}{2\sqrt{2}\mu} \mathrm{e}^{\mathrm{i}\frac{\pi}{4}} \int_{-\infty}^{\infty} y^{-1/2} \int_{-\infty}^{\infty} \theta^4 \exp\left[2\mathrm{i}\left(\mu\theta_\gamma^2 y + \frac{1}{3}y^3\right)\right] \mathrm{d}\theta \mathrm{d}y \\ &= \frac{3\sqrt{\pi}}{2\sqrt{2}\mu} \mathrm{e}^{\mathrm{i}\frac{\pi}{4}} \int_{-\infty}^{\infty} y^{-1/2} \int_{-\infty}^{\infty} \theta^4 \exp\left[2\mathrm{i}\mu\gamma^2 y\theta^2\right] \mathrm{d}\theta \exp\left[2\mathrm{i}\left(\mu y + \frac{1}{3}y^3\right)\right] \mathrm{d}y \\ &= -\mathrm{i}\frac{9\pi}{8\sqrt{2}\mu} (2\mu\gamma^2)^{-5/2} \int_{-\infty}^{\infty} y^{-3} \exp\left[2\mathrm{i}\left(\mu y + \frac{1}{3}y^3\right)\right] \mathrm{d}y \\ &= \frac{9\sqrt{3}\pi}{128\mu^3\gamma^5} \left\{2\left[G(x) - F(x)\right] + \mu^{-3/2} H(x)\right\} \\ &= \frac{3\pi}{4\sqrt{3}\gamma^5 x^2} \left[\frac{2}{3x} H(x) + G(x) - F(x)\right]. \end{aligned} \tag{A.2.17}$$

Integral T_7

$$T_7 = \int_{-\infty}^{\infty} \theta_\gamma^4 \theta^2 K_{1/3}^2 \left(\frac{1}{2}\theta_\gamma^3 x\right) \mathrm{d}\theta = \frac{\pi}{4\sqrt{3}\gamma^3 x^2} \left[\frac{2}{x} H(x) - G(x) + F(x)\right] \tag{A.2.18}$$

Derivation. We use what we had from the derivation of integral T_1, and get

$$\begin{aligned} T_7 &= \frac{3\sqrt{\pi}}{2\sqrt{2}\mu} \mathrm{e}^{\mathrm{i}\frac{\pi}{4}} \int_{-\infty}^{\infty} y^{-1/2} \int_{-\infty}^{\infty} \theta_\gamma^2 \theta^2 \exp\left[2\mathrm{i}\left(\mu\theta_\gamma^2 y + \frac{1}{3}y^3\right)\right] \mathrm{d}\theta \mathrm{d}y \\ &= \frac{3\sqrt{\pi}}{2\sqrt{2}\mu} \mathrm{e}^{\mathrm{i}\frac{\pi}{4}} \int_{-\infty}^{\infty} y^{-1/2} \int_{-\infty}^{\infty} (\theta^2 + \gamma^2\theta^4) \exp\left[2\mathrm{i}\mu\gamma^2 y\theta^2\right] \mathrm{d}\theta \exp\left[2\mathrm{i}\left(\mu y + \frac{1}{3}y^3\right)\right] \mathrm{d}y \\ &= T_1 + \gamma^2 T_6 \\ &= \frac{\pi}{\sqrt{3}\gamma^3 x^2} \left[F(x) - G(x)\right] + \frac{3\pi}{4\sqrt{3}\gamma^3 x^2} \left[\frac{2}{3x} H(x) + G(x) - F(x)\right] \\ &= \frac{\pi}{4\sqrt{3}\gamma^3 x^2} \left[\frac{2}{x} H(x) - G(x) + F(x)\right]. \end{aligned} \tag{A.2.19}$$

Integral T_8

$$T_8 = \int_{-\infty}^{\infty} \theta_\gamma^5 \theta^2 K_{1/3}\left(\frac{1}{2}\theta_\gamma^3 x\right) K_{2/3}\left(\frac{1}{2}\theta_\gamma^3 x\right) \mathrm{d}\theta = \frac{\pi}{3\sqrt{3}\gamma^3 x^3} \left[F(x) + G(x)\right] \tag{A.2.20}$$

Derivation. Using the result from integral T_4, we get

$$\begin{aligned} T_8 &= -\mathrm{i}\frac{3\sqrt{\pi}}{2\sqrt{2}\mu^{3/2}} e^{\mathrm{i}\frac{\pi}{4}} \int_{-\infty}^{\infty} y^{1/2} \int_{-\infty}^{\infty} \theta_\gamma^2 \theta^2 \exp\left[2\mathrm{i}\left(\mu\theta_\gamma^2 y + \frac{1}{3}y^3\right)\right] \mathrm{d}\theta \mathrm{d}y \\ &= -\mathrm{i}\frac{3\sqrt{\pi}}{2\sqrt{2}\mu^{3/2}} e^{\mathrm{i}\frac{\pi}{4}} \int_{-\infty}^{\infty} y^{1/2} \int_{-\infty}^{\infty} (\theta^2 + \gamma^2\theta^4) \exp\left[2\mathrm{i}\left(\mu\theta_\gamma^2 y + \frac{1}{3}y^3\right)\right] \mathrm{d}\theta \mathrm{d}y \end{aligned}$$

$$
\begin{aligned}
&= T_4 - \mathrm{i}\frac{3\sqrt{\pi}\gamma^2}{2\sqrt{2}\mu^{3/2}} e^{\mathrm{i}\frac{\pi}{4}} \int_{-\infty}^{\infty} y^{1/2} \int_{-\infty}^{\infty} \theta^4 \exp\left[2\mathrm{i}\mu\gamma^2 y\theta^2\right] \mathrm{d}\theta \exp\left[2\mathrm{i}\left(\mu y + \frac{1}{3}y^3\right)\right] \mathrm{d}y \\
&= T_4 - \frac{9\pi\gamma^2}{8\sqrt{2}\mu^{3/2}} (2\mu\gamma^2)^{-5/2} \int_{-\infty}^{\infty} y^{-2} \exp\left[2\mathrm{i}\left(\mu y + \frac{1}{3}y^3\right)\right] \mathrm{d}y \\
&= T_4 - \frac{9\sqrt{3}\pi}{64\mu^{9/2}\gamma^3} \left[G(x) - F(x)\right] = T_4 - \frac{\pi}{\sqrt{3}\gamma^3 x^3} \left[G(x) - F(x)\right] \\
&= \frac{\pi}{3\sqrt{3}\gamma^3 x^3} \left[F(x) + G(x)\right]. \qquad \text{(A.2.21)}
\end{aligned}
$$

A.3 General modified Bessel function integrals

In this section we will present the relevant equations to derive the functions $\mathcal{J}_n$, $\mathcal{L}_n$ and $\mathcal{R}_n$ in Eq. (5.2.14), that is

$$\mathcal{J}_n = \int_0^\infty x^{n-2} F(x) \mathrm{d}x = \int_0^\infty x^{n-1} \int_x^\infty K_{5/3}(\xi) \mathrm{d}\xi \mathrm{d}x = \frac{\frac{2}{3}+n}{n} \mathcal{L}_n, \qquad \text{(A.3.1a)}$$

$$\mathcal{L}_n = \int_0^\infty x^{n-2} G(x) \mathrm{d}x = \int_0^\infty x^{n-1} K_{2/3}(x) \mathrm{d}x = 2^{n-2}\Gamma\left(\frac{n}{2} - \frac{1}{3}\right)\Gamma\left(\frac{n}{2} + \frac{1}{3}\right), \qquad \text{(A.3.1b)}$$

$$\mathcal{R}_n = \int_0^\infty x^{n-2} H(x) \mathrm{d}x = \int_0^\infty x^{n-1} K_{1/3}(x) \mathrm{d}x = 2^{n-2}\Gamma\left(\frac{n}{2} - \frac{1}{6}\right)\Gamma\left(\frac{n}{2} + \frac{1}{6}\right), \qquad \text{(A.3.1c)}$$

as in [12]. We begin from the useful relation[2] [46]

$$\int_0^\infty x^{n-1} K_\nu(x) \mathrm{d}x = 2^{n-2}\Gamma\left(\frac{1}{2}n - \frac{1}{2}\nu\right)\Gamma\left(\frac{1}{2}n + \frac{1}{2}\nu\right). \qquad \text{(A.3.2)}$$

This integral is valid for $\mathrm{Re}(n) > |\mathrm{Re}(\nu)|$. It is clear that the derivations of $\mathcal{L}_n$ and $\mathcal{R}_n$ are straightforward, however we require additional work for $\mathcal{J}_n$. First we consider the integral which we define as

$$I(x) \equiv \int_0^\infty x^{n-1} \int_x^\infty K_{\nu+1}(\xi) \mathrm{d}\xi \mathrm{d}x. \qquad \text{(A.3.3)}$$

We start by making the substitution $\xi = x + u$, which gives us

$$I(x) = \int_0^\infty \int_x^\infty x^{n-1} K_{\nu+1}(x+u) \mathrm{d}u \mathrm{d}x. \qquad \text{(A.3.4)}$$

Now making another substitution with $v = x + u$ and $w = x - u$, which corresponds to $\mathrm{d}u\mathrm{d}x = \frac{1}{2}\mathrm{d}w\mathrm{d}v$. The limits over the new variable w will then go from $-v$ to v. Consequently, the integral may be written as

$$I(x) = \frac{1}{2}\int_0^\infty K_{\nu+1}(v) \int_{-v}^{v} \left[\frac{1}{2}(v+w)\right]^{n-1} \mathrm{d}w\mathrm{d}v. \qquad \text{(A.3.5)}$$

The innermost integral over w is

$$\int_{-v}^{v} \left[\frac{1}{2}(v+w)\right]^{n-1} \mathrm{d}w = 2\frac{v^n}{n}, \qquad \text{(A.3.6)}$$

and so

$$I(x) = \frac{1}{n}\int_0^\infty v^n K_{\nu+1}(v) \mathrm{d}v. \qquad \text{(A.3.7)}$$

[2] The derivation of this relation is complicated and we proceed with no proof. The relation is the equation 11.4.22 in [46], as well as 10.43.19 in [65], and we reference the reader to chapter 13.21 of [42] for further context.

Using Eq. (A.3.2), we find that

$$\begin{aligned} I(x) &= \frac{1}{n}2^{n-1}\Gamma\left(\frac{1}{2}(n+1)-\frac{1}{2}(\nu+1)\right)\Gamma\left(\frac{1}{2}(n+1)+\frac{1}{2}(\nu+1)\right) \\ &= \frac{2}{n}2^{n-2}\Gamma\left(\frac{1}{2}n-\frac{1}{2}\nu\right)\Gamma\left(\frac{1}{2}n+\frac{1}{2}\nu+1\right) \\ &= \frac{2}{n}2^{n-2}\frac{1}{2}(n+\nu)\Gamma\left(\frac{1}{2}n-\frac{1}{2}\nu\right)\Gamma\left(\frac{1}{2}n+\frac{1}{2}\nu\right) \\ &= \frac{n+\nu}{n}\int_0^\infty x^{n-1}K_\nu(x)\mathrm{d}x, \end{aligned} \tag{A.3.8}$$

where we have used the property that $\Gamma(z+1) = z\Gamma(z)$ in the second to last line. The integral $\mathcal{J}_n$ follows by simply inserting $\nu = 2/3$ in the expression for $I(x)$.

Appendix B

Second order pitch angle distribution approximation

In Sec. 5.2 we performed an approximation of $\phi(\alpha)\sin\alpha$ to first order, and we now wish to consider the effects on the polarisation if the second order approximation is made. This treatment was attempted by De Búrca and Shearer [62], motivated by the degree of circular polarisation exceeding 1 for strong magnetic fields as seen in Fig. 5.4. We will in this appendix present a derivation of the Stokes parameters in the second order pitch angle distribution approximation, as well as discuss the relevance of the resulting polarisation degrees.

B.1 Emission-polarisation tensor

Following a similar approach to that in chapter 5, we may write, to second order,

$$\begin{aligned}\phi(\alpha)\sin\alpha = f(\alpha) &= f(\psi) + f'(\psi)(\alpha-\psi) + \frac{1}{2}f''(\psi)(\alpha-\psi)^2 \\ &= f(\psi) + g(\psi)\theta + \frac{1}{2}h(\psi)\theta^2,\end{aligned} \tag{B.1.1}$$

where $f(\alpha)$ and $g(\alpha)$ are the functions defined in Eq. (5.2.3), and

$$h(\alpha) \equiv f''(\alpha) = \phi''(\alpha)\sin\alpha + 2\phi'(\alpha)\cos\alpha - \phi(\alpha)\sin\alpha. \tag{B.1.2}$$

The emission-polarisation tensor in Eq. (5.2.2) becomes

$$j = \int_0^\infty n_e(\gamma)\int_{-\infty}^{\infty}\left[f(\psi) + g(\psi)\theta + \frac{1}{2}h(\psi)\theta^2\right]\rho_x \mathrm{d}\theta\mathrm{d}\gamma, \tag{B.1.3}$$

where the range of θ is taken between $-\infty$ and ∞. It is clear that the second order pitch angle distribution approximation implies the addition of the integral

$$j^{(2)} \equiv \int_0^\infty n_e(\gamma)\int_{-\infty}^{\infty}\frac{1}{2}h(\psi)\theta^2\rho_x \mathrm{d}\theta\mathrm{d}\gamma = \int_0^\infty I_x^{(2)} n_e(\gamma)\mathrm{d}\gamma \tag{B.1.4}$$

to the emission-polarisation tensor obtained in the first order approximation. We have here defined

$$I_x^{(2)} \equiv \int_{-\infty}^{\infty}\frac{1}{2}h(\psi)\theta^2\rho_x \mathrm{d}\theta. \tag{B.1.5}$$

Calculation of j_{11}

Considering the first component of the polarisation tensor $j^{(2)}$, we get that

$$\begin{aligned} I^{(2)}_{x_{11}} &= \frac{3e^2}{4\pi^2 c}\omega_B x^2\gamma^2\frac{1}{2}h(\psi)\int_{-\infty}^{\infty}\theta^2\theta_\gamma^4 K^2_{2/3}\left(\frac{1}{2}\theta_\gamma^3 x\right)\mathrm{d}\theta \\ &= \frac{3e^2}{8\pi^2 c}\frac{eB}{\gamma mc}x^2\gamma^2 h(\psi)\frac{\pi}{4\sqrt{3}\gamma^3x^2}\left[\frac{10}{3x}H(x)+G(x)-F(x)\right] \\ &= \frac{\sqrt{3}e^3B}{32\pi mc^2}h(\psi)\frac{1}{\gamma^2}\left[\frac{10}{3x}H(x)+G(x)-F(x)\right], \end{aligned} \tag{B.1.6}$$

using Eq. (A.2.9) in the second line. The addition of this term is not consistent with the approximation in $1/\gamma$ followed throughout chapter 5. We proceed however without investigating the possible higher order additions to the frequency polarisation tensor ρ_x in Eq. (5.1.17).

We note that

$$\frac{1}{\gamma^2} = \frac{3}{2}\frac{\nu_{B_0}\sin\psi}{\nu}x, \tag{B.1.7}$$

and recall the expression for $n_e(\gamma)\mathrm{d}\gamma$ in Eq. (5.2.13). Integrating over the Lorentz factor γ gives then

$$\begin{aligned} j^{(2)}_{11} &= \int_0^\infty I^{(2)}_{x_{11}} n_e(\gamma)\mathrm{d}\gamma \\ &= \int_0^\infty \frac{3\sqrt{2}e^3B}{128\pi mc^2}h(\psi)\left[\frac{10}{3x}H(x)+G(x)-F(x)\right]C\left(\frac{3}{2}\right)^{p/2}\frac{(\nu_{B_0}\sin\psi)^{(p+1)/2}}{\nu^{(p+1)/2}}x^{(p-1)/2}\mathrm{d}x \\ &= \frac{3h(\psi)}{16}\left(\frac{\nu_{B_0}}{\nu}\right)C\frac{e^3B}{4\sqrt{2}\pi mc^2}\left(\frac{3}{2}\right)^{p/2}(\sin\psi)^{(p+1)/2}\left(\frac{\nu_{B_0}}{\nu}\right)^{(p-1)/2}I_{j_{11}}, \end{aligned} \tag{B.1.8}$$

where

$$\begin{aligned} I_{j_{11}} &\equiv \int_0^\infty\left[\frac{10}{3x}H(x)+G(x)-F(x)\right]x^{(p-1)/2}\mathrm{d}x \\ &= \frac{10}{3}\mathcal{R}_{(p+1)/2}+\mathcal{L}_{(p+3)/2}-\mathcal{J}_{(p+3)/2}, \end{aligned} \tag{B.1.9}$$

by using the functions in Eq. (5.2.14). Including the $j^{(2)}_{11}$ term to the emission-polarisation tensor term j_{11} from Eq. (5.2.18), we get that in the second approximation,

$$\begin{aligned} j_{11} = C\frac{e^3B}{4\sqrt{2}\pi mc^2}\left(\frac{3}{2}\right)^{p/2}(\sin\psi)^{(p+1)/2}\left(\frac{\nu_{B_0}}{\nu}\right)^{(p-1)/2} \\ \times\left\{\phi(\psi)\left[\mathcal{J}_{(p+1)/2}+\mathcal{L}_{(p+1)/2}\right]+\frac{3h(\psi)}{16}\left(\frac{\nu_{B_0}}{\nu}\right)\left[\frac{10}{3}\mathcal{R}_{(p+1)/2}+\mathcal{L}_{(p+3)/2}-\mathcal{J}_{(p+3)/2}\right]\right\}. \end{aligned} \tag{B.1.10}$$

Calculation of j_{22}

We first note that as we are considering a higher order approximation in $1/\gamma$, we need to include the term proportional to $g(\psi)$ in Eq. (5.2.20). In the first order pitch angle distribution approximation, we therefore have to include the term

$$I'_{x_{22}} = \frac{\sqrt{3}e^3B}{16\pi mc^2}g(\psi)\cot\psi\frac{1}{\gamma^2}\left[\frac{2}{x}H(x)-G(x)+F(x)\right]. \tag{B.1.11}$$

We see that this is the same expression as the expression in Eq. (B.1.6) multiplied by 2, except for that the function $H(x)/x$ is now proportional to 2 and not 10/3, as well as the signs in front

of $G(x)$ and $F(x)$ are reversed. The function $h(x)$ is also replaced with $g(x)\cot\psi$. It is then simple to find that

$$j'_{22} = \frac{3g(\psi)\cot\psi}{8}\left(\frac{\nu_{B_0}}{\nu}\right) C\frac{e^3B}{4\sqrt{2}\pi mc^2}\left(\frac{3}{2}\right)^{p/2}(\sin\psi)^{(p+1)/2}\left(\frac{\nu_{B_0}}{\nu}\right)^{(p-1)/2} I'_{j_{22}}, \tag{B.1.12}$$

where

$$I'_{j_{22}} \equiv 2\mathcal{R}_{(p+1)/2} - \mathcal{L}_{(p+3)/2} + \mathcal{J}_{(p+3)/2}. \tag{B.1.13}$$

Now for the term in the second order pitch angle distribution approximation, we get that

$$\begin{aligned} I^{(2)}_{x_{22}} &= \frac{3e^2}{4\pi^2 c}\omega_B x^2\gamma^4\frac{1}{2}h(\psi)\int_{-\infty}^{\infty}\theta^2\left(\theta^2\theta_\gamma^2 + \frac{\theta\theta_\gamma^4}{\gamma^2}\cot\alpha\right)K_{1/3}^2\left(\frac{1}{2}\theta_\gamma^3 x\right)\mathrm{d}\theta \\ &= \frac{3e^2}{8\pi^2 c}\frac{eB}{\gamma mc}x^2\gamma^4 h(\psi)\int_{-\infty}^{\infty}\theta^4\theta_\gamma^2 K_{1/3}^2\left(\frac{1}{2}\theta_\gamma^3 x\right)\mathrm{d}\theta \\ &= \frac{3e^3B}{8\pi^2 mc^2}x^2\gamma^3 h(\psi)\frac{3\pi}{4\sqrt{3}\gamma^5 x^2}\left[\frac{2}{3x}H(x) + G(x) - F(x)\right] \\ &= \frac{3\sqrt{3}e^3B}{32\pi mc^2}h(\psi)\frac{1}{\gamma^2}\left[\frac{2}{3x}H(x) + G(x) - F(x)\right]. \end{aligned} \tag{B.1.14}$$

In the second line we have removed the second term within the parenthesis as this becomes odd in θ and disappears upon integration, and in the following line we have used Eq. (A.2.16). Once again, we see the similarities with (B.1.6), and get that

$$j^{(2)}_{22} = \frac{9h(\psi)}{16}\left(\frac{\nu_{B_0}}{\nu}\right) C\frac{e^3B}{4\sqrt{2}\pi mc^2}\left(\frac{3}{2}\right)^{p/2}(\sin\psi)^{(p+1)/2}\left(\frac{\nu_{B_0}}{\nu}\right)^{(p-1)/2} I_{j_{22}}, \tag{B.1.15}$$

where

$$I_{j_{22}} \equiv \frac{2}{3}\mathcal{R}_{(p+1)/2} + \mathcal{L}_{(p+3)/2} - \mathcal{J}_{(p+3)/2}. \tag{B.1.16}$$

In the second order approximation, we therefore obtain the component

$$\begin{aligned} j_{22} = C\frac{e^3B}{4\sqrt{2}\pi mc^2}&\left(\frac{3}{2}\right)^{p/2}(\sin\psi)^{(p+1)/2}\left(\frac{\nu_{B_0}}{\nu}\right)^{(p-1)/2} \\ &\times\Bigg\{\phi(\psi)\left[\mathcal{J}_{(p+1)/2} - \mathcal{L}_{(p+1)/2}\right] \\ &\quad + \frac{3g(\psi)\cot\psi}{8}\left(\frac{\nu_{B_0}}{\nu}\right)\left[2\mathcal{R}_{(p+1)/2} - \mathcal{L}_{(p+3)/2} + \mathcal{J}_{(p+3)/2}\right] \\ &\quad + \frac{9h(\psi)}{16}\left(\frac{\nu_{B_0}}{\nu}\right)\left[\frac{2}{3}\mathcal{R}_{(p+1)/2} + \mathcal{L}_{(p+3)/2} - \mathcal{J}_{(p+3)/2}\right]\Bigg\}. \end{aligned} \tag{B.1.17}$$

Calculation of j_{12} and j_{21}

By the same procedure as in Sec. 5.1, we consider only j_{21} and know that $j_{12} = -j_{21}$. We get

$$\begin{aligned} I^{(2)}_{x_{21}} &= \mathrm{i}\frac{3e^2}{4\pi^2 c}\omega_B x^2\gamma^3\frac{1}{2}h(\psi)\frac{1}{2\gamma^2}\cot\psi\int_{-\infty}^{\infty}\theta^2\theta_\gamma^5 K_{2/3}\left(\frac{1}{2}\theta_\gamma^3 x\right)K_{1/3}\left(\frac{1}{2}\theta_\gamma^3 x\right)\mathrm{d}\theta \\ &= \mathrm{i}\frac{3e^2}{16\pi^2 c}\frac{eB}{\gamma mc}x^2\gamma h(\psi)\cot\psi\frac{\pi}{3\sqrt{3}\gamma^3 x^3}\left[F(x) + G(x)\right] \\ &= \mathrm{i}\frac{\sqrt{3}e^3B}{48\pi mc^2}h(\psi)\cot\psi\frac{1}{\gamma^3 x}\left[F(x) + G(x)\right], \end{aligned} \tag{B.1.18}$$

using Eq. (A.2.20). We have that

$$\frac{1}{\gamma^3 x} n_e(\gamma)\mathrm{d}\gamma = C\frac{3}{4}\left(\frac{3}{2}\right)^{p/2} \frac{(\nu_{B_0}\sin\psi)^{p/2+1}}{\nu^{p/2+1}} x^{p/2-1}, \tag{B.1.19}$$

and so

$$\begin{aligned} j_{21}^{(2)} &= \int_0^\infty I_{x21}^{(2)} n_e(\gamma)\mathrm{d}\gamma \\ &= \int_0^\infty \mathrm{i}\frac{\sqrt{3}e^3 B}{64\pi mc^2} h(\psi)\cot\psi\left[F(x)+G(x)\right] C\left(\frac{3}{2}\right)^{p/2} \frac{(\nu_{B_0}\sin\psi)^{p/2+1}}{\nu^{p/2+1}} x^{p/2-1}\mathrm{d}x \\ &= \frac{3h(\psi)}{8}\left(\frac{\nu_{B_0}}{\nu}\right)\mathrm{i}C\frac{e^3 B}{8\sqrt{3}\pi mc^2}\left(\frac{3}{2}\right)^{p/2}\cot\psi(\sin\psi)^{p/2+1}\left(\frac{\nu_{B_0}}{\nu}\right)^{p/2} I_{j_{21}}, \end{aligned} \tag{B.1.20}$$

where

$$I_{j_{21}} \equiv \int_0^\infty \left[F(x)+G(x)\right] x^{p/2-1}\mathrm{d}x = \mathcal{J}_{p/2+1} + \mathcal{L}_{p/2+1}. \tag{B.1.21}$$

Finally, the last component of the emission-polarisation tensor j in the second order pitch angle distribution approximation is

$$\begin{aligned} j_{21} = \mathrm{i}C\frac{e^3 B}{8\sqrt{3}\pi mc^2}&\left(\frac{3}{2}\right)^{p/2}\cot\psi(\sin\psi)^{p/2+1}\left(\frac{\nu_{B_0}}{\nu}\right)^{p/2} \\ &\times\Bigg\{\left[\phi'(\psi)\tan\psi+\phi(\psi)\right]\left[4\mathcal{L}_{p/2}-2\mathcal{J}_{p/2}\right] + \phi(\psi)\left[3\mathcal{R}_{p/2+1}+2\mathcal{L}_{p/2}-\mathcal{J}_{p/2}\right] \\ &\quad + \frac{3h(\psi)}{8}\left(\frac{\nu_{B_0}}{\nu}\right)\left[\mathcal{J}_{p/2+1}+\mathcal{L}_{p/2+1}\right]\Bigg\}. \end{aligned} \tag{B.1.22}$$

Isotropic velocity distribution

For an isotropic velocity distribution we used in Sec. 5.1 that $\phi'(\psi) = 0$. Then $\phi''(\psi) = 0$ as well, and we have that the functions f, g and h become

$$f(\psi) = \phi(\psi)\sin\psi, \tag{B.1.23a}$$
$$g(\psi) = \phi(\psi)\cos\psi, \tag{B.1.23b}$$
$$h(\psi) = -\phi(\psi)\sin\psi. \tag{B.1.23c}$$

Simplifying the components of the emission-polarisation tensor consequently give

$$\begin{aligned} j_{11} = C\frac{e^3 B}{4\sqrt{2}\pi mc^2}&\left(\frac{3}{2}\right)^{p/2}(\sin\psi)^{(p+1)/2}\left(\frac{\nu_{B_0}}{\nu}\right)^{(p-1)/2}\phi(\psi) \\ &\times\left\{\left[\mathcal{J}_{(p+1)/2}+\mathcal{L}_{(p+1)/2}\right] - \frac{3\sin\psi}{16}\left(\frac{\nu_{B_0}}{\nu}\right)\left[\frac{10}{3}\mathcal{R}_{(p+1)/2}+\mathcal{L}_{(p+3)/2}-\mathcal{J}_{(p+3)/2}\right]\right\}, \end{aligned} \tag{B.1.24a}$$

$$\begin{aligned} j_{12} = -\mathrm{i}C\frac{\sqrt{3}e^3 B}{8\pi mc^2}&\left(\frac{3}{2}\right)^{p/2}\cot\psi(\sin\psi)^{p/2+1}\left(\frac{\nu_{B_0}}{\nu}\right)^{p/2}\phi(\psi) \\ &\times\left\{\left[\mathcal{R}_{p/2+1}+2\mathcal{L}_{p/2}-\mathcal{J}_{p/2}\right] - \frac{\sin\psi}{8}\left(\frac{\nu_{B_0}}{\nu}\right)\left[\mathcal{J}_{p/2+1}+\mathcal{L}_{p/2+1}\right]\right\}, \end{aligned} \tag{B.1.24b}$$

$$\begin{aligned} j_{21} = \mathrm{i}C\frac{\sqrt{3}e^3 B}{8\pi mc^2}&\left(\frac{3}{2}\right)^{p/2}\cot\psi(\sin\psi)^{p/2+1}\left(\frac{\nu_{B_0}}{\nu}\right)^{p/2}\phi(\psi) \\ &\times\left\{\left[\mathcal{R}_{p/2+1}+2\mathcal{L}_{p/2}-\mathcal{J}_{p/2}\right] - \frac{\sin\psi}{8}\left(\frac{\nu_{B_0}}{\nu}\right)\left[\mathcal{J}_{p/2+1}+\mathcal{L}_{p/2+1}\right]\right\}, \end{aligned} \tag{B.1.24c}$$

$$
\begin{aligned}
j_{22} = C\frac{e^3 B}{4\sqrt{2}\pi mc^2}\left(\frac{3}{2}\right)^{p/2}(\sin\psi)^{(p+1)/2}\left(\frac{\nu_{B_0}}{\nu}\right)^{(p-1)/2}\phi(\psi) \\
\times\Bigg\{\left[\mathcal{J}_{(p+1)/2}-\mathcal{L}_{(p+1)/2}\right] \\
+\frac{3\cos\psi\cot\psi}{8}\left(\frac{\nu_{B_0}}{\nu}\right)\left[2\mathcal{R}_{(p+1)/2}-\mathcal{L}_{(p+3)/2}+\mathcal{J}_{(p+3)/2}\right] \\
-\frac{9\sin\psi}{16}\left(\frac{\nu_{B_0}}{\nu}\right)\left[\frac{2}{3}\mathcal{R}_{(p+1)/2}+\mathcal{L}_{(p+3)/2}-\mathcal{J}_{(p+3)/2}\right]\Bigg\}. \qquad \text{(B.1.24d)}
\end{aligned}
$$

B.2 Stokes parameters and polarisation

We now consider the Stokes parameters as defined in Sec. 5.3. We will assume an isotropic velocity distribution and therefore use the components of the emission-polarisation tensor in Eq. (B.1.24). The Stokes parameters are then

$$
\begin{aligned}
j_I = C\frac{e^3 B}{2\sqrt{2}\pi mc^2}\left(\frac{3}{2}\right)^{p/2}(\sin\psi)^{(p+1)/2}\left(\frac{\nu_{B_0}}{\nu}\right)^{(p-1)/2}\phi(\psi) \\
\times\Bigg\{\mathcal{J}_{(p+1)/2}+\frac{3\cos\psi\cot\psi}{16}\left(\frac{\nu_{B_0}}{\nu}\right)\left[2\mathcal{R}_{(p+1)/2}-\mathcal{L}_{(p+3)/2}+\mathcal{J}_{(p+3)/2}\right] \\
-\frac{\sin\psi}{8}\left(\frac{\nu_{B_0}}{\nu}\right)\left[2\mathcal{R}_{(p+1)/2}+3\mathcal{L}_{(p+3)/2}-3\mathcal{J}_{(p+3)/2}\right]\Bigg\}, \qquad \text{(B.2.1a)} \\
j_Q = C\frac{e^3 B}{2\sqrt{2}\pi mc^2}\left(\frac{3}{2}\right)^{p/2}(\sin\psi)^{(p+1)/2}\left(\frac{\nu_{B_0}}{\nu}\right)^{(p-1)/2}\phi(\psi) \\
\times\Bigg\{\mathcal{L}_{(p+1)/2}-\frac{3\cos\psi\cot\psi}{16}\left(\frac{\nu_{B_0}}{\nu}\right)\left[2\mathcal{R}_{(p+1)/2}-\mathcal{L}_{(p+3)/2}+\mathcal{J}_{(p+3)/2}\right] \\
-\frac{\sin\psi}{16}\left(\frac{\nu_{B_0}}{\nu}\right)\left[\mathcal{R}_{(p+1)/2}-3\mathcal{L}_{(p+3)/2}+3\mathcal{J}_{(p+3)/2}\right]\Bigg\}, \qquad \text{(B.2.1b)} \\
j_U = 0, \qquad \text{(B.2.1c)} \\
j_V = C\frac{\sqrt{3}e^3 B}{4\pi mc^2}\left(\frac{3}{2}\right)^{p/2}\cot\psi(\sin\psi)^{p/2+1}\left(\frac{\nu_{B_0}}{\nu}\right)^{p/2}\phi(\psi) \\
\times\left\{\left[\mathcal{R}_{p/2+1}+2\mathcal{L}_{p/2}-\mathcal{J}_{p/2}\right]-\frac{\sin\psi}{8}\left(\frac{\nu_{B_0}}{\nu}\right)\left[\mathcal{J}_{p/2+1}+\mathcal{L}_{p/2+1}\right]\right\}. \qquad \text{(B.2.1d)}
\end{aligned}
$$

The difference in the stokes parameters in the second order approximation as opposed to the first order approximation is the addition of the terms proportional to ν_{B_0}/ν within the curly brackets. We have that

$$
\frac{\nu_{B_0}}{\nu} \simeq \frac{10^6}{\nu} B\left[\frac{\text{Hz}}{\text{G}}\right], \qquad \text{(B.2.2)}
$$

and for e.g. the frequency $\nu \simeq 10^{14}\,\text{Hz}$, this factor only contributes significantly when B is very large. It has to be of the order $10^6 - 10^8\,\text{G}$, also depending on the angle ψ, to contribute to the Stokes parameters. We therefore expect the degree of circular and linear polarisation to deviate from the first order approximation at high values of the magnetic field strength B. In Fig. B.1 and B.2 we see exactly this. The degree of circular and linear polarisation changes significantly from the first order approximation once the magnetic field strength reaches high enough values for the additional terms to contribute.

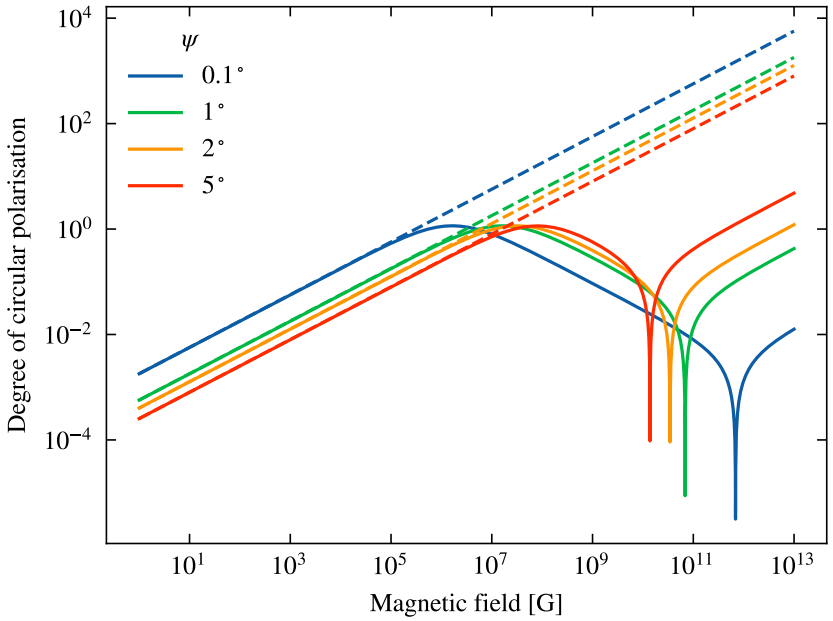

Figure B.1: Degree of circular polarisation for a power-law electron distribution as function of magnetic field strength B for different pitch angle deviations ψ in the second order pitch angle distribution approximation. The first order pitch angle distribution approximation is showed in dashed lines. The other parameters are fixed, with frequency $\nu = 5 \times 10^{14}$ Hz and particle distribution index $p = 1.4$.

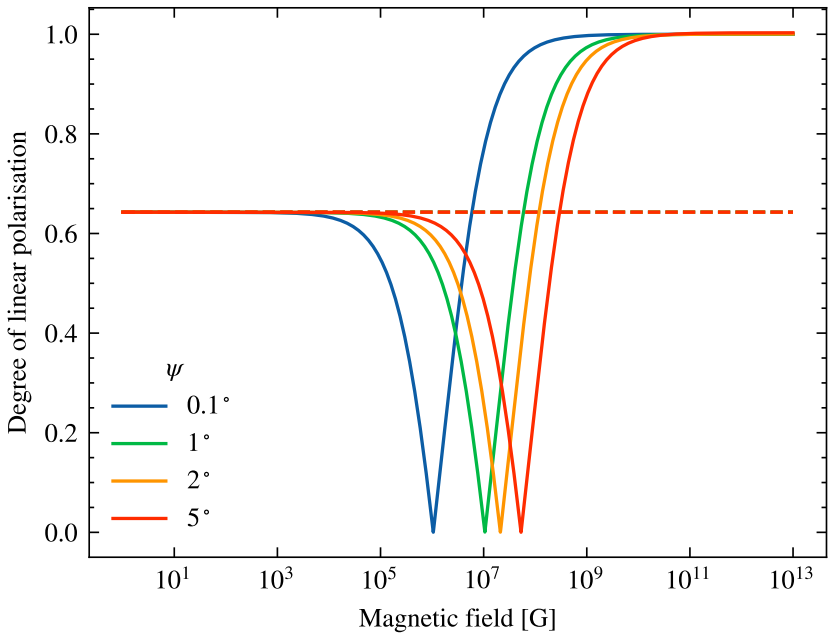

Figure B.2: Degree of linear polarisation for a power-law electron distribution as function of magnetic field strength B for different pitch angle deviations ψ in the second order pitch angle distribution approximation. The first order pitch angle distribution approximation is showed in dashed lines. The other parameters are fixed, with frequency $\nu = 5 \times 10^{14}$ Hz and particle distribution index $p = 1.4$.

B.3 Discussion

There are several major differences from the work of De Búrca and Shearer [62] compared to our results. In both cases the circular and linear polarisation degree changes behaviour in the approximate range of magnetic field strength $10^5 - 10^8$ G. In [62], the degree of circular polarisation does not exceed 1, but this is not true with our calculations. In fact, the maximum circular polarisation degree is about 1.15 for all ψ in the range where the second order approximation deviates from the first. The circular polarisation also clearly exceeds 1 for even stronger magnetic fields. We may note, however, that upon using the formulas of [62], the circular polarisation degree does exceed 1 for larger values of the particle distribution index p. For the frequency $\nu = 5 \times 10^{14}$ Hz and pitch angle deviation $\psi = 1°$, the maximum circular polarisation degree as function of p using the formulas of [62] is plotted in Fig. B.3. Here we have used the particle pitch angle distribution

$$\phi(\alpha) = \frac{\sin\alpha}{\sin\alpha_{\max}}, \tag{B.3.1}$$

where $\sin\alpha_{\max}$ is a constant that drops out upon calculating the polarisation degrees. The degree of circular polarisation exceeds 1 for values of p greater than approximately 7.8. Although these high values of p describe unlikely physical situations, these situations are entirely possible.

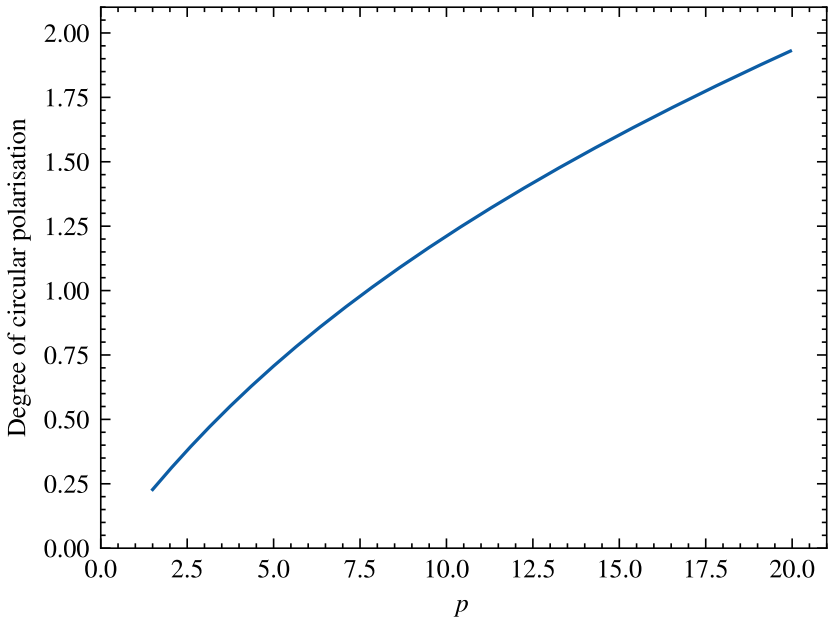

Figure B.3: Maximum degree of circular polarisation function of particle distribution index p in the second order pitch angle distribution approximation by [62]. The frequency is $\nu = 5 \times 10^{14}$ Hz and the pitch angle deviation is $\psi = 1°$.

In Sec. 8.1 we argue that the degree of circular polarisation is only valid for weak magnetic fields. It is therefore reasonable to assume that considering the second order pitch angle distribution is redundant as it does not change the behaviour in the relevant range of B. The somewhat strange behaviour of the polarisation degrees in the second order pitch angle distribution may therefore be irrelevant to analyse any further.

It is still interesting to discuss the differences from the article [62] to the work done here. The first thing to note is the approximation made in γ^{-1} in the derivation of the components of the radiation field. We have used an approximation to the order γ^{-2}, while [62] have only considered the order γ^{-1}. That is, the component proportional to $\cot\alpha$ in Eq. (3.5.22) has not

been included in the article. Legg and Westfold [12] argue that the higher order approximation is necessary for the degree of circular polarisation.

Furthermore, we note the integrals used by [62] and derived in their supplementary materials. The general θ-integrals

$$\Theta_1 \equiv \int_{-\infty}^{\infty} \theta_\gamma^a \theta^{2b} K_{1/3}^2 \left(\frac{1}{2}\theta_\gamma^3 x\right) \mathrm{d}\theta, \tag{B.3.2a}$$

$$\Theta_2 \equiv \int_{-\infty}^{\infty} \theta_\gamma^a \theta^{2b} K_{2/3}^2 \left(\frac{1}{2}\theta_\gamma^3 x\right) \mathrm{d}\theta, \tag{B.3.2b}$$

$$\Theta_3 \equiv \int_{-\infty}^{\infty} \theta_\gamma^a \theta^{2b} K_{1/3} \left(\frac{1}{2}\theta_\gamma^3 x\right) K_{2/3} \left(\frac{1}{2}\theta_\gamma^3 x\right) \mathrm{d}\theta, \tag{B.3.2c}$$

are defined for integers a and b. These are consequently simplified to

$$\Theta_1 = \sqrt{3} \int_0^{\infty} \int_0^{2\pi} \left(1 + R^2 \sin^2\phi\right)^{a-2} \left(\frac{R\sin\phi}{\gamma}\right)^{2b} \times \left(1+R^2\right)^{1/2} K_{1/3}\left[x\left(1+R^2\right)^{3/2}\right] \frac{1}{\gamma} R \mathrm{d}\phi \mathrm{d}R, \tag{B.3.3a}$$

$$\Theta_2 = \sqrt{3} \int_0^{\infty} \int_0^{2\pi} \left(1 + R^2 \sin^2\phi\right)^{a-4} \left(\frac{R\sin\phi}{\gamma}\right)^{2b} \left(\frac{3R^2}{2}+1\right) \times \left(1+R^2\right)^{1/2} K_{1/3}\left[x\left(1+R^2\right)^{3/2}\right] \frac{1}{\gamma} R \mathrm{d}\phi \mathrm{d}R, \tag{B.3.3b}$$

$$\Theta_3 = \sqrt{3} \int_0^{\infty} \int_0^{2\pi} \left(1 + R^2 \sin^2\phi\right)^{a-3} \left(\frac{R\sin\phi}{\gamma}\right)^{2b} \times \left(1+R^2\right) K_{2/3}\left[x\left(1+R^2\right)^{3/2}\right] \frac{1}{\gamma} R \mathrm{d}\phi \mathrm{d}R, \tag{B.3.3c}$$

and solved using modified Bessel function integrals easily derived from the properties in Eq. (A.1.5). This is done by conveniently making the substitution $\xi = x\left(1+R^2\right)^{3/2}$ and integrating over ξ instead of R. Then the new limits over ξ are from x to ∞. However, the simplifications from Eq. (B.3.2) to Eq. (B.3.3) are not valid for arbitrary integers a and b. As an example, we plot Eq. (B.3.2b), denoted LHS, against Eq. (B.3.3b), denoted RHS, for some selected values of a and b in Fig. B.4. Clearly, the cases $\{a,b\} = \{2,0\}$, $\{2,1\}$ and $\{4,1\}$ are not correct, while the case $\{a,b\} = \{4,0\}$ seems to be accurate. There is a need for some restriction on the integers a and b which is not given by [62].

The expressions in Eq. (B.3.3) are correct for most of the relevant set of integers $\{a,b\}$ used in the calculations by [62]. The only case used in the article where the simplification is not valid is for Θ_2 with $a=4$ and $b=1$ as seen in Fig. B.4. The given expression by [62] is

$$\int_{-\infty}^{\infty} \theta_\gamma^4 \theta^2 K_{2/3}^2 \left(\frac{1}{2}\theta_\gamma^3 x\right) \mathrm{d}\theta = \frac{\pi}{2\sqrt{3}\gamma^3 x} \int_x^{\infty} \left[3\left(\frac{\xi}{x}\right)^{4/3} - 4\left(\frac{\xi}{x}\right)^{2/3} + 1\right] K_{1/3}(\xi)\mathrm{d}\xi. \tag{B.3.4}$$

Using that[1]

$$\int_x^{\infty} \left(\frac{\xi}{x}\right)^{4/3} K_{1/3}(\xi)\mathrm{d}\xi = K_{4/3}(x) = K_{2/3}(x) + \frac{2}{3x} K_{1/3}(x), \tag{B.3.5a}$$

$$\int_x^{\infty} \left(\frac{\xi}{x}\right)^{2/3} K_{1/3}(\xi)\mathrm{d}\xi = K_{2/3}(x), \tag{B.3.5b}$$

[1] These integrals can be shown by using the properties of the modified Bessel functions in Eq. (A.1.5).

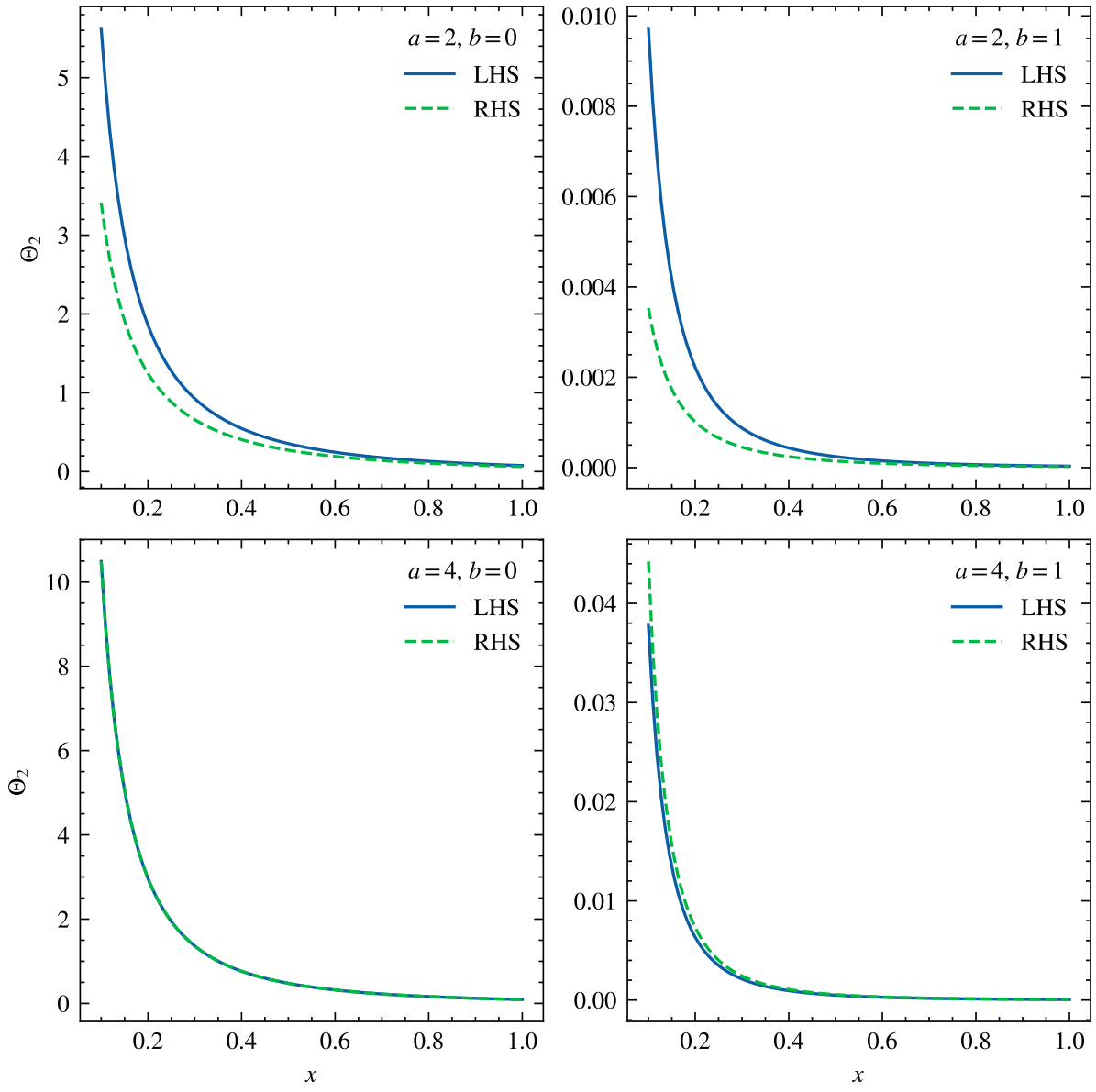

Figure B.4: The function Θ_2 in terms of x. Four set of values of a and b are chosen, and $v = 0.999c$ is used.

$$\int_x^\infty K_{1/3}(\xi)\mathrm{d}\xi = 2K_{2/3}(x) - \frac{1}{x}F(x), \tag{B.3.5c}$$

this integral is simplified to

$$\int_{-\infty}^{\infty} \theta_\gamma^4\theta^2 K_{2/3}^2\left(\frac{1}{2}\theta_\gamma^3 x\right)\mathrm{d}\theta = \frac{\pi}{2\sqrt{3}\gamma^3x^2}\left[\frac{2}{x}H(x) + G(x) - F(x)\right]. \tag{B.3.6}$$

This is not consistent with our derivation in appendix A.2, which resulted in integral T_3 of Eq. (A.2.9). The difference is the factor 2 in front of the function $H(x)$, where we found that this factor should be 10/3. Our correction of the integral is minor, and the effect on the polarisation degree should not necessarily be significant.

Appendix C

Nomenclature

Throughout the thesis we have used several abbreviations, symbols and physical constants. Here, we present an overview of the most important ones for easy reference for the reader.

C.1 Abbreviations

AMS	Alpha Magnetic Spectrometer
C-BASS	C-Band All Sky Survey
CMB	cosmic microwave background
CR	cosmic ray
DM	dispersion measure
EBL	extragalactic background light
EHT	Event Horizon Telescope
FD	Faraday depth
FOV	field of view
GMF	Galactic magnetic field
GRM	Galactic rotation measure
ISM	interstellar medium
ISS	International Space Station
LHS	left-hand side
LIS	local interstellar spectra
LoS	line-of-sight
MAD	mean absolute deviation
MHD	magnetohydrodynamic
ODE	ordinary differential equation
PDE	partial differential equation
QED	quantum electrodynamics
RHS	right-hand side
RM	rotation measure
RMS	root mean square
RRM	residual rotation measure
RTE	radiative transfer equation
SD	standard deviation
TA	Telescope Array
UHECR	ultra-high-energy cosmic ray

C.2 Symbols

In the following list, symbols representing the most important quantities used in the thesis are presented along with their names and units. The most standard symbols such as v for velocity, E for energy, etc. are not included. Furthermore, no vectors are included, but we specify that vectors in the text are written in bold, e.g. $\mathbf{v}$ for the velocity such that its norm is $v \equiv |\mathbf{v}|$. Note also that the list contains subscripts only when strictly necessary for the context.

Symbol	Name	Unit
ω_B	Angular frequency of rotation	s^{-1}
L_c	Correlation length	cm
ω_c	Critical angular frequency	s^{-1}
ν_c	Critical frequency	s^{-1}
Π	Degree of polarisation	—
D	Diffusion coefficient	$\mathrm{cm}^2\,\mathrm{s}^{-1}$
n_e	Electron number density[1]	cm^{-3}
ρ	Emission-polarisation tensor	$\mathrm{cm}^2\,\mathrm{g}\,\mathrm{s}^{-3}$
j	Emission-polarisation tensor[2]	$\mathrm{cm}^{-1}\,\mathrm{g}\,\mathrm{s}^{-2}$
j_ν	Emissivity	$\mathrm{cm}^{-1}\,\mathrm{g}\,\mathrm{s}^{-2}\,\mathrm{sr}^{-1}$
ν	Frequency	s^{-1}
ρ_x	Frequency polarisation tensor	$\mathrm{cm}^2\,\mathrm{g}\,\mathrm{s}^{-2}$
I_ν	Intensity	$\mathrm{g}\,\mathrm{s}^{-2}\,\mathrm{sr}^{-1}$
γ	Lorentz factor	—
B	Magnetic field strength	$\mathrm{G} = \mathrm{cm}^{-1/2}\,\mathrm{g}^{1/2}\,\mathrm{s}^{-1}$
n_k	Number of turbulent modes	—
p	Particle distribution index	—
α	Pitch angle	rad
ψ	Pitch angle deviation	rad
ϕ	Pitch angle distribution function	—
θ	Polar angle[3]	rad
P	Power per frequency	$\mathrm{cm}^2\,\mathrm{g}\,\mathrm{s}^{-2}$
$\mathcal{P}$	Power per frequency per unit volume	$\mathrm{cm}^{-1}\,\mathrm{g}\,\mathrm{s}^{-2}$
a	Radius of curvature	cm
E_0	Rest mass energy	$\mathrm{erg} = \mathrm{g}\,\mathrm{cm}^2\,\mathrm{s}^{-2}$
z_t	Scale height	cm

C.3 Physical constants

Relevant physical constants with values converted to Gaussian-cgs units from the NIST Constant Index [66] are presented below.

[1] The electron number density is sometimes only denoted by n, dropping the subscript.

[2] Both ρ and j are called "emission-polarisation tensor", however the latter refers to a distribution of electrons.

[3] "Polar angle" is used in lack of a better name. The angle θ is for the most part not referenced by a specified name in the text.

Symbol	Name	Value	
k_B	Boltzmann's constant	1.380649×10^{-16}	$\mathrm{cm^2\,g\,s^{-2}\,K^{-1}}$
e	Electron charge	$4.8032047 \times 10^{-10}$	$\mathrm{cm^{3/2}\,g^{1/2}\,s^{-1}}$
m_e	Electron mass[4]	$9.1093837015(58) \times 10^{-28}$	g
$\hbar$	Reduced Planck's constant	$1.054571817 \times 10^{-27}$	$\mathrm{cm^2\,g\,s^{-1}}$
c	Speed of light in vacuum	$2.99792458 \times 10^{10}$	$\mathrm{cm\,s^{-1}}$

[4]In the text we have in many places only written m for the electron mass, dropping the subscript.

Bibliography

[1] R. Wielebinski. "Technical Report: History of Synchrotron Radiation in Astrophysics". In: *Synchrotron Radiation News* 19.5 (2006), pp. 4–9.

[2] G. C. Fox. "Generation X-ray–A Coming of Age". In: *ARBOR Ciencia, Pensamiento y Cultura* 191.772 (2015), a221.

[3] R. Beck and R. Wielebinski. "Magnetic Fields in the Milky Way and in Galaxies". In: *Planets, Stars and Stellar Systems: Volume 5: Galactic Structure and Stellar Populations*. Ed. by G. Gilmore. Springer, 2013. Chap. 13.

[4] R. Wielebinski. "A History of Radio Astronomy Polarisation Measurements". In: *Journal of Astronomical History and Heritage* 15.2 (2012), pp. 76–95.

[5] J. J. Condon and S. M. Ransom. *Essential Radio Astronomy*. Princeton University Press, 2016.

[6] G. F. Smoot. "The Cosmic Background Radiation, Snowmass Workshop". In: *arXiv preprint astro-ph/9505139* (1995).

[7] J. Singal et al. "The Second Radio Synchrotron Background Workshop: Conference Summary and Report". In: *Publications of the Astronomical Society of the Pacific* 135.1045 (2023), p. 036001.

[8] J. P. Leahy. "Polarization structures in the northern hemisphere: fractional polarization and constraints on field tangling". In: Radio Synchrotron Background Conference. June 2022. URL: `https://agenda.infn.it/event/28184/contributions/143591/attachments/92542/126021/Leahy_BAM_2022.pdf`.

[9] G. B. Rybicki and A. P. Lightman. *Radiative Processes in Astrophysics*. John Wiley & Sons, 1991.

[10] M. S. Longair. *High Energy Astrophysics*. Cambridge University Press, 2011.

[11] K. C. Westfold. "The Polarization of Synchrotron Radiation". In: *Astrophysical Journal* 130 (1959), p. 241.

[12] M. P. C. Legg and K. C. Westfold. "Elliptic Polarization of Synchrotron Radiation". In: *Astrophysical Journal* 154 (1968), p. 499.

[13] S. Galtier. *Introduction to Modern Magnetohydrodynamics*. Cambridge University Press, 2016.

[14] F. Boulanger et al. "IMAGINE: A comprehensive view of the interstellar medium, Galactic magnetic fields and cosmic rays". In: *Journal of Cosmology and Astroparticle Physics* 2018.08 (2018), p. 049.

[15] D. Manreza Paret et al. "Magnetic fields in compact stars and related phenomena". In: *Revista mexicana de física* 66.5 (2020), pp. 538–558.

[16] B. W. Carroll and D. A. Ostlie. *An Introduction to Modern Astrophysics*. Cambridge University Press, 2017.

[17] M. Haverkorn. “Magnetic Fields in the Milky Way”. In: *Magnetic Fields in Diffuse Media*. Springer, 2014, pp. 483–506.

[18] M. I. R. Alves et al. “The Local Bubble: a magnetic veil to our Galaxy”. In: *Astronomy & Astrophysics* 611 (2018), p. L5.

[19] K. Akiyama et al. “First Sagittarius A* Event Horizon Telescope Results. VII. Polarization of the Ring”. In: *The Astrophysical Journal Letters* 964.2 (2024), p. L25.

[20] Telescope Array Collaboration et al. “An extremely energetic cosmic ray observed by a surface detector array”. In: *Science* 382.6673 (2023), pp. 903–907.

[21] M. Unger and G. R. Farrar. “Where Did the Amaterasu Particle Come From?” In: *The Astrophysical Journal Letters* 962.1 (2024), p. L5.

[22] M. Unger and G. R. Farrar. “The Coherent Magnetic Field of the Milky Way”. In: *arXiv:astro-ph.GA/2311.12120* (2023).

[23] R. Jansson and G. R. Farrar. “The Galactic Magnetic Field”. In: *The Astrophysical Journal Letters* 761.1 (2012), p. L11.

[24] R. Adam et al. “Planck intermediate results. XLII. Large-scale Galactic magnetic fields”. In: *Astronomy & Astrophysics* 596 (2016), A103.

[25] G. Giacinti, M. Kachelriess, and D. V. Semikoz. “Reconciling cosmic ray diffusion with Galactic magnetic field models”. In: *Journal of Cosmology and Astroparticle Physics* 2018.07 (2018), p. 051.

[26] N. Oppermann et al. “An improved map of the Galactic Faraday sky”. In: *Astronomy & Astrophysics* 542 (2012), A93.

[27] K. Ferrière, J. L. West, and T. R. Jaffe. “The correct sense of Faraday rotation”. In: *Monthly Notices of the Royal Astronomical Society* 507.4 (2021), pp. 4968–4982.

[28] R. Adam et al. “Planck 2015 results. I. Overview of products and scientific results”. In: *Astronomy & Astrophysics* 594 (2016), A1.

[29] A. R. Choudhuri. *Astrophysics for Physicists*. Cambridge University Press, 2010.

[30] S. B. Pope. *Turbulent Flows*. Cambridge University Press, 2000.

[31] J. Latt et al. “Palabos: Parallel Lattice Boltzmann Solver”. In: *Computers & Mathematics with Applications* 81 (2021), pp. 334–350.

[32] M. Blytt, M. Kachelrieß, and S. Ostapchenko. “ELMAG 3.01: A three-dimensional Monte Carlo simulation of electromagnetic cascades on the extragalactic background light and in magnetic fields”. In: *Computer Physics Communications* 252 (2020), p. 107163.

[33] J. Giacalone and J. R. Jokipii. “Charged-Particle Motion in Multidimensional Magnetic Field Turbulence”. In: *The Astrophysical Journal* 430.2.2 (1994), pp. L137–L140.

[34] J. Giacalone and J. R. Jokipii. “The Transport of Cosmic Rays across a Turbulent Magnetic Field”. In: *The astrophysical journal* 520.1 (1999), p. 204.

[35] C. Evoli et al. “Cosmic-Ray Nuclei, Antiprotons and Gamma-rays in the Galaxy: a New Diffusion Model”. In: *Journal of Cosmology and Astroparticle Physics* 2008.10 (2008), p. 018.

[36] R. Jansson and G. R. Farrar. “A New Model of the Galactic Magnetic Field”. In: *The Astrophysical Journal* 757.1 (2012), p. 14.

[37] J. M. Cordes and T. J. W. Lazio. “NE2001. I. A New Model for the Galactic Distribution of Free Electrons and its Fluctuations”. In: *arXiv:astro-ph/0207156* (2002).

[38] J. M. Yao, R. N. Manchester, and N. Wang. “A New Electron Density Model for Estimation of Pulsar and FRB Distances”. In: *The Astrophysical Journal* 835.1 (2017), p. 29.

[39] C. L. Bennett et al. "Nine-Year Wilkinson Microwave Anisotropy Probe (WMAP) Observations: Final Maps and Results". In: *The Astrophysical Journal Supplement Series* 208.2 (2013), p. 20.

[40] Y. Akrami et al. "Planck 2018 results. IV. Diffuse component separation". In: *Astronomy & Astrophysics* 641 (2020), A4.

[41] D. J. Watts et al. "COSMOGLOBE DR1 results. I. Improved Wilkinson Microwave Anisotropy Probe maps through Bayesian end-to-end analysis". In: *Astronomy & Astrophysics* 679 (2023), A143.

[42] G. N. Watson. *A treatise on the theory of Bessel functions*. 2nd ed. Cambridge University Press, 1966.

[43] R. P. Walker. "Synchrotron radiation". In: *CAS - CERN Accelerator School: 5th General Accelerator Physics Course* (1994), pp. 437–459.

[44] A. Gonoskov et al. "Charged particle motion and radiation in strong electromagnetic fields". In: *Reviews of Modern Physics* 94.4 (2022), p. 045001.

[45] C. F. Bohren and E. E. Clothiaux. *Fundamentals of Atmospheric Radiation: An Introduction with 400 Problems*. John Wiley & Sons, 2006.

[46] M. Abramowitz and I. A. Stegun. *Handbook of Mathematical Functions with Formulas, Graphs, and Mathematical Tables*. Vol. 55. US Government printing office, 1972.

[47] J. Dexter. "A public code for general relativistic, polarised radiative transfer around spinning black holes". In: *Monthly Notices of the Royal Astronomical Society* 462.1 (2016), pp. 115–136.

[48] J. Hižak and R. Logožar. "A Derivation of the Mean Absolute Distance in One-Dimensional Random Walk". In: *Tehnički glasnik* 5.1 (2011), pp. 10–16.

[49] D. Andreucci et al. "Fick and Fokker—Planck Diffusion Law in Inhomogeneous Media". In: *Journal of Statistical Physics* 174 (2019), pp. 469–493.

[50] L. C. Evans. *Partial Differential Equations*. Vol. 19. American Mathematical Society, 2022.

[51] V. L. Ginzburg and S. I. Syrovatskii. *The Origin of Cosmic Rays*. Pergamon, 1964.

[52] M. Aguilar et al. "Towards Understanding the Origin of Cosmic-Ray Positrons". In: *Physical review letters* 122.4 (2019), p. 041102.

[53] M. Aguilar et al. "Precision Measurement of the (e+ + e-) Flux in Primary Cosmic Rays from 0.5 GeV to 1 TeV with the Alpha Magnetic Spectrometer on the International Space Station". In: *Physical review letters* 113.22 (2014), p. 221102.

[54] M. S. Potgieter. "Solar Modulation of Cosmic Rays". In: *Living Reviews in Solar Physics* 10 (2013), pp. 1–66.

[55] D. Bisschoff, M. S. Potgieter, and O. P. M. Aslam. "New very local interstellar spectra for electrons, positrons, protons, and light cosmic ray nuclei". In: *The Astrophysical Journal* 878.1 (2019), p. 59.

[56] A. C. Cummings et al. "Galactic Cosmic Rays in the Local Interstellar Medium: Voyager 1 Observations and Model Results". In: *The Astrophysical Journal* 831.1 (2016), p. 18.

[57] O. Adriani et al. "Time dependence of the e- flux measured by PAMELA during the July 2006 - December 2009 solar minimum". In: *The Astrophysical Journal* 810.2 (2015), p. 142.

[58] G. Di Bernardo et al. "Cosmic Ray Electrons, Positrons and the Synchrotron emission of the Galaxy: consistent analysis and implications". In: *Journal of Cosmology and Astroparticle Physics* 2013.03 (2013), p. 036.

[59] A. de Oliveira-Costa et al. “A Model of Diffuse Galactic Radio Emission from 10 MHz to 100 GHz”. In: *Monthly Notices of the Royal Astronomical Society* 388.1 (2008), pp. 247–260.

[60] C. G. T. Haslam et al. “A 408-MHZ All-Sky Continuum Survey. II. The Atlas of Contour Maps”. In: *Astronomy and Astrophysics Supplement Series* 47 (1982), p. 1.

[61] V. Heesen et al. “Detection of magnetic fields in the circumgalactic medium of nearby galaxies using Faraday rotation”. In: *Astronomy & Astrophysics* 670 (2023), p. L23.

[62] D. de Búrca and A. Shearer. “Circular polarization of synchrotron radiation in high magnetic fields”. In: *Monthly Notices of the Royal Astronomical Society* 450.1 (2015), pp. 533–540.

[63] M. Remazeilles et al. “An improved source-subtracted and destriped 408-MHz all-sky map”. In: *Monthly Notices of the Royal Astronomical Society* 451.4 (2015), pp. 4311–4327.

[64] K. M. Gorski et al. “HEALPix: A Framework for High-Resolution Discretization and Fast Analysis of Data Distributed on the Sphere”. In: *The Astrophysical Journal* 622.2 (2005), p. 759.

[65] F. Olver et al. *NIST Handbook of Mathematical Functions*. Cambridge University Press, 2010.

[66] E. Tiesinga et al. “CODATA Recommended Values of the Fundamental Physical Constants: 2018”. In: *Reviews of Modern Physics* 93 (2021), p. 025010.

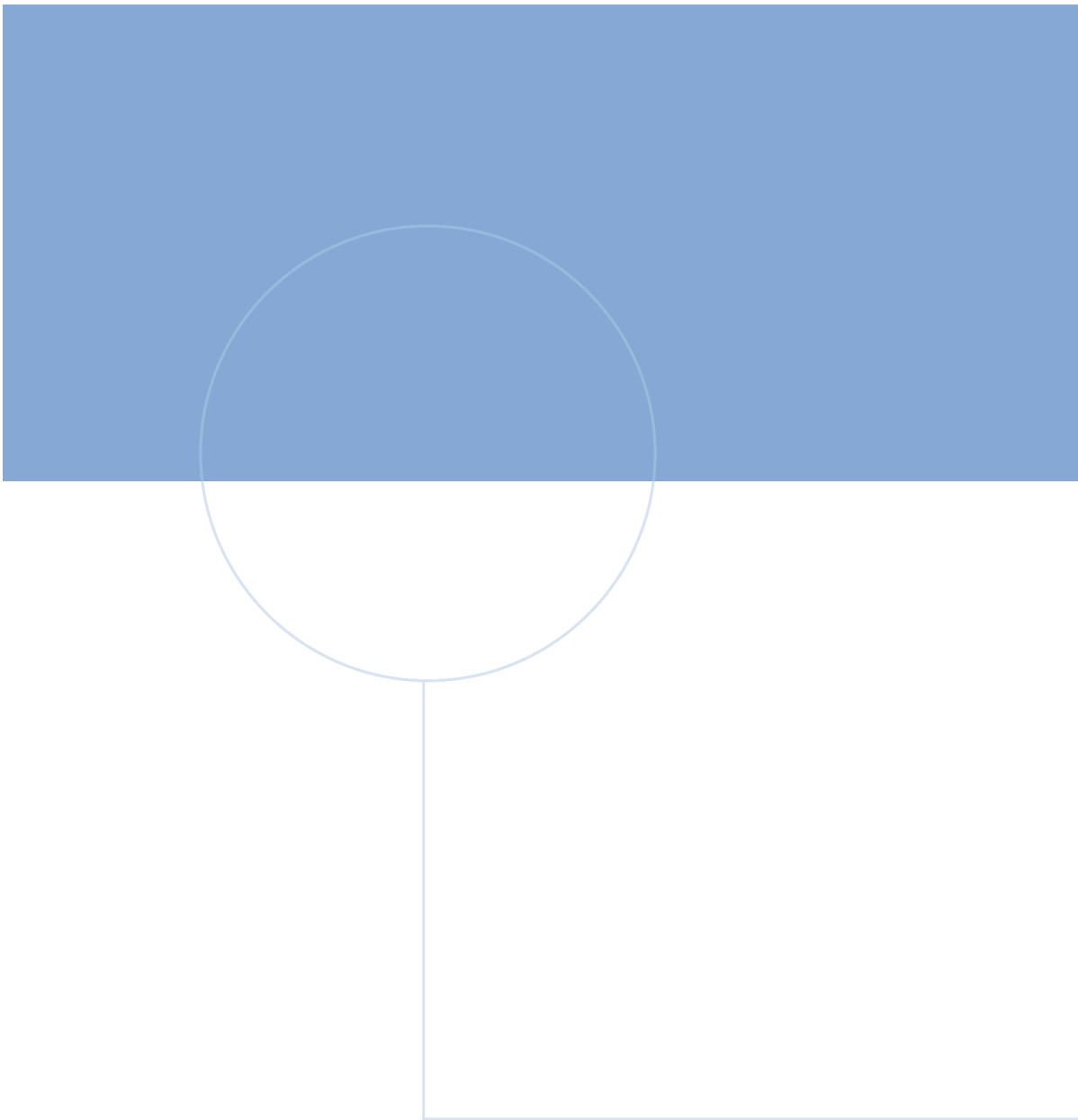

NTNU

Norwegian University of
Science and Technology